CHEMICAL REVIEWS

pubs.acs.org/CR

Review

Vanadium Oxide: Phase Diagrams, Structures, Synthesis, and Applications

Peng Hu,*,# Ping Hu,# Tuan Duc Vu, Ming Li, Shancheng Wang, Yujie Ke, Xianting Zeng, Liqiang Mai,* and Yi Long*

Cite This: *Chem. Rev.* 2023, 123, 4353–4415

Read Online

ACCESS | Metrics & More | Article Recommendations

ABSTRACT: Vanadium oxides with multioxidation states and various crystalline structures offer unique electrical, optical, optoelectronic and magnetic properties, which could be manipulated for various applications. For the past 30 years, significant efforts have been made to study the fundamental science and explore the potential for vanadium oxide materials in ion batteries, water splitting, smart windows, supercapacitors, sensors, and so on. This review focuses on the most recent progress in synthesis methods and applications of some thermodynamically stable and metastable vanadium oxides, including but not limited to V_2O_3, V_3O_5, VO_2, V_3O_7, V_2O_5, V_2O_2, V_6O_{13}, and V_4O_9. We begin with a tutorial on the phase diagram of the V−O system. The second part is a detailed review covering the crystal structure, the synthesis protocols, and the applications of each vanadium oxide, especially in batteries, catalysts, smart windows, and supercapacitors. We conclude with a brief perspective on how material and device improvements can address current deficiencies. This comprehensive review could accelerate the development of novel vanadium oxide structures in related applications.

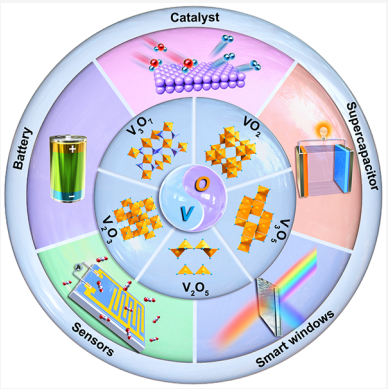

CONTENTS

Received: August 4, 2022
Published: March 27, 2023

https://doi.org/10.1021/acs.chemrev.2c00546
Chem. Rev. 2023, 123, 4353−4415

1. INTRODUCTION

1.1. Vanadium

Vanadium was first discovered by Andrés Manuel del Rio in Mexico City from $Pb_5(VO_4)_3Cl$ in 1801.[1] However, it was wrongly identified as a form of chromium by Hippolyte Victor Collet-Descotils in 1805.[2] Until 1831, Swedish chemist Nil Gabriel Self-ström in Stockholm named the element vanadium, which is from the Norse Goddess Vanadis and means beauty and fertility.[3] In the Earth's crust, vanadium is the 20th most abundant element and the sixth most abundant element among the transition metals.[3−5] However, some literature indicates that vanadium is the fourth most abundant transition metal after iron, titanium, and manganese.[5−8] High purity vanadium (about 99.7%) was first produced in 1925 by reducing vanadium pentoxide (V_2O_5) with calcium metal.[1] Pure vanadium exhibits a transition metal feature, which shows a high melting point and good corrosion resistance at low temperatures. Vanadium can be dissolved in nitric and sulfuric acids but is insoluble in hydrochloric acid.[9] In nature, vanadium is difficult to exist in metal form because it easily reacts with oxygen, even nitrogen and carbon at elevated temperatures.[2,10] Vanadium is an important component of specific steel alloys, which provides additional tensile strength and extra protection against rust and corrosion of these materials.

1.2. Vanadium Oxides

Vanadium has the electronic configuration $[Ar]4s^23d^3$. Therefore, the oxidation state of vanadium can range from +5 to −3, and the valences of +5, +4, +3, and +2 are most commonly observed.[11,12] Four vanadium oxides feature single oxidation states (+2 for VO, +3 for V_2O_3, +4 for VO_2, and +5 for V_2O_5), and others have mixed oxidation states. Different oxidation states exhibit various colors: +5 (orange to yellow), +4 (blue), and +3 (green).[9] The vanadium oxides exhibit crystalline structures with different oxygen coordinations, which result in the formation of octahedral, pentagonal bipyramids, square pyramids, and tetrahedral sharing corners, edges, or faces.[12] The oxidation state of the vanadium cations dramatically affects the physicochemical properties of the vanadium oxides with different phases.

Due to the multioxidation states and various crystalline structures, the vanadium oxides exhibit excellent intercalation properties to host−guest molecules or ions,[5] giving excellent catalytic activities,[4] strong electron−electron correlations,[13] outstanding phase transitions (metal−insulator transition),[14] and high electrical conductivity.[5] Furthermore, the abundant nanostructures of vanadium oxides can be achieved by different preparation methods, which not only shorten the transportation distance of ions or electrons and yield a faster solid-state diffusion in electrochemical energy conversion systems,[15,16] but also provide more active positions for the interaction with other molecules or ions and more exposed active crystal facets for catalysis applications.[17,18] Thus, the vanadium oxides provide promising applications in energy conversion/saving fields,[19,20] such as ion batteries,[21−25] water splitting,[26] smart windows,[27,28] supercapacitors,[29,30] sensors,[31] and so on.

A series of vanadium oxides with strong electron−electron correlations exhibit metal−insulator transition (MIT). The V_2O_3, VO_2, and V_2O_5 with single oxidation undergo MIT at 160 K,[32] 340 K,[33] and 530 K,[34] respectively. These phase transitions are reversible and accompanied by a change of crystallographic, magnetic, optical, and electrical properties. The mixed-valence vanadium oxides belong to either Magnéli series (V_nO_{2n-1}) or Wadsley series (V_nO_{2n+1}). For the Wadsley series, V_3O_7 and V_6O_{13} exhibit the phase transition at 5.2 and 155 K, respectively.[35,36] Except for V_7O_{13} (metallic), all the Magnéli series show a transition from a paramagnetic to an antiferromagnetic state and consequently exhibit an antiferromagnetic ground state at low temperatures, including V_3O_5 (430 K), V_4O_7 (250 K), V_5O_9 (135 K), V_6O_{11} (170 K), and V_8O_{15} (70 K) with different phase transition temperatures, respectively.[37]

1.3. Scope of the Review

Vanadium oxides have a long history and rapid development in recent years as they are one of the most promising candidates in versatile applications in batteries, energy-saving smart windows, sensors, catalysts, optoelectronic devices, and so on. Therefore, many research papers and reviews have been published. Pioneering reviews on the chemistry of oxovanadium were published in 1965.[38] The synthesis of vanadium oxides through hydrothermal and gas phase was reviewed by Whittingham,[39] Livage,[40] and Bahlawane.[41] The atomic layer deposition of vanadium oxides was summarized by Papakonstantinou.[12] The synthesis, properties, and applications of vanadium oxide nanotube were described by Kianfar.[6] The catalytic applications of vanadium oxides have been described by Delferro,[3] Hess,[42] Carrero,[43] and Granozzi.[44] The Raman spectroscopy of vanadium oxides was recently reviewed by Shvets.[45] The sensing properties of vanadium oxide nanostructures were described by Sheikhi[46] and Madanagurusamy.[31] The energy-related applications of vanadium oxides were reviewed by Xie,[5,20] Jiang,[4] and Streb.[47] A large number of reviews described the progress in metal ions batteries, including those by Chen,[25] O'Dwyer,[22] Mai,[21,24,48] Lowe,[23] Whittingham,[49] Rashada,[50] Lee,[51] Yang,[52] Zheng,[53] Kim,[54] Liang,[55] and Cao.[56] The vanadium oxides in supercapacitors were reviewed by Chen,[30] Dutta,[57] and Li.[29] Furthermore, our group also reviewed the multistimuli responsive properties and energy applications of some vanadium oxides.[19,27,58,59]

The great potential of vanadium oxides for new applications and accelerated industrialization led to the dramatically increase of the importance of vanadium oxides over the last 5−10 years. Furthermore, due to the complexity of various oxidation states of vanadium, vanadium oxides show a large variety of stable and metastable structures, which pose an inevitable challenge to synthesize vanadium oxides with high purity, well controlled stoichiometry, and meticulously designed nanostructures, a must for high performance devices. Even though lots of reviews have been published, most of them focus on a specific kind or application of vanadium oxides, such as batteries, spectra, supercapacitors, and so on. No comprehensive reviews illustrate the different vanadium oxides with different applications. In this

https://doi.org/10.1021/acs.chemrev.2c00546
Chem. Rev. 2023, 123, 4353−4415

review, we focus on the most recent progress on the structure, synthesis, and applications of five thermodynamically stable vanadium oxides (V_2O_3, V_3O_5, VO_2, V_3O_7, V_2O_5) and some metastable vanadium oxides (V_2O_2, V_6O_{13}, V_4O_9, etc.), which can provide a better understanding of a specific vanadium oxide phase and their process-structure−property interrelationships. Figure 1 summarizes the main contents of this review. This

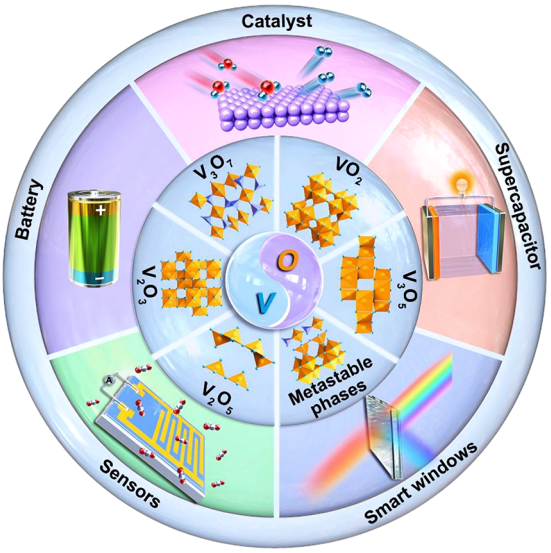

Figure 1. Schematic illustration of the thermodynamically stable vanadium oxides and their applications.

review begins with the phase diagram of the V−O system to show the different vanadium oxide phases, followed by the vanadium oxides with different stoichiometries. For each vanadium oxide, the structures, synthesis methods, and applications in several fields will be covered. The last section presents the future prospects and a summary of this review.

2. PHASE DIAGRAM OF THE V−O SYSTEM

The V−O binary phase diagram was compiled according to previously reported experimental data in 1989.[60] The oxygen-rich phases are well-defined, which reveal more than 20 compounds.[41] However, the vanadium-rich phases exhibit broad homogeneity ranges and high nonstoichiometry.[61,62]

Several groups have calculated the V−O binary phase diagram.[61−64] Figure 2a shows a calculated phase diagram of the V−O system in the entire composition range at 1 atm. In the V-rich range, four types of solid solutions exist. The α and β solid solutions are formed by a certain amount of oxygen dissolved in the vanadium. The maximum solubilities of oxygen in α-V and β-V phase are up to 17.9 atom % and 27.4 atom %, respectively. The β-phase exhibits a wide range of homogeneities. With the increase of oxygen content, the γ and δ solid solutions phase can be formed. The γ-phase is monoclinic and δ-phase has the stoichiometry of VO with NaCl-type structure.

For the stoichiometric phases, only five phases are thermodynamically stable compositions as pure compounds, which include divanadium trioxide (V_2O_3, cubic, $Ia3$), trivanadium pentoxide (V_3O_5, monoclinic, $P2/c$), vanadium dioxide (VO_2, tetragonal, $P4_2/mnm$), trivanadium heptaoxide (V_3O_7, monoclinic, $C2/c$), and divanadium pentoxide (V_2O_5, orthorhombic, $Pmnm$). Other metastable phases or unstable phases are likely to decompose to stable phases. All the stable

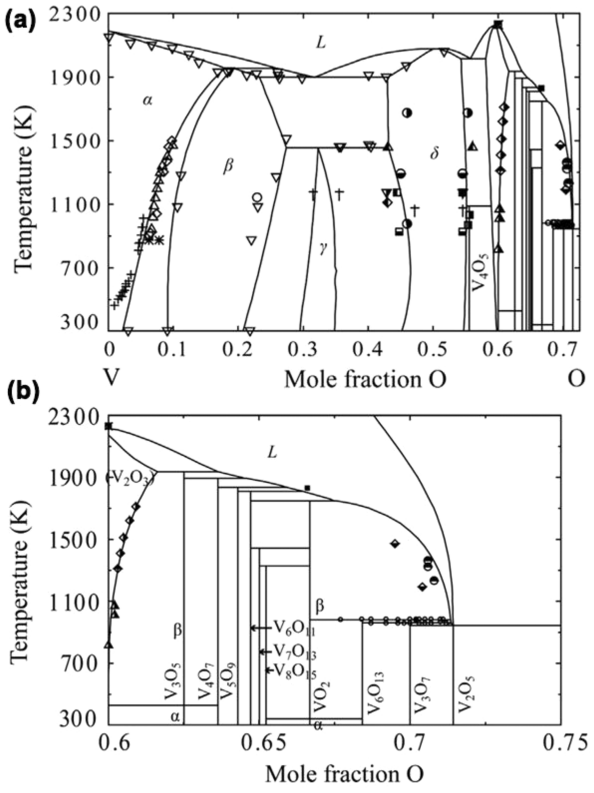

Figure 2. (a) Calculated phase diagram of the V−O system in the entire composition range at 1 atm. (b) Enlarged phase diagram of the V_2O_3−V_2O_5 system at 1 atm. Reproduced with permission from ref 61. Copyright 2015 Elsevier.

and metastable phases are listed in the enlarged phase diagram of the V_2O_3−V_2O_5 system, which is shown in Figure 2b.

There are two types of vanadium oxides with a mixed valence of vanadium. One is the Magnéli series, which is defined by the general stoichiometric formula:

$$V_nO_{2n-1} = V_2O_3 + (n-2)VO_2 \text{ where } 3 \le n \le 9$$

This type of homologous series has been reported for molybdenum oxides for the first time by Magnéli.[65] The other homologous series is the Wadsley series, which has the general formula of V_nO_{2n+1} ($n \ge 3$). All the Magnéli phases maintain a triclinic symmetry ($P1$) and are metastable. They are expected to yield VO_2 and V_3O_5 after lowering the system entropy. For the Wadsley series, V_3O_7 exhibits lower formation entropy compared with other Wadsley phases, which indicates the phase is more stable. Other Wadsley phases, such as V_4O_9 and V_6O_{13}, can be decomposed into a mixture of VO_2 and V_3O_7.[41] V_4O_9 and V_6O_{13} show multiple metastable crystalline structures due to the close formation energies. Therefore, these compounds are candidates for polymorphism, where three crystalline structures were identified for V_6O_{13} and two for V_4O_9.[60]

3. V_2O_3

3.1. Structures and Synthesis

V_2O_3 has a typical corundum-type hexagonal structure (space group: $R\bar{3}c$) with lattice parameters of $a = b = 4.9492(2)$ Å, $c = 13.988(1)$ Å at room temperature.[66,67] The crystal structures of V_2O_3 viewed in different directions are illustrated in Figure 3. It is interesting that after being calcined at 600 °C for several hours, vanadium vacancies (red circle in Figure 3a) formed, which is

https://doi.org/10.1021/acs.chemrev.2c00546
Chem. Rev. 2023, 123, 4353−4415

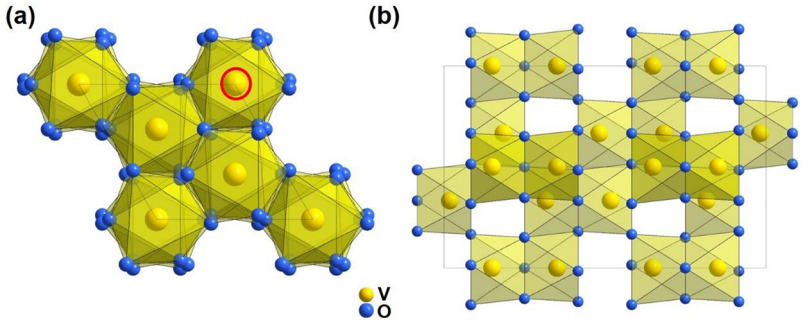

Figure 3. Perspective view of V_2O_3: (a) along the (001) direction; (b) along the (110) direction.

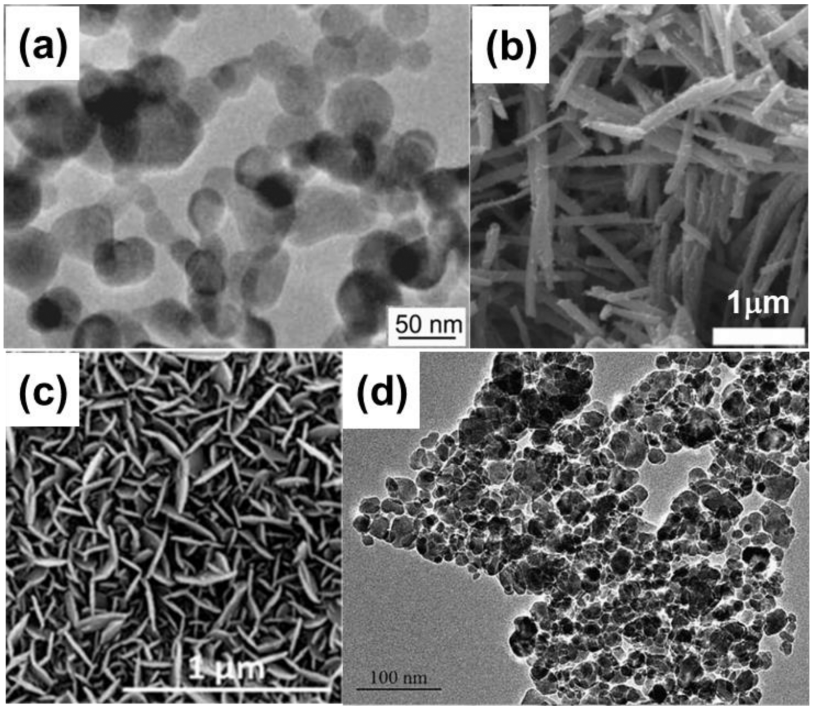

Figure 4. (a) Typical TEM image of V_2O_3 nanocrystals. Reproduced with permission from ref 69. Copyright 2012 Elsevier. (b) SEM image of V_2O_3 nanorods after reduction (time = 3 h and temperature = 600 °C). Reproduced with permission from ref 70. Copyright 2008 American Chemical Society. (c) SEM images of V_2O_3 nanosheets. Reproduced with permission from ref 73. Copyright 2018 Royal Society of Chemistry. (d) TEM of V_2O_3 nanocrystals. Reproduced with permission from ref 74. Copyright 2004 Elsevier.

suitable for aqueous zinc metal batteries.[67] From another viewing direction, V_2O_3 possesses an open tunnel structure consisting of a 3D V−V framework (Figure 3b).[68] Such tunnel structures could efficiently facilitate the insertion of alkali metal ions, which provide potential application in metal ion batteries.

V_2O_3 with different morphologies can be obtained by several methods, including reduction, oxidation, and hydrothermal approaches. For the reduction pathway, V_2O_5 was employed as initial materials, and hydrogen or ammonia gas was used as reducing agents, whereas vanadium metal was used as a starting material for the oxidation method. In the hydrothermal route, vanadium alkoxides or sulfides with some small organic molecules (e.g., thiourea, benzyl alcohol, etc.) were added together to the autoclave to grow V_2O_3.

Li et al.[69] designed a plasma hydrogen reduction system to synthesize V_2O_3 nanocrystals via a single precursor of V_2O_5 powders. The coarse-grained V_2O_5 powders are injected into the hydrogen plasma by a powder feeder, reducing the V_2O_5 powders into V_2O_3 by hydrogen. Such single crystalline V_2O_3 nanocrystals have a spherical shape with average sizes in the range of 35−50 nm (Figure 4a). The morphology of the raw materials determines the V_2O_3 morphology. Seshadri et al.[70] first synthesized the V_2O_5 nanorods via a hydrothermal reaction followed by reducing in 5% H_2:95% N_2 (reduction time = 3 h and reduction temperature = 600 °C) to obtain V_2O_3 nanorods (Figure 4b). The ammonia gas (NH_3) is another agent to reduce V_2O_5 to V_2O_3.[71] V_2O_3 shows a much larger size with several micrometers, and the morphologies of the V_2O_3 particles were micrometer layered structures that were assembled by nanometer or micrometer sheets. Tao et al.[72] reported that the V_2O_3 nanoparticles had been synthesized by supercritical ethanol fluid reduction of VOC_2O_4 with an average size of 50 μm. Madanagurusamy et al. employed the oxidation way to obtain the V_2O_3 nanosheets.[73] High-density vertically aligned V_2O_3 nanosheets on glass substrates were obtained via a simple one-step sputtering technique. Vanadium metal was first deposited on the well-cleaned glass substrates followed by oxidation in the argon and oxygen mixture gas with a ratio of 3:1. Well-ordered, ultrathin, vertically aligned V_2O_3 nanosheets with voids were obtained (Figure 4c).

https://doi.org/10.1021/acs.chemrev.2c00546
Chem. Rev. 2023, 123, 4353−4415

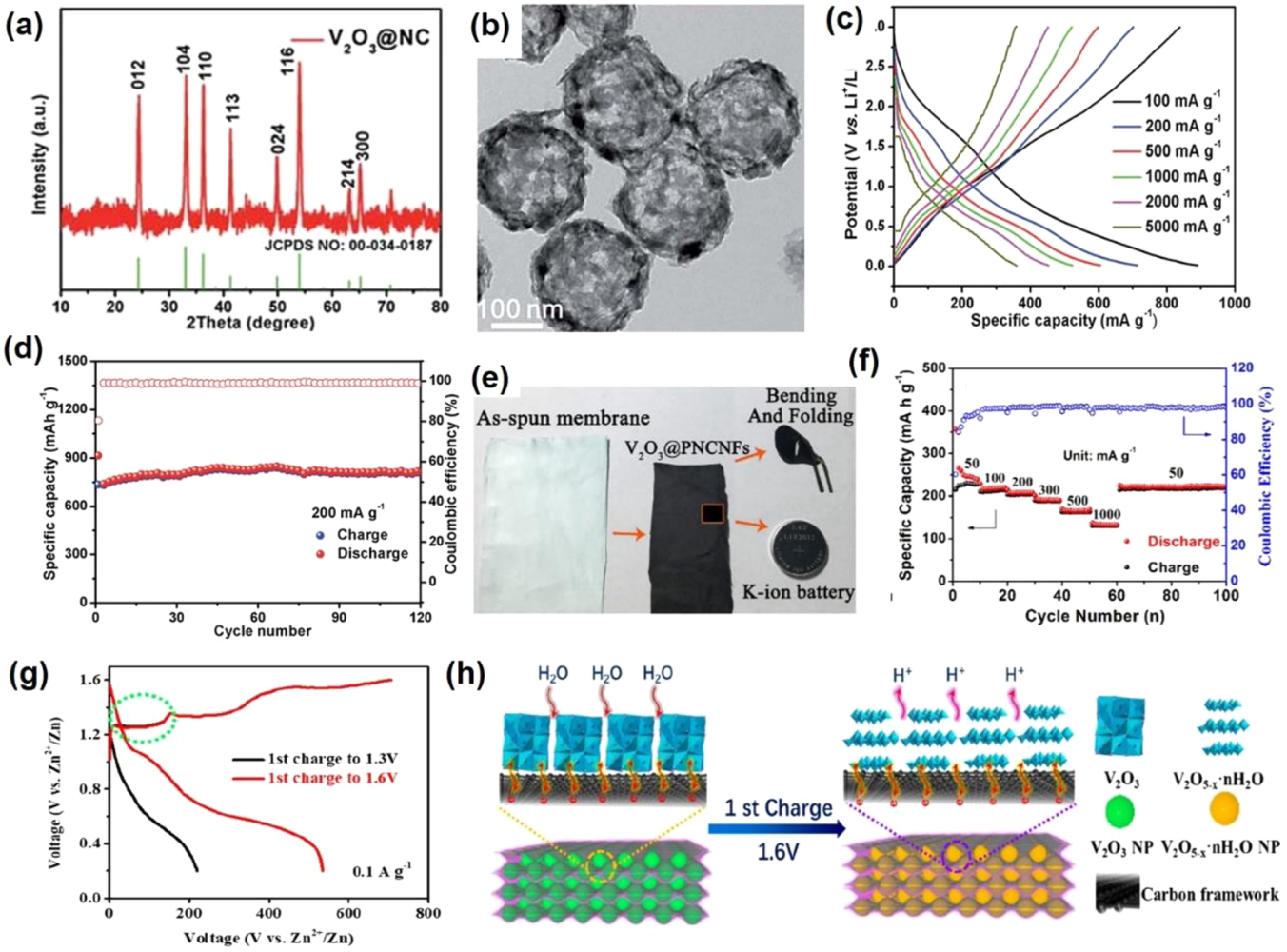

Figure 5. XRD pattern (a), SEM image (b), charge/discharge profiles (c), and cycling performance (d) of V_2O_3@NC hollow spheres. Reproduced with permission from ref 76. Copyright 2018 Royal Society of Chemistry. The digital photos of the as-spun membrane and the self-standing (e), and rate performance (f) of V_2O_3@PNCNFs. Reproduced with permission from ref 68. Copyright 2018 Elsevier. The charge/discharge profiles at different voltage window (g) and schematic illustration of the oxidation at full charge state (h) of V_2O_3. Reproduced with permission from ref 77. Copyright 2020 American Chemical Society.

Hydrothermal is one of the most popular methods for crystal growth, which is conducted under moderate temperature and a high vapor pressure environment in sealed containers with the unique advantages of being easy to handle and environmentally friendly. Compared with the reduction and oxidation methods, the hydrothermal reaction is more convenient for synthesis the V_2O_3 with various morphologies. Niederberger et al.[74] adopted vanadium alkoxides and benzyl alcohol as precursors to synthesize V_2O_3 nanocrystals through hydrothermal reaction sizes ranging from 20 to 50 nm with good yields (Figure 4d). Without using any surfactant and template, Su et al.[75] successfully synthesized dandelion-like V_2O_3 microspheres with core−shell structures. With increasing reaction time, the morphology of V_2O_3 can be tuned from a solid sphere to dandelion-like. If the reaction time is further increased, some broken V_2O_3 microspheres with core−shell structures could be observed with an average diameter of the core−shell microspheres of 2 μm.

3.2. Applications

3.2.1. Batteries. As the low valence of V^{3+} in vanadium oxide, corundum-type V_2O_3 with a metallic behavior shows that the electrons in the V-3d orbital travel along the V−V chains. The 3D V−V framework provides an intrinsic tunnel structure, which is suitable for ion transport and intercalation. Mai et al. reported uniform nitrogen-doped carbon-confined V_2O_3 (V_2O_3@NC) hollow spheres (Figure 5a). The *in situ* carbonization hollow structure can provide high ion/electron conductivity, short diffusion distance, and excellent structure adaptability, which is beneficial for lithium-ion storage (Figure 5b). The V_2O_3@NC delivers an average discharge capacity of 785, 599, 528, and 361 mAh g^{-1} at a current density of 100, 500, 1000, and 5000 mA g^{-1}, respectively (Figure 5c). Furthermore, 811 mAh g^{-1} can be maintained after 120 cycles at a current density of 200 mA g^{-1} (Figure 5d).[76] In addition, V_2O_3 can also be used as other ions ($Na^+/K^+/Zn^{2+}$) storage material. Jiao's group[68] fabricated a flexible and self-standing electrode of V_2O_3 nanoparticles embedded in porous N-doped carbon nanofibers (V_2O_3@PNCNFs) through electrospinning assisted high-temperature sintering method, which can directly be used as a KIB anode material (Figure 5e). V_2O_3@PNCNFs deliver a capacity of 240 and 134 mAh g^{-1} at a current density of 50 and 1000 mA g^{-1}, respectively. High-capacity retention of 94.5% can be maintained after 500 cycles (Figure 5f). The density functional theory (DFT) results demonstrate that 1 mol K^+ can insert into the V_2O_3 crystal forming KV_2O_3, with the K^+

https://doi.org/10.1021/acs.chemrev.2c00546
Chem. Rev. 2023, 123, 4353−4415

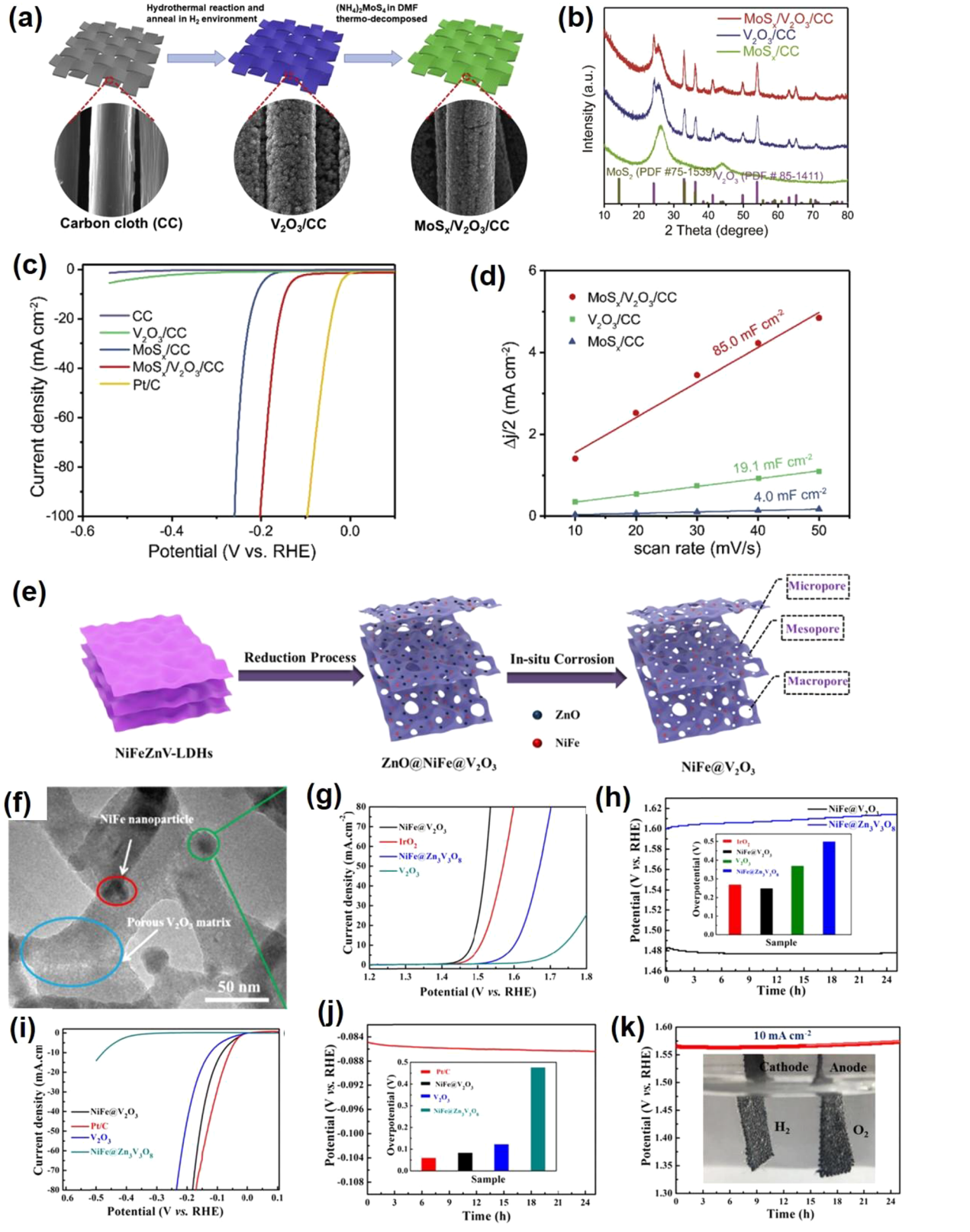

Figure 6. (a) Schematic diagram of the main steps in the synthesis of the MoS_x/V_2O_3/CC. (b) XRD patterns of MoS_x/V_2O_3/CC, V_2O_3/CC, and MoS_x/CC. (c) Polarization curves for MoS_x/V_2O_3/CC. (d) Double-layer capacitance for MoS_x/V_2O_3/CC. Reproduced with permission from ref 82. Copyright 2020 Elsevier. (e) Synthetic strategy for preparing 3D hierarchical nanoporous NiFe@V_2O_3. (f) High-magnification TEM image of NiFe@V_2O_3. (g) OER polarization curves of NiFe@V_2O_3. (h) Long-term durability test conducted at 10 mA cm^{-2} of NiFe@V_2O_3. (i) HER polarization curves of NiFe@V_2O_3. (j) Long-term durability test conducted at 10 mA cm^{-2} of NiFe@V_2O_3. (k) Long-term potential-time curve set at 10 mA cm^{-2} of NiFe@V_2O_3||NiFe@V_2O_3 in 1.0 M KOH. Reproduced with permission from ref 80. Copyright 2019 American Chemical Society.

https://doi.org/10.1021/acs.chemrev.2c00546
Chem. Rev. 2023, 123, 4353−4415

occupying the 6e sites of the KV_2O_3 crystal. The main capacity of V_2O_3 in KIB is main contribution from capacitance (surface or near-surface redox reactions), which is very different from the conversion reaction of conventional transition metal oxides for ion storage. When K^+ inserts into the tunnels of V_2O_3@PNCNFs, the material exhibits no structural phase transitions, which indicates that V_2O_3@PNCNFs can exhibit excellent K^+ rate/cycling performance. This work suggests that the pseudocapacitive electrode materials could be suitable for a large-scale energy storage system. Generally, the conventional low valent V_2O_3 cannot effectively accommodate Zn^{2+} intercalation during the discharging process due to its inherently unsuitable structure and inferior physicochemical properties. Luo et al.[77] attempted to utilize V_2O_3 in aqueous ZIBs by the *in situ* anodic oxidation strategy, and the hierarchical microcuboid structure V_2O_3 can accommodate nearly 2 electrons intercalation. Moreover, they found H_2O is a reactant that participates in the first charge oxidation process of V_2O_3. Furthermore, the porous structure with a higher specific surface area of the V_2O_3 leads to more reaction sites and a faster phase transition from V_2O_3 to $V_2O_{5-x}{\cdot}nH_2O$ (Figure 5h). Meanwhile, the high surface and the small size of V_2O_3 nanoparticles benefit the first charge oxidation reaction process. The V_2O_3 delivers a Zn^{2+} discharging capacity of 625 mAh g^{-1} at 0.1 A g^{-1}, corresponding to 1.75-electron intercalation (Figure 5g). Specifically, the capacities can maintain 87% and 78% when the current increases to 10 and 20 A g^{-1}, respectively. The V_2O_3 can maintain 100% after 10000 cycles at 10 A g^{-1}, which is better than some previously reported ZIB cathode materials.

3.2.2. Catalysts. V_2O_3 and its composites have been widely used as catalysts for chemical looping dry reforming of methane,[78] ammonium perchlorate decomposition,[79] the hydrogen evolution reaction (HER),[30,80] the oxygen evolution reaction (OER),[80] water splitting,[80] etc.

3.2.2.1. Propane Dehydrogenation and Ammonium Perchlorate Decomposition. Very recently, Zhu et al.[81] examined the catalytic properties of propane dehydrogenation through single transition metal atom doping of a V_2O_3 (0001) surface by self-consistent DFT calculation. The results indicated that the single atoms act as promoters and active sites, and Mn–V_2O_3 is a good candidate as a catalyst for propane dehydrogenation. Huang et al.[79] synthesized V_2O_3 and V_2O_3/carbon composites by a facile hydrothermal route, which exhibited excellent performance for ammonium perchlorate decomposition. The decomposition temperature decreased by 49 and 73 K for V_2O_3 and V_2O_3/carbon composites, respectively.

3.2.2.2. HER, OER, and Water Splitting. Electrocatalytic water splitting consisted of two half-reactions: HER and OER. Electrocatalysis is used to accelerate the rate of a chemical reaction through lowering the activation energy to reduce the electrochemical overpotentials.

V_2O_3 composited with other functional materials can exhibit efficient electrocatalysis performance. Zhang et al.[82] reported a self-supported MoS_x/V_2O_3 heterostructure for the HER. Two steps were involved in the synthesis process (Figure 6a). V_2O_3/carbon cloth (CC) was first obtained by a hydrothermal method, and the dense V_2O_3 was uniformly distributed on CC fibers. The as-prepared V_2O_3/CC was immersed in an ammonium thiomolybdate solution and dried under a vacuum. Then, followed by a thermal decomposition process, the final MoS_x/V_2O_3/CC was successfully achieved with the same morphology as V_2O_3/CC. The XRD pattern (Figure 6b) shows the composite contains the MoS_x and hexagonal V_2O_3. MoS_x/V_2O_3/CC displayed an overpotential of 146 mV to achieve a 10 mA cm^{-2} HER current density (Figure 6c), which is lower than that of MoSx/CC (221 mV). The Tafel slope of MoS_x/V_2O_3/CC is around 45 mV dec^{-1}, suggesting the HER process obeys the Volmer-Heyrovsky mechanism. Meanwhile, the MoS_x/V_2O_3/CC presents a higher double-layer capacitance (C_{dl}: 85 mF cm^{-2}) than MoS_x/CC (4 mF cm^{-2}), indicating V_2O_3 can create more active sites for the HER (Figure 6d). Furthermore, the MoS_x/V_2O_3/CC electrocatalyst has great stability in the acid electrolyte for the HER. Two reasons for the MoS_x/V_2O_3/CC electrocatalyst were given to understand the improved HER activity: (1) V_2O_3 enhanced the electrochemically active surface area with more active sites for the HER; (2) better electron transfer between MoS_x and V_2O_3. Qiu et al.[80] synthesized V_2O_3 nanosheets anchored with NiFe nanoparticles as a bifunctional electrode for overall water splitting. A self-templated strategy was employed to synthesize the NiFe@V_2O_3 (Figure 6e). By a calcined reduction process, ZnO@NiFe@V_2O_3 nanosheets can be obtained. In-situ alkaline media corrosion was performed to dissolve the ZnO NPs and produce the porous NiFe@V_2O_3 nanosheets, which exhibit a clear V_2O_3 porous matrix and NiFe nanoparticles (Figure 6f). The porous NiFe@V_2O_3 exhibits good OER performance in an alkaline medium with an overpotential of 255 mV at 10 mA cm^{-2} and good stability (Figure 6g,h). Meanwhile, the NiFe@V_2O_3 also gave good HER performance in the same alkaline medium. It shows an overpotential of 84 mV at 10 mA cm^{-2} and good stability (Figure 6i,j). Furthermore, the porous NiFe@V_2O_3 delivers a small Tafel slope of 51 mV dec^{-1} for OER and a Tafel slope of 85.4 mV dec^{-1} for the HER, respectively. Considering the excellent HER and OER performance, two identical NiFe@V_2O_3 electrodes are integrated into a two-electrode cell to investigate the water splitting performance. The catalyst shows a cell potential of 1.56 V to reach 10 mA cm^{-2} with an ignorable cell voltage increase during 20 h measurements (Figure 6k).

The stability of the catalyst is a key parameter for practical applications, which is crucial to determine whether the catalyst can be commercialized.[83] Several factors limit the catalytic stability, such as poor chemical/electrochemical stability of the catalysts under operation, abandoned gas evolution leading to the physical detachment of catalysts, dissolution of the catalysts in the electrolytes with different pHs, poor mechanical stability, and so on.[84−86] For example, Schmidt et al.[87] proved that the metal atoms are thermodynamic unstable during the OER process due to metal oxide released lattice oxygen, which leads to the low stability of the catalysts. From the theoretical perspective, there are three critical criterion of the catalysts that should be considered: excellent water dissociation performance, suitable Gibbs adsorption energy of H* (ΔG_H*), and faster H_2 desorption.[83] Such properties enable the fast release of the active site without destroying the active site and further improve the stability of the catalysts.

3.2.3. Supercapacitors and Electromagnetic Wave Absorber. Supercapacitors (SCs) have attracted attention in recent years to bridge between a classic electrolytic capacitor and rechargeable battery, which are characterized by high power density and good cyclic stability. SCs are capable of storing electrical energy via two mechanisms: the electrochemical double layer capacitors having a nonfaradaic charge character and the pseudocapacitors based on faradaic electrochemical redox reactions.[88] The theoretical specific capacitance of a pseudocapacitive electrode is proportional to the number of electrons involved in a specific redox reaction, and vanadium

https://doi.org/10.1021/acs.chemrev.2c00546
Chem. Rev. 2023, 123, 4353−4415

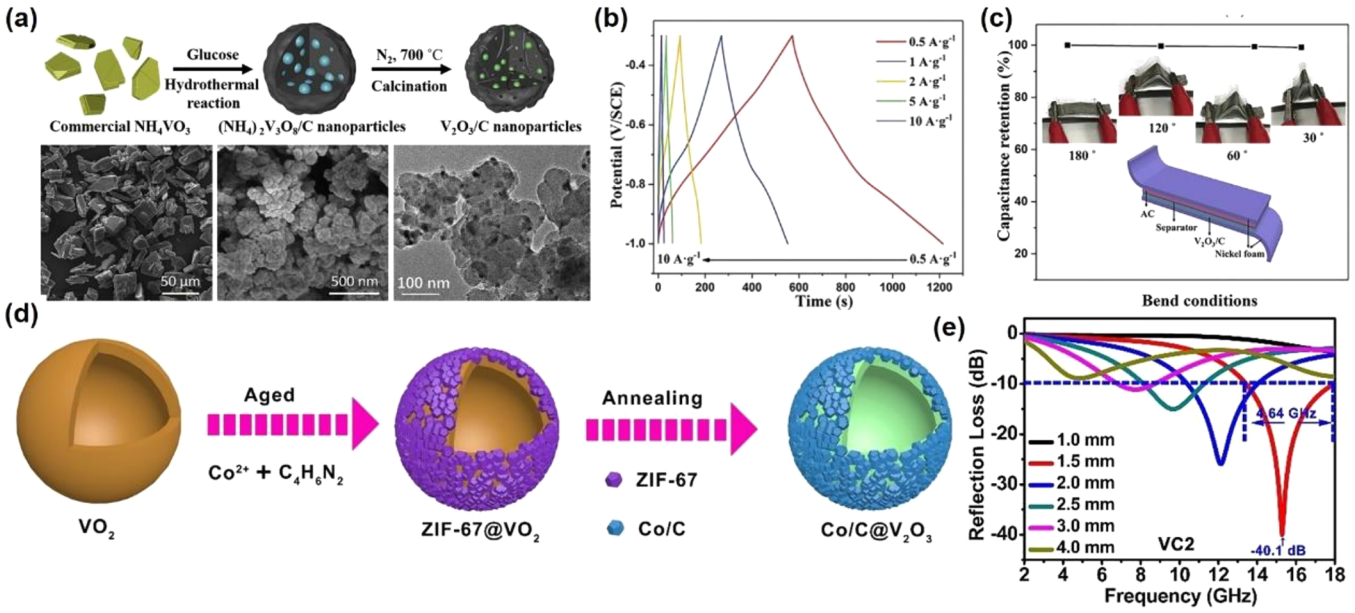

Figure 7. (a) A schematic illustration of the synthesis of highly dispersed VO-C. (b) GCD curves of VO-C collected at different current densities. (c) Capacitance retention of the VO-C||AC device measured under different bend conditions. Reproduced with permission from ref 93. Copyright 2019 Elsevier. (d) The synthesis process of hierarchical Co/C@V_2O_3 hollow spheres. (e) Reflection loss as a function of the frequency. Reproduced with permission from ref 95. Copyright 2019 John Wiley and Sons.

oxides possess four readily accessible valence states, making vanadium oxides especially promising for high pseudocapacitance.[89] The conductivity of V_2O_3 ($\sim 10^3\ \Omega^{-1}\ cm^{-1}$) is higher than monoclinic VO_2 ($\sim 4\ \Omega^{-1}\ cm^{-1}$) and comparable with Ru ($\sim 10^4\ \Omega^{-1}\ cm^{-1}$).[90] Meanwhile, V_2O_3 is stable in both acid and base mediums.[91] Thus, V_2O_3 is a suitable material for energy storage, especially for SCs. However, the reported specific capacitances of V_2O_3-based materials are not good enough, suggesting that design and synthesis of new structured V_2O_3-based materials with high performance are required.[92] Cao et al.[93] synthesized V_2O_3 nanoparticles highly dispersed in amorphous carbon composites through the calcination of the $(NH_4)_2V_3O_8$/C precursor, which was fabricated through the hydrothermal reaction by using commercial NH_4VO_3 and glucose (Figure 7a). The as-prepared V_2O_3-based composites exhibit a specific capacitance of the electrode of 458.6 F g^{-1} at a current density of 0.5 A g^{-1} (Figure 7b), which is higher than other reported V_2O_3-based composites.[94] Meanwhile, the asymmetric supercapacitors assembled by the as-prepared V_2O_3-based composites display good flexibility properties (Figure 7c). The capacitances are almost constant with the bending from 180° to 30°. The V_2O_3-based composites are one kind of high-efficiency electromagnetic wave absorber. Yan et al.[95] produced the hierarchical Co/C@V_2O_3 hollow spheres by hydrothermal, aging, and annealing methods (Figure 7d). The VO_2 spheres were first fabricated through a hydrothermal method followed by coating with ZIF-67 by precipitation. After that, the ZIF-67@VO_2 composite was calcined in H_2/Ar to form the hierarchical Co/C@V_2O_3 hollow spheres. The Co/C@V_2O_3 hollow spheres exhibited excellent electromagnetic wave absorption performance with a reflection loss of @40.1 dB and a broad bandwidth of 4.64 GHz at a small thickness of only 1.5 mm (Figure 7e). The good performance is mainly due to the impedance matching and low density, which come from the combination of hollow V_2O_3 spheres and porous Co/C.

4. V_3O_5

4.1. Structures and Synthesis

V_3O_5 crystal structure was first reported in 1954,[96] which possesses a monoclinic symmetry (space group $P2/c$).[97] The crystal structure is shown in Figure 8. The oxygen atoms are occupied in the octahedral sites, and vanadium atoms are located in the center of octahedron. There are two types of octahedra chains along the c axis: face-shared octahedra via edge-sharing and corner-sharing octahedra. Such chains formed a framework with many large open spaces, which is capable of accommodating lithium ions.[98]

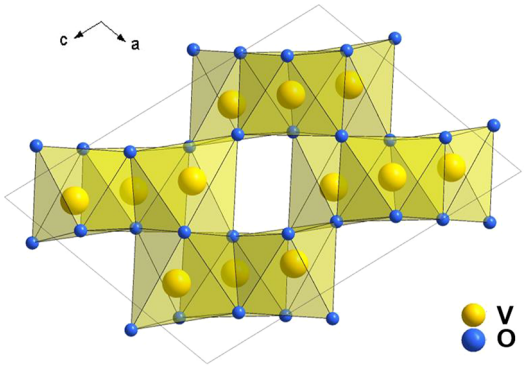

Figure 8. Crystal structure of V_3O_5.

It is difficult to stabilize the V_3O_5 phase by using solid-state chemistry and to control the stoichiometry between oxygen and vanadium by using a solution method, which makes V_3O_5 an uncommon phase used for electrochemical and other applications.[98,99] Therefore, the reported synthetic method for V_3O_5 is very limited. Reduction of V_2O_5 by different reductants is commonly used to obtain the V_3O_5 polycrystalline powders. Reisner et al.[100] selected vanadium metal as a reductant to

https://doi.org/10.1021/acs.chemrev.2c00546
Chem. Rev. 2023, 123, 4353−4415

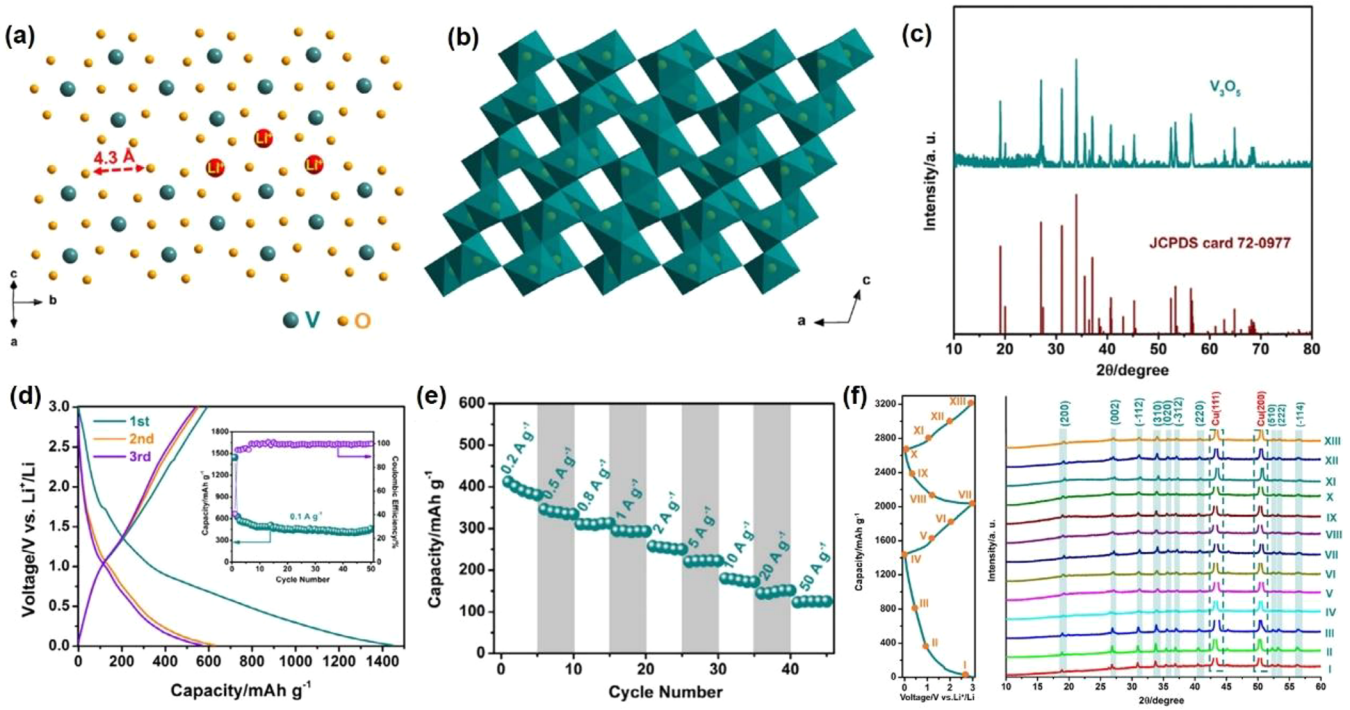

Figure 9. [101] projection illustrating the hexagonal close packing of oxygen atoms (a), the connection of VO_6 octahedral (b), the XRD pattern (c), charge/discharge profiles (inset: corresponding cycling performance at 100 mA g^{-1}) (d), rate performance (e) and *ex-situ* XRD patterns (f) of V_3O_5. Reproduced with permission from ref 98. Copyright 2019 under CC BY license.

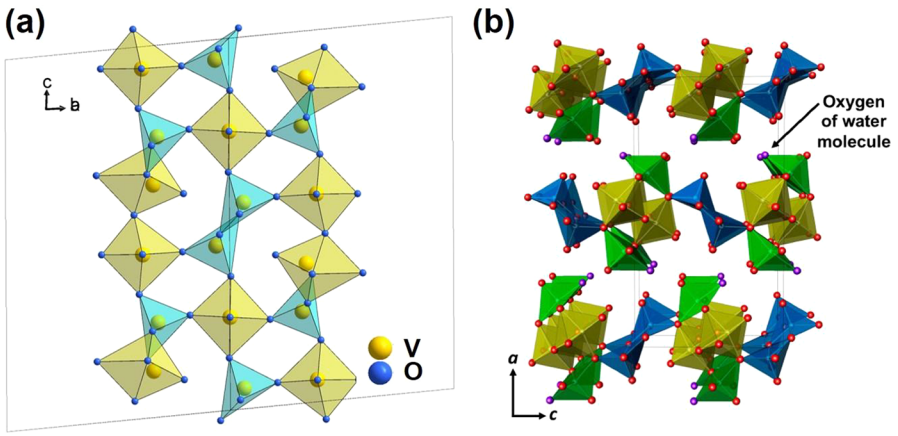

Figure 10. (a) Crystal structure of V_3O_7 with VO_6 octahedra (yellow) and VO_5 (blue). (b) Crystal structure of $V_3O_7{\cdot}H_2O$ ($H_2V_3O_8$), with VO_6 octahedra (yellow) and VO_5 (green) and VO_5 (blue) polyhedra. Hydrogen atoms are bonded to the oxygen atoms (purple), which are not shown. Reproduced with permission from ref 108. Copyright 2018 American Chemical Society.

reduce V_2O_5, and the V_3O_5 polycrystalline powders were synthesized according to the following chemical reaction: V + $V_2O_5 \rightarrow V_3O_5$. Vanadium powder and V_2O_5 powder were mixed together and pressed into bars, which were sealed in a quartz ampule and heated for 24 h at 870 K and for 100 h at 1220 K. The V_3O_5 polycrystalline powders exhibit a size around 10 μm. Alternatively, Yu et al.[98] used sulfur powders as a reductant. The mixture of sulfur and V_2O_5 powders were vigorously grounded and calcined at 1023 K in a tube furnace under a vacuum for 2 h. The V_3O_5 microcrystals can be obtained by washing the calcined powders with nitrogen tetrasulfide several times. The obtained V_3O_5 microcrystals range from 1 to 3 μm. The large size single crystal of V_3O_5 was grown by chemical vapor transport in the 1970s.[101,102] V_3O_5 powders or V_2O_3−VO_2 mixed powders were used as starting materials, and $TeCl_4$ was used as a transport agent. Both starting materials and transport agent were sealed in a quartz tube with low pressure (~1 × 10^{-5} mbar), and then the tube was put into a two-zone furnace. Generally, the source zone has higher temperature, while the crystallization zone has a lower temperature, and the temperature gradient is around 100 to 150 K. The size of final V_3O_5 single crystal is as large as 1 cm.

4.2. Applications

4.2.1. Batteries. V_3O_5 is relatively less-studied though it exhibits a three-dimensional open-framework structure, which is due to the strict synthesis condition. Yu's group[98] successfully synthesized V_3O_5 microcrystals via vacuum calcination and first employed it as an LIB anode material. The oxygen atoms are closely arranged in a hexagonal shape, and the vanadium atoms take up three-fifths of the octahedral interstices (Figure 9a). The

https://doi.org/10.1021/acs.chemrev.2c00546
Chem. Rev. 2023, 123, 4353−4415

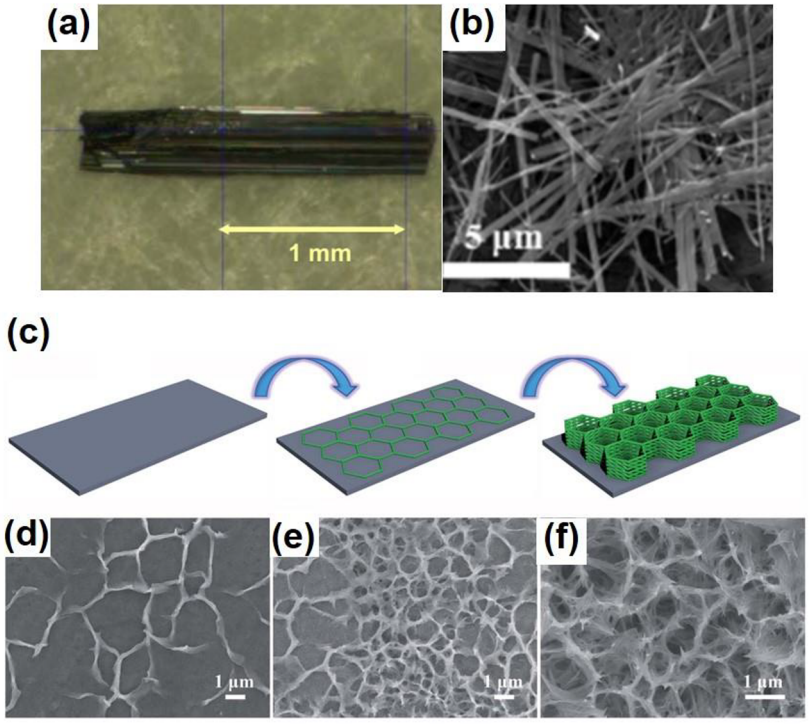

Figure 11. (a) Optical images of bulk V_3O_7 single crystals. Reproduced with permission from ref 110. Copyright 2009 Elsevier. (b) The SEM image of V_3O_7 nanobelts obtained through a soft chemical topotactic synthesis and hydrothermal process. Reproduced with permission from ref 111. Copyright 2016 Royal Society of Chemistry. (c) Schematic synthesis process for nest-like V_3O_7. (d–f) SEM images of V_3O_7 prepared with the hydrothermal times of 1, 5, and 10 h. Reproduced with permission from ref 112. Copyright 2018 Royal Society of Chemistry.

3D open-framework structure of V_3O_5 is formed with chain connections, which contain distorted, sharing corners, edges, and faces of VO_6 octahedral, respectively (Figure 9b). The 3D framework of V_3O_5 with much large open space endows the capacity of Li^+ intercalation/deintercalation. No impurity peaks from the XRD pattern are observed (Figure 9c), which indicates that the V_3O_5 powder shows a single-phase nature with a monoclinic structure within the $P2/c$ space group (JCPDS card 72-0977). It delivers a high capacity of 628 mAh g^{-1} at 100 mA g^{-1}, a good rate (125 mAh g^{-1} at 50 A g^{-1}), and a long stable cycling performance (117 mAh g^{-1} after 2000 cycles) (Figure 9d,e). There is no obvious crystal structure change of the V_3O_5 with Li^+ intercalation, which is the main reason for the good rate and cycling performance (Figure 9f).

4.2.2. Other Applications. V_3O_5 thin films exhibit a photoinduced insulator-to-metal phase transition, which results in a strong nonlinear optical response.[103−105] Fernández et al.[104] deposited the V_3O_5 directly on the SiO_2 substrates by DC magnetron sputtering to form thin films. The ultrafast nonlinear optical response was probed by using a pump−probe scattering technique. A reduction in the transient relative scattered light signal was observed, which showed an ∼10% decrease within 800 fs. Such a response is due to the changes in the material's optical constants and very likely related to the photoinduced insulator-to-metal phase transition.[106] The photoinduced screening of electron correlations followed by melting of polaronic Wigner crystal and coalescence of V−O octahedra is the main reason for the order−disorder structural transition.[103]

5. V_3O_7

5.1. Structures and Synthesis

Figure 10a shows the crystal structure of V_3O_7. The unit cell contains 36 vanadium atoms (12 vanadium atoms are inside the octahedra and 24 vanadium atoms are five-coordinated).[107] The V_3O_7 consists of VO_6 octahedra and VO_5 polyhedra, which are linked by corners and edges to form a three-dimensional framework. The crystal structure of $V_3O_7{\cdot}H_2O$ shows a two-dimensional structure compared with V_3O_7 (Figure 10b). Each V_3O_8 layer consists of corner- or edge-shared VO_6 octahedra and VO_5 polyhedra.[108] The water molecules are located at the sides of the V_3O_8 layer, where the hydrogen atoms are directly bonded to the vanadium atom of a VO_5 polyhedron and hydrogen bonds connect two neighboring V_3O_8 layers.[7,109]

Bulk V_3O_7 single crystal can be grown by a typical chemical vapor transport method using V_3O_7 polycrystalline powders as starting materials and NH_4Cl as a transport agent.[110] The mixed V_3O_7 polycrystalline powders and NH_4Cl were pressed into a pellet and heated at 823 K in an evacuated silica tube for 7 days. The black needle-like single crystals of V_3O_7 were formed with a length of 2 mm (Figure 11a). Nanostructured V_3O_7 was generally obtained by a typical hydrothermal method. The precursor solution dramatically affects the morphology of the V_3O_7 nanostructures. Wen et al. combined a soft chemical topotactic synthesis and hydrothermal process to prepare V_3O_7 nanobelts.[111] In the beginning, layered structured KV_3O_8 plate-like particles were first prepared as the precursor by a hydrothermal method of V_2O_5 and KOH. The H^+-form vanadate (HVO) nanobelt colloidal solution was subsequently obtained by reacting KV_3O_8 plate-like particles with HNO_3. Finally, the one-dimensional (1D) pure single crystal V_3O_7 nanobelts were successfully prepared after hydrothermally

https://doi.org/10.1021/acs.chemrev.2c00546
Chem. Rev. 2023, 123, 4353−4415

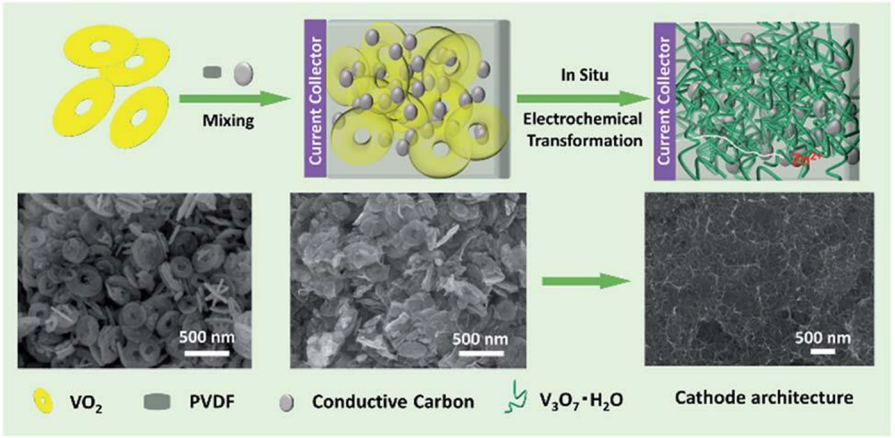

Figure 12. Schematic illustration of the preparation of the nanogrid-shaped $V_3O_7{\cdot}H_2O$. Reproduced with permission from ref 119. Copyright 2019 Royal Society of Chemistry.

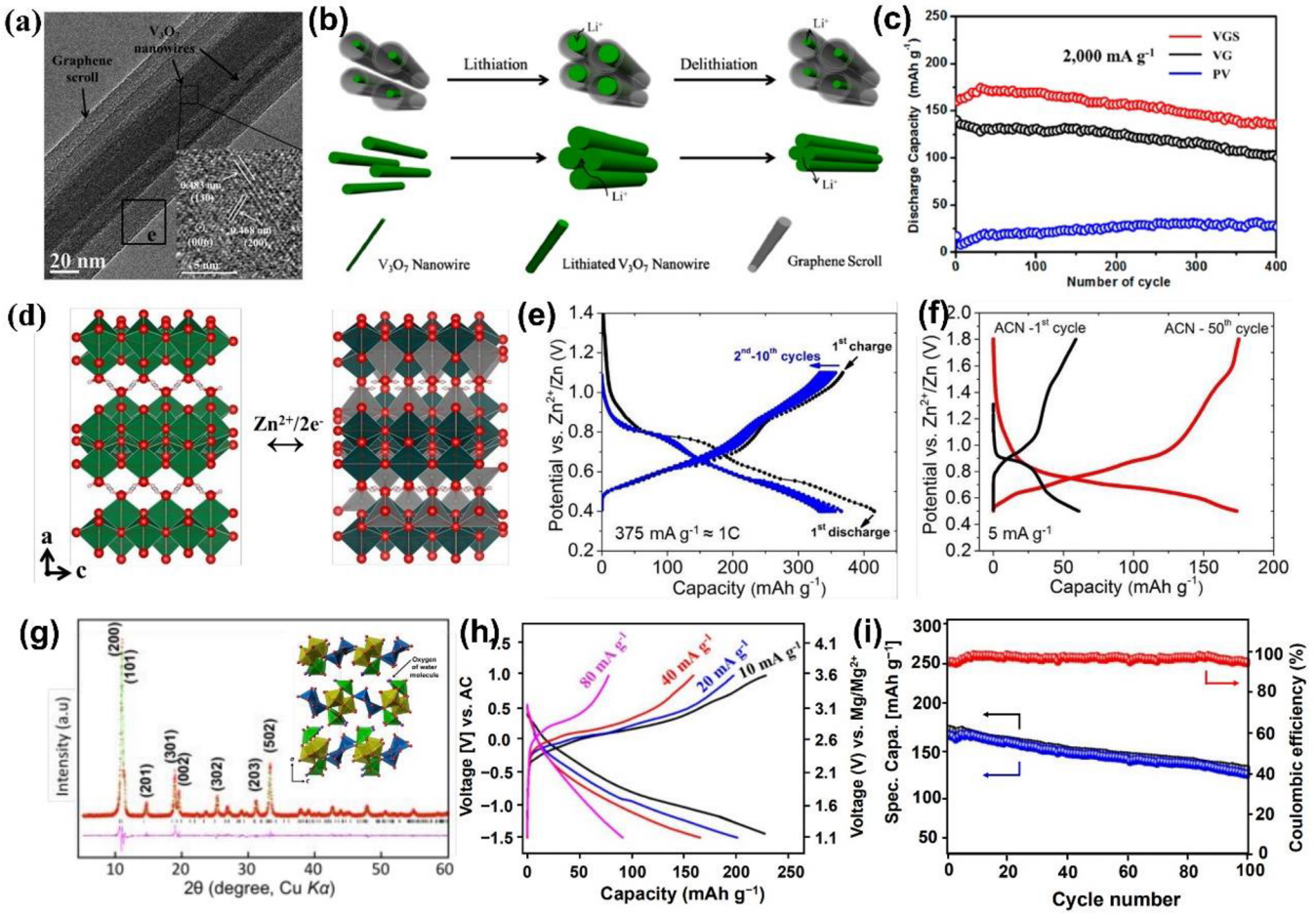

Figure 13. TEM image of VGS (the inset gives an HRTEM image of a V_3O_7 nanowire in graphene scrolls) (a), schematic of the VGS nanoarchitecture with continuous electron and Li ion transfer channels (b), and cycling performances (c) of VGS, V_3O_7 nanowire/graphene, and V_3O_7 nanowire. Reproduced with permission from ref 120. Copyright 2013 American Chemical Society. The schematic illustration of reaction mechanism (d), charge/discharge profiles in aqueous (e), and nonaqueous (f) electrolytes of $Zn//V_3O_7{\cdot}H_2O$ batteries. Reproduced with permission from ref 121. Copyright 2018 Royal Society of Chemistry. The powder X-ray Rietveld refinement profile and crystal structure (g), charge/discharge profiles (h), and cycling performance (i) of $V_3O_7{\cdot}H_2O$ nanowires in MIBs. Reproduced with permission from ref 108. Copyright 2018, American Chemical Society.

treating the colloidal solution at 180 °C for 12 h (Figure 11b). By using NH_4VO_3 and HCl as starting materials, the nest-like V_3O_7 self-assembled by porous V_3O_7 nanowires on Ti foil was also synthesized through a hydrothermal method.[112] In the beginning, a layer of V_3O_7 nanosheets was deposited on the Ti substrate, which was subsequently placed in the NH_4VO_3−HCl solution and kept at 160 °C for 10 h for a hydrothermal method. With the increase of hydrothermal time, the nest-like V_3O_7 is self-assembled by nanowires. The schematic synthesis process and SEM images for nest-like V_3O_7 are shown in Figure 11c−f.

https://doi.org/10.1021/acs.chemrev.2c00546
Chem. Rev. 2023, 123, 4353−4415

The V_3O_7 fibers can be obtained by thermal treatment of the electrospun NH_4VO_3/PVP nanofibers in the presence of reductant.[113] The thermal treatment condition dramatically affects the final products, and V_2O_5 may be obtained together with V_3O_7.

The hydrothermal reaction is also a facile way to synthesize $V_3O_7{\cdot}H_2O$ nanostructures. The $V_3O_7{\cdot}H_2O$ nanobelts can be achieved by using V_2O_5, phenolphthalein and distilled water as starting materials through a hydrothermal method for 4 days of reaction at 180 °C.[114] By changing phenolphthalein to ethanol or glucose, $V_3O_7{\cdot}H_2O$ nanobelts were also successfully synthesized at 180 °C, while the reaction time was shortened to 12 h.[115,116] In above-mentioned the methods, phenolphthalein, ethanol, or glucose is used as the reductant. Without the reductant, the $V_3O_7{\cdot}H_2O$ nanobelts or nanowires can be obtained by a hydrothermal reaction of only V_2O_5 or NH_4VO_3.[117,118] The key point is the pH of the precursor solution. After adjusting the pH to 3 by adding concentrated HCl, $V_3O_7{\cdot}H_2O$ nanobelts and nanowires were obtained by a reaction at 190 °C for 24 h and 160 °C for 3 h, respectively. Furthermore, ultrafine $V_3O_7{\cdot}H_2O$ nanogrids can be obtained through electrochemical oxidation.[119] In the beginning, the nsutite-type VO_2 black powder was synthesized by a hydrothermal method. Then, a three electrode system was employed to electrochemically transform the VO_2 precursor to $V_3O_7{\cdot}H_2O$. The slurry, consisting of VO_2 nanoplates, was coated on the working electrode. With a constant current density of 50 mA cm^{-2} and a cutoff potential of 1.7 V, $V_3O_7{\cdot}H_2O$ nanogrids were obtained (Figure 12).

5.2. Applications

5.2.1. Batteries. V_3O_7 is a mixed-valence vanadium oxide for metal-ion storage. Yan et al.[120] designed and synthesized a V_3O_7 nanowire templated graphene scroll (VGS) via an "oriented assembly" and "self-scroll" strategy. They used joint experimental-MD simulation to investigate the construction and formation mechanisms of VGS. The systemic energy, the curvature of nanowires, and the reaction time determined the length and formation process of the semihollow bicontinuous structure. Through this strategy, the VGS with a length up to 30 μm has interior cavities between the nanowire and scroll (Figure 13a). The unique structure of VGS with the nanowire templated graphene scroll offers a continuous Li^+/ion transfer channel and free volume expansion space during Li^+ de/intercalation (Figure 13b). The VGSs exhibit a high capacity of 321 mAh g^{-1} and good cycle stability (87.3% after 400 cycles), which is better than the pure V_3O_7 nanowire and V_3O_7 nanowire/graphene structure (Figure 13c).

In addition, Nazar et al.[121] synthesized layered $V_3O_7{\cdot}H_2O$ nanobelts with single crystalline via a microwave solvothermal method and applied it to a ZIB cathode in nonaqueous and aqueous electrolytes. The electrochemical studies and *in situ* XRD results demonstrate the different electrochemical behaviors of layered $V_3O_7{\cdot}H_2O$ in nonaqueous and aqueous electrolytes. Combining the DFT calculations, ~2 mol Zn^{2+} can insert into $V_3O_7{\cdot}H_2O$ per the formula in the $ZnSO_4/H_2O$ aqueous electrolyte (Figure 13d). The $V_3O_7{\cdot}H_2O$ delivers a capacity of 400 mAh g^{-1} (>2 mol Zn^{2+} insertion) with an average voltage of ~0.65 V at the first discharge process, and maintains 375 mAh g^{-1} at the subsequent charge process (Figure 13e), while in the $Zn(CF_3SO_3)_2$/acetonitrile nonaqueous electrolyte, the $V_3O_7{\cdot}H_2O$ exhibits a poor Zn^{2+} storage performance (59 and 175 mAh g^{-1} for the first and 50th cycles at 5 mA g^{-1}, respectively) (Figure 13f).

Magnesium-ion battery (MIB) as another multivalent ion battery has been attracting more attention due to its high abundance in the Earth and low redox potential (−2.37 V vs. SHE). $V_3O_7{\cdot}H_2O$ with high electronic conductivity ($V^{+4.67}$) has been widely used as a cathode material in LIB/NIB and hybrid Li^+/Mg^{2+} batteries. Hong et al.[108] synthesized $V_3O_7{\cdot}H_2O$ nanowires via a one-step hydrothermal method and applied them to a high-energy MIB cathode (Figure 13g). The electrochemical tests and structural characterization results demonstrate that the structured water in $V_3O_7{\cdot}H_2O$ will remain stable during the cycling. 0.97 mol Mg^{2+} inserts into $V_3O_7{\cdot}H_2O$, accompanying the formation of $Mg_{0.97}H_2V_3O_8$ at the first discharged state. $V_3O_7{\cdot}H_2O$ exhibits an initial discharge capacity of 231 mAh g^{-1} at 10 mA g^{-1} with an average discharge voltage of ~1.9 V, and the energy density can reach 440 Wh kg^{-1} (Figure 13h). Meanwhile, $V_3O_7{\cdot}H_2O$ delivers a 171 mAh g^{-1} and maintains 132 mAh g^{-1} (77%) after 100 cycles at 40 mA g^{-1} (Figure 13i). The excellent Mg^{2+} storage performance is attributed to the unique crystal structure with direct bonding. This strategy of applying water-metal bonding and hydrogen bonding provides a new idea to search for new oxide-based MIB materials with stable and high energy density.

5.2.2. Ammonium Perchlorate Decomposition. Ammonium perchlorate, a common oxidizer, plays a key role in the combustion of composite solid propellants. Furthermore, the catalyst greatly affected the performance of composite solid propellants by the thermal decomposition of ammonium perchlorate.[122,123] Huang et al.[124] found that the thermal decomposition temperatures of ammonium perchlorate in the presence of $V_3O_7{\cdot}H_2O$ nanobelts and $V_3O_7{\cdot}H_2O$@C core−shell structures can be dramatically reduced. Both $V_3O_7{\cdot}H_2O$ nanobelts and $V_3O_7{\cdot}H_2O$@C core−shell structures were synthesized by a hydrothermal method. Especially, the core−shell structures are synthesized by using $V_3O_7{\cdot}H_2O$ nanobelts as the cores and glucose as the source of carbon. A well-defined nanobelt morphology with a length up to several micrometers can be observed (Figure 14a), which consists of a $V_3O_7{\cdot}H_2O$ core and carbon shell (Figure 14b). The thermogravimetric analysis (TGA) indicated that the addition of $V_3O_7{\cdot}H_2O$ or $V_3O_7{\cdot}H_2O$@C in ammonium perchlorate exhibited a significant reduction in the decomposition temperature of ammonium perchlorate (Figure 14c). The thermal decomposition temperature was lowered by 70 and 89 °C by adding $V_3O_7{\cdot}H_2O$ or $V_3O_7{\cdot}H_2O$@C, respectively. The $V_3O_7{\cdot}H_2O$@C core−shell structures exhibited a higher catalytic activity than $V_3O_7{\cdot}H_2O$, with two possible mechanisms proposed. First, the partially filled 3d orbit in the vanadium atom promoted the electrotransfer process by accepting electrons from ammonium perchlorate and further accelerated the thermal decomposition of ammonium perchlorate. Second, the amorphous carbon shell possessed lots of active groups (such as C═C, C═O), which could facilitate the thermal decomposition of ammonium perchlorate.

5.2.3. Supercapacitors. V_3O_7 and $V_3O_7{\cdot}H_2O$ are promising supercapacitor materials due to their layered structure and mixed oxidation states of +4 and +5. V_3O_7 can be converted to V_6O_{13} at the lowest potential of −0.6 V and V_2O_5 at the highest potential of 0.2 V. Thus, the working potential window is in the range of −0.6 and 0.2 V. Huang et al.[112] fabricated porous V_3O_7 nanowire self-assembled nest-like V_3O_7 and investigated the supercapacitor properties. The pure nest-like V_3O_7 exhibits worse supercapacitor performance compared with N-doped

https://doi.org/10.1021/acs.chemrev.2c00546
Chem. Rev. 2023, 123, 4353−4415

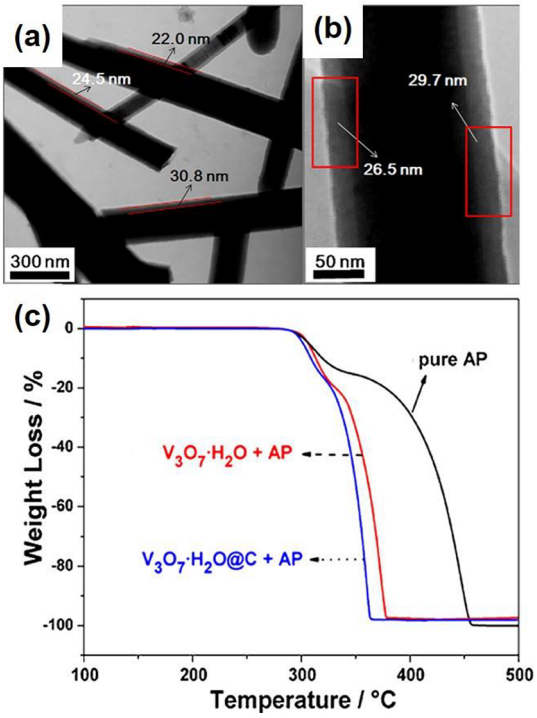

Figure 14. (a) and (b) TEM images of $V_3O_7{\cdot}H_2O$@C core−shell structures, (c) TGA curves of pure ammonium perchlorate, $V_3O_7{\cdot}H_2O$ with ammonium perchlorate and $V_3O_7{\cdot}H_2O$@C with ammonium perchlorate. Reproduced with permission from ref 124. Copyright 2011 Elsevier.

carbon coated nest-like V_3O_7 composites. The N-doped carbon coated nest-like V_3O_7 electrode showed a higher specific capacity of 660.63 F g^{-1} at 0.5 A g^{-1} compared to V_3O_7 (362.63 F g^{-1}). Even at a higher current density of 50 A g^{-1}, the N-doped carbon - V_3O_7 electrode still exhibits a better performance (187.72 F g^{-1}) than V_3O_7 (33.18 F g^{-1}), as shown in Figure 15a. Furthermore, the N-doped carbon coated nest-like V_3O_7 electrode also delivers better stability (80.47% capacitance retention after 4000 cycles) compared with pure V_3O_7 (23.16% capacitance retention after 4000 cycles). The superior performance of N-doped carbon coated nest-like V_3O_7 is mainly due to the unique three-layer structure: V_3O_7 core/carbon/nitrogen doped carbon (Figure 15b). Such a unique three-layer structure can not only stabilize V_3O_7, but also provide high-speed ionic and electronic transmission channels, which is responsible for the good supercapacitor performance of N-doped carbon coated nest-like V_3O_7. Yu et al.[125] reported the growth of V_3O_7 nanowires on a carbon fiber cloth through a hydrothermal method. The obtained V_3O_7/carbon fiber cloth composites show a spider web-like morphology, which exhibits robust adhesion. The composite electrode gives a maximum specific capacitance of 151 F g^{-1} at a current density of 1 A g^{-1} with ultrahigh cycling stability of 97% (after 100000 cycles) in a full cell configuration (Figure 15c). Meanwhile, the V_3O_7/carbon fiber cloth composites reveal maximum power and energy densities of 5.128 kW kg^{-1} and 24.7 Wh kg^{-1}, respectively by using 1-ethyl-3-methylimidazolium trifluoromethanesulfonate as the electrolyte. Furthermore, coin cell-type configuration with the V_3O_7- carbon fiber cloth composites electrode was assembled. The symmetric supercapacitors successfully and effectively power light-emitting diodes to produce blue light (Figure 15d). Huang et al.[115] reported that $V_3O_7{\cdot}H_2O$ nanobelts exhibited a capacitance of 447.6 F g^{-1}. However, the cycling performance is limited by the poor conductivity and high solubility in an aqueous electrolyte. Therefore, composing with another conductive phase could be an alternative way to fabricate high-performance $V_3O_7{\cdot}H_2O$ based materials. When the $V_3O_7{\cdot}H_2O$ nanobelt is incorporated with carbon nanotube and reduced graphene, the formed 3D hierarchical porous composites exhibit outstanding electrochemical performance with a high specific capacitance (685 F g^{-1} at 0.5 A g^{-1}) and excellent cycle stability (99.7% after 10,000 cycles) (Figure 15e,f).[126] Meanwhile, the composites also give relatively high energy densities and power densities of 34.3 Wh kg^{-1} and 150 W kg^{-1}, respectively. The better electrochemical performance can be attributed not only to the highly conductive carbon materials, but also to the 3D hierarchical porous structure. The carbon materials offer the transport pathway bridges, leading to the rapid transfer of charges. Meanwhile, the 3D porous structure minimizes the diffusion distance and supplies a large surface area with abundant active sites.

In general, vanadium oxides have received massive interest as supercapacitor electrodes that exhibit high theoretical specific capacity than most of the other transition metal oxides due to their variable valence state from V^{2+} to V^{5+}. In addition, the layered structure of vanadium oxides facilitates the intercalation/deintercalation of electrolyte ions during the charging/discharging process. However, vanadium oxides-based supercapacitor electrode materials still suffer from poor long-term cycling stability, which is usually caused by the collapse of a layered crystal structure, severe agglomeration of particles, and low electrical conductivity. The electrochemical stability of vanadium oxide-based supercapacitors can be improved by material modification, optimization of the structure, or combining with other materials with excellent electrical conductivity. Developing vanadium oxide nanomaterials with suitable micro-/nanostructures is an important factor to improve the cycling stability. 3D vanadium oxides with micro-/nanostructures are often employed, including microspheres and hollow spheres, which can inherit the superior high surface area characteristics of nanobuilding blocks, and simultaneously possess a decent structural stability.[127−130] Furthermore, the 3D structure can effectively reduce the agglomeration of particles, which is beneficial for the cycling and rate performance.[131] Integrating vanadium oxides with carbon materials has been demonstrated to be effective to suppress the structural degradation upon cycling. The carbon materials, such as porous carbons and graphene, can serve as elastic buffering layers to release the strain within metal oxides during cycling.[132] To some extent, carbon materials can avoid loose attachment between the electrode material and current collector, which helps improve both the conductivity and the stability of the supercapacitor.

5.2.4. Electrochromism. Nanostructured V_3O_7 thin films showed electrochromic properties by using lithium perchlorate as the electrolyte, which was prepared by a nebulizer spray pyrolysis technique.[133] The color of the films is changed from yellow to pale blue by applying an external potential of 1.5 V for intercalation of Li^+ ions, while the color is reversed by applying an external potential of −1.5 V for deintercalation of Li^+ ions. Such results indicate that the nanostructured V_3O_7 thin films could be effectively used for smart window applications. In general, several models are proposed to explain the electrochromic phenomenon, such as the color center model (Deb model), electrochemical redox model, and so on.[134] The "Deb's

https://doi.org/10.1021/acs.chemrev.2c00546
Chem. Rev. 2023, 123, 4353−4415

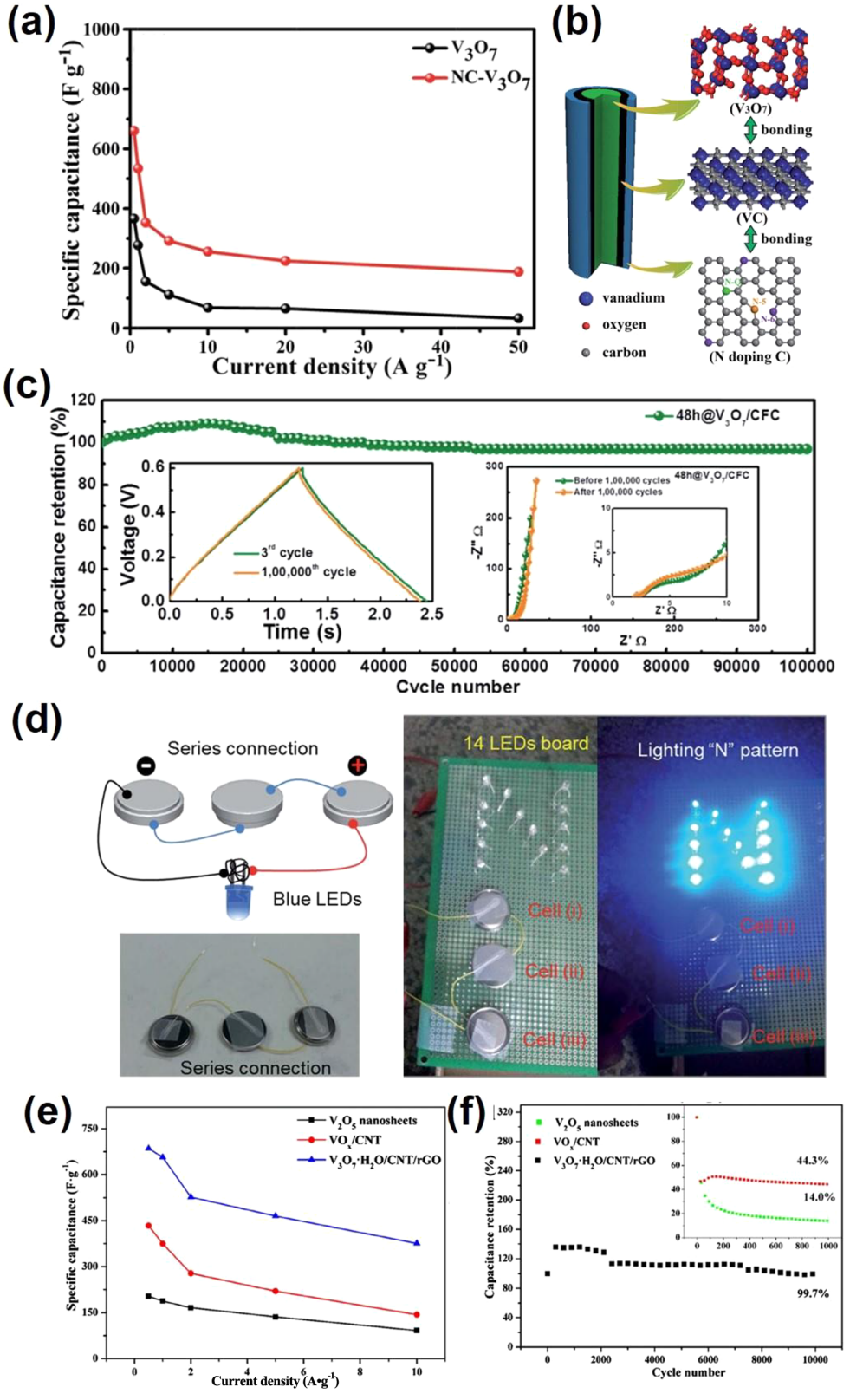

Figure 15. (a) Rate capability of V_3O_7 and N-doped carbon coated nest-like V_3O_7 calculated from the charge/discharge curves as a function of current density, (b) schematic diagram of the crystal structure and bonding in N-doped carbon coated nest-like V_3O_7. Reproduced with permission from ref 112. Copyright 2018 Royal Society of Chemistry. (c) Cycling stability of V_3O_7- carbon fiber cloth symmetric supercapacitors devices at a constant current density of 10 A g^{-1} for 100 000 cycles, (d) series connection of three-coin cells for practical applications, charging process of serially connected coin cells, and a demonstration of LEDs lit with charged coin cells. Reproduced with permission from ref 125. Copyright 2018 Royal Society of Chemistry. (e) Comparison of specific capacitance at different current densities from GCD curves, (f) cycling performance at 100 mV s^{-1} of V_2O_5 nanosheets, VO_x/CNT, and $V_3O_7{\cdot}H_2O$/CNT/rGO. Reproduced with permission from ref 126. Copyright 2018 Elsevier.

https://doi.org/10.1021/acs.chemrev.2c00546
Chem. Rev. 2023, 123, 4353−4415

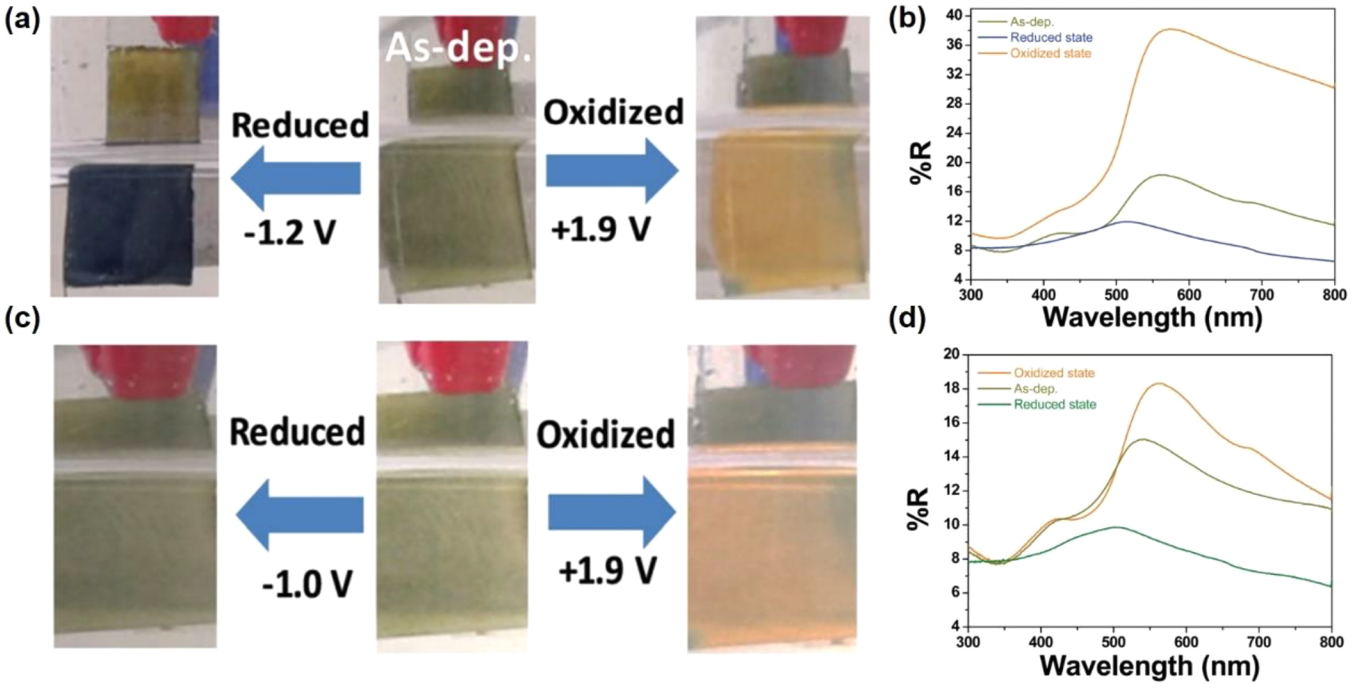

Figure 16. (a) The visual appearance of $V_3O_7{\cdot}H_2O$ films in the reduced and oxidized states in LiTFSI, (b) diffuse reflectance spectra for the $V_3O_7{\cdot}H_2O$ films cycled in Li-electrolyte/Pt vs SCE, in reduction at −1.2 V and reoxidized at +1.9 V, (c) the visual appearance of $V_3O_7{\cdot}H_2O$ films in the reduced and oxidized states in NaTFSI, (d) diffuse reflectance spectra for the $V_3O_7{\cdot}H_2O$ films cycled in Na-electrolyte/Pt vs SCE, in reduction at −1 V and reoxidized at +1.9 V. Reproduced with permission from ref 138. Copyright 2020 Royal Society of Chemistry.

color center model" is in nature related to the defects (such as oxygen vacancies) induced change of the visible light absorption, which is generally independent of the external electric field,[135] while in the "electrochemical redox model" it is believed that the injection and trapping of a large density of electron and hole lead to coloration.[136] The mechanism of electrochromism for V_3O_7 thin films is the variation of the band structure caused by intercalation/deintercalation of Li^+ ions, which belongs to the electrochemical redox model. During the application of negative bias, Li^+ ions are absorbed onto the surface of V_3O_7 and diffuse into the lattice of V_3O_7. The intercalated Li^+ ions react with O^{2-} ions to introduce oxygen vacancies in the lattice and reduce the V^{5+} in the mixed state V_3O_7 to V^{4+}. As the result, the optical transparency of the film changes.[137] Moreover, the intercalation of Li^+ ions upshifts the Fermi level close to the conduction band, which leads to an increased transmittance of V_3O_7. The process can be reversed by deintercalating of Li^+ ions through applying positive bias. Furthermore, the $V_3O_7{\cdot}H_2O$ thick films also show good electrochromic properties (good reversibility and good color switching between reduced and oxidized states).[138] By using lithium bis-trifluoromethanesulfonimide (LiTFSI) as the electrolyte, the color of the $V_3O_7{\cdot}H_2O$ films changes from green to orange by applying a positive potential of 1.9 V, while it changes from green to blue by applying a negative potential of −1.2 V (Figure 16a). Such film presented a maximum optical reflectance modulation of 29% at 590 nm (Figure 16b). The $V_3O_7{\cdot}H_2O$ films still exhibited color changes by using a Na-based electrolyte (Figure 16c) and a maximum optical reflectance modulation of 10% at 590 nm (Figure 16d). The maximum optical reflectance modulation of Na-based electrolyte is lower than that in the Li-based electrolytes, which is mainly due to a larger faradaic contribution resulting from the larger cation size of Na^+ ions.

6. VO_2

6.1. Structures and Synthesis

Vanadium dioxide (VO_2) can exist in various polymorphic phases, including but not limited to VO_2 (B), VO_2 (A), VO_2 (M), VO_2 (R), VO_2 (D), and VO_2 (P).[139] Some of these phases and their corresponding lattice parameters are shown in Figure 17. The discussion will focus more on VO_2 (R) and its reversible MIT to VO_2 (M) as well as on VO_2 (B) due to its application as cathode materials in electrochemical devices.

VO_2 was first demonstrated to undergo MIT in 1959 by Morin. At the critical temperature (τ_C) of about 340 K, VO_2 transforms from high-temperature, conducting rutile VO_2 (R) to

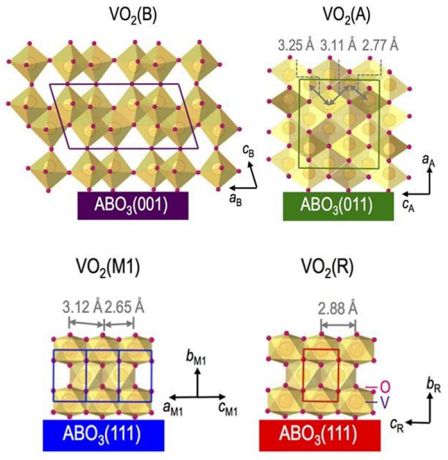

Figure 17. Different phases of VO_2 with respective lattice parameters. Reproduced with permission from ref 147. Copyright 2016 under CC BY 4.0 license.

https://doi.org/10.1021/acs.chemrev.2c00546
Chem. Rev. 2023, 123, 4353−4415

low-temperature, insulating monoclinic VO_2 (M). There are two mechanisms that have been used to describe this ultrafast phase transition phenomenon in VO_2, namely the Peierls model and Mott-Hubbard model. The Peierls model describes the nature of MIT as the change from a shared d-orbital between all vanadium atoms to localized d-orbital in the V−V dimer, which is a result of the change in the V−V distance from 2.88 Å in VO_2 (R) to 2.65 and 3.12 Å in VO_2 (M).[20] Therefore, the Peierls model stated that the structural distortion is the cause of MIT. Wentzcovitch et al. applied the local-density approximation to study the electronic and structural change of VO_2 during the MIT.[140] From the view of band theory, a monoclinic distorted state is in good agreement with the experiment result. Meanwhile, the structural distortion enhances the bonding between neighboring V atoms, which is expected in the Peierls model. Moreover, Baum et al. utilized four-dimensional (4D) femtosecond electron diffraction to visualize the phase transformation process of VO_2.[141] They pointed out that during the MIT, the displacement of atoms happened within picoseconds, and followed by the sound wave shear motion of the crystal in the time scale of nanoseconds. The observation indicates the occurrence of fast structural distortion during the MIT.

On the other hand, the Mott-Hubbard model states that MIT would occur when the electron density (n_e) and Bohr radius (a_H) satisfy $n_e^{1/3}a_H \approx 0.2$.[142] Compared with the Peierls model, the Mott-Hubbard model has the advantage in explaining the phenomenon such as the anomalously low conductivity in the metallic phase.[143] Whittaker et al. summarized multiple experiment cases and pointed out that the metallic phase of VO_2 might be introduced without the structural phase transformation if the excitation of carriers reaches a threshold density.[144] Their observation provides key evidence in revealing the nature of MIT. While there remains a debate on which mechanism best describes the MIT, the usage of both models is strongly encouraged due to the transition kinetics[145] as well as the stimuli involved during the transition. Shao et al.[146] reported recent progress in understanding the mechanism and kinetics of MIT, including the lattice distortion and electron correlations (Peierls phase transition, Mott phase transition) and modulation methods (elemental doping, external electric field, light irradiation, and strain engineering).

Upon application of suitable external stimuli (i.e., photons, heat, electric, magnetic, electrochemical, and stress) to initiate the MIT, physical properties of VO_2, such as electrical resistance, optical transmittance, and thermal conductivity, are reversibly and drastically changed. Long et al.[27] have summarized the connections between the stimuli and responses of VO_2-based devices in detail. This flexibility in external stimuli and corresponding responses is the main reason why VO_2 is a material of interest in multiple novel devices spanning from thermally,[139,148] electrically,[149−151] to optically[152,153] activated devices. The functional performance of these devices is thus highly dependent on, but not limited to, the physical attributes, such as dimension, morphology, doping level, and crystallinity, of the fabricated VO_2. Multiple techniques have been used to fabricate functional VO_2 devices, each with their own strengths and weaknesses. Some of these fabrication processes are reviewed with polymer-assisted deposition methods,[154] hydrothermal,[139] sol−gel,[155] chemical vapor deposition (CVD),[19] and physical vapor deposition (PVD)[156] methods discussed in detail regarding the controlled synthesis of VO_2 for thermochromic application.

6.2. Applications

In recent years, multiple omnibus reviews[157−159] have been done in attempts to give the most encompassed view of VO_2 research progress, often including a combination of the following topics: MIT mechanism, kinetics, fabrication techniques, and applications. While these reviews could offer wide coverage of VO_2 research progress in multiple topics, in-depth discussion of each topic, applications in this case, is in much needed demand. In subsequent sections, reported applications of VO_2 in functional devices both based and not based on MIT in recent years, especially in the last three years, are classified and discussed in different categories: optical, electrical, and mechanical applications.

6.2.1. Optical Applications. The operations of these VO_2-based optical devices are often based on the changes in refractive index, n, and extinction coefficient, k of VO_2 upon crossing the MIT. The changes to n and k at different temperatures are shown in Figure 18. These optical functional devices are further divided into two main groups: infrared regulators and optical switches.

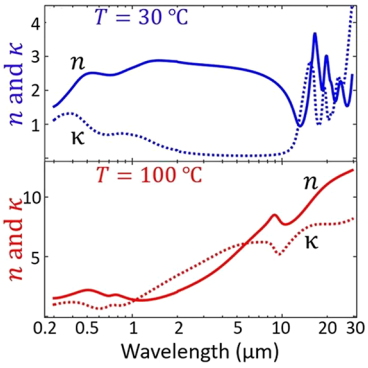

Figure 18. Optical constants n and k of VO_2 film with respect to the wavelength and the temperature changes. Reproduced with permission from ref 160. Copyright 2019 John Wiley and Sons.

6.2.1.1. Infrared Regulators. Since its first introduction in 1985,[161] the smart window has attracted much attention due to rising energy consumption in the commercial building sector, which contributes up to 40% of total consumption globally and leads to 30% of global greenhouse gas emissions today.[162] VO_2 is the prime candidate for smart window materials due to its ability to seamlessly and rapidly regulate the amount of infrared (IR) across MIT with miniscule side effects to the visible transmission. However, intrinsic limitations (high $\tau_C \approx 68$ °C, low luminous transmittance (T_{lum}) < 40%, poor solar modulation (ΔT_{sol}) < 10%, and poor durability) prevent pristine VO_2 from meeting the requirements for commercial smart window applications. The most common way to reduce τ_C is by elemental (i.e., W, Mo, Ti, F, Mg, etc.) doping as summarized by Cui et al.[163] Different approaches exist to enhance T_{lum} and ΔT_{sol} via advanced device morphological engineering such as multilayered VO_2,[164] biomimetic structure,[165−168] nanothermochromism,[169] porous,[170] and gridded structure.[171−173] Zhou et al. recently reported a new customized VO_2 composite structure in which a new factor, the incident angle, was considered in the development of smart window devices. Figure 19a shows a schematic of how different incident angles in the summer and winter can be taken advantage of with the reported customizable composite structure. The VO_2 composite structure was

https://doi.org/10.1021/acs.chemrev.2c00546
Chem. Rev. 2023, 123, 4353−4415

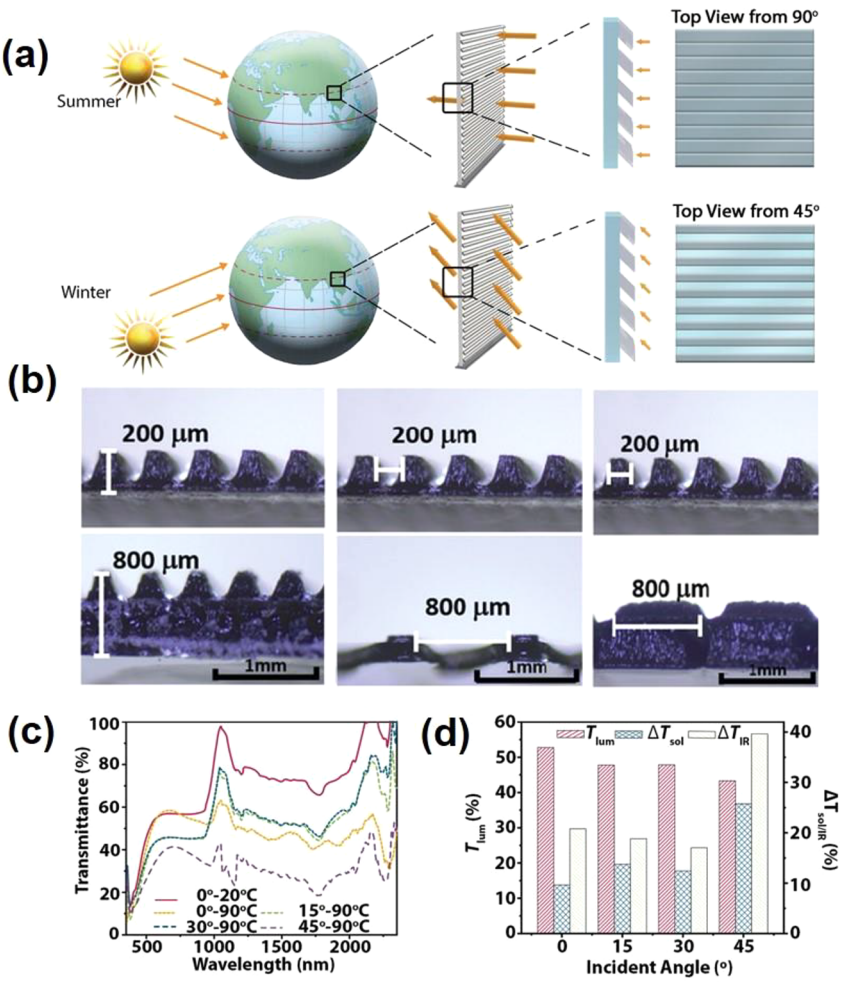

Figure 19. (a) Schematic design of the 3D printed smart windows design. (b) Optical microscopic pictures of the printed composite structures with identical 0° tilted angles with a range of thickness, spacing, and width. (c) UV−vis−NIR transmittance spectrum of the printed composite structure with respect to different incident angles and temperature. (d) T_{lum}, ΔT_{sol}, and ΔT_{IR} diagram of the printed composite structures with different incident angles. Reproduced with permission from ref 173. Copyright 2020 John Wiley and Sons.

fabricated through a 3D printing procedure, enabling the flexibility of device dimensions. Several samples of different thicknesses, widths, and spacing are demonstrated in Figure 19b. The incident-angle dependency properties of this structure are shown in Figure 19c,d in which modulating performance of the 3D printed device improves significantly, and ΔT_{sol} improves from 9.7% to 25.8% with respect to an increase in the incident angle from 0° to 45°.[173]

Aside from NIR transmittance regulation in smart windows, VO_2 also has an unusual ability to change its long-wave infrared emissivity (ε_{LWIR}) upon crossing the MIT. An ideal smart window should have high transparency in the visible region (380−780 nm), while having a transparent state in the winter and an opaque state in the summer (Figure 20a). Moreover, the ideal smart window should have a high ε_{LWIR} at a high temperature to promote radiative cooling (RC) and a low ε_{LWIR} at a low temperature to suppress RC. Based on this concept, Long et al.[174] fabricated a VO_2-based multilayer structure which was able to regulate NIR transmittance and ε_{LWIR} spontaneously (Figure 20b). Through forming a Fabry−Perot resonator, the passive RC regulating thermochromic (RCRT) smart window possessed an ε_{LWIR} of 0.21 at 20 °C, while the ε_{LWIR} increased to 0.61 above τ_c. In addition, the RCRT window kept a promising T_{lum} of 27.8% and a ΔT_{sol} of 9.3% (Figure 20c). With the actual building energy consumption simulation conducted with a 12-story building, the RCRT window yielded a higher energy savings compared with a commercial low-E window across different climate zones (Figure 20d). Meantime, Wu et al.[175] designed a flexible temperature-adaptive radiative coating (TARC) through embedding lithographically patterned W-doped VO_2 in a dielectric BaF_2 layer on top of a reflective gold layer (Figure 20e). The TARC film had a low ε_{LWIR} (~0.2) in the insulation state and a high ε_{LWIR} (~0.9) at the metallic state (Figure 20f), and the observation agreed with the simulation (Figure 20g). Long et al.[176] further expanded the concept of RC regulation from window to wall by preparing a switchable interwoven structure. As shown in Figure 20h, through pulling the block of interwoven structure, the original exposed block on the top side becomes concealed, and the underneath block becomes exposed. As a result, the structure switches its phase from phase 0 to phase 1. Taking into account different requirements of windows and walls, Long's group designed on-demand interwoven structures. Figure 20i shows the interwoven structure for window and wall applications. As discussed in Figure 20a, a window requires high visible transmittance and dual-band regulation for NIR and LWIR ranges. An ITO/VO_2/PVC combination was employed for windows. In this structure, VO_2 was used to regulate NIR, while

https://doi.org/10.1021/acs.chemrev.2c00546
Chem. Rev. 2023, 123, 4353−4415

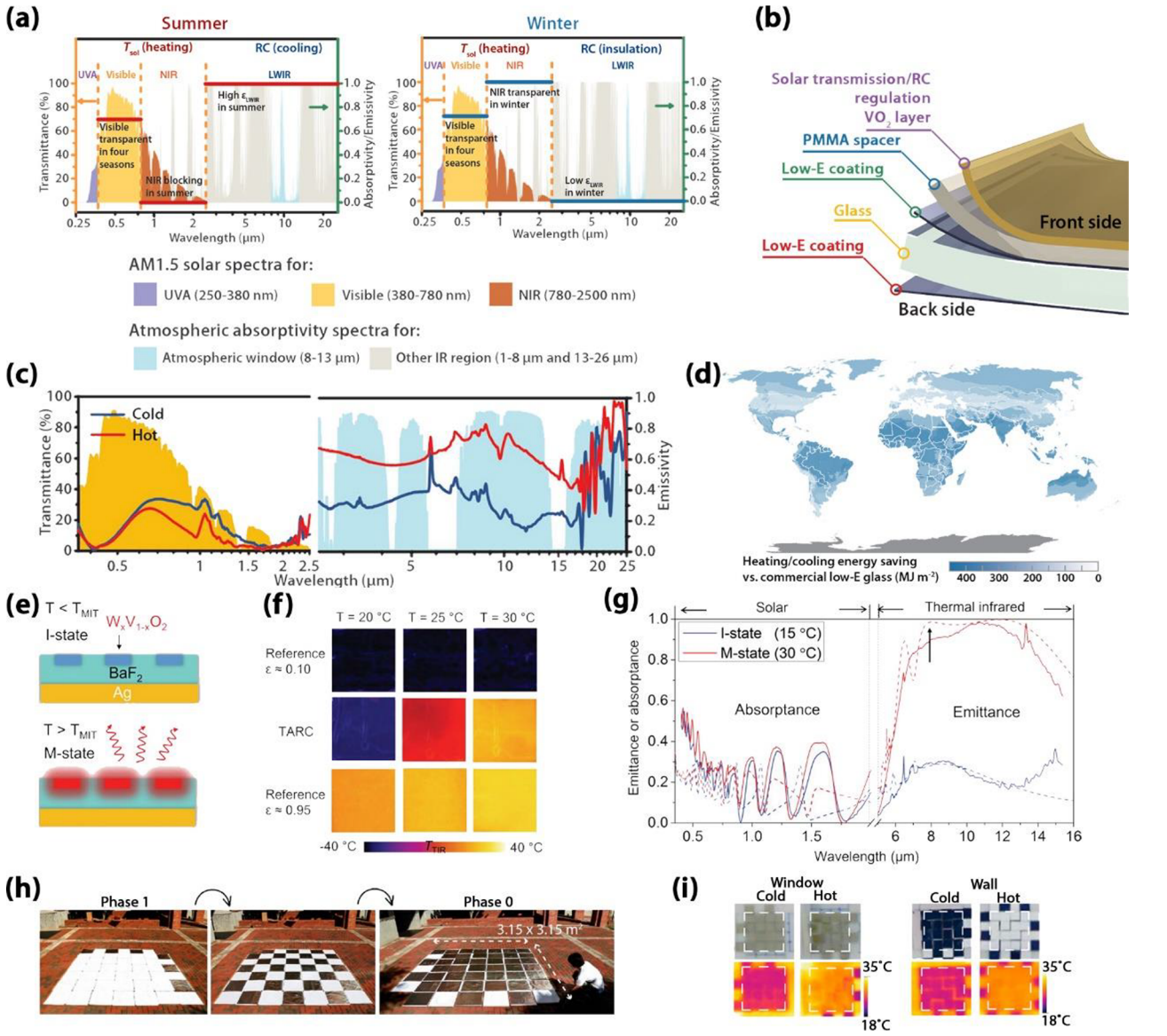

Figure 20. (a) Concept of the ideal energy-saving smart window. The red and blue lines represent the spectra for an ideal energy-saving smart window in the summer and winter. (b) Schematic structure of the RCRT window. (c) Spectra of the sample with RC regulation in the visible-NIR and LWIR range at 20 °C (blue line) and 90 °C (red line) against a normalized AM1.5 global solar spectrum (yellow shadow) and LWIR atmospheric transmittance window (blue shadow). (d) Estimated world heating and cooling energy-savings of a W-doped max $\Delta\varepsilon$ sample against a commercial low-E glass as the baseline. Reproduced with permission from ref 174. Copyright 2021 American Association for the Advancement of Science. (e) Schematics of materials composition and working mechanism of the TARC. (f) IR images of TARC compared with those of two conventional materials (references) with constantly low or high thermal emittance showing the temperature-adaptive switching in the thermal emittance of TARC. (g) Solar spectral absorptance and part of the thermal spectral emittance of TARC at a low temperature and a high temperature. Measurements (solid curves) show consistency with theoretical predictions (dashed curves). Reproduced with permission from ref 175. Copyright 2021 American Association for the Advancement of Science. (h) Demonstration of the surface transition in a meter-scale Al-paper sample. (i) Photographs and corresponding thermal images of the ITO/VO_2/PVC sample ("window" in the figure) and the ITO/black paint/PVDF-HFP sample ("wall" in the figure) on the two phases. Effective areas are marked by the dashed lines. Reproduced with permission from ref 176. Copyright 2022 American Chemical Society.

the ε_{LWIR} was regulated by alternatively exposing low-E ITO and high-E PVC. On the other hand, an ideal wall has high solar absorption and low ε_{LWIR} in the winter, and low solar absorption and high ε_{LWIR} in the summer. An ITO/black paint/PVDF-HFP combination was utilized to cater to this demand. On cold days, visible transparent ITO is exposed, and sunlight will be absorbed by black paint underneath, while on hot days, the highly solar reflective high-E PVDF-HFP is exposed to prompt RC. Hence, compared with a conventional performance index T_{lum} and ΔT_{sol}, the newly proposed ε_{LWIR} needs to be included to gauge the real energy-saving performance.[177] Moreover, VO_2 is notoriously known for poor durability, which is the bottleneck for the applications in smart windows. There are two recent reports to embed VO_2 in the V_2O_5 matrix, and such a strategy could increase the lifetime up to 33 years.[178,179]

Besides the application in building, the unique property of emissivity switching makes VO_2 the material of interest for IR camouflage and passive radiator for military and aerospace applications because VO_2-based devices can function entirely on the thermal trigger with no additional sources, electrical or

https://doi.org/10.1021/acs.chemrev.2c00546
Chem. Rev. 2023, 123, 4353−4415

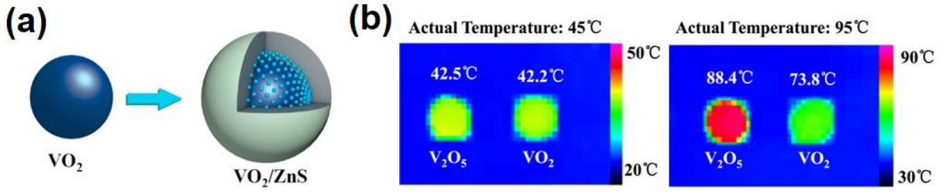

Figure 21. (a) Schematic of the VO_2/ZnS core−shell nanopowder design. (b) The infrared thermal images of same actual temperature for VO_2/ZnS core−shell nanopowder and reference V_2O_5 pellets at 45 °C (upper) and 90 °C (lower). Reproduced with permission from ref 182. Copyright 2018 Elsevier.

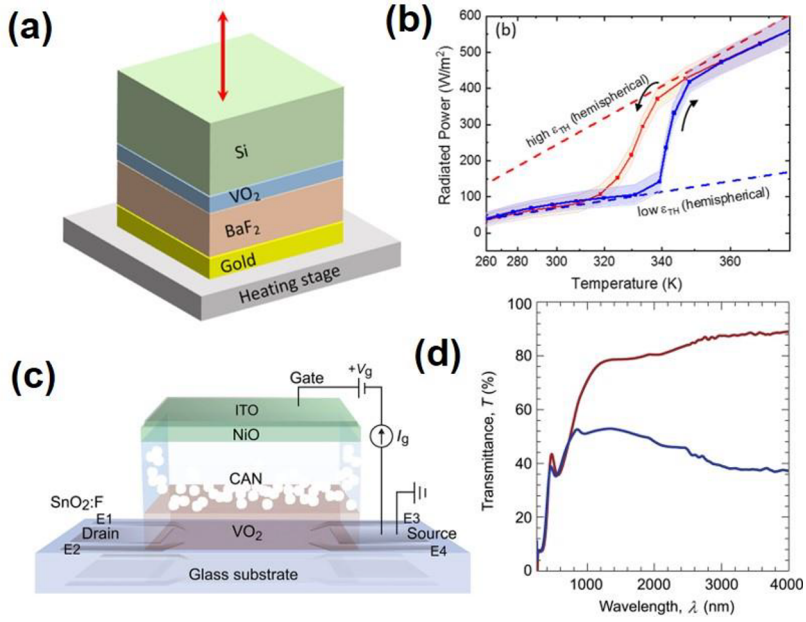

Figure 22. (a) Schematic of the Si/VO_2/BaF_2/Au passive radiator design. (b) Radiated thermal power of the Si/VO_2/BaF_2/Au device, with heating and cooling indicated with arrows; the dotted line is the simulation data for VO_2 (M) and VO_2 (R) respectively. Reproduced with permission from ref 184. Copyright 2019 under CC BY 4.0 license. (c) Schematic of the three-terminal transistor design. (d) Optical transmittance spectra measured before (red line) and after (blue line) applying V = +12 V. Reproduced with permission from ref 186. Copyright 2017 under CC BY license.

otherwise, required. VO_2-based camouflage devices work by reducing the amount of IR emitted into the environment, shrouding the user from being detected with an IR detector such as most night-vision technologies. Examples include VO_2/graphene/CNT heterostructure by Xiao et al.,[180] VO_2/carbon hybrid by Wang et al.,[181] and VO_2/ZnS core−shell structure (Figure 21a) by Ji et al.[182] As seen in Figure 21b, under a similar IR detector and temperature, the VO_2/ZnS core−shell pallets exhibit the ability to control their IR radiation intensity and lower their detected temperature as compared to V_2O_5 pallets with constant emissivity.

Different from a camouflage device, a VO_2-based passive radiator requires modification to the device structure to counter the lower emissivity at the higher temperature. This intrinsic problem could be overcome by depositing VO_2 on a highly reflective metal substrate with[183,184] or without[185] a spacer layer. Figure 22a is a multilayer Si/VO_2/BaF_2/Au structure reported by Kim et al.,[184] which was designed and tested specifically for simulated space (vacuum) applications. Figure 22b demonstrates the radiated thermal power of the multilayer device. Experimental data were compared with simulated ones for both high and low-temperature operations. The measured radiated power at 300 and 373 K was 72 W/m^2 and 552 W/m^2, respectively, showing a massive jump in emitted radiation upon crossing the MIT threshold.[184] Due to the typical multilayer design of a VO_2-based passive radiator, factors such as functional emissivity difference between low and high temperature as well as the wavelength of emitted light can be further fine-tuned by adjusting the substrate/spacer/film combination. The electrochromic setup has also been shown to also result in IR regulating behavior in VO_2-based devices.[186] Figure 22c is the schematic of a three-terminal thin-film-transistor-type electrochromic device by Katase et al.[186] Upon application of external voltage (+12 V according to literature), the VO_2 channel undergoes protonation, and the device becomes IR opaque, similar to smart window applications. When a reversed voltage is applied, deprotonation happens, and the device becomes IR transparent once again. Figure 22d shows optical transmittance spectra measured during this transition with +12 V stimulus. The optical transmittance modulation ratio at λ of 3000 nm was 49%.[186] Electrical input into a VO_2-based device can also be utilized as a Joule heating source for MIT. To realize this, VO_2 can be combined with transparent conductive electrode materials such as ITO, Ag NWs, CNT, etc.[187,188] to become an electro-optic modulator. An example of such a modulator is a VO_2+Au/GaN/Al_2O_3 device by Fan et al.,[189] which has the ability to change the transmission step-by-step according to the applied voltage.

6.2.1.2. Optical Switches. Based on the sudden change in the optical constants n and k of VO_2 across MIT, radio frequency (RF) switches or waveguides can be fabricated to control the

https://doi.org/10.1021/acs.chemrev.2c00546
Chem. Rev. 2023, 123, 4353−4415

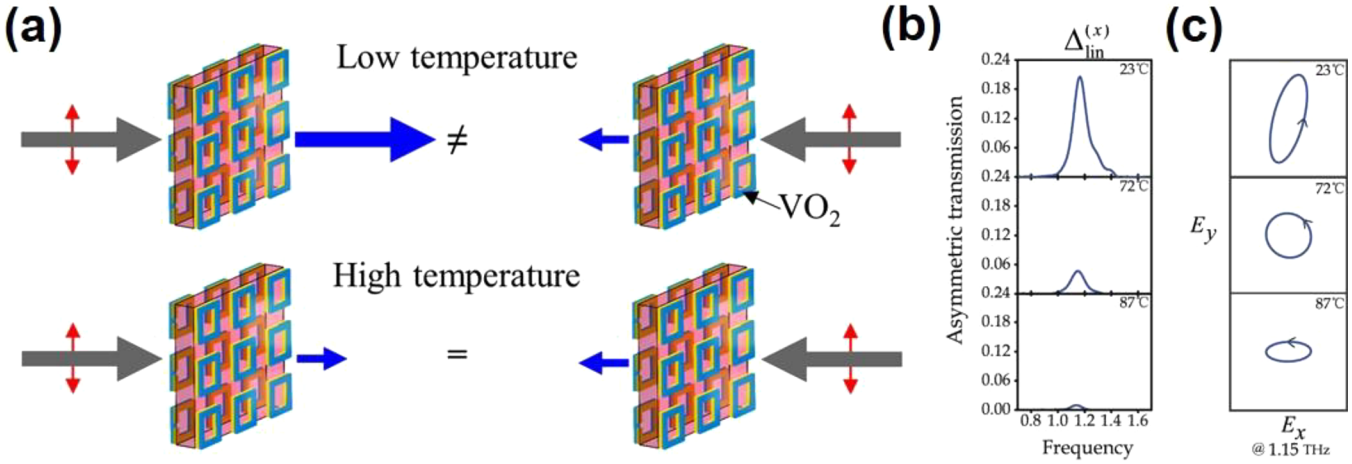

Figure 23. (a) Schematic of the temperature-controlled VO_2 metamaterial asymmetric optical switch. (b) Frequency dependence of the asymmetric transmission parameter for linearly polarized waves, and (c) transmitted polarization state at 1.15 THz for illumination with x-polarized waves. Reproduced with permission from ref 194. Copyright 2019 under CC BY 4.0 license.

flow of electromagnetic waves (i.e., microwave and radio-wave).[190] Even though the design of each device is largely dependent on whether it is thermally[191] or electrically activated,[120] the mechanism for turning from the ON to OFF state is still entirely based on the transition from VO_2(M) to VO_2(R) respectively. Examples of RF-switches are the thermally configurable hybrid Al nanoholes/VO_2 photonic switch by Sun et al.,[192] metamaterial design by Ding et al. which can act as an absorber from 0.562 to 1.232 THz at room temperature and a high-efficiency halfwave plate at high temperature,[193] and temperature controlled asymmetric optical switch by Liu et al.[194] Figure 23a shows the working principal of this design in which different output of the same polarized electromagnetic wave input can be achieved at low temperature by physically reverting the device by 180° while achieving similar output at high temperature. This asymmetrical mechanism is demonstrated in Figure 23b,c. A large asymmetry exceeding 20% was detected at 23 °C, while it disappeared almost entirely at 87 °C (Figure 23b). With incident x-polarized waves, the device gave y-polarized waves output at 23 °C, and this can be considered the ON state. Upon heating to 87 °C, output waves returned to approximately x-polarized, similar to input waves, turning the switch OFF (Figure 23c).[194] While the thermal- and electrical-activated optical switches mainly depend on the change of optical constant upon MIT, the optical-activated switches of VO_2 focus on the speed of the transition as the defining factor. However, the details of the ultrafast induced phase transition of VO_2 are not the focus of this review; it can be found in a summary and discussion by Wegkamp et al.[195] VO_2 ability to switch between the insulator and metal state within picoseconds is promising for the field of nanophotonics as well as all-optical integrated circuits (i.e., switches, modulators, and data-storage devices). VO_2 integrated metamaterials have been reported to exhibit nonlinear transmittance by Liu et al.[153] in the THz range as well as broadband responses spanning from the visible to mid-infrared range by Guo et al.[196] VO_2/Au nanoplate memory device was also reported by Lei et al.,[197] giving a stepwise tuning ability with the use of successive laser pulses.

6.2.1.3. Plasmonic Applications. The reversible crystal phase transition makes VO_2 very unique among plasmonic materials. It undergoes a crystal phase transition from the monoclinic semiconductor state to rutile metallic state with significantly promoted conductivity and free carrier density,[27] leading to a significant difference in its plasmonic property. Recently, VO_2 nanoparticles (NPs) have been reported with thermal-responsive localized surface plasmonic resonance (LSPR) in the NIR region.[168,198] Based on the colloidal lithography method,[59] Long's group successfully produced the hexagonally patterned VO_2 NPs on quartz with controllable average diameters from ∼70 to ∼280 nm.[198] It was observed that the LSPR position of metallic VO_2 shifts to the longer wavelength on the larger NPs (∼1120 to ∼1220 nm) or under the increasing reflective index of the surrounding medium (∼1120 to ∼1360 nm) (Figure 24a). Besides, the NIR LSPR is temperature-responsive that is quenched on a low-temperature semiconductor state and can be gradually switched on from 20 to 100 °C (Figure 24b). They further investigated the LSPR-induced absorbance and scattering effects of VO_2 plasmonics through a finite-difference time-domain method.[168] On a single VO_2 NP, it is revealed that both the absorbance and scattering are low at the semiconductor state (monoclinic, M), while a strong absorbance emerges in the metallic state (rutile, R) (Figure 24c). This result suggests that the LSPR in metallic VO_2 is characterized as a strong absorbance enhancement and a relatively weak scattering effect. Moreover, they reported the dispersity- and strain-induced LSPR response on VO_2 NPs in the polydimethylsiloxane (PDMS) elastomer matrix (Figure 24d,e).[28] The dispersity-induced LSPR position can be attributed to the changes in average gaps among VO_2 NPs in the matrix, which is consistent with the simulation result (Figure 24d), while the strain-dependent LSPR position change can be explained by the local reflective index change induced by the delamination between the NP and matrix under applied strains as being demonstrated by the finite element method (Figure 24e,f). A more recent report used a similar approach to tailor the VO_2 surface plasmon by manipulating its atomic defects and establishing a universal quantitative understanding.[199] Record high tunability is achieved for LSPR energy from 0.66 to 1.16 eV and a transition temperature range from 40 to 100 °C. The Drude model and DFT calculation reveal that the charge of cations plays a dominant role in the numbers of valence electrons to determine the free electron concentration. It is believed the investigation of VO_2 LSPR is still in its early stage. The reversible crystal transition makes VO_2 an intrinsic active

https://doi.org/10.1021/acs.chemrev.2c00546
Chem. Rev. 2023, 123, 4353−4415

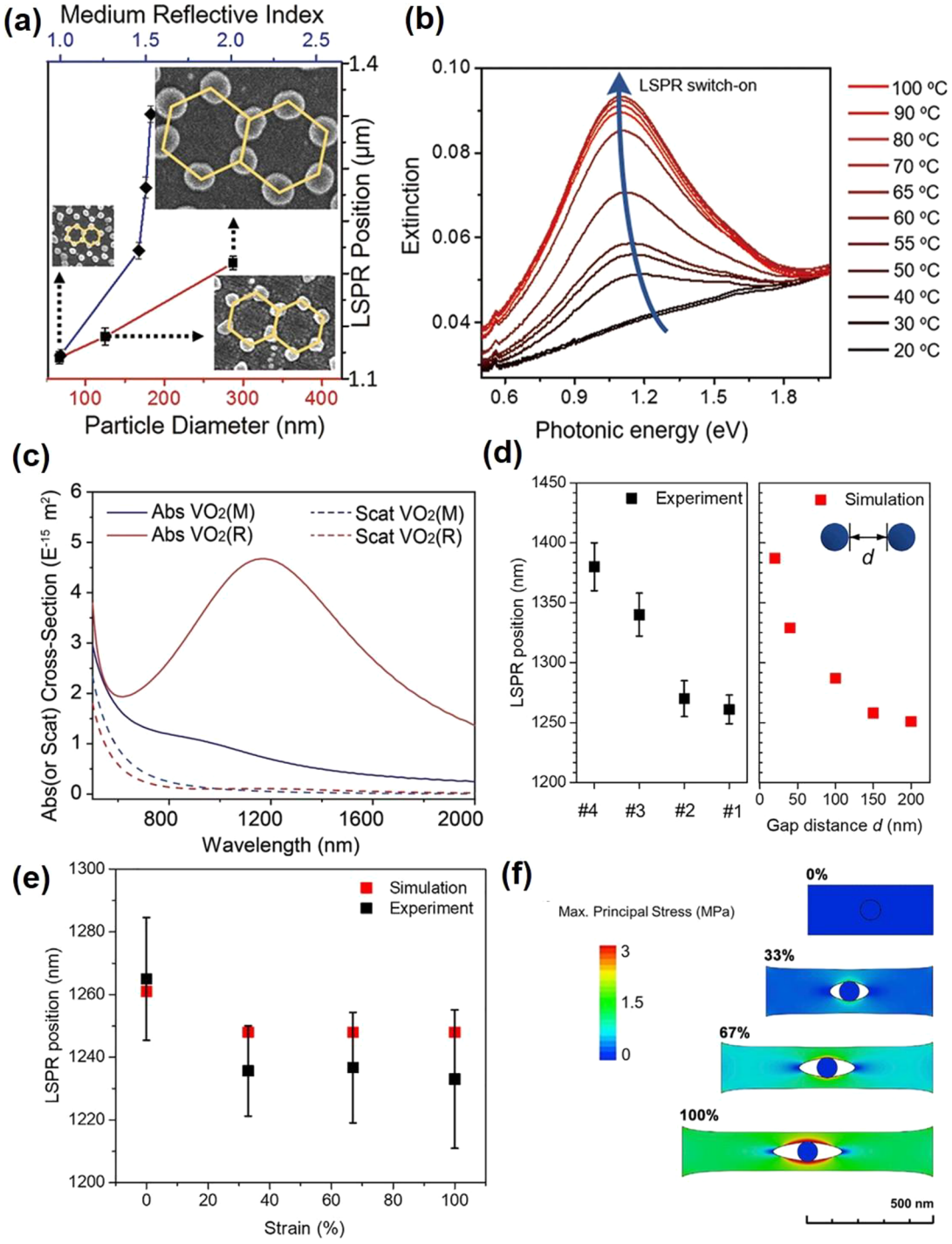

Figure 24. (a) Effects of the particle diameter and medium reflective index to the LSPR position. Insets are the SEM images of VO_2 NPs with corresponding diameters, and the array structures are highlighted as yellow hexagons. (b) Extinction spectrum of VO_2 NP under different temperatures from 20 to 100 °C. Reproduced with permission from ref 198. Copyright 2017 American Chemical Society. (c) Simulated absorbance and scattering intensity crossing a VO_2 NP embedded in PDMS matrix. Reproduced with permission from ref 168. Copyright 2020 Elsevier. (d) Experimental LSPR position of VO_2 NPs with different dispersion degrees in PDMS, and the simulation result of two adjacent VO_2 NPs with a different gap. (e) Experimental and simulation results of the LSPR position of VO_2−PDMS composites under applied strains from 0% to 100%. (f) Simulated stress contours of the representative VO_2−PDMS composite under applied strain from 0% to 100%. Reproduced with permission from ref 28. Copyright 2019, Cell Press.

plasmonic material, which is unique among the plasmonic field. It is expected for researchers to further understand the VO_2 plasmonic and to explore its potential applications.

6.2.2. Electrical Applications. Not only optical constants, but the electrical conductivity of VO_2 is also altered dramatically upon transitioning from insulating VO_2 (M) to metallic VO_2 (R). This measurable electrical response to various external stimuli makes VO_2 the prime candidate for electrical applications such as sensors or transistors. The following section

https://doi.org/10.1021/acs.chemrev.2c00546
Chem. Rev. 2023, 123, 4353−4415

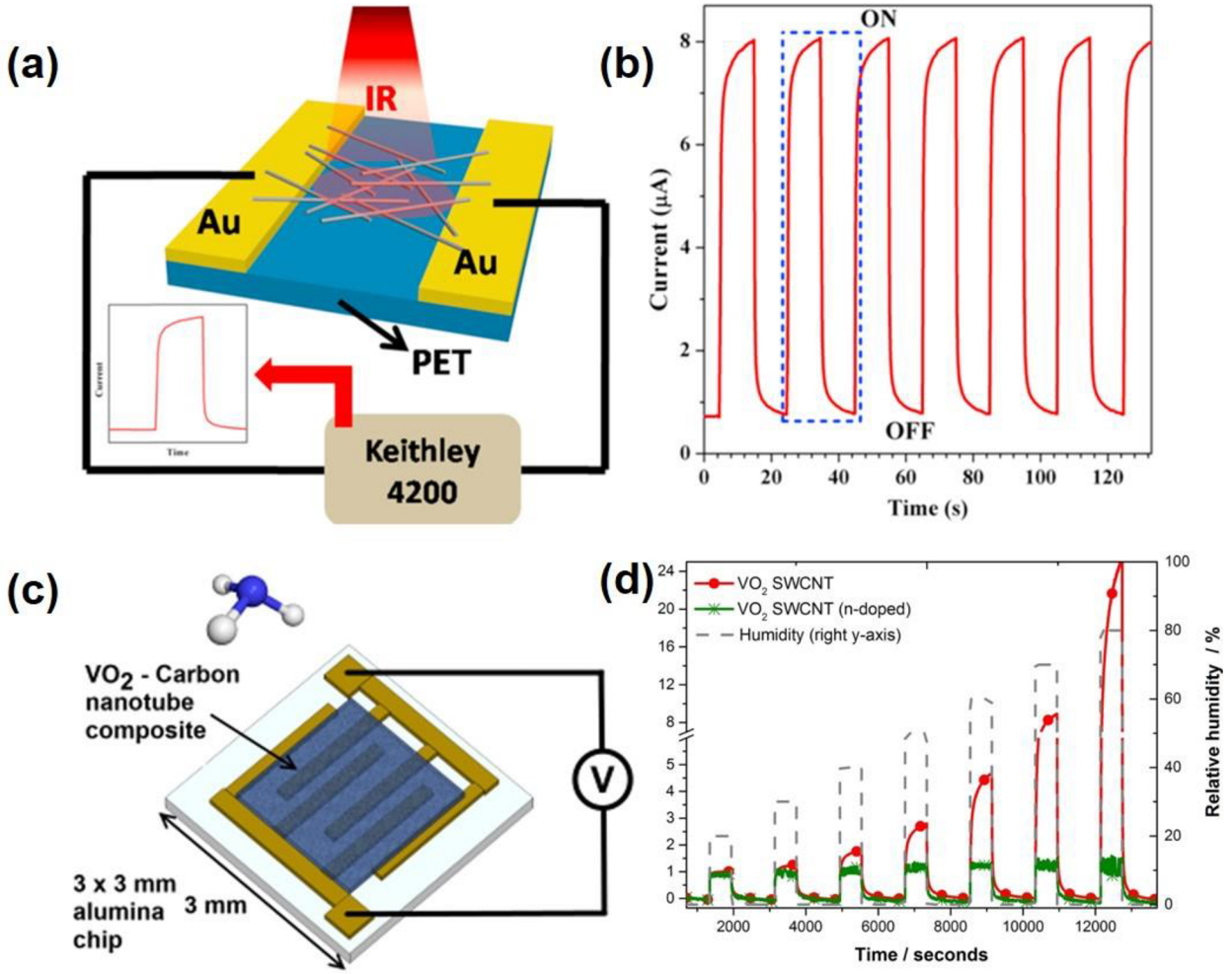

Figure 25. (a) Schematic of the VO_2 nanowire photodetector. (b) Time-dependent photodetection capabilities of the VO_2 nanowire device. Reproduced with permission from ref 202. Copyright 2018 Elsevier. (c) Schematic of the VO_2/CNT gas sensor. (d) Time-dependent humidity sensing capabilities of the VO_2/SWCNT and n-doped variant at different humidity levels. Reproduced with permission from ref 206. Copyright 2018 Elsevier.

discusses the electrical applications of VO_2 and their corresponding devices.

6.2.2.1. Sensors. A sensor is defined by its ability to measure physical input and translate these measurements into interpretable data. Based on the significant conductivity changing of VO_2 across the MIT, it is possible to convert physical environmental input into a readable electrical signal. Some examples of VO_2-based sensors include temperature sensors, photodetectors, flexible strain sensors, and gas sensors. Intrinsically, VO_2 is not suitable for temperature sensing applications because the change in its electrical conductivity only happens at 68 °C, even though Kim et al.[200] managed to fabricate a programmable VO_2 critical temperature sensor. VO_2 was deposited on an Al_2O_3 (1010) substrate and between two nickel (Ni) electrodes. A voltage can be applied across these electrodes to cause the τ_C of VO_2 to decrease, causing the VO_2 (M) film to go into an intermediate phase before fully transitioning into VO_2 (R). During this intermediate phase, the measured current through the device was found to be linear with the change in temperature. At a voltage of 20 V, the τ_C is found to be ~20 °C, enabling full range sensing capabilities from 20 to 68 °C. Another approach, which is based on the sensing ability resulting from an abrupt change of the dielectrically constant of VO_2 during MIT instead of conductivity, was done by Yang et al.[201] As mentioned in the previous section, optically stimulated applications of VO_2 are promising due to the ultrafast transition mechanics, stability, as well as the broadband optical response of VO_2-based devices. Hou et al.[202] demonstrated the device stability and speed of response using a VO_2 (M) nanowire on Au electrode setup (Figure 25a). It was reported that the device needs less than 1.6 s to detect IR (980 nm) and <1.0 s to recover (Figure 25b). The device was also reported to maintain responsivity for more than 500 cycles. Another design from Takeya et al.[203] combined the photoresponsivity of VO_2 film and the localized surface plasmon resonance of silver nanorods. The results indicated a correlation between the incident light transmission and resistivity within a wavelength of 400−900 nm. While the VO_2 acted as a photosensitive component, the nanorod array introduced a wavelength and polarization sensitivity to the photodetector. Because the MIT of VO_2 results in the change in the lattice structure and constant, it is also possible to induce MIT by causing changes to the lattice through mechanical force, which serves as the basis for VO_2 flexible strain sensor application. Hu et al.[204] showed that a VO_2 strain sensor device could be fabricated by bonding one single VO_2 nanobeam to a polystyrene (PS) substrate with silver paste and measuring the resistivity of the nanobeam as tensile and compressive stress is applied along the length of the nanobeam. In this study, VO_2 (R)

https://doi.org/10.1021/acs.chemrev.2c00546
Chem. Rev. 2023, 123, 4353−4415

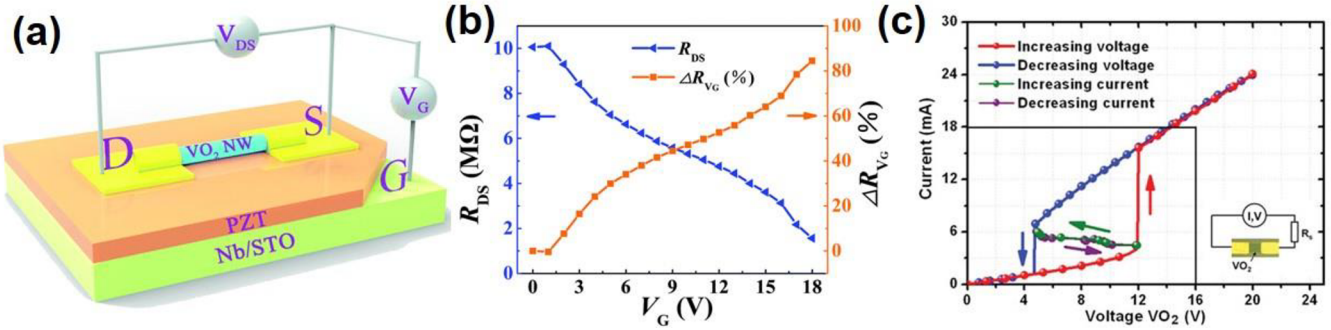

Figure 26. (a) Schematic of the VO_2−NW-FeFET design. (b) Resistance change of the VO_2−NW-FeFET ranging from 0 to 18 V. Reproduced with permission from ref 211. Copyright 2020 Royal Society of Chemistry. (c) *I*−*V* characteristic in voltage- and current-mode of a device incorporating a VO_2 pattern; inset is the schematic test circuit. Reproduced with permission from ref 216. Copyright 2012 Cambridge University Press and the European Microwave Association.

was not formed, and only the VO_2 (M_2) phase was formed due to the constraint of force applied (only 0.25% as compared to the required 2% at room temperature). However, the device showed remarkable potential when exhibiting a stepwise response to as small as 0.05% tensile or compressive strain.

A typical gas sensor design is demonstrated in Figure 25c. For gas sensor application, the semimetallic VO_2 (B) phase is more commonly used than the insulating VO_2 (M) phase to maintain sensing capability at room temperature. VO_2, regardless of the phase, responds to humidity, ammonia (NH_3), and nitrogen dioxide (NO_2).[205,206] Compositing VO_2 with carbon species such as single- or multiwalled carbon nanotubes (SWCNTs or MWCNTs) was reported by Evans et al.[206] The setup was effective in creating a stable, responsive VO_2−CNT gas sensor. Figure 25d shows excellent response and good recovery of VO_2−SWCNT to different humidity levels. The resistive response was increased dramatically from 0.5 for pure VO_2 (B) to 2.7 for VO_2−SWCNT and 7.1 for VO_2-MWCNT at 50% humidity. This p-type gas sensing response was also reported for NH_3 in the same study despite the longer and lower recovery level recorded. Depending on the applications, property change across the MIT is not the only viable option to use VO_2 in a functional device.

6.2.2.2. Electrical Switches, FETs, Oscillators, and Memristors. Different from sensing applications, the MIT of VO_2 can be deliberately triggered with programmable duration and patterns to great advantage in electrical switching, FET, oscillator, and memory devices. Similar to optical switches in the previous section, by toggling VO_2 across the MIT, it is possible to create an ON/OFF switching mechanism based on the difference in electrical resistance of VO_2 (M) and VO_2 (R). It has been demonstrated by Zhou et al.[207] that a two-terminal VO_2-based switching device can have ultrafast, reliable 2 orders of magnitude ON/OFF toggling ability within 2 ns. While the MIT in this report was induced by an applied current, an electrical switch activated by Joule heating was also reported in a separate study by Li et al.[208] Mott FET is a gated FET device in which the conventional semiconductor channel is swapped with a Mott insulator, a material with the ability to switch from insulator to metal through external voltage to the gate. VO_2, as a Mott insulator, is the prime material for novel Mott FET studies. An example of a typical Mott FET setup was reported by Yajima et al.[209] in which a large current modulation can be observed at 315 K, indicating a positive-bias gate-controlled MIT near τ_C of VO_2. Another novel Mott FET design was also fabricated by Shukla et al.[210] with a VO_2 as a source terminal. This design functioned well at room temperature (300 K) with reversible MIT triggered by the critical applied current. Taking advantage of the VO_2-based Mott FET designs and combining it with a ferroelectric material, Zhang et al.[211] fabricated a nonvolatile ferroelectric FET (FeFET) device with VO_2 nanowires as the channel and $Pb(Zr_{0.52}Ti_{0.48})O_3$ (PZT) thin film as the dielectric gate (Figure 26a). The novel FeFET device was reported to achieve up to 85% resistance change under a gate voltage of 18 V (Figure 26b). Interestingly, the presence of the ferroelectric materials created a polarization effect after the applied voltage was removed, in which the channel resistance could attain up to 50%. Through this mechanism, it is possible to achieve multiple resistive states by the sweeping suitable gate voltage. To overcome the disadvantage of solid-gate oxide dielectric FET, such as current leakage, which might interfere with the MIT of VO_2, ionic liquid (IL) and solid-state electrolyte gating have been the research interest for VO_2 FET devices in recent years.[212] However, the mechanism in which IL drives the MIT of VO_2 is still a debate between different studies. Nanako et al.[151] suggested that the underlying mechanism is the bulk carrier delocalization caused by the electrostatic effect. On a different train of thought, Jeong et al.[213] attributed the transition to the field-induced creation of oxygen vacancies, rather than the purely electrostatic effect. Ji et al.[214] and Shibuya et al.,[215] however, suggested that electrochemical protonation was the origin of the modulation of electrical property in VO_2, similar to what was observed in the electrochromic setup in the previous section. An electronic oscillator is a common component in modern electronic circuitry which can produce periodic signals such as a square wave or a sine wave. Due to the periodicity of the output, it is often used to convert a direct current (DC) input into an alternate current output. The two main types of electronic oscillators are the linear (harmonic) and nonlinear (relaxation) oscillator. Because of the ability to undergo a nonlinear MIT, VO_2 can be used as the basis for a nonlinear oscillator with a relaxation behavior stimulated by external electricity input. A VO_2-based oscillator design by Leroy et al.[216] and its *I*−*V* characteristic curve is shown in Figure 26c. The inset shows the schematic of the oscillator circuit in which a resistor (R_s) is connected to the VO_2 device to produce a current-controlled negative differential resistance (NDR). The NDR portion happens when VO_2 enters the transitive state between VO_2 (M) and VO_2 (R). It was reported that by controlling R_s, the VO_2-based oscillator circuit can become self-sustaining, and the frequency can range from kHz to 1 MHz.[152] Aside from the standard setup as shown in Figure 26c, studies have also been

https://doi.org/10.1021/acs.chemrev.2c00546
Chem. Rev. 2023, 123, 4353−4415

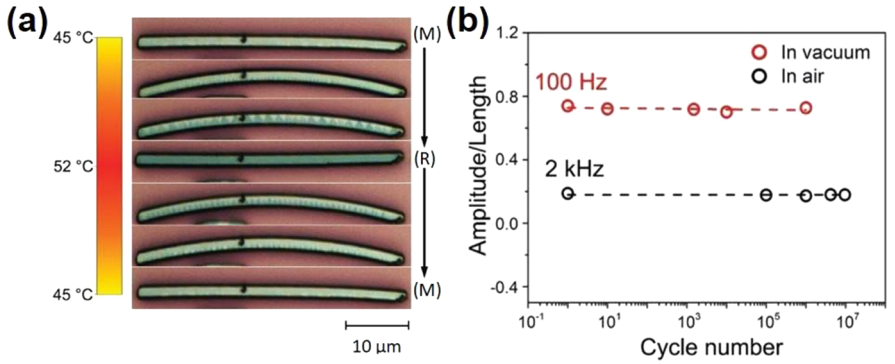

Figure 27. (a) Optical images of the VO_2 nanobeam undergoing MIT. (b) Amplitude versus cycle number plots of the nanobeam subjected to a chopped laser (100 Hz in a vacuum and 2000 Hz in air). Reproduced with permission from ref 227. Copyright 2019 John Wiley and Sons.

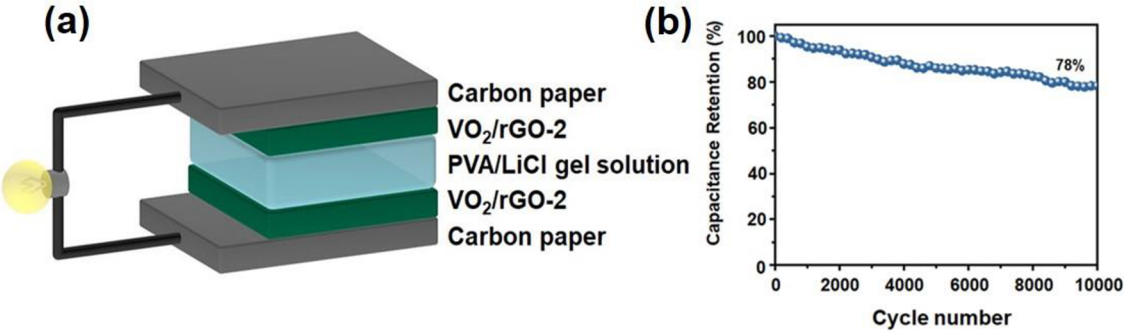

Figure 28. (a) Schematic illustration of the all-solid-state supercapacitor. (b) Cyclic stability test of the VO_2/rGO supercapacitor device. Reproduced with permission from ref 235. Copyright 2019 under CC BY 4.0 license.

done in which two oscillators are coupled with a resistor, a capacitor, or FET in between.[217] A memristor is a nonvolatile electronic memory device which has a programmable resistance. The resistance of a memristor is retained even after removal of the power and is dependent on the original applied voltage. It is crucial that the resistance can be reversed or reprogrammed. Thus, a two-terminal VO_2 electrical device with the nonvolatile switching of resistance across the MIT can also be adapted into memristors.[149] Bae et al.[150] demonstrated a two-terminal memristor based on a single VO_2 nanobeam. The nanobeam undergoes MIT when a bias of 3 and 5 V was applied for 0.25 s; the resistance of the device goes from an initial 10^{11} Ω to 10^9 and 10^8 Ω respectively. The resistance change can be reset with a zero-voltage bias. VO_2 has also been utilized in other memory devices including a multistate free-standing VO_2/TiO_2 cantilever,[218] resistive random-access memory (ReRAM) devices.[219] and 3D memory array.[189] Not included in the above discussion is the minor application of VO_2 in field emitter and spintronic devices which are based on the abrupt drop in resistance across thermal- and magnetical-activated MIT, respectively. Studies on VO_2/ZnO core−shell nanotetrapod thermal-activated field emitters were reported by Yin et al. in 2014.[220] On the other hand, VO_2-based spintronic devices and the behavior of the magnetoresistance of VO_2 were reported in detail by Li et al.,[221] Choi et al.,[222] and Singh et al.[223]

6.2.3. Mechanical Applications. The actuator is typically a component in a machine or a system which converts provided energy into mechanical motion. The concept of the actuator has been widely adapted into novel scientific research, especially in the field of microrobotics or micro-/nanoelectromechanics.[224] VO_2, which has a high theoretical work density (≈ 7 J cm^{-3}) and fast response rate to external stimuli, is suitable for actuator applications. It offers the ability to offset disadvantageous low work density and the slow response rate of common actuator materials such as piezoelectric ceramics or polymers and CNT, respectively.[225] In device fabrication, single crystal VO_2 or composite bimorph of VO_2 can be designed to respond to specific external stimuli such as light, heat, or electrical current. An example of a photodriven VO_2 bimorph design was reported by Ma et al.[226] in 2018. The VO_2/CNC device was conceived by combining the carbon nanocoil (nanosprings twisted by hollow carbon nanofibers) core with a VO_2 shell. When exposed to 980 nm radiation, the temperature of the spring increases unevenly, forming a temperature gradient from tip to end. This results in a transition gradient in which the tip becomes VO_2(R) first and shrinks, creating the curvature. The VO_2/CNC actuator delivers a large displacement-to-length ratio (∼0.4), fast response rate (9400 Hz), and long durability (>10^7 cycles). More recently, Shi et al.[227] fabricated thermal-activated single-crystalline VO_2 actuators (SCVAs) which were designed so that the τ_C of a single VO_2 nanobeam is a gradient along the radial direction. When exposed to heat, one side of the fabricated W-doped VO_2 nanobeam with lower τ_C would undergo MIT first and shrink, creating a bending as seen in Figure 27a. It was reported that this SCVAs design performed competitively with other reported VO_2 bimorph actuator designs with an extremely high displacement-to-length ratio (∼1), high energy efficiency (∼0.83%), fast response rate in the order of kHz, and long durability (>10^7 cycles) (Figure 27b). VO_2 electrothermal devices with joule heating activation for oscillator[228] and microelectromechanical systems (MEMS)[229] have also been fabricated with variable degrees of success. A resonator is a device that exhibits resonance at its eigenfrequency. With VO_2, the eigenfrequency of a resonator can be dynamically controlled

https://doi.org/10.1021/acs.chemrev.2c00546
Chem. Rev. 2023, 123, 4353−4415

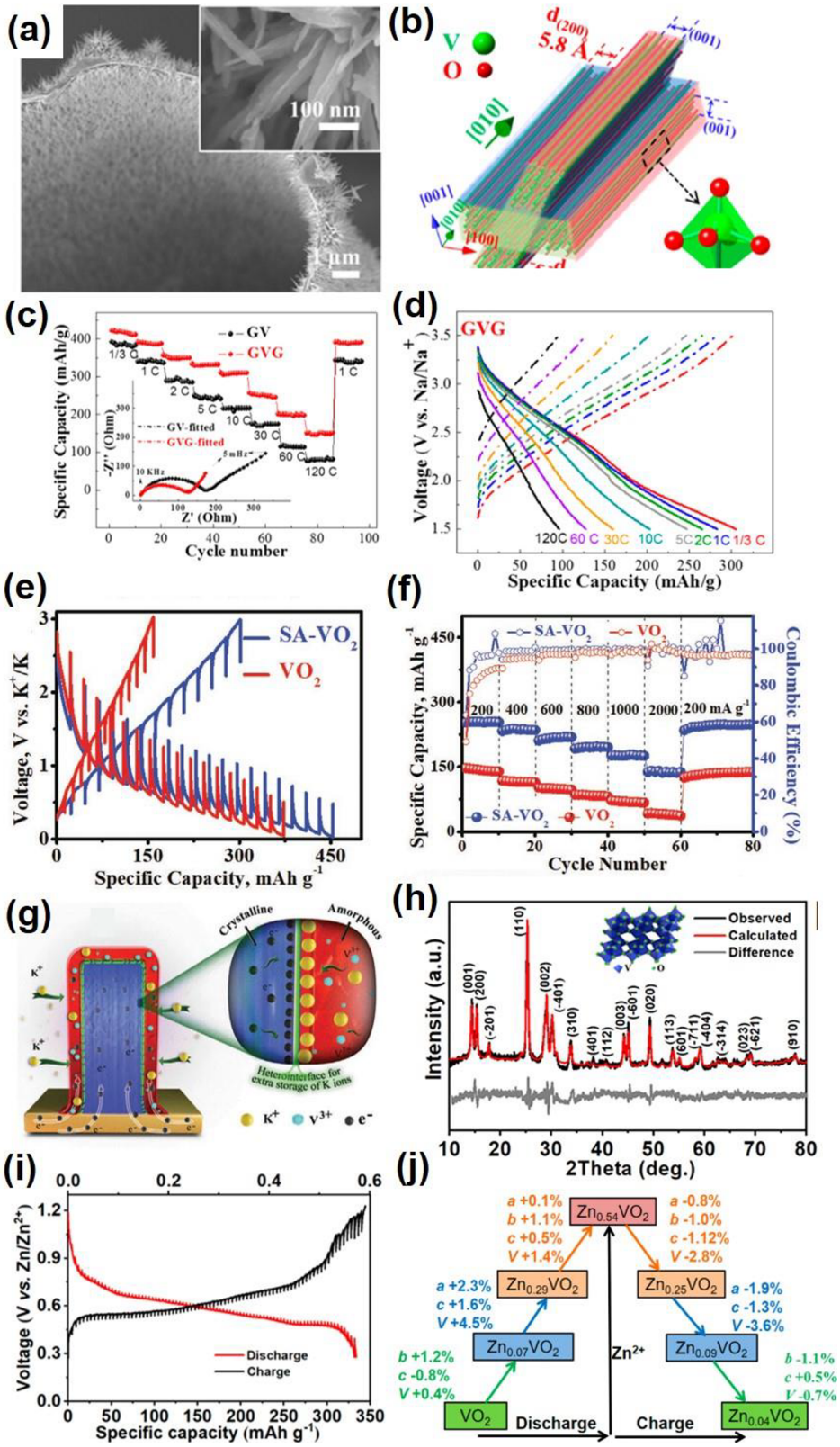

Figure 29. SEM image (a), geometrical model (b), LIB rate performance (c), and SIB charge/discharge profiles (d) of bilayered VO_2 nanobelt. Reproduced with permission from ref 237. Copyright 2015 American Chemical Society. The GITT curves (e), rate performances (f) of SA-VO_2 and VO_2, and the schematic of the enhanced K ion storage ability (g) of SA-VO_2. Reproduced with permission from ref 238. Copyright 2020 John Wiley & Sons. The Rietveld refinement result from the XRD data and crystallographic structure (h), GITT curve (i), and most significant changes of lattice parameter in each stage (j) of VO_2. Reproduced with permission from ref 239. Copyright 2019 American Chemical Society.

by thermally triggering the MIT. This specific frequency is positively related to Young's modulus of VO_2, which is widely different between the monoclinic phase (151 ± 2 GPa) and the rutile phase (218 ± 3 GPa).[230] Studies have been made to

https://doi.org/10.1021/acs.chemrev.2c00546
Chem. Rev. 2023, 123, 4353−4415

determine the effects of elemental doping on the frequency modulating ability of VO_2-based resonators. Rúa et al.[231] compared the Cr-doped VO_2 resonator with the undoped one and concluded that the doped sample had a higher frequency change due to a lower Young's modulus. Other strategies to improve performance such as changing the shape from a simple cantilever have also been done by Manca et al.[232]

6.2.4. Supercapacitors. VO_2 (B) with its layered structure and multioxidation states is ideal as an electrode material with charge storage through insertion and fast surface Faradaic reaction.[233] However, being in common with all metastable VO_2 phases, VO_2 (B) structural instability is not suitable for cyclic stability of SC application. Multiple studies have been done to combine VO_2 (B) with various carbon composites to create stable electrode materials.[234] An example of a VO_2 and reduced graphene oxide (VO_2 (B)/rGO) device by Liu et al.[235] is shown in Figure 28. The schematic diagram of the all-solid-state sandwich-structured supercapacitor design is shown in Figure 28a, where symmetrical VO_2 (B)/rGO and PVA/LiCl gel are used as electrodes and electrolytes, respectively. The performance of this design was reported to have a superior specific capacitance of 353 F g^{-1} at 1 A g^{-1} and a maximum power density of 7152 W kg^{-1} at an energy density of 3.13 Wh kg^{-1}. By compositing VO_2 (B) with rGO, 78% capacitance was retained after 10000 cycles, improving the stability of the device immensely (Figure 28b).

6.2.5. Magnetic Refrigeration. Magnetic refrigeration is a cooling technique that is based on the magnetocaloric effect (MCE). The MCE describes the phenomenon in which a suitable material can be heated up or cooled down when exposed to a changing magnetic field. Due to the changing magnetization when crossing the MIT, VO_2 was first shown to be suitable for magnetic refrigeration application by Wu et al.[236] in 2011 with a single crystalline nanorod fabrication technique. Although the potential was shown for VO_2 in magnetic refrigeration applications, studies to further improve this are still limited.

6.2.6. Batteries. VO_2 formed by edge-sharing VO_6 octahedra with a unique bilayer structure exhibits a large lattice spacing that can accommodate Li^+ (0.76 Å), Na^+ (1.02 Å), K^+ (1.38 Å), and Zn^{2+} (0.74 Å) insertion/extraction. Fan et al.[237] designed and synthesized a binder-free VO_2 cathode via biface VO_2 arrays directly growing on a graphene foam (GF) network (Figure 29a). They constructed a geometric model of bilayered VO_2 nanobelts through the growth direction and lattice spacings (Figure 29b). The relatively high stacking rate of the "steplike" VO_6 octahedra along the [010] direction determines the preferred growth direction. As a result, the (001) facet of the VO_2 nanobelt is the thinnest, and the interlayers between the (200) crystal planes provide a facile channel for Li^+ and Na^+ diffusion. Meanwhile, the graphene quantum dots (GQDs) coating on the VO_2 surfaces can act as highly efficient surface protection to further enhance the Li^+/Na^+ storage. When as-prepared GF-supported GQD-anchored VO_2 arrays (GVGs) are directly used as a LIBs/NIBs cathode, it exhibits two advantages: high ion diffusion sensitization and charge transport kinetics are beneficial to obtain high-rate capacities, and the homogeneous GQDs suppress VO_2 dissolution which is in favor of retaining long-term cycles. The GVG electrode delivers a high specific capacity of 421 mAh g^{-1} at 1/3 C for Li^+, which is much higher than that of the uncoated GF@VO_2 electrode (391 mAh g^{-1}). It can maintain 151 mAh g^{-1} even at 120 C,and 94% of the initial capacity can be retained after 1500 cycles (Figure 29c). When it is used as an NIB cathode, it exhibits a specific capacity of 306 mAh g^{-1} at 1/3 C and good capacity retention (Figure 29d). These results demonstrate that the GVG is an excellent electrode material for Li^+/Na^+ storage.

Zhang et al.[238] first designed and synthesized a surface amorphized VO_2 (B) nanorod (SA-VO_2) with a crystalline core and a surface-amorphized shell heterostructure by an interfacial engineering strategy. The crystalline/amorphous heterointerface in SA-VO_2 substantially narrows the bandgap, lowers the surface energy, and reduces the K^+ diffusion barrier of VO_2 (B) via DFT calculations. Therefore, the as-obtained SA-VO_2 electrode exhibits a higher reversible capacity of 288.3 mAh g^{-1} (at 50 mA g^{-1}), superior rate capacity (141.4 mAh g^{-1}), and long-term cyclability (86% after 500 cycles at 500 mA g^{-1}) (Figure 29e), while the VO_2 only delivers a specific capacity of 147.2 mAh g^{-1} at 50 mA g^{-1} and maintains 16.5% capacity after 200 cycles at 500 mA g^{-1} (Figure 29f). Compared with oxygen-rich defect amorphous shell VO_2, the crystalline/amorphous heterointerface SA-VO_2 enhances the K^+ storage capacity and enables rapid K^+/electron transfer, which results in large capacity and outstanding rate capability (Figure 29g).

Mai et al.[240] reported VO_2 hollow microspheres with a high surface area and excellent structural stability via a facile and controllable ion-modulating approach. VO_2 hollow microspheres deliver the best Li^+ storage performance compared to six-armed microspindles and random nanowires. The highest surface area of VO_2 hollow microspheres can provide efficient self-expansion, self-shrinkage buffering, and self-aggregation during lithiation/delithiation, which delivers 3 times higher capacity than that of random nanowires. In addition, they also synthesized highly homogeneous VO_2 nanorods by a rapid and simple hydrothermal method for aqueous ZIBs cathode material (Figure 29h).[239] The *in situ* XRD and *ex-situ* XPS/TEM results demonstrate that the VO_2 undergoes a single-phase reaction during the discharge process, accompanying a phase transition process of VO_2–$Zn_{0.07}VO_2$–$Zn_{0.29}VO_2$–$Zn_{0.54}VO_2$ with a unit cell volume expansion of 6.69%. On the contrary, the evolution of $Zn_{0.54}VO_2$–$Zn_{0.25}VO_2$–$Zn_{0.09}VO_2$–$Zn_{0.04}VO_2$ occurs during the Zn^{2+} deintercalation from the $Zn_{0.54}VO_2$. Meanwhile, detailed qualitative analysis verified that the VO_2 unit cell expands in the *a*, *b*, and *c* directions sequentially during the discharge/charge processes. Satisfactorily, the VO_2 nanorods deliver a high specific capacity of 325.6 mAh g^{-1} and excellent long cycle performance (86% after 3000 cycles), which is outstanding performance among the reported cathode materials of the aqueous ZIBs (Figure 29i,j).

6.2.7. HER, OER, and Water Splitting. VO_2 is a well-known semiconductor material with a band gap of 0.7 eV, which is seldom considered as a candidate material as a catalyst or photocatalyst for the production of hydrogen.[241] VO_2 can be used as a photocatalyst for hydrogen evolution through phase engineering. Ajayan et al.[242] synthesized the body-centered-cubic nanostructured VO_2, which shows excellent photocatalytic activity with a hydrogen production rate up to 800 mmol m^{-2} h^{-1} from a mixture of water and ethanol under UV light at a power density of ~27 mW cm^{-2}. Furthermore, vanadium oxide composites have the great potential to accelerate water dissociation kinetics and reduce charge-transfer resistance.[243,244] Tao et al.[245] synthesized MoS_2/VO_2 hybrids by using a two-step hydrothermal method. The phase transition of VO_2 exhibits a significant effect on hydrogen evolution properties of the heterostructures (an onset potential of 99 mV and a Tafel slope of 85 mV dec^{-1}). The enhanced performance is mainly due to the faster electron transport as well

https://doi.org/10.1021/acs.chemrev.2c00546
Chem. Rev. 2023, 123, 4353−4415

as the strain effect on MoS_2. Tu et al.[246] fabricated Co_3O_4/VO_2 heterogeneous nanosheet structures on carbon cloth (Co_3O_4/VO_2/CC) by the combination of hydrothermal and electrodeposition methods. The Co_3O_4/VO_2/CC composites gave good HER performance with a low overpotential of 108 mV at 10 mA cm^{-2} and a Tafel slope of 98 mV dec^{-1}, which results from the abundant active sites, effective electron transport, and improved hydrogen binding energy. Najafi et al.[247] prepared room temperature-stable metallic rutile VO_2 nanosheets by the topochemical transformation of two-dimensional VSe_2. By an O_2 plasma pretreatment of the VSe_2 nanosheets, the obtained VO_2 nanosheets show a porous structure, which shows good HER and OER performances in either acidic or alkaline media. The symmetric two-electrode water splitting cell based on the porous VO_2 nanosheets as both the anode and cathode delivers a current density of 10 mA cm^{-2} at cell voltages of 1.710 and 1.660 V in 0.5 M H_2SO_4 and 1 M KOH, respectively.

7. V_2O_5

7.1. Structures and Synthesis

V_2O_5 has the highest oxygen state in vanadium−oxygen systems and is the most stable member of the series of vanadium oxides. V_2O_5 has multiple distinctive polymorphs, including α-V_2O_5 (orthorhombic), β-V_2O_5 (monoclinic or tetragonal), and γ-V_2O_5 (orthorhombic). Among them, the most common α-V_2O_5 is the thermodynamically stable phase (the unit cell structure belonging to the *Pmnm* space group with lattice parameters of a = 11.150 Å, b = 3.563 Å, and c = 4.370 Å), and the other two phases (β-V_2O_5 and γ-V_2O_5) can be transformed from the α-V_2O_5 phase under high pressure and high-temperature conditions.[248] The orthorhombic structure of α-V_2O_5 is shown in Figure 30, in which each single layer of V_2O_5 consists

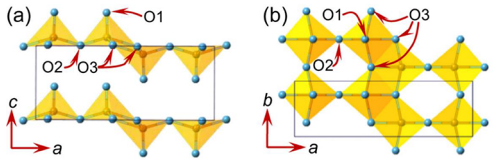

Figure 30. Perspective view (a) along the *b*-axis and (b) along the *c*-axis of two layers of V_2O_5, V atoms are gray balls, O atoms are red balls, and weak van der Waals bonds are omitted for clarity. Reproduced with permission from ref 249. Copyright 2018 Elsevier.

of edge- and corner-sharing square pyramids, and the adjacent layers are bonded together along the *c*-axis by weak van der Waals bonds between the vanadium and oxygen of neighboring pyramids. Additionally, three different oxygens atoms, O_1, O_2, O_3, have different coordinations depending on the position in each layer. The terminal/apical and bridging (corner-sharing) coordinated vanadyl oxygen atoms O_1 and O_2 have V−O bond lengths about of 1.54 and 1.77 Å, respectively; the triply coordinated O_3 links three vanadium atoms via edge-sharing VO_5 square pyramids, and the three corresponding V−O bond lengths are 1.88, 1.88, and 2.02 Å.[249]

The outstanding characteristics of V_2O_5, such as a layered structure, a direct band gap in the visible-light region, high chemical and thermal stability, electrochemical safety, low cost, and easy preparation, make V_2O_5 a suitable material for electrochemical energy conversion and storage,[250] catalysis,[251−253] solar cells,[254] gas sensors,[31] electrochromic devices,[255] and optoelectronic devices.[256] Compared with bulk V_2O_5, the nanostructured ones have higher surface to volume ratios, which is beneficial to improve various performances. Over the past few years, a variety of methods, such as sol−gel, hydrothermal, chemical vapor deposition, magnetron sputtering, and atomic layer deposition, have been developed to prepare V_2O_5 nanostructures.

The sol−gel method has been used to fabricate V_2O_5 thin films and nanopowders through V_2O_5 sols, which were prepared by ion exchange, alkoxide hydrolysis, peroxide-assisted hydrolysis, and melt-quenching. The disadvantage of using an ion exchange is the difficulty to control the vanadium concentration as it varies throughout the whole process. In addition, some foreign ions such as Na^+ may remain in the gel after ion exchange.[257] The alkoxide hydrolysis always involves some expensive raw materials, and the molten V_2O_5 quenching process will produce toxic gas.

Hence the synthesis of V_2O_5 sol by peroxide-assisted hydrolysis stands out due to its advantages of being environmental friendly, inexpensive, and requiring simple fabrication. Vanadium metal or commercial V_2O_5 powders are commonly used as a vanadium source that can be dissolved vigorously in a solution of hydrogen peroxide. According to Alonso et al. the dissolution of V_2O_5 into H_2O_2 produces unstable diperoxo $[VO(O_2)_2]^-$ and then is dissociated to the aqueous solution of $[VO_2]^+$ and $[H_2V_{10}O_{28}]^{4-}$.[258] Etman et al. also found $[H_2V_{10}O_{28}]^{4-}$ is the main species via real-time nuclear magnetic resonance.[259] It is noted that, not related to the preparation method, the V_2O_5 sols are comprised of a fibrous structure, dissimilar from many inorganic sols that are typified by a random aggregate of particle structure.[260] These fibrous structures can self-assemble into V_2O_5 nanofibers upon long-term aging through a coagulation mechanism.[261] The obtained V_2O_5 sol was applied onto substrates via coating techniques, including spin coating, dip-coating, and spray process, and the subsequent drying and heat treatment are necessary to obtain V_2O_5 films.[262−264] Figure 31a highlight the evaporation, hydrolysis, and subsequent solidification procedure during the formation of V_2O_5 thin films by dip-coating.[265] Figure 31b,c shows TEM diffraction patterns and corresponding FFT of V_2O_5 thin films formed from low concentration dilution (LCP) and high concentration dilution (HCP) using PEG-400 as an additive (HCP-PEG), respectively. V_2O_5 thin films formed from an LCP precursor show the formation of grains of orthorhombic V_2O_5 with defined grain boundaries (Figure 31b), while the HCP-PEG samples have a polycrystalline structure without uniformed grain (Figure 31c). Meanwhile, as shown in AFM images in Figure 31d−g, thin films formed from higher concentration precursors have a larger surface roughness (R_S). Thermal treatment can further increase the R_S due to the formation of crystallites on the thin film surface. The thin film formed from LCP-PEG precursor has the lowest R_S of 0.2 nm. Liu et al. studied the substrate effect on the structure and electrical properties of nanocrystalline V_2O_5 thin films prepared by the sol−gel method.[266] They found the annealed V_2O_5 film on the Si substrate exhibited more uniform rod-like morphology, and electrical measurements indicated the typical n-type semiconducting behavior. Senapati et al. prepared nanoscale V_2O_5 films having thicknesses ranging from 92 to 137 nm by spin coating V_2O_5 sol at different stages of aging.[267] They reported the decrease of strain in the films with aging, and the electrical conductivity increased with aging due to the improved crystallinity of the films.

https://doi.org/10.1021/acs.chemrev.2c00546
Chem. Rev. 2023, 123, 4353−4415

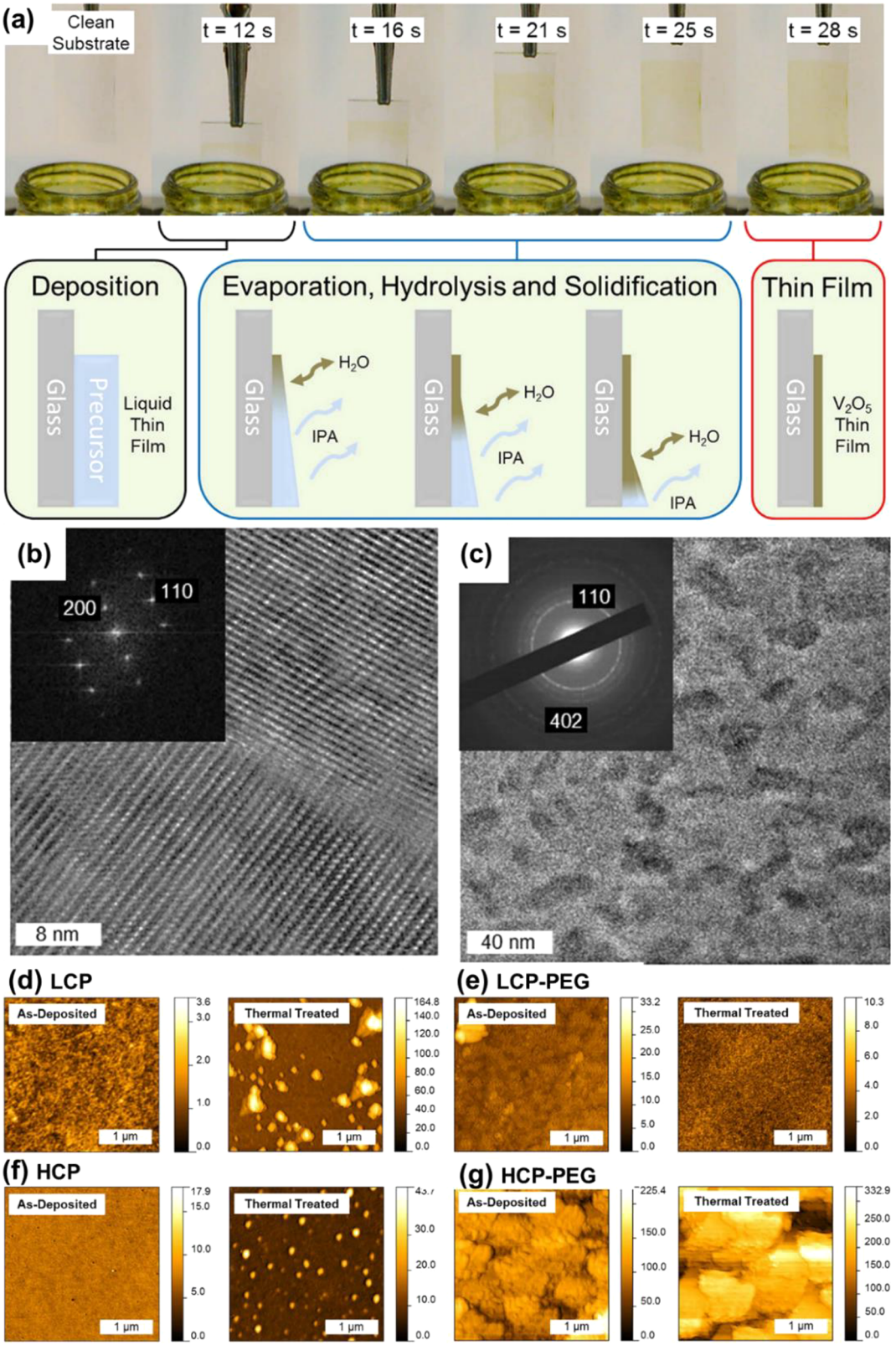

Figure 31. (a) The formation process of V_2O_5 thin film through a combination of evaporation, hydrolysis, and solidification is shown optically and schematically; TEM diffraction patterns and corresponding FFT of V_2O_5 thin films formed from (b) low concentration dilution (LCP) and (c) high concentration dilution using PEG-400 as an additive (HCP-PEG); AFM surface images of as-deposited and post-thermally treated orthorhombic V_2O_5 films that were dip-coated from (d) LCP, (e) LCP-PEG, (f) HCP, and (g) HCP-PEG solutions. Reproduced with permission from ref 265. Copyright 2015 under CC BY 4.0 license.

Besides thin films, the sol−gel method also provides good control over the size, morphology, doping, and chemical composition of V_2O_5 powders.[268−271] Li et al. reported the flower-like V_2O_5 powders prepared by coagulating V_2O_5 sol and

https://doi.org/10.1021/acs.chemrev.2c00546
Chem. Rev. 2023, 123, 4353−4415

subsequent annealing crystallization.[272] V_2O_5/graphene hybrid aerogel was prepared by Wu et al. at ambient pressure through a simple one-pot sol−gel method from commercial V_2O_5 powder.[273] Figure 32a illustrates the fabrication process and

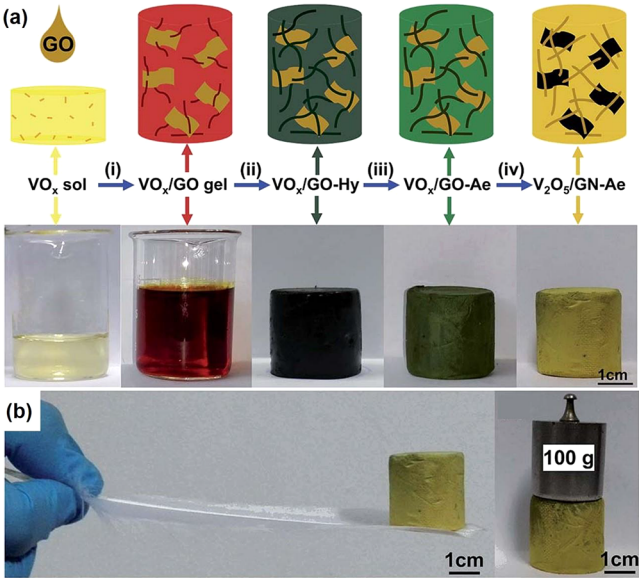

Figure 32. (a) The fabrication process and structure of the V_2O_5/graphene hybrid aerogel and the corresponding digital images of different formation stages: (i) hydrolysis of VO_x oligomers and self-assembled coordination of VO_x nanofibers and graphene oxide sheets; (ii) aging of VO_x/graphene oxide gel and growth of VO_x nanofibers along graphene oxide sheets; (iii) solvent replacement and drying, and (iv) thermal reduction of graphene oxide, oxidation, and partly crystallization of V_2O_5. (b) Lightweight V_2O_5/graphene hybrid aerogel standing on a feather; it can support the weight of 100 g. Reproduced with permission from ref 273. Copyright 2015 Royal Society of Chemistry.

images of VO_x nanofibers and graphene oxide sheets. First, graphene oxide (GO) aqueous solution was added to the V_2O_5 sol under vigorous stirring to induce hydrolysis and in situ recombination of the GO sheets and VO_x oligomers. Then, a dark red VO_x/GO hybrid gel was obtained after about 5 min because of the rapid formation of intermediate vanadium phases and the growth of nanofibers. After aging for 2 days, the gel gradually changed to deep green, and the V_2O_5 nanofibers are anchored and in situ grown on the graphene surfaces. The V_2O_5/graphene hybrid aerogel is so light that it can be lifted by a feather, but it is strong enough to support the weight of 100 g (Figure 32b).

The hydrothermal method has been widely used for the synthesis of a vast range of V_2O_5 nanostructures with a desired size and morphology, such as nanoparticles,[274] nanowires,[275] nanotube,[276] nanosheets,[277] and micro-/nanostructures.[278,279] The importance of solubility of precursors, the pH value, the surfactant, as well as the hydrothermal temperature, reaction time, and solution filling factor are highlighted in many references. Li's research group conducted extensive research on the hydrothermal treatment of V_2O_5 sol.[280] They prepared V_2O_5 nanoparticles and ultralong nanobelts with the usage of an inorganic V_2O_5 sol precursor (Figure 33a,b).[261,274] The obtained single-crystalline V_2O_5 nanobelts have a large specific surface area, with width and thickness of 30−200 nm and length in millimeters or even longer (Figure 33b). Strong evidence

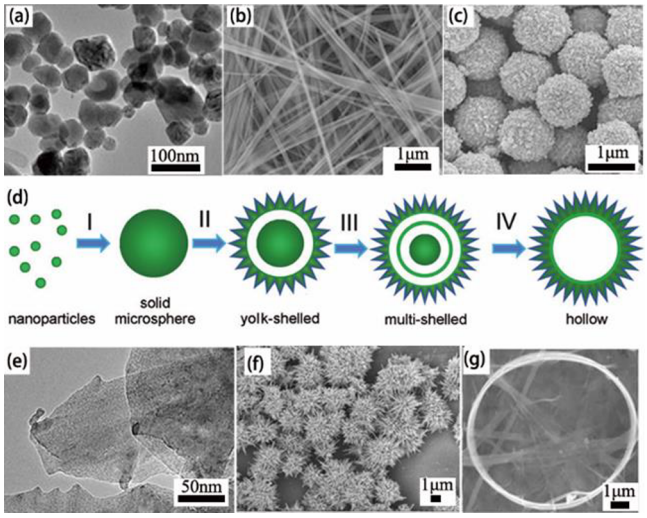

Figure 33. V_2O_5 with different morphologies: (a) Nanoparticles. Reproduced with permission from ref 274. Copyright 2015 Elsevier. (b) Ultralong nanobelts. Reproduced with permission from ref 261. Copyright 2011 Royal Society of Chemistry. (c) Hollows spheres and (d) growth mechanism. Reproduced with permission from ref 281. Copyright 2013 Wiley. (e) 2D nanosheets. Reproduced with permission from ref 283. Copyright 2015 Elsevier. (f) Urchin-like microflowers. Reproduced with permission from ref 284. Copyright 2012 American Chemical Society. (g) Nanoring. Reproduced with permission from ref 285. Copyright 2010 under CC BY 2.0 license.

suggested that the oriented attachment growth mechanism was responsible for the formation of V_2O_5 nanobelts. Pan et al. reported a one-step solvothermal method to form V_2O_5 hollow spheres without adding surfactants.[281,282] As shown in Figure 33c, the SEM image of the V_2O_5 hollow spheres has a uniform size of around 1 μm in diameter. They investigated the time-dependent interior structural evolution by TEM and gave the possible growth mechanism of the V_2O_5 microspheres (Figure 33d): vanadium oxide nanoparticles are first generated by the hydrolysis of VOC_2O_4 and then aggregation to form solid microspheres in stage I. The solid spheres undergo the initial inside-out Ostwald ripening process and transform to the yolk−shelled structure (stage II). With extended solvothermal reaction, secondary Ostwald-ripening takes place on the preformed solid cores, resulting in the formation of a multishelled structure (stage III). Finally, completely hollow microspheres are obtained as a result of the thorough dissolution and recrystallization of the less stable interior architectures (stage IV). Hence, the interior structure of the VO_2 microspheres could be effectively tailored by simply controlling the reaction duration and concentration of the precursor.

The fabrication of two-dimensional (2D) V_2O_5 nanosheets has been studied by Cao et al.[283] As cathode materials for lithium-ion batteries, the resulting 2D V_2O_5 nanosheets (Figure 33e) exhibit remarkable electrochemical performances, including high reversible capacity, good cyclic stability, and great rate capability. 3D hierarchical vanadium oxide microstructures, including urchin-like microflowers (Figure 33f), have been successfully synthesized by Lou et al. through a solvothermal method.[284] The morphologies of the microstructures can be easily tailored by varying the concentration of the vanadium oxalate solution, and the obtained V_2O_5 microflowers are highly porous with a surface area of 33.64 $m^2\ g^{-1}$ giving high lithium storage capacity, and enhanced cycling stability and rate

https://doi.org/10.1021/acs.chemrev.2c00546
Chem. Rev. 2023, 123, 4353−4415

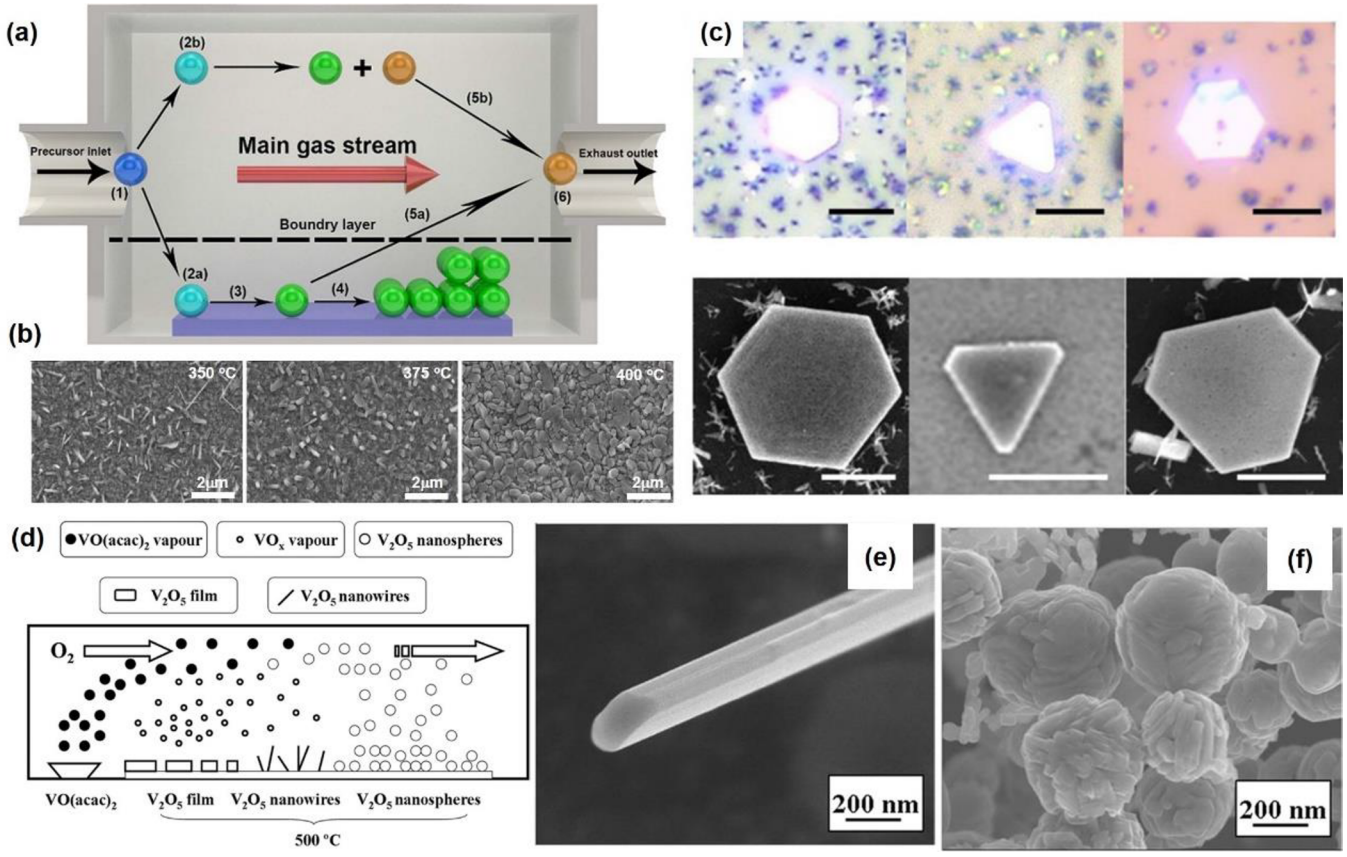

Figure 34. (a) Schematic diagram of the CVD process. Reproduced with permission from ref 19. Copyright 2018 Elsevier. (b) SEM images of AACVD grown V_2O_5 films at 350 °C, 375 °C, 400 °C. Reproduced with permission from ref 287. Copyright 2016 Elsevier. (c) Representative optical and SEM images of the as-synthesized V_2O_5 nanosheets with well-defined shapes, such as hexagon, triangle, and truncated triangle. All scale bars are 3 μm. Reproduced with permission from ref 288. Copyright 2018 American Chemical Society. (d) The growth schematic diagram of the V_2O_5 nanomaterials prepared by chemical vapor deposition using $VO(acac)_2$ powder as the precursor, and the formed (e) nanowire and (f) nanospheres at a distance of 18 and 30 cm away from the source, respectively. Reproduced with permission from ref 289. Copyright 2010 Institute of Physics.

capability. V_2O_5 nanorings and microloops are rarely reported, but they are very interesting morphologies (Figure 33g). The cation-induced asymmetric strain is the main driving force in making a layered V_2O_5 coil into a ring structure.[285]

CVD is widely used for depositing high-quality and high-performance solid materials. As shown in Figure 34a, CVD involves the transfer of precursor molecules, which are either liquid or gaseous to a reaction chamber by a carrier gas (step 1), and then it is followed by the reaction and/or decomposing on the surface of the substrate to produce the desired films (steps 2a, 3, and 4) or powders (step 2b), and the byproducts and unreacted precursor are transported out from the chamber at the end of the process (step 5a, 5b).[19] There are several types of CVD systems such as atmospheric pressure CVD, aerosol-assisted chemical vapor deposition (AACVD), atomic layer CVD, plasma enhanced CVD, metal−organic CVD, and so forth.[286] The morphology, size, crystal phase, and specific surface area of V_2O_5 can be affected by various parameters, namely the reaction time, substrate temperature, pressure, precursor properties, and reaction position during the CVD method. SEM images in Figure 34b display the effect of growth temperature on the morphological characteristics of V_2O_5 coatings. V_2O_5 grown at 350 and 375 °C has rod-like structures of nonuniform thickness and width, while at 400 °C pellet-like features of V_2O_5 are observed, and the morphology evolution could be due to the coexistence of both α-V_2O_5 and β-V_2O_5.[287]

Chun et al. prepared V_2O_5 nanosheets via the reaction of VCl_3 vapor with oxygen in the CVD system without a vacuum system.[288] Figure 34c shows representative optical images and their corresponding SEM images of the obtained V_2O_5 nanosheets and three distinguished shapes: hexagons, triangles, and truncated triangles. Wang et al. used the CVD method to control the morphologies of V_2O_5 by changing the reaction distance from the source position using vanadyl acetylacetonate ($VO(acac)_2$) as the vanadium precursor.[289] They found that VO_x vapor and $VO(acac)_2$ vapor existed simultaneously during the growth process, and the different supersaturation distributions of these two vapors led to three main growth areas. 1. V_2O_5 thin-films were formed at a high concentration and supersaturation of VO_x in the region near the source material (Figure 34d); 2. nanowires with a length of about 10 μm and width about 200 nm were formed at a distance of 18 cm from the source due to the low vapor concentration of VO_x (Figure 34e); 3. nanospheres with a diameter of about 200−500 nm were obtained when the source material was far away (about 30 cm) due to the high concentration and supersaturation of $VO(acac)_2$ that was oxidized to V_2O_5 nanospheres (Figure 34f).[289]

ALD is considered a specific type of CVD, which was first introduced in the 1960s and is currently receiving ever-growing attention as a method of choice for the growth of conformal coatings on nanostructures with high aspect ratios.[12] Figure 35a depicts the typical ALD process, in which the precursor gases

https://doi.org/10.1021/acs.chemrev.2c00546
Chem. Rev. 2023, 123, 4353−4415

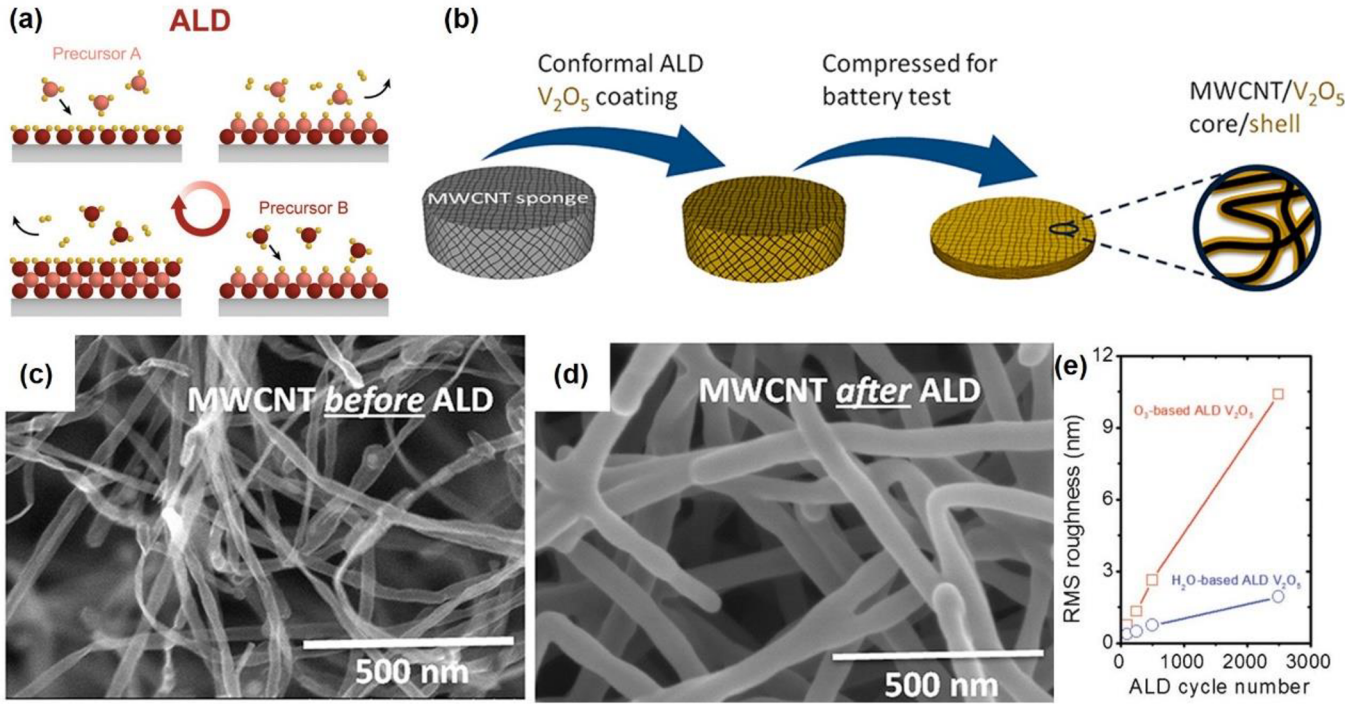

Figure 35. (a) Schematic of a single ALD cycle consisting of half-cycles of Precursor A and Precursor B separated by purge steps to remove excess precursor and byproducts. Reproduced with permission from ref 290. Copyright 2020 Royal Society of Chemistry. (b) Schematic of experimental flow to fabricate MWCNT/V_2O_5 sponge, and SEM images of MWCNT sponge (c) before and (d) after ALD V_2O_5 coating. Reproduced with permission from ref 291. Copyright 2012 American Chemical Society; (e) Compares the RMS roughness of the O_3-based and the H_2O-based films prepared by ALD as a function of cycle number. Reproduced with permission from ref 293. Copyright 2013 Royal Society of Chemistry.

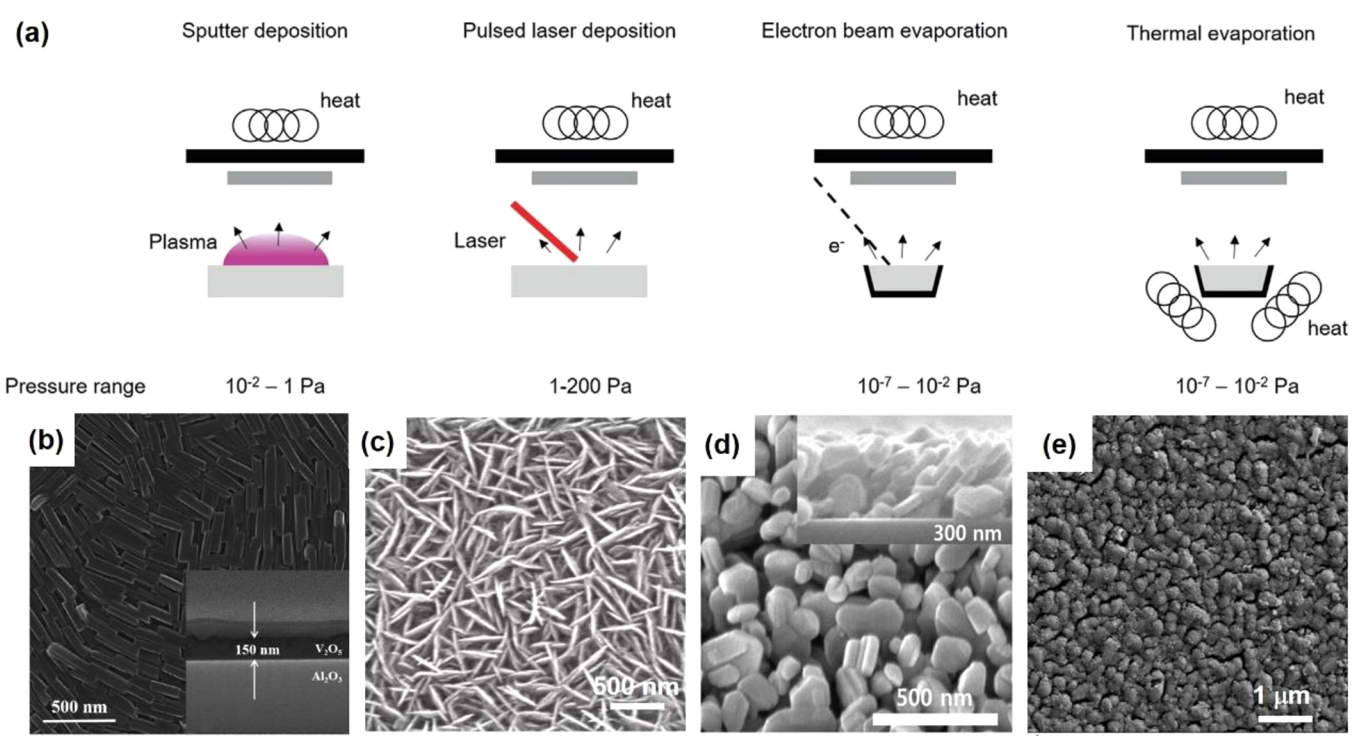

Figure 36. (a) Schematic illustration of different physical vapor deposition techniques: sputter deposition, pulsed laser deposition, electron beam evaporation, and thermal evaporation. In evaporation, atoms are removed from the source by thermal means, while in sputtering they are dislodged from a solid target via bombardment by gaseous ions. Reproduced with permission from ref 296. Copyright 2021 John Wiley and Sons. SEM images of V_2O_5 prepared by (b) megnetron sputtering. Reproduced with permission from ref 297. Copyright 2021 Elsevier. (c) PLD. Reproduced with permission from ref 299. Copyright 2021 Elsevier. (d) Electron beam evaporation. Reproduced with permission from ref 301. Copyright 2017 Elsevier. (e) Thermal evaporation. Reproduced with permission from ref 306. Copyright 2019 American Chemical Society.

https://doi.org/10.1021/acs.chemrev.2c00546
Chem. Rev. 2023, 123, 4353−4415

sequentially react with a surface to form an ultrathin film through a self-limiting process, and all byproducts and unreacted precursor molecules are purged out of the reactor.[290] The primary advantages of ALD lie in subnanometer film thickness and conformality control that profit from the cyclic, self-saturating nature of ALD processes. Moreover, the ALD is unique as it is able to coat complex 3D structures with a high degree of uniformity and smoothness.[291,292] Chen et al. successfully fabricated a multiwall carbon nanotube (MWCNT)/V_2O_5 core/shell sponge by ALD.[291] Figure 35b shows the experimental flow schematically: the MWCNT sponge structure exhibits a very low density (~7 mg/cm^3) and high porosity (>99%), allowing for a high amount of active material loading; the V_2O_5 layer of about 16 nm is subsequently deposited on the MWCNT sponge by 1000 cycles of H_2O-based ALD; finally, the MWCNT/V_2O_5 sponge is compressed and assembled in a coin cell battery, which enables de/lithiation in active material within a very short time. Figure 35c,d shows SEM images of the MWCNT sponge before and after ALD V_2O_5 coating, giving uniform and smooth V_2O_5 coating. Two different oxidants, O_3 and H_2O, have been studied during the ALD process, and it was found that as the ALD cycle numbers increased from 100 to 2500, the roughness for the O_3-based films kept increasing from 0.7 to 10.4 nm while that for H_2O-based films only increased from 0.4 to 1.9 nm (Figure 35e).[293] Østreng et al. prepared V_2O_5 films by ALD using the β-diketonate $VO(thd)_2$ and ozone as precursors.[294] They found that the crystallographic orientation, optical properties, band gap, and surface roughness of the V_2O_5 films were correlated and could be varied by controlling the deposition temperature and film thickness.

PVD techniques (Figure 36a) involve evaporation and many different modes of physical sputter deposition, in which the primary source of the depositing species is a solid or liquid, as opposed to generally gaseous precursors in CVD. However, chemical reactions can and do occur in PVD systems, such as in the reactive sputtering deposition. The presence of the reactive gas (oxygen or nitrogen) in the chamber can significantly alter the PVD source.[295] PVD possesses some unique advantages for the creation of uniform and dense solid thin films that strongly adhere to the substrates. Meanwhile, the thickness, composition, crystallinity, and crystal orientation of the thin film can be well controlled by changing the growth conditions with minimal risk of contamination due to the absence of organic reactants. Another advantage is to sequentially deposit several materials to form well-defined multilayer systems as well as special alloy compositions and structures.[296] Magnetron sputtering is one of the most used PVD methods to fabricate a large range of materials, including metal oxides. The application of a negative voltage to the cathode will generate positively charged argon ions that can bombard the target ions to be ejected toward the substrate to form a film. Magnets are used in order to increase ion bombardment. This technique has been developed on an industrial scale to make large surface deposits with a wide variety of materials. V_2O_5 film consisted of fine long strip particles deposited by radio frequency magnetron sputtering, and the thickness of the V_2O_5 film was determined to be approximately 150 nm according to the cross-sectional SEM image (Figure 36b). V_2O_5 films underwent four different thermal transition behaviors to other vanadium oxides that were closely related to the oxygen proportion of the annealing ambient.[297] Amorphous V_2O_5 film can be used as a hole injection layer in quantum dot light-emitting diodes, which exhibited a maximum luminance of 198.5 cd/m^2, a turn-on voltage of 1.7 V, and a max external quantum efficiency of about 8.3%.[298]

Pulsed laser deposition (PLD) is another PVD method, which has been preferred to grow different structures ranging from high-quality epitaxial thin films to various nanostructured layers. During PLD, a high-power pulsed laser beam is focused on a target of the desired composition. Material vaporized from the target is deposited as a thin film on a substrate that faces the target in an ultrahigh vacuum (UHV) environment. Polycrystalline V_2O_5 thin film in the desired orientation can be prepared by PLD, which has aligned nanorod morphology on a flexible stainless steel substrate (Figure 36c).[299] Huotari et al. found the film surface morphology varied largely according to oxygen partial pressure: lower O_2 partial pressures resulted in a denser and thinner film, while higher O_2 partial pressures gave a film surfaces formed with randomly agglomerated nanoparticles or agglomerates with pillar-like morphology.[300]

Electron-beam deposition (EBD) is another form of PVD where a target anode is bombarded with a high-energy electron beam that is given off from a charged tungsten filament under a high vacuum. The electron beam leads to joule heating and converts the target into the gaseous phase, which subsequently precipitates into the solid form on the desired substrate. Han et al.[301] reported the growth of nanocolumnar V_2O_5 molecules that were aggregated with each other and collapsed after annealing treatment (Figure 36d). Most of the nanosized V_2O_5 columns' structure could retain its original shape during the annealing process by changing the source from V_2O_5 to VO_2. Highly oriented V_2O_5 thin films with nanosized grains were grown by EBD, and the film thickness was found to be in the range of 800−1200 nm that varied by adjusting the substrate position.[302] Meanwhile, the mobility and carrier concentration of the oriented V_2O_5 thin films increased with the increase of V_2O_5 film thickness. Thermal evaporation is the vaporization of a material by heating to a temperature that the vapor pressure becomes appreciable, and the materials are sublimated from the target surface in a vacuum. By this method, heterojunctions,[303] nanorods,[304] nanoparticles,[305] or highly crystalline V_2O_5 films[306] have been studied in several reports. Wang et al. synthesized Ga-doped V_2O_5 nanorods by thermal evaporation at 850 °C and found interstitial Ga and Ga−O phases influence the photoluminescence properties of V_2O_5 nanorods.[304] Berouaken et al. used thermal evaporation to prepare V_2O_5 nanoplatelets on the quartz crystal microbalance, followed by rapid thermal annealing.[307] The obtained V_2O_5 nanoplatelets exhibited good sensing performance toward NH_3 vapor at room temperature: a fast response time, a short recovery time, good stability, reproducibility, reversibility, and linearity. Velmurugan et al. prepared highly crystalline V_2O_5 films with a controlled thickness of about 530 nm and an average particle size of around 560 nm using a thermal evaporation process (Figure 36e).[306] The films were fabricated in electrochemical microcapacitors and subjected to various electrochemical characterizations, which display improved reliability and excellent capacitance retention.

7.2. Applications

7.2.1. Batteries. V_2O_5 is a feasible cathode material for metal-ion storage due to its high output voltage and unique crystal structure with large interlayer spacing (4.4 Å). Mai et al.[308] designed and synthesized a V_2O_5 hollow microclew (V_2O_5−HM) through a facile solvothermal assisted calcination method. The amorphous V_2O_5−HM precursor can convert into

https://doi.org/10.1021/acs.chemrev.2c00546
Chem. Rev. 2023, 123, 4353−4415

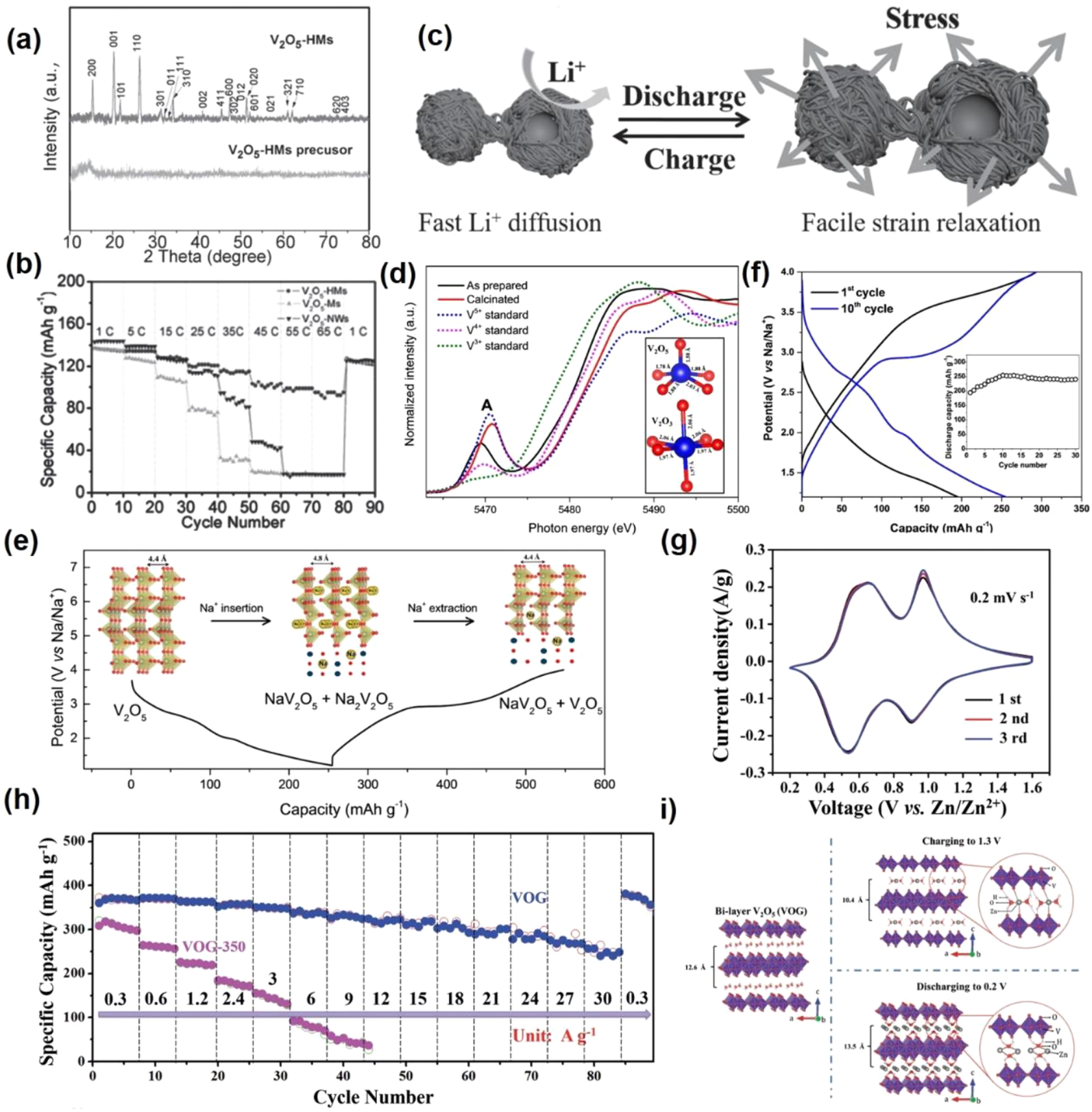

Figure 37. XRD patterns (a), rate performances (b) of V_2O_5−HMs, V_2O_5-Ms, and V_2O_5−NWs. Schematic illustration of the V_2O_5−HMs during charge/discharge process (c). Reproduced with permission from ref 308. Copyright 2016 John Wiley & Sons. The XANES spectra of as prepared and after calcination at 400 °C are plotted with solid lines (d), the Na^+ de/intercalation channels crystal structure (e), charge/discharge profiles and cycling performance (f) of orthorhombic V_2O_5/C. Reproduced with permission from ref 309. Copyright 2016 American Chemical Society. The CV curves (g), rate performances (h), and the proposed crystal structures at different states (i) of $V_2O_5 \cdot H_2O$/graphene. Reproduced with permission from ref 310. Copyright 2018 John Wiley & Sons.

crystalline V_2O_5 through calcination (Figure 37a). Compared with crystalline V_2O_5 (V_2O_5-Ms) and V_2O_5 nanowires (V_2O_5−NWs), the V_2O_5−HMs exhibit the best Li^+ storage performance (145.3 and 94.8 mAh g^{-1} at 0.67 and 65 C, respectively), which is due to the 3D hierarchical microstructure with intertangled nanowires (Figure 37b). This 3D hierarchical microstructure not only inherits fast electrolyte penetration, and short ionic and electronic transport pathways, but also significantly alleviates the strain during the Li^+ intercalation/deintercalation. Meanwhile, compared to disordered V_2O_5 nanowires, a unique V_2O_5−HM structure effectively helps improve the tap density, which is more suitable for commercial applications (Figure 37c). V_2O_5 can be used as other metal ions ($Na^+/K^+/Zn^{2+}$) electrode material except for LIB storage material. Chung group synthesized a nanosized V_2O_5/C composite cathode by ball milling the nanosized V_2O_5 with acetylene black and investigating the reaction mechanism in the NIB system.[309] Generally, compared with other vanadium oxides (VO_2, V_2O_3, et al.), V_2O_5 consists of

https://doi.org/10.1021/acs.chemrev.2c00546
Chem. Rev. 2023, 123, 4353−4415

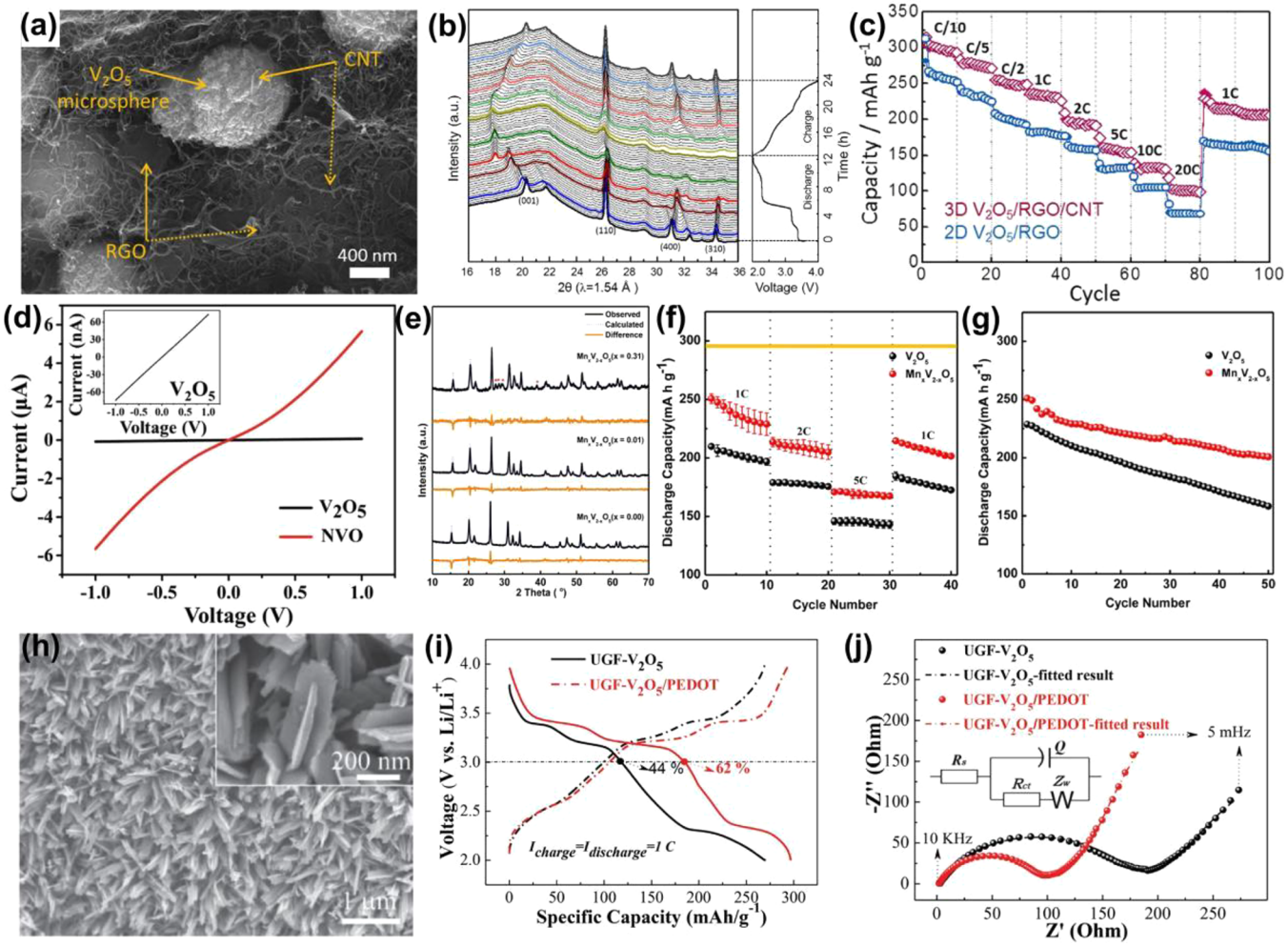

Figure 38. FESEM image (a), in situ XRD (b), and rate performance (c) of 3D V_2O_5/rGO/CNT composite. Reproduced with permission from ref 311. Copyright 2016 under CC BY 4.0 license. The *I*−*V* curves of $Na_{0.33}V_2O_5$ (NVO) and V_2O_5 (d). Reproduced with permission from ref 312. Copyright 2018 John Wiley and Sons. Rietveld refined XRD patterns of the $Mn_xV_{2-x}O_5$ compounds (e), rate performance (f), and cycle performance (g) at 300 mA g^{-1} of $Mn_{0.01}V_{1.99}O_5$ and V_2O_5. Reproduced with permission from ref 313. Copyright 2015 American Chemical Society. The SEM image of UGF-V_2O_5/PEDOT (h), the charge/discharge profiles (i), Nyquist plots at fully charged stage (j) of UGF-V_2O_5/PEDOT and UGF-V_2O_5. Reproduced with permission from ref 314. Copyright 2014 John Wiley and Sons.

the square-based pyramid with the highly distorted environment and exhibits the highest pre-edge intensity from the X-ray absorption near edge structure (XANES) result. Thus, the average vanadium oxidation state of the calcinated V_2O_5/C sample is +4.83 (Figure 37d), which may be due to the calcined carbon reduction (a slight difference with standard V_2O_5 in the pre-edge peak position). They used *ex-situ* XRD to demonstrate the major NaV_2O_5 with a minor $Na_2V_2O_5$ phase formed at the first discharge state, accompanying a *c* lattice parameter increase by 9.09% and unit cell volume increase by 9.2%. At the subsequent charge, the NaV_2O_5 + $Na_2V_2O_5$ will transform into NaV_2O_5 + V_2O_5 along with a $V^{4+} \rightarrow V^{5+}$ change (Figure 37e). The V_2O_5/C delivers an initial discharge capacity of 195 mAh g^{-1}, and increases to 255 mAh g^{-1} at the 10th cycle corresponding to 1.7 Na^+ inserts into per unit formula (Figure 37f). Besides LIB/NIB cathodes, V_2O_5 can be investigated as an aqueous zinc-ion battery (ZIB) cathode material, and the intercalation of water into the vanadium oxide can increase the interlayer distance, which is in favor of expanding the gallery for Zn^{2+} intercalation. Yang et al.[310] reported V_2O_5·H_2O/graphene (VOG) synthesized via a freeze-drying method. They investigated the critical role ("lubricating" effect) of structural H_2O on the Zn^{2+} intercalation into bilayer V_2O_5·*n*H_2O, and H_2O-solvated Zn^{2+} possesses a largely reduced effective charge and improves electrochemical performance. VOG delivers a high capacity of 381 mAh g^{-1} at 60 mA g^{-1} and maintains 248 mAh g^{-1} at a high current density of 30 A g^{-1}, which are much higher than those of most aqueous ZIB cathode materials (Figure 37g,h). The interlayer distances of VOG are 12.6, 13.5, and 10.4 Å at initial, discharge, and charge states by ex-situ XRD and MAS NMR (Figure 37i). These results demonstrate that water in vanadium oxide layers plays an important role in the performance of an aqueous ion battery.

To investigate the electrical conductivity and structural mechanism during lithium insertion/deinsertion of V_2O_5, Yoon et al.[311] developed a 3D V_2O_5/rGO/CNT with short Li^+ diffusion, and high continuous 3D conductive network, and investigated its structural mechanism during Li^+ intercalation/deintercalation by in situ XRD/XANES analysis (Figure 38a). The 3D V_2O_5/rGO/CNT delivers a high discharge capacity of 100 mAh g^{-1} at 20 C, which is much higher than 2D V_2O_5/rGO (68 mAh g^{-1}). There are numerous metastable phases of $Li_xV_2O_5$ during Li^+ intercalation into V_2O_5. The α-$Li_{0.26}V_2O_5$, ε-$Li_{0.93}V_2O_5$, δ-$Li_{1.27}V_2O_5$, γ-$Li_{1.93}V_2O_5$, and ω-$Li_{2.65}V_2O_5$ phase

https://doi.org/10.1021/acs.chemrev.2c00546
Chem. Rev. 2023, 123, 4353−4415

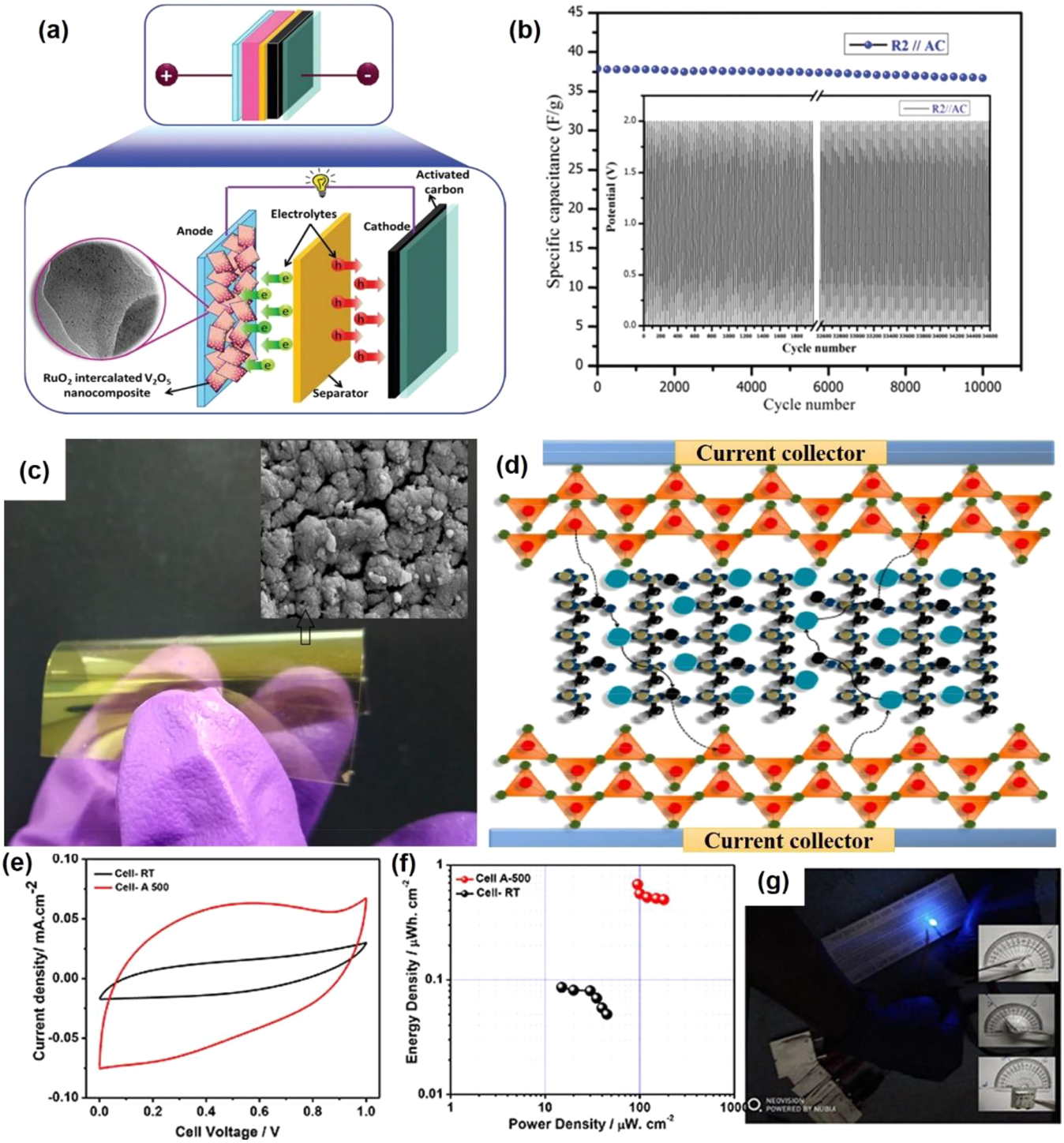

Figure 39. (a) Schematic illustration of the 3 wt % RuO_2 in V_2O_5 asymmetric supercapacitor device and (b) cyclic stability 3 A g^{-1}. Reproduced with permission from ref 315. Copyright 2021 Royal Society of Chemistry. (c) As-fabricated V_2O_5 flexible thin film, and the inset view is the FESEM image of the film. (d) Schematic representation of the symmetric V_2O_5 capacitor. (e) Comparison of CV curves of the symmetric SCs with V_2O_5 electrode prepared at room temperature (RT) and 50 °C (A-500) at a scan rate of 50 mV s^{-1}. (f) Ragone plot comparison of both symmetric-RT and symmetric A-500 capacitors. (g) Lighting of LED using symmetric A-500 connected in series (inset: various bent position of the symmetric A-500). Reproduced with permission from ref 306. Copyright 2019 American Chemical Society.

form in turn during the first discharge to 3.4, 3.3, 3.19, 2.28, and 2.01 V, respectively. In addition, the most reflection will return to the same position at a pristine state during the subsequent charge process, which can confirm the high structural reversibility of V_2O_5 in the ternary composite upon Li^+ intercalation/deintercalation (Figure 38b). The 3D V_2O_5/rGO/CNT delivers a high discharge capacity of 100 mAh g^{-1} at 20 C, which is higher than 2D V_2O_5/rGO (68 mAh g^{-1}) (Figure 38c). The preintercalation interlayer metal ions can act as pillars to increase the electronic conductivity, ion diffusion rate, and stability of layered vanadium oxides. Mai et al.[312] designed and assembled $Na_{0.33}V_2O_5$ (NVO) and V_2O_5 single

https://doi.org/10.1021/acs.chemrev.2c00546
Chem. Rev. 2023, 123, 4353−4415

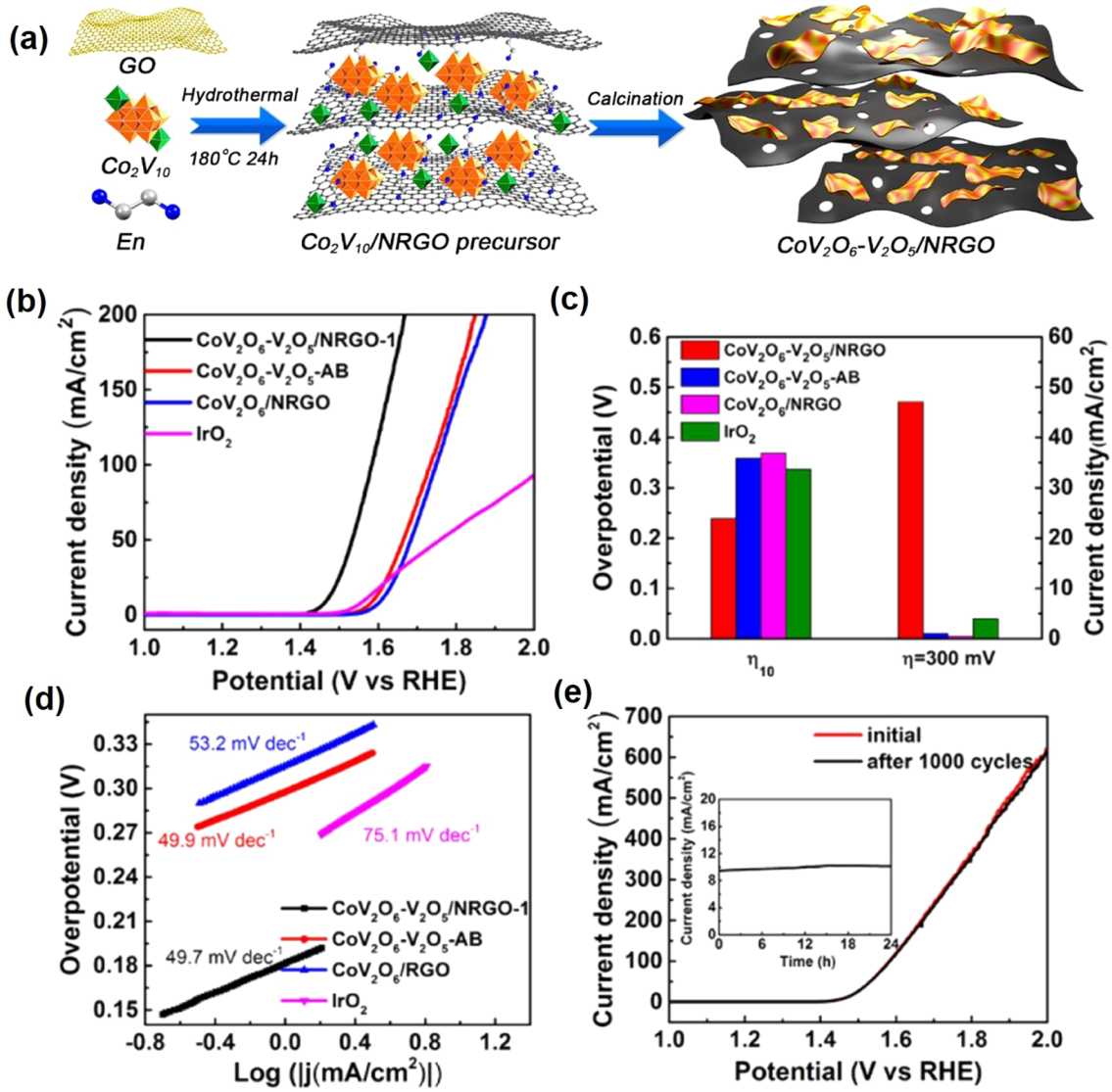

Figure 40. (a) Schematic illustration of the synthetic process of CoV_2O_6–V_2O_5/NRGO composite, (b) polarization curves, (c) comparison of catalysts' overpotential at a current density of 10 mA cm^{-2}, corresponding current density at an overpotential of 300 mV, and (d) corresponding Tafel plots. (e) Initial polarization curves of CoV_2O_6–V_2O_5/NRGO and after 1000 CV cycles. Inset: time-dependent current density curve of CoV_2O_6–V_2O_5/NRGO under a potential of 239 mV for 24 h. Reproduced with permission from ref 320. Copyright 2017 American Chemical Society.

nanowire devices to investigate the effect on the intrinsic electrical conductivity of Na^+ intercalation. The conductivity of NVO is 5.9×10^4 S m^{-1}, while the conductivity of V_2O_5 is 7.3 S m^{-1}, which indicates that the electronic conductivity of V_2O_5 is greatly improved by the Na^+ intercalation (Figure 38d). Stucky et al.[313] fabricated a series of nanostructured Mn-doped V_2O_5 cathode materials and found that the larger Mn doping in the modified V_2O_5 structure can increase the cell volume, which facilitates high Li^+ diffusion and improves the electronic conductivity (Figure 38e). The $Mn_{0.01}V_{1.99}O_5$ delivers a high discharge capacity (251 mAh g^{-1} at 1 C) and excellent cycling stability (80% after 50 cycles), which is much higher than V_2O_5 (215 mAh g^{-1} vs. 70%) (Figure 38f,g). Fan et al.[314] reported lightweight, freestanding V_2O_5 nanoarray-based positive electrodes (UGF-V_2O_5/PEDOT), which were prepared by growing a V_2O_5 nanobelt array directly on 3D ultrathin graphite foam (UGF), followed by coating the V_2O_5 with a mesoporous thin layer of the conducting polymer poly(3,4-ethylenedioxythiophene) (PEDOT) (Figure 38h). In addition, the PEDOT coating constructs an integrated conductive network for the V_2O_5, providing decreased electrode polarization, improved charge transfer kinetics, and a prolonged discharge plateau of V_2O_5 (Figure 38i,j), and therefore it can lead to an increased proportion of high-voltage capacity and energy density than that without PEDOT.

7.2.2. Supercapacitors. Among all types of vanadium oxides, V_2O_5 has attracted attention for the application of SCs due to its broad oxidation states, high specific capacitance, and low acquisition cost. Palani et al. fabricated RuO_2 nanoparticle-decorated V_2O_5 nanoflakes by a solvothermal method.[315] Figure 39a illustrates the corresponding schematic of the fabricated asymmetric cell that exhibited a high specific capacitance of 421 F g^{-1} at a current density of 1 A g^{-1} with excellent cyclic retention of 94.6% over 10000 cycles (Figure 39b). The symmetric device of V_2O_5||PVA-KOH||V_2O_5 was fabricated using thin flexible substrate by Velmurugan et al. (Figure 39c), where both annealed (A-500) and as-prepared (RT) V_2O_5 films were used as electrode material separately.[306] A schematic

https://doi.org/10.1021/acs.chemrev.2c00546
Chem. Rev. 2023, 123, 4353–4415

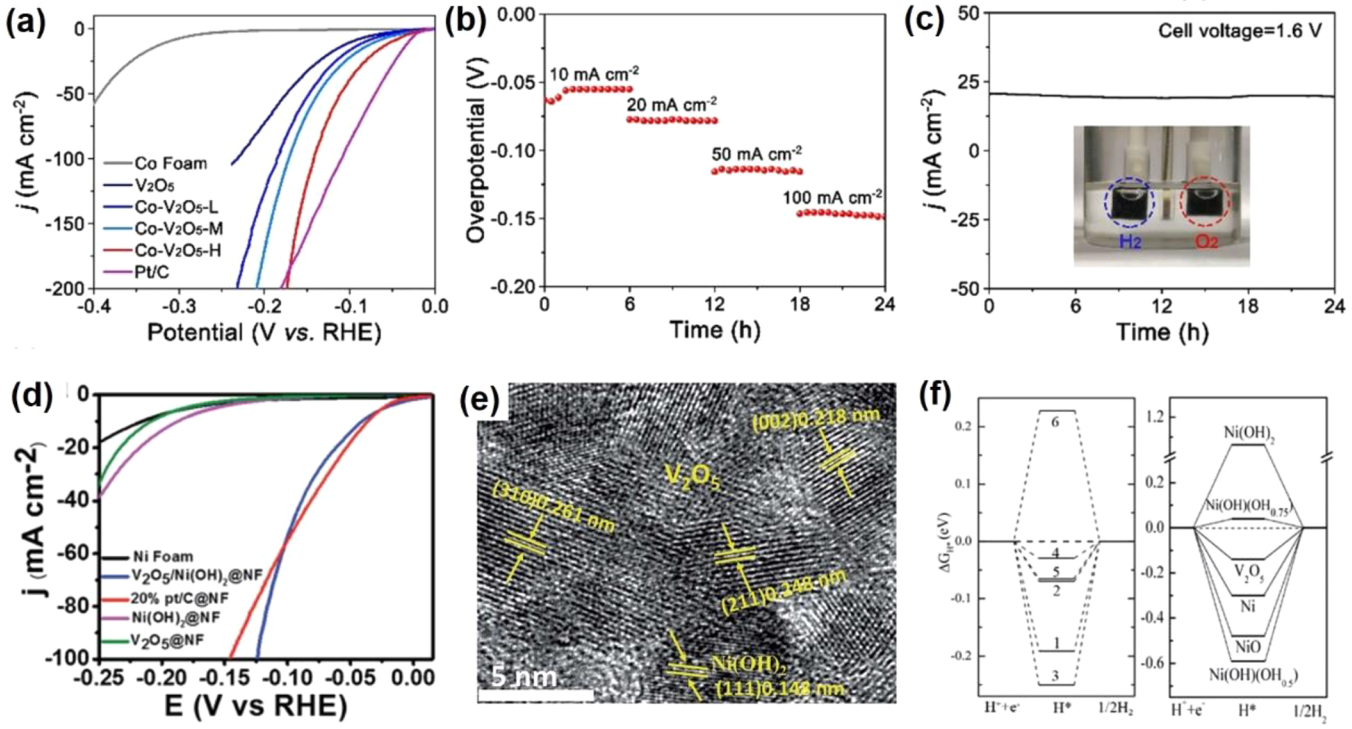

Figure 41. (a) HER polarization curves of the Co−V_2O_5−H sample, (b) stability of the Co−V_2O_5−H at 10−100 mA cm^{-2}, (c) stability of the Co−V_2O_5−H // Co−V_2O_5−H couple at 1.6 V for overall water splitting. Reproduced with permission from ref 328. Copyright 2020 Elsevier. (d) Polarization curves of NF, 20% Pt/C@NF, V_2O_5@NF, $Ni(OH)_2$@NF, and V_2O_5/$Ni(OH)_2$@NF at a scan rate of 2 mV s^{-1}, (e) HRTEM image of V_2O_5/$Ni(OH)_2$@NF, (f) calculated free energies at sites 1 to 6 (1: the reconstructed Ni-surface, 2: the Ni-site of $Ni(OH)_2$@Ni, 3: the Ni-site between V_2O_5@Ni and $Ni(OH)_2$@Ni, 4: the Ni-site of V_2O_5@Ni, 5: the O-site on the V_2O_5 surface, 6: the O-site inside the V_2O_5 channel) and various individual pristine materials. Reproduced with permission from ref 329. Copyright 2019 Royal Society of Chemistry.

representation of the structural image of the V_2O_5 is provided in Figure 39d. The CV curves in Figure 39e denote that the symmetric A-500 gives a larger area under the curve than the symmetric-RT, suggesting the improved performance of the annealed sample. The A-500 devices display a maximum energy density of 0.68 μWh cm^{-2}, which is obviously much higher than that of the RT electrodes (0.05 μWh cm^{-2}, Figure 39f). Moreover, the symmetric A-500 shows excellent cycle life up to 30000 cycles with a Coulombic efficiency of 99%. As shown in Figure 39g, the practical feasibility of the as-fabricated devices was demonstrated by lighting blue light-emitting diodes. Several groups reported the hybrid structure of V_2O_5 with carbon materials fabricated by different strategies for enhancing the SC property. For example, Sahu et al.[316] synthesized graphene nanoribbon @V_2O_5 nanostrip composites to improve the conductive property of V_2O_5, which displays a high energy density of 42.09 Wh kg^{-1} and power density of 475 W kg^{-1}. W. Sun et al.[317] prepared a 3D monolithic aerogel composed of uniform carbon nanofibers/V_2O_5 core/shell nanostructures. The composite aerogel exhibits high specific capacitance (595.1 F g^{-1}), excellent energy density (82.65 Wh kg^{-1}), and good cycling behavior (>12000). Zhu et al. proposed a simple "liquid phase impregnation template" strategy to successfully synthesize hierarchically porous V_2O_5/C nanocomposites that exhibits a specific capacitance of 492.1 F g^{-1}, as well as an energy density of 87.6 Wh kg^{-1}.[318] Yao et al. successfully synthesized SCs based on 3D networks hybrids of reduced graphene oxide and V_2O_5 nanobelts through a simple hydrothermal method.[319] The rGO/V_2O_5 hybrid aerogel electrodes showed a high energy density of 249.7 W kg^{-1} and excellent long-term cycle stability (remaining 90.2% after 5000 cycles).

7.2.3. Catalysts. *7.2.3.1. OER.* V_2O_5 exhibited good OER performance due to the multivalent states of the V element, which can enrich active intermediates (*OH, *O, and *OOH) by regulating the valence electron structure of the V element.[275,320] The OER performance could be enhanced by fabricating the composites with other materials. Lan et al.[320] synthesized CoV_2O_6-V_2O_5/nitrogen-doped reduced graphene oxide composites (CoV_2O_6-V_2O_5/NRGO) by a one-pot hydrothermal method integrating polyoxovanadate, ethylenediamine (EN), and graphene oxide (GO) for the precursor and postcalcined process (Figure 40a). Without V_2O_5, the CoV_2O_6/NRGO delivered a relatively acceptable OER performance with an overpotential of 379 mV at a current density of 10 mA cm^{-2}, which is comparable to that of IrO_2 (337 mV). By adding V_2O_5, the OER performance could be enhanced with an overpotential of 239 mV at a current density of 10 mA cm^{-2} (Figure 40b). Furthermore, the CoV_2O_6−V_2O_5/NRGO exhibits a higher current density (47.08 mA cm^{-2}) at an overpotential of 300 mV compared with CoV_2O_6/NRGO (0.45 mA cm^{-2}) and IrO_2 (3.95 mA cm^{-2}) (Figure 40c). Meanwhile, the CoV_2O_6−V_2O_5/NRGO shows the fastest reaction kinetics with a Tafel slope of 49.7 mV dec^{-1}, which could be due to the enhanced charge transport (Figure 40d). The CoV_2O_6−V_2O_5/NRGO gives good stability from the polarization curves, which are almost overlapping before and after 1000 cycles (Figure 40e). The theoretical calculation found that the existence of the hydrogen bond between V_2O_5 and intermediate HOO* of OER decreases the adsorption energy, which may be responsible for the low overpotential.

7.2.3.2. HER. In general, V_2O_5 is generally considered as an HER-inactive material due to the weak H* adsorption on V sites,

https://doi.org/10.1021/acs.chemrev.2c00546
Chem. Rev. 2023, 123, 4353−4415

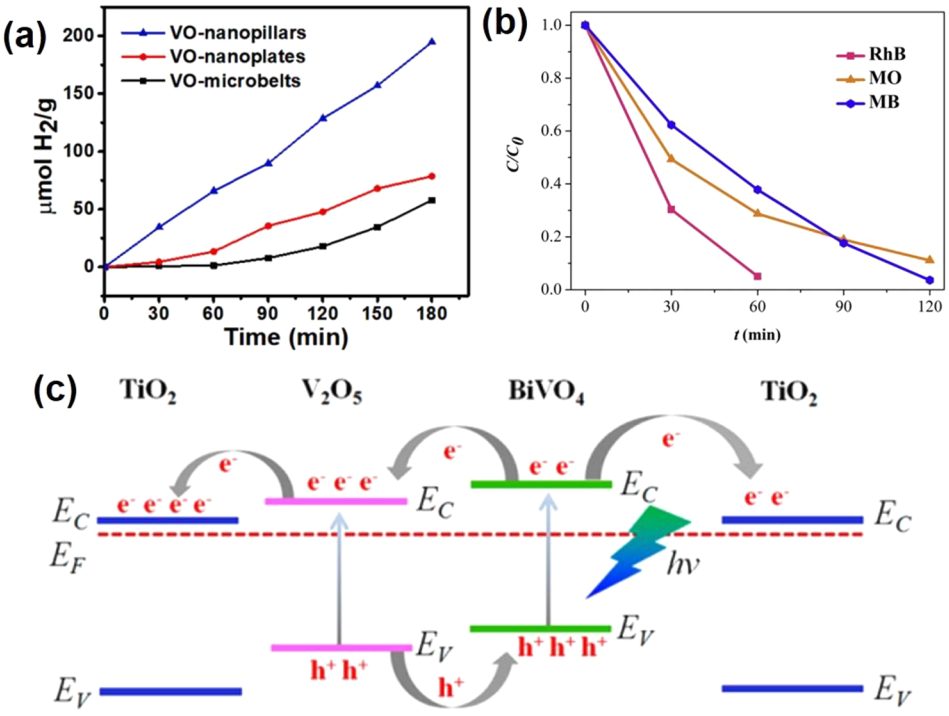

Figure 42. (a) The hydrogen generation curves for VO-microbelts, VO-nanoplates, and VO-nanopillars with a sacrificial agent. Reproduced with permission from ref 335. Copyright 2021 Elsevier. (b) The photodegradation performance of g-C_3N_4/V_2O_5 photocatalyst for RhB, MO, and MB degradation under visible light irradiation. Reproduced with permission from ref 344. Copyright 2016 Elsevier. (c) Schematic diagram of lectron−hole pairs separation of the V_2O_5/$BiVO_4$/TiO_2 nanocomposites under visible-light irradiation. Reproduced with permission from ref 349. Copyright 2014 American Chemical Society.

which limits the formation of H* at the active site.[321,322] Three main methods can be adopted to promote the HER performance of V_2O_5: defects creation, interfacial engineering, and forming composites. First of all, creating defects, especially vacancies, is regarded as an efficient way to enhance the HER performance.[323−325] Oxygen vacancy (V_O) in transition metal oxides can accelerate the adsorption of the H* intermediates by activating the delocalized electrons of the metal center, which could lead to a better HER performance.[326,327] Li et al.[328] synthesized the V_2O_5 nanosheet arrays with V_O on Co foam through a hydrothermal reaction. The highest V_O concentration of 34.2% of the V_2O_5 nanosheet arrays on the Co foam (Co−V_2O_5−H) is easily obtained by controlling the pH = 1 of the NH_4VO_3 precursor solution. The Co−V_2O_5−H exhibits a low overpotential of 51 mV at a current density of 10 mA cm^{-2}, which shows better performance compared to the V_2O_5 powder and low V_O concentration samples (Figure 41a). Meanwhile, the catalyst shows a negligible potential drop at different current densities, indicating long-time stability (Figure 41b). The Co−V_2O_5−H is employed as both a cathode and anode to establish a two-electrode alkaline electrolyzer for overall water splitting, which can maintain a steady output current at a cell voltage of 1.6 V for 24 h (Figure 41c). Second, the interfacial engineering between V_2O_5 and transition metal also provides a route to improve the HER performance. Kim et al.[329] directly grew the V_2O_5 particles on Ni foam via a one-step hydrothermal method. The as-prepared V_2O_5/$Ni(OH)_2$@NF catalyst shows a low overpotential of 39 mV at a current density of 10 mA cm^{-2}, which is comparable to Pt (35 mV @ 10 mA cm^{-2}). The $Ni(OH)_2$@NF samples show an overpotential of 188 mV at 10 mA cm^{-2}, which indicates that the V_2O_5 plays an important role in the HER performance (Figure 41d). DFT calculation was performed to investigate the active sites of the V_2O_5/$Ni(OH)_2$@NF catalyst. The exposed facet of V_2O_5 is the (010), (001), and (310) planes, which is confirmed by TEM (Figure 41e). The H adsorption energy of the V_2O_5 (001) and (310) surfaces is larger than that of V_2O_5 (010), which indicates that V_2O_5 (010) is the active surface. Furthermore, the ΔG_{H^*} values of the Ni-sites at the edges of interfaces in $Ni(OH)_2$@Ni and V_2O_5@Ni and the O-site of V_2O_5 (corresponding to 2, 4, and 5, respectively, as shown in Figure 41f) are close to zero, which is nearly equal to that of the Pt(111)-surface. The calculation indicated the edges of the interfaces in V_2O_5/$Ni(OH)_2$@NF play a significant role in the HER process. Moreover, the hierarchical V_2O_5@Ni_3S_2 hybrid nanoarray also exhibited a good overpotential of 95 mV at 10 mA cm^{-2},[330] which is also due to the interfaces between V_2O_5 and Ni_3S_2. Third, V_2O_5 is also used as an additive with other materials to form a composite and further enhance the HER performance. By doping phosphorus and adding V_2O_5 into Pt/graphene, the prepared catalysts exhibit a good HER performance of the initial potential of 32 mV and a Tafel slope of 23 mV dec^{-1}.[331]

7.2.3.3. Photocatalysis. It is well documented that V_2O_5 has a typical narrow band gap (~2.3 eV) and wide optical absorption range and is a high electron mobility semiconductor, which exhibits good photoresponsive properties by capturing visible light and is widely used in the electro-photocatalytic field, such as for hydrogen production, environmental pollutant degradation, etc.[332−334] Garcia et al.[335] found that the morphology of V_2O_5 nano-/microparticles dramatically affected the hydrogen production by photocatalysis. The V_2O_5 with microbelts, nanoplates, and nanopillars morphology can be obtained by using sunflowers' petals and the center of the sunflower as biodegradable templates during the synthesis.[335] The nanopillar

https://doi.org/10.1021/acs.chemrev.2c00546
Chem. Rev. 2023, 123, 4353−4415

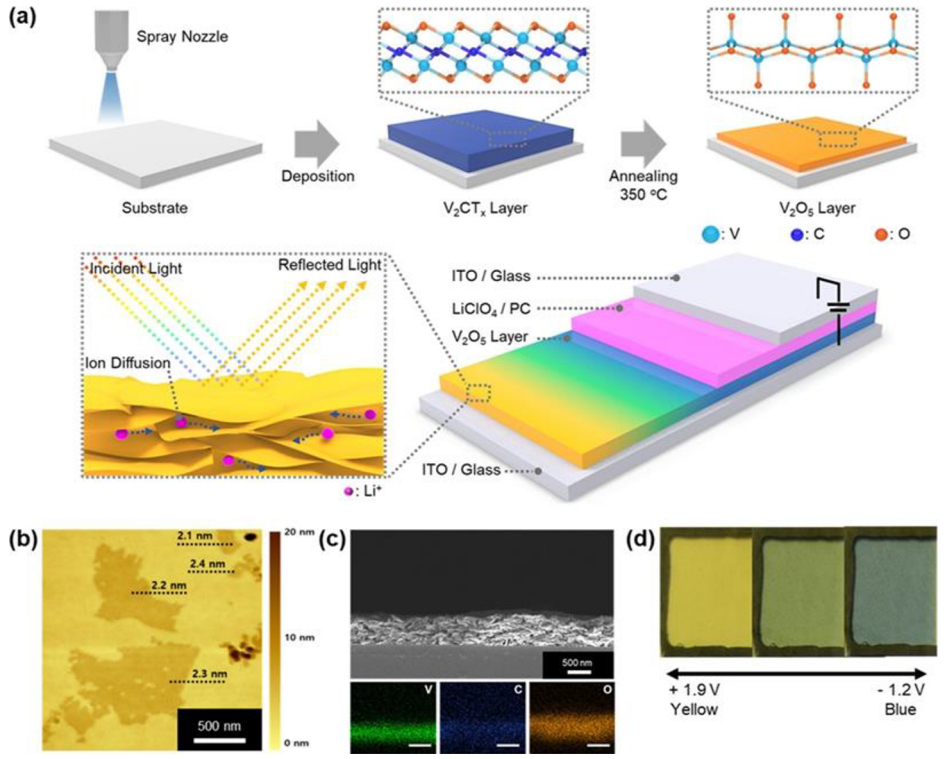

Figure 43. Fabrication of a 2D V_2O_5 nanosheet based electrochromic device. (a) Schematic for fabrication of an electrochromic device based on a V_2CT_x-derived 2D V_2O_5 nanosheet, resulting in minimized optical scattering and enhanced ion diffusion. (b) Representative AFM image of single layer V_2CT_x with a submicron lateral size. (c) SEM image of cross-section of 2D V_2O_5 nanosheet based electrochromic layer and corresponding EDS analysis in terms of vanadium, carbon, and oxygen. (d) Digital image of electrochromic device operating from +1.9 V to −1.2 V. Reproduced with permission from ref 366. Copyright 2023 Elsevier.

V_2O_5 delivers a maximum hydrogen generation rate in the presence of Na_2SO_3 as a sacrificial agent with 65.5 μmol g^{-1} h^{-1}, which is higher than microbelts (26.3 μmol g^{-1} h^{-1}) and nanoplates V_2O_5 (19.4 μmol g^{-1} h^{-1}) (Figure 42a). The high hydrogen generation rate is attributed to the large surface area, high absorbance in the UV−vis range, high photocurrent, and high content of defects of the V_2O_5 nanopillars. By fabricating the nanocomposite with V_2O_5 containing 1 or 2 heterojunctions, the hydrogen generation rate will be further improved, which is due to the delayed electron−hole recombination.[335] For example, graphitic carbon nitride nanosheets/V_2O_5 composites (578 μmol g^{-1} h^{-1}),[336] $Na_2Ti_3O_7/V_2O_5/g\text{-}C_3N_4$ composites (11000 μmol g^{-1} h^{-1}),[337] $Na_2TiO_3/V_2O_5/g\text{-}C_3N_4$ composites (567 μmol g^{-1} h^{-1}),[337] and Nb-doped SnO_2/V_2O_5 (1346 μmol g^{-1} h^{-1}).[338] Transition metal oxides (TiO_2, ZnO, etc.) have been applied in the removal of environmental pollutants in water, which could completely decompose organic pollutants into CO_2 and H_2O by photocatalytic oxidation.[339,340] Hollow V_2O_5 microspheres consisting of randomly packed platelets showed an enhanced UV light absorption compared to the commercial V_2O_5 powder, which led to the highest activity for degrading rhodamine B under UV light.[341] Composites, consisting of 1D V_2O_5 nanorod and 2D carbon-based materials, are promising photocatalysts for environmental pollutant degradation. The V_2O_5 nanorods/graphene oxide and V_2O_5 nanorods/graphene nanocomposites showed good degradation performance of Victoria blue dye and methylene blue dye (>95% degradation within 90 min), respectively.[342,343] Especially, the nanocomposites exhibited the best degradation performance under direct sunlight irradiation compared to UV and visible light. The $g\text{-}C_3N_4$ is also used to construct the heterojunctions with V_2O_5 for a high-performance degradation catalyst.[344] The photoexcited electron in the conduction band of $g\text{-}C_3N_4$ shows a strong reducing ability, while the photoexcited hole on the valence band of V_2O_5 exhibits a strong oxidizing ability. Thus, the $g\text{-}C_3N_4$ /V_2O_5 heterojunctions exhibited efficient degradation performance of rhodamine B, methyl orange (MO), and methylene blue (MB) dyes under visible light (Figure 42b). Besides the graphene or $g\text{-}C_3N_4$, the V_2O_5 composites with other inorganic photocatalytic oxides also showed enhanced photocatalytic properties for degradation of organic pollutants, such as $V_2O_5/BiVO_4$,[332,345] V_2O_5/CeO_2,[346] V_2O_5/TiO_2,[347,348] and so on. The V_2O_5-based composite can degrade not only the dye molecules in solution, but also some small solvent molecules in the gas phase. The ternary $V_2O_5/BiVO_4/TiO_2$ nanocomposites exhibited a well-aligned band structure and increasing photoinduced charge carriers through the charges separation across their multiple interfaces, which resulted in good light absorption from the UV to the visible region and better photocatalytic activity for the decomposition of gaseous toluene compared to pure TiO_2 and $V_2O_5/BiVO_4$ under visible light irradiation (Figure 42c).[349]

7.2.4. Electrochromism. Since Colton et al. did the pioneering work on the electrochromism of V_2O_5 in 1976−1977,[350,351] V_2O_5 has attracted increasing attention among transition metal oxides because it can exhibit both anodic and cathodic coloration.[352] From 1975 to 1999, studies focused on the absorption-transmission spectra modulation in visible and infrared light, while, after 2000, V_2O_5 with various micro- and nanostructures were emerging, and researchers paid attention to improve some important key figures of merit to evaluate the electrochromic performance, such as the coloration efficiency,

https://doi.org/10.1021/acs.chemrev.2c00546
Chem. Rev. 2023, 123, 4353−4415

cycling life, switching time, and so on.[353−358] Recently, several reviews were published on the electrochromic application of V_2O_5 film, which provide more specific and detailed information on this topic.[256,352,359,360] For V_2O_5, the discoloration mechanism is explained as the result of injection/extraction of electrons and electrolyte cations and variation of valence change of vanadium ions, which is widely accepted.[361,362]

In order to improve the performance of V_2O_5 as an electrochromic device, many strategies have been designed. Especially, V_2O_5 nanostructures with small sizes and large specific surface areas are expected to facilitate the ion intercalation/deintercalation process, thereby enhancing the electrochromic properties. Panagopoulou et al.[363] successfully prepared Mg-doped V_2O_5 thin films using RF sputtering, and found the 15 atom % Mg-doped films displayed optimal electrochromic properties with the fastest switching time of t_c = 10/4 s (intercalation/deintercalation), the best coloration efficiency of 71.3 cm^2 C^{1-} at 560 nm, higher visible transmittance of 85%, and the highest contrast value between the coloration states of ΔT (34.4% @ 560 nm). Qi et al.[364] fabricated flexible V_2O_5 nanosheets/graphene oxide films, which exhibit ultrafast coloring response time (1.6 s) and bleaching time (2 s) attributed to the reduced charge transport distances of the ultrathin nanosheet structure (4−40 nm). They also display an excellent transmittance contrast of 57.5% at 425 nm and reversible yellow/green/blue-gray multicolor changes. Tong et al.[365] fabricated a 3D crystalline V_2O_5 nanorod architecture on ITO substrates by a colloidal crystal-assisted electrodeposition method. Such architecture exhibits a highly reversible Li-ion insertion/extraction process (Columbic efficiency up to 96.9%), five distinct color change, good transmittance modulation ΔT (38.48% @ 460 nm), and acceptable response times (8.8 s for coloration and 9.3 s for bleaching), making it a promising film electrode for electrochromic devices. Kim et al.[366] prepared highly crystalline 2D V_2O_5 nanosheets by using single-layer V_2CT_x film as a sacrifice template (Figure 43a). The mean thickness and lateral size of V_2CT_x are 2.38 nm and 0.78 μm, respectively (Figure 43b). Figure 43c shows the SEM image of V_2O_5 nanosheets film after annealing of V_2CT_x at 350 °C. The 2D V_2O_5 nanosheets based electrochromic device has sharp multicolor transformations with a robust optical contrast from yellow to green to blue (Figure 43d). The corresponding optimal electrochromic performance shows a high optical contrast (53.98% @ 700 nm) and a fast response time (6.5 s for coloration and 5.0 s for bleaching).

8. OTHER VANADIUM OXIDES

8.1. V_2O_2

V_2O_2 is generally used as a tool to investigate the nature of metal−oxygen bonds, which is crucial to provide a proper rationalization of the relationship between structure and properties at an atomic scale.[367] Stable V_2O_2 could not be synthesized by a traditional solid-state reaction or solution methods. However, it can be observed by IR spectroscopy on V, Ne, and O_2 codeposited matrices.[368] The calculation results show two possible vanadium bonding situations: 1) no bonds between the two vanadium atoms; 2) a short distance between the two vanadium atoms, which indicated multiple bonding (Figure 44a).[368−370] However, Himmel et al.[368] found that there is a multiple vanadium−vanadium bond in V_2O_2 molecules. There are three V−V bonding and antibonding orbitals, which are occupied by 1.70, 1.58, 1.50 electrons and 0.42, 0.40, 0.49 electrons, respectively. Thus, 4.78 electrons are in V−V bonding orbitals, and 1.31 electrons are in V−V antibonding orbitals. Furthermore, five bond critical points (four points between the oxygen and the vanadium atoms and one point in the center between the vanadium atoms) and two ring critical points (between the center of the cluster and the oxygen atoms) can be identified in V_2O_2 molecules (Figure 44b), which confirms the presence of a V−V bond. The presence of the strong V−V bond may lead to unique optical and magnetic properties.

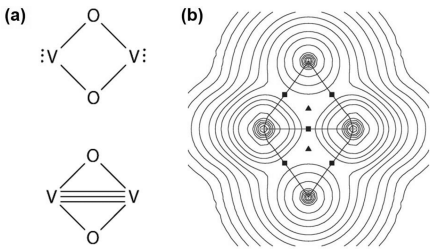

Figure 44. (a) Two possible Lewis representations highlighting the unclear bonding situation in V_2O_2. (b) Plot of the electron density within the molecular plane. Rectangles: bond critical points; triangles: ring critical points. Reproduced with permission from ref 368. Copyright 2017 John Wiley and Sons.

8.2. V_4O_9

V_4O_9 has an orthorhombic structure with a space group of *Cmcm*, which processes three types of VO polyhedra (Figure 45a). The VO_5 pyramids and VO_6 octahedra make pairs, which are connected by corner oxygen atoms from the VO_4 tetrahedra.[371] The valence of the vanadium ion in the octahedron and pyramid is +4, while that in the tetrahedron is +5. V_4O_9 is difficult to synthesize by a solid-state reaction from the mixture of binary V_2O_5 and V_2O_3 (or VO_2), but it can be synthesized by the reduction of V_2O_5 using reducing agents of carbon, SO_2, and sulfur.[371,372] The amount of reducing agents dramatically affects the final products, which may consist of other vanadium oxides, such as V_6O_{13} and VO_2. Consequently, reducing V_2O_5 by the solvothermal method is a facile way to obtain V_4O_9. Different solvents (tetraethylene glycol, 2-propanol, and tetrahydrofuran) are used to synthesize V_4O_9 with different morphologies, such as nanoflakes, nanosheets, and so on.[373−375] Liang et al.[375] investigated the aqueous zinc ion batteries of V_4O_9. It is found that the V_4O_9 exhibits fast zinc ion and electron diffusion, which is due to the unique tunnel structure and the V^{5+}/V^{4+} mixed-valences induced metallic behavior. The V_4O_9 cathode shows a high reversible discharge capacity (420 mA h g^{-1} at 0.5 C). Even at a high current density of 50 C, it also exhibits an impressive discharge capacity of 234.4 mA h g^{-1}, suggesting a fast Zn^{2+} storage ability of V_4O_9 (Figure 45b). Furthermore, V_4O_9 delivers an energy density of 175.8 W h kg^{-1} at a high power of 17625 W kg^{-1}, which gives a high power density compared with other vanadium-based cathode materials in aqueous zinc ion batteries, such as V_2O_5,[376] V_6O_{13},[377] LiV_3O_8,[378] $Na_3V_2(PO_4)_3$,[379] VO_2,[380] and VS_2.[381]

The 2D single layered V_4O_9 nanosheet assembled 3D microflowers exhibit good supercapacitor performance with a specific capacitance of 392 F g^{-1} at a current density of 0.5 A g^{-1} and 75% retained capacitance after 2000 cycles (Figure 45c).[373] The flower-like structure assembled from ultrathin and well-separated nanosheets was unchanged during the charge−discharge cycles, which is responsible for the high capacitance and stability. Meanwhile, the V_4O_9 flower demonstrates a good

https://doi.org/10.1021/acs.chemrev.2c00546
Chem. Rev. 2023, 123, 4353−4415

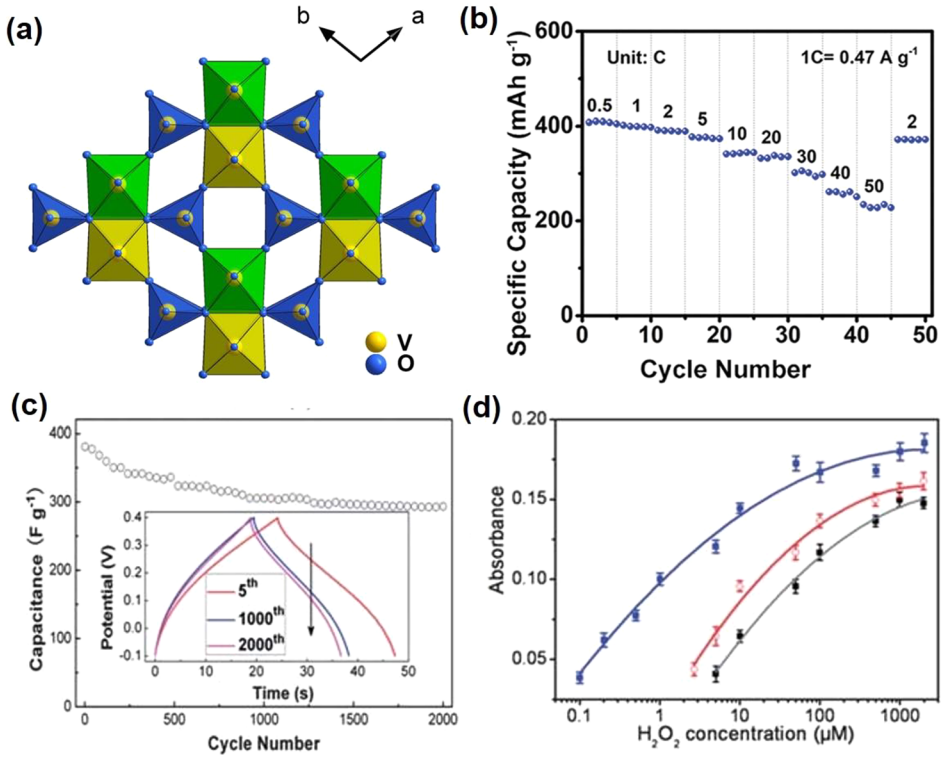

Figure 45. (a) Crystal structure of V_4O_9 with VO_6 octahedron (yellow), VO_5 pyramid (green), and VO_4 tetrahedron (blue). (b) Rate performance at various currents ranging from 0.5 to 50 C of the aqueous Zn//V_4O_9 second battery. Reproduced with permission from ref 375. Copyright 2021 Royal Society of Chemistry. (c) The cycling stability of the specific capacitance of flower V_4O_9 at 2 A g^{-1}. The inset shows the charge−discharge curves at different cycle numbers. (d) UV−vis absorbance curve (with polynomial fitting) of 75 mg flower V_4O_9 (blue) at varying H_2O_2 concentrations. Reproduced with permission from ref 373. Copyright 2013 Royal Society of Chemistry.

ability to sense H_2O_2 and methanol with a detection limit of ∼0.1 μM and ∼60 μM, respectively (Figure 45d).

8.3. V_6O_{13}

The mixed-valence V_6O_{13} attracts extensive attention because it can be used in a variety of ion batteries, such as Li^+, Na^+, Mg^{2+}, Zn^{2+}, and so on. As shown in Figure 46a, V_6O_{13} is composed of alternating single and double vanadium oxide layers. There are two types of VO_6 octahedra: V^{4+} occupied the yellow octahedra, and V^{5+} occupied the blue octahedra. All the octahedra are connected with corner O atoms, which form a tunnel-like structure.[49,382] The solvothermal reaction is widely used to obtain V_6O_{13} nanostructures, particles, and related composites, such as V_6O_{13} nanogrooves,[383] V_6O_{13}@hollow carbon microspheres,[384] nest-like V_6O_{13},[385] V_6O_{13} nanosheets,[386] V_6O_{13} nanowires,[387] V_6O_{13} nanorods,[388] and so on (Figure 46b). Cao et al.[389] recently developed a new strategy to synthesize V_6O_{13} nanosheets by microwaves, which could reduce the thickness of V_6O_{13} nanosheets greatly compared to that prepared by a hydrothermal method (Figure 46c,d).

Due to the tunnel-like structure and mixed-valence, V_6O_{13} exhibits a metallic character at room temperature, which is beneficial for high-rate charge and discharge. When it is used as an LIB electrode material, 8 mol Li^+ intercalated per formula unit endowing a high theoretical specific capacity of 417 mAh g^{-1} and energy density of 900 Wh kg^{-1}. The Yu group[383] synthesized a 3D V_6O_{13} nanotextile with interconnected 1D nanogrooves via a facile solution-redox-based self-assembly route at room temperature (Figure 47a). They confirmed that the precursor concentration affected the mesh size in the textile structure. The 3D V_6O_{13} delivers a high capacity of 326 mAh g^{-1}

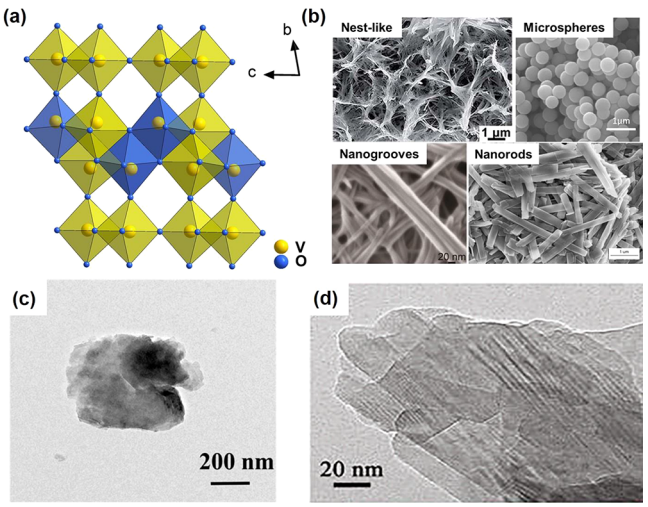

Figure 46. (a) Crystal structure of V_6O_{13} with V two types of VO_6 octahedra. (b) Different morphologies of V_6O_{13} synthesized by a solvothermal method. Reproduced with permission from ref 385 (Copyright 2020 Royal Society of Chemistry), ref 384 (Copyright 2021 Elsevier), ref 383 (Copyright 2015 American Chemical Society), and ref 390 (Copyright 2019 Elsevier). (c, d) V_6O_{13} nanosheet obtained by hydrothermal and microwave-assisted synthesis. Reproduced with permission from ref 386 (Copyright 2021 Elsevier) and ref 389 (Copyright 2022 Elsevier).

at 20 mA g^{-1} and maintains 80% capacity after 100 cycles at 500 mA g^{-1}. The energy density can reach 780 Wh kg^{-1}, which is much higher than those of commercialization cathodes ($LiFePO_4$ and $LiCoO_2$) (Figure 47b). The excellent electro-

https://doi.org/10.1021/acs.chemrev.2c00546
Chem. Rev. 2023, 123, 4353−4415

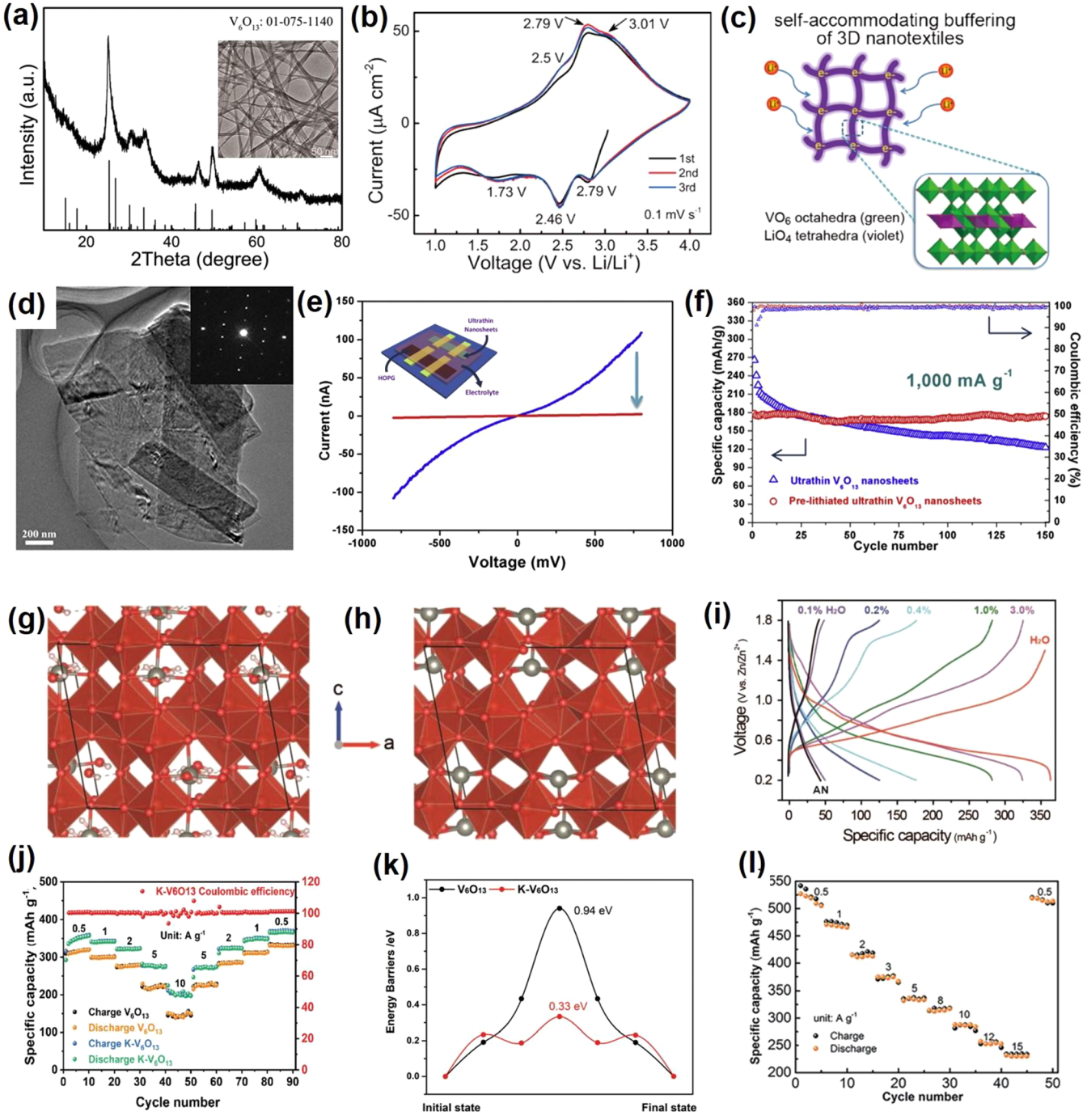

Figure 47. XRD pattern and SEM image (a), different CV curves (b), and the schematic diagram of the Li^+ intercalation process (c) of 3D V_6O_{13} nanotextile electrodes in LIB. Reproduced with permission from ref 383. Copyright 2015 American Chemical Society. The TEM image of ultrathin lithiated V_6O_{13} nanosheets (d), the transport properties (e), and cycling performance at 1000 mA g^{-1} (f) of nonlithiated ultrathin and ultrathin lithiated V_6O_{13} nanosheets. Reproduced with permission from ref 391. Copyright 2014 Elsevier. Optimized geometry of Zn intercalated V_6O_{13} with water (g) and without water (h), the galvanostatic voltage-capacity profiles for V_6O_{13} cycled in electrolytes with different water contents in 1 M $Zn(CF_3SO_3)_2$ acetonitrile (i). Reproduced with permission from ref 392. Copyright 2019 John Wiley & Sons. (j) Charge/discharge curves of K–V_6O_{13} at different rates. (k) The migration energy barriers of K–V_6O_{13} and V_6O_{13}. Reproduced with permission from ref 394. Copyright 2022 Royal Society of Chemistry. (l) Rate capability under various currents of V_6O_{13} on carbon cloth. Reproduced with permission from ref 385. Copyright 2020 Royal Society of Chemistry.

chemical performance is due to the unique structure of 3D textiles, which can be maintained upon cycling and are beneficial for ion transport and cycle stability (Figure 47c). In addition, Mai et al.[391] synthesized a novel ultrathin prelithiated V_6O_{13} nanosheet by a secondary hydrothermal prelithiation process (Figure 47d). A single-nanosheet device was employed to *in situ* probe the intrinsic advantages of prelithiated nanosheets. Compared with nonlithiated V_6O_{13} nanosheets, the ultrathin prelithiated V_6O_{13} nanosheets exhibit a higher electrical conductivity and maintain the same conductance level after the Li^+ intercalation (Figure 47e). Meanwhile, the specific capacity of the ultrathin prelithiated V_6O_{13} nanosheets can be

https://doi.org/10.1021/acs.chemrev.2c00546
Chem. Rev. 2023, 123, 4353−4415

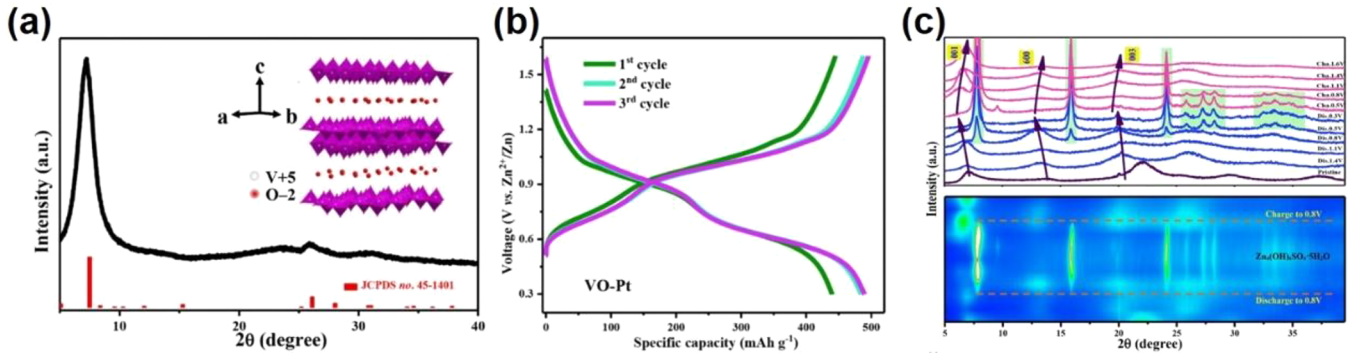

Figure 48. XRD pattern (a), charge/discharge profiles (b), and *in situ* XRD patterns and 2D contour map of peak intensities of $V_5O_{12}·6H_2O$−Pt (c). Reproduced with permission from ref 395. Copyright 2021 John Wiley & Sons.

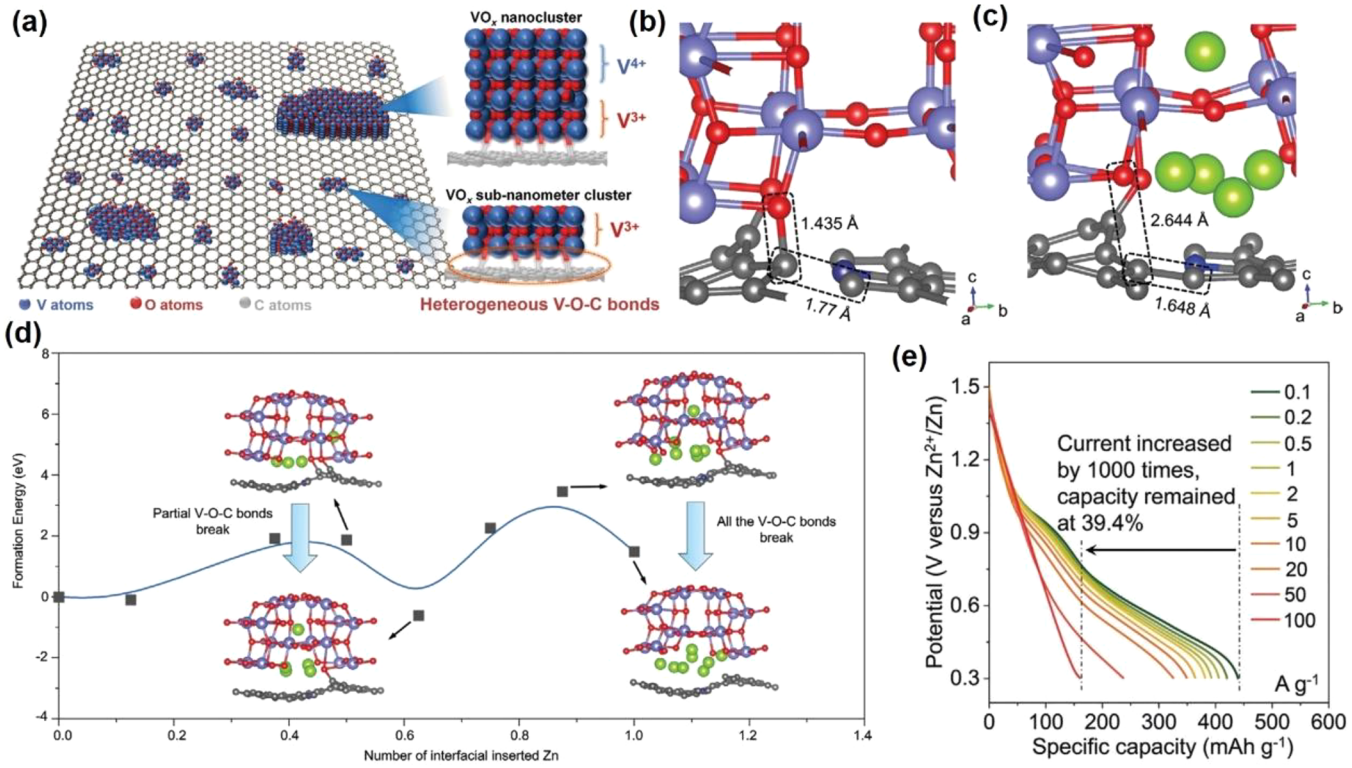

Figure 49. Characterization of the interfacial configuration in the VO_x-G heterostructure and its anomalous Zn^{2+} storage mechanism (a), DFT simulations in pristine (b) and fully discharged (c) states, formation energy evolution during Zn^{2+} ion insertion into the interface (d), galvanostatic discharge curves varying from 0.1 to 100 A g^{-1} (e) of VO_x-G heterostructure. Reproduced with permission from ref 396. Copyright 2021 John Wiley & Sons.

maintained at 98% after 150 cycles at a current density of 1000 mA g^{-1}, which is much higher than 46% capacity of nonlithiated V_6O_{13} nanosheets (Figure 47f). These results demonstrate that prelithiation is a strategy to obtain high-energy and long-cycling energy storage cathode materials.

Doping of various metal ions can improve the electrochemical performance and achieve a good capacity of the battery. The V_6O_{13} with Al/Ga, Al/Fe, and Al/Na doping delivered an initial discharge specific capacity of 411.5 mA h g^{-1}, 426.9 mA h g^{-1}, and 514 mA h g^{-1} at 0.1 C, respectively.[388] However, the electrochemical performances were poor at a high current density. V_6O_{13} was also employed in multivalent ion (Zn^{2+}, Mg^{2+}) batteries.[384,385,389,392,393] Choi et al.[392] applied V_6O_{13} as the ZIB cathode material and investigated its electrochemical behavior for Zn^{2+}. In particular, they analyzed the effect of water in the electrolyte on the Zn^{2+} storage to investigate the physicochemical characteristics of V_6O_{13}. DFT calculation results demonstrate that the coordination environments of Zn show a big difference with/without water (Figure 47g,h). It will form octahedral coordination with water, but undercoordination without water. The Zn^{2+} storage of V_6O_{13} increases with increasing water content in the electrolyte, and it can deliver a high capacity of 360 mAh g^{-1} and be maintained at 92% after 2000 cycles in an aqueous $Zn(CF_3SO_3)_2$ (~1 M) electrolyte (Figure 47i). Even at a high current density of 24 A g^{-1}, it maintains a relatively high capacity of 145 mAh g^{-1}.[16] This work highlights that cointercalating water molecules play a vital role in enhancing the electrochemical performance of the aqueous ion storage system. Zhao et al.[394] found that the K^+ intercalated V_6O_{13} exhibited a specific capacity of 367 mAh g^{-1} at 0.5 A g^{-1} and 198.8 mAh g^{-1} at 10 A g^{-1} (Figure 47j). Meanwhile, the capacity could be maintained at 90% after 2000 cycles at 10 A

https://doi.org/10.1021/acs.chemrev.2c00546
Chem. Rev. 2023, 123, 4353−4415

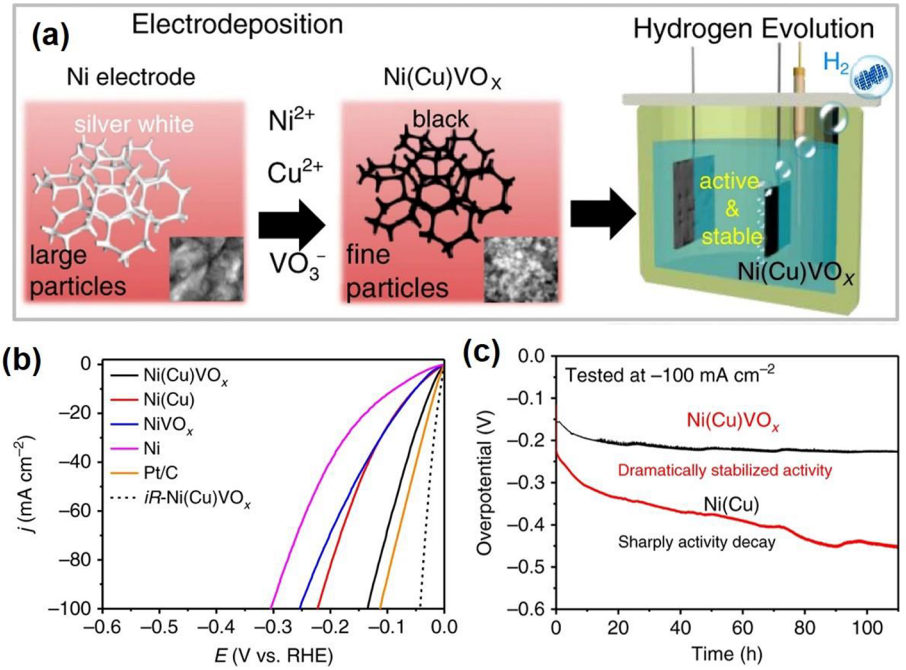

Figure 50. (a) Schematic to prepare the Ni(Cu)VO_x electrode for HER electrolysis. (b) LSV curves for Ni(Cu)VO_x and control samples without *iR* compensation. The black dotted curve is the HER activity on the Ni(Cu)VO_x electrode with *iR* correction. (c) Chronopotentiometric curve of Ni(Cu)VO_x in comparison with Ni(Cu). Reproduced with permission from ref 397. Copyright 2020 under CC BY license.

g^{-1}. The DFT calculation suggested that K^+ intercalation could significantly contribute to the reduction of the Zn^{2+} diffusion energy barrier (from 0.94 to 0.33 eV), which enables Zn ions to migrate away from the intercalation sites more easily (Figure 47k). Thus, K^+ intercalated V_6O_{13} showed good battery performance. Furthermore, by growing the V_6O_{13} on carbon cloth and using the $ZnSO_4$ as the electrolyte, the V_6O_{13} cathode showed a capacity of 520 mAh g^{-1} (at a current density of 0.5 A g^{-1}) and good cycle life (a stable capacity of 335 mAh g^{-1} over 1000 cycles) (Figure 47l).[385]

8.4. Other Vanadium Oxides for Energy-Related Application

$V_5O_{12}{\cdot}6H_2O$ is another layered monoclinic vanadium oxide separated by water pillars with a large interlayer spacing of 1.179 nm. Wang et al.[395] added a small amount of platinum (Pt, 1.5 wt %) into the interlayer of $V_5O_{12}{\cdot}6H_2O$. The obtained $V_5O_{12}{\cdot}6H_2O$−Pt electrode delivers a specific capacity of 440 mAh g^{-1} at 500 mA g^{-1}, and increases to 489 mAh g^{-1} for the third cycle, much higher than $V_5O_{12}{\cdot}6H_2O$ electrodes (270 mAh g^{-1} at 500 mA g^{-1}) (Figure 48a,b). They also demonstrated that the Pt additive makes no contribution, and is even counterproductive to conductivity, but facilitates a significant enhancement of pseudocapacitance. Therefore, it is clear that there is a strong relationship between Pt and the new phase $Zn_4SO_4(OH)_6{\cdot}5H_2O$. The *in situ* XRD patterns show that obvious characteristic peaks shifted to lower angles during the discharge process and returned to the pristine state during charging, indicating the interlayer spacing gradual enlargement and recovery upon Zn^{2+} intercalation/deintercalation. Meanwhile, the formation/disappearance of the zinc hydroxyl complex is accompanied by Zn^{2+} insertion/extraction (Figure 48c).

Mai et al.[396] artificially constructed a VO_x cluster/reduced graphene oxide (rGO) cathode material with interfacially inserted Zn^{2+} repelling the pristine-bonded C atom into the plane of the rGO and constructing interfacial V−O−C bonds (Figure 49a). Meanwhile, the VO_x consists of subnanoclusters (less than 1 nm per dimension) and partial nanoclusters (slightly larger than 1 nm). In combination with the electrons transferred to the rGO during the discharge process (Figure 49b−d), the reduced degree of defect is additional proof of the interfacial Zn^{2+} storage. As a result, they have discovered a new mechanism in which Zn^{2+} ions are stored mainly at the interface between VO_x and rGO, which leads to anomalous valence changes compared to conventional mechanisms and exploits the storage capacity of the nonenergy storing active but highly conductive rGO. The obtained VO_x-G heterostructure delivers a superior rate performance with a capacity of 174.4 mAh g^{-1} at an ultrahigh current density of 100 A g^{-1}, with capacity retention of 39.4% for a 1000-fold increase in current density (Figure 49e). To the best of our knowledge, the rate performance is one of the best among ZIBs.

Besides the battery application, the nanostructured VO_x materials/composites have been considered as a good catalyst for the HER due to the creation of the more active site and modification of the adsorption and desorption of H atoms.[397] Guan et al.[398] prepared 2D Zn-VO_x-Co ultrathin nanosheets on carbon fiber paper by an electrodeposition method. The Zn-VO_x-Co electrocatalysts contain the amorphous Co metal phase and crystalline Zn−Co alloy phase, which gives the materials a good HER performance (an overpotential of 46 mV at 10 mA cm^{-2} and a Tafel slope of 75 mV dec^{-1}). Furthermore, Zhao et al.[397] adopted the same method to fabricate a Ni(Cu)VO_x catalyst by changing Zn and Co to Ni and Cu (Figure 50a). The Ni(Cu)VO_x electrode displays a small overpotential of 21 mV at a current density of 10 mA cm^{-2} and a Tafel slope of 28 mV dec^{-1} (Figure 50b), which is comparable to the commercial 20% Pt/C catalyst (15 mV @ j = 10 mA cm^{-2} and 25 mV dec^{-1}). Meanwhile, the Ni(Cu)VO_x electrode also remains relatively stable for more than 100 h HER at 100 mA cm^{-2} (Figure 50c). The good HER performance is due to the existence of Ni−O−VO_x sites, which promote the formation of highly disordered

https://doi.org/10.1021/acs.chemrev.2c00546
Chem. Rev. 2023, 123, 4353−4415

Table 1. Electrochemical Properties of the Typical Vanadium Oxides for Metal-Ion Batteries

materials	battery types	Ccapacity (mAh g^{-1})/ current density (A g^{-1})	retention (%)/Ccycle numbers/ current density (A g^{-1})	rate capacity (mAh g^{-1})/ current density (A g^{-1})	ref
VO_x−rGO heterostructure	ZIBs	443/0.1	∼92%/1000/20	174.4/100	396
V_2O_3 hollow spheres	LIBs	785/0.1	Over 100%/700/2	361/2	76
V_2O_3 porous nanofibers	KIBs	240/0.05	94.5%/500/0.05	134/1	68
V_2O_3	ZIBs	625/0.1	97.7%/1000/5	486/20	77
V_2O_3 with CNTs	SIBs	612/0.1	100%/6000/2 70%/10000/10	207/10	361
Carbon-confined V_2O_3	ZIBs	633.1/0.2	90.3%/10000/12	271.4/24	401
V_3O_5	LIBs	412/0.2	78.5%/2000/50	125/50	98
Graphene quantum dots coated onto the VO_2 surfaces	LIBs	421/0.1	94%/1500/18	151/36	237
Graphene quantum dots coated onto the VO_2 surfaces	NIBs	306/0.1	88%/1500/18	93/36	237
VO_2 (B) nanorods	KIBs	209.2/0.05	86%/500/0.5	141.4/2	238
VO_2 (B) nanorods	MIBs	391/0.025	41.9%/60/0.85	341/0.1	402
VO_2 hollow microspheres	LIBs	203/0.1	80%/1000/2	134/2	240
VO_2 interwoven nanowires coated with Carbon quantum dots	LIBs	427/0.1	112%/500/19.2	168/19.2	403
VO_2 with graphene ribbons	LIBs	415/0.4	93%/1000/37.2	204/37.2	404
VO_2 (B) nanobelt forest	LIBs	475/0.1	63%/47/0.1	100/27	405
VO_2 nanorods	ZIBs	325.6/0.05	86%/5000/3	72/5	239
VO_2 nanofibers	ZIBs	357/0.1	N.A.	171/51.2	406
V_3O_7 nanowire templated graphene scrolls	LIBs	321/0.1	87.3%/400/2	162/3	120
$V_3O_7{\cdot}H_2O$	ZIBs	370/0.375	80%/200/3	270/3	121
$H_2V_3O_8$	MIBs	231/0.01	77%/100/0.04	97/0.08	108
$H_2V_3O_8$ nanowires	ZIBs	423.8/0.1	94.3%/1000/5	113.9/5	407
$H_2V_3O_8$ nanowires with graphene	ZIBs	394/0.1	87%/2000/6	270/6	408
V_4O_7	LIBs	291/0.05	∼100%/100/3	159/3	409
V_4O_9	ZIBs	420/0.235	78.8%/1000/9.4	233.4/23.5	375
3D V_6O_{13} nanotextiles	LIBs	326/0.02	80%/100/0.5	134/0.5	383
V_6O_{13} nanosheet	LIBs	331/0.1	98%/150/1	150/2	391
V_6O_{13}	ZIBs	360/0.2	92%/2000/4	145/24	392
V_6O_{13} microflowers	SIBs	159.8/0.16	73.5%/30/0.16	N.A.	410
Oxygen-deficient V_6O_{13}	ZIBs	401/0.2	95%/200/0.2	223/5	411
$V_5O_{12}{\cdot}6H_2O$	ZIBs	440/0.5	∼95%/400/10	158/15	395
$V_5O_{12}{\cdot}6H_2O$ nanobelt	ZIBs	354.8/0.5	∼94%/1000/2	228/5	412
$V_{10}O_{24}{\cdot}12H_2O$	ZIBs	164.5/0.2	90.1%/3000/10	80/10	413
$V_{10}O_{24}{\cdot}12H_2O$	ZIBs	365.3/0.2	83.2%/3000/5	127.2/80	414
V_7O_{16} nanotube	ZIBs	314.6/0.1	80.5%/950/2.4	87.8/9.6	415
V_2O_5 hollow microclew	LIBs	145.3/0.1	94.4%/50/0.1	94.8/10	308
V_2O_5 hollow nanosphere	SIBs	159.3/0.04	72.6%/100/0.16	112.4/0.64	416
V_2O_5 nanowires	AIBs	305/0.125	89.5%/20/0.125	N.A.	417
V_2O_5	ZIBs	470/0.2	91.1%/4000/5	386/10	418
V_2O_5 nanosheet	ZIBs	224/0.1	81.3%/30/0.1	N.A.	419
V_2O_5 nanofibers	ZIBs	319/0.02	81%/500/0.6	104/3	376
Porous V_2O_5	LIBs	142/0.075	∼90%/100/0.075	86.7/8.2	420
V_2O_5/C	SIBs	255/0.015	95%/30/0.015	170/0.294	309
V_2O_5-polyaniline superlattice	MIBs	270/0.1	61.5%/500/4	130/4	421
Polyaniline intercalated V_2O_5	NIBs	307/0.5	42%/100/5	69/20	422
$V_2O_5{\cdot}nH_2O$	SIBs	338/0.05	73%/50/0.5	96/1	423
$V_2O_5{\cdot}nH_2O$	ZIBs	372/0.3	71%/900/6	248/30	310
$V_2O_5{\cdot}nH_2O$	CIBs	204/0.14	86%/350/0.7	28/2.8	424
3D V_2O_5/RGO/CNT	LIBs	304/0.0294	90%/80/0.294	100/5.88	311
$Na_{0.33}V_2O_5$	ZIBs	367.1/0.1	93%/1000/1	96.4/2	312
$Mn_{0.01}V_{1.99}O_5$	LIBs	251/0.294	80%/50/0.294	171/1.47	313
UGF-V_2O_5/PEDOT	LIBs	297/0.294	98%/1000/17.64	85/23.52	314

metallic Ni structures and further induce electron transfer from Ni to VO_x.

The VO_x based composites also exhibit good OER performance. Dong et al.[399] synthesized 3D nanoflower-like VO_x nanosheets (VO_x/NiS/NF) by a hydrothermal method, which showed the OER performance with a low overpotential (330 mV at 50 mA cm^{-2}) and a small Tafel slope (121 mV dec^{-1}). Yang et al.[400] synthesized a ternary Co-VO_x-P catalyst with a nanoflower

https://doi.org/10.1021/acs.chemrev.2c00546
Chem. Rev. 2023, 123, 4353−4415

Table 2. Electrochemical Properties of the Typical Vanadium Oxides for Supercapacitors

materials	electrolyte	Specific capacitance (F g^{-1})/Current density (A g^{-1})	Retention (%)/Cycle numbers	ref
VOOH nanosheets	1 M $LiClO_4$/PPC	323/0.2	70%/2000	425
V_2O_3 nanoflakes@C core−shell composites	1 M $NaNO_3$	205/0.05	76%/500	94
V_2O_3/C nanocomposites	5 M LiCl	458.6/0.5	86%/1000	93
V_2O_3@C core−shell nanorods	5 M LiCl	228/0.5	81%/1000	426
V_2O_3@C core−shell nanorods	1 M Na_2SO_4	192/1	66%/1000	427
V_2O_3@C core−shell composites	1 M Na_2SO_4	223/0.1	39.7%/100	428
N-doped carbon coated nest-like V_3O_7	1 M Na_2SO_4	660.63/0.5	80.47%/4000	112
		187.72/50		
V_3O_7 nanowires on carbon fiber cloth	1 M Na_2SO_4	198/1	97%/100000	125
$V_3O_7{\cdot}H_2O$ nanobelts/CNT/rGO composites	5 M LiCl/PVA	685/0.5	99.7%/10000	126
V_3O_7-rGO-polyaniline composites	1 M H_2SO_4	579/0.2	95%/2500	429
VO_2(B) nanobelts/rGO composites	0.5 M K_2SO_4	353/1	78%/10000	235
VO_2 nanosheet	1 M $LiClO_4$/PPC	405/1	82%/6000	430
VO_2 nanosheet	6 M KOH	663/10	99.4%/9000	431
VO_2(B)/C core−shell composites	1 M Na_2SO_4	203/0.2	10.4%/100	432
Graphene foam/VO_2 nanoflakes/hydrogen molybdenum bronze composites	1 M K_2SO_4	485/2	97.5%/5000	433
		306/32		
VO_2 microarrays	1 M Na_2SO_4	265/1	100%/3000	434
VO_2@polyaniline coaxial nanobelts	0.5 M Na_2SO_4	246/0.5	28.6%/1000	435
V_4O_9 nanosheets	1.5 M KOH	392/0.5	75%/2000	373
V_6O_{13}@C	1 M Na_2SO_4	545/0.5	88.3%/2000	436
V_6O_{13} sheets	1 M $NaNO_3$	285/0.05	96.7%/300	437
V_6O_{13}	1 M $LiNO_3$	456/0.6	65%/2000	438
Sulfur-doped V_6O_{13-x}@C	5 M LiCl	1353/1.9	92.3%/10000	439
RuO_2 nanoparticle decorated V_2O_5 nanoflakes	1 M KCl	421/1	94.6%/10000	315
Graphene nanoribbons @ V_2O_5 nanostrips	0.5 M Na_2SO_4	335.8/1	∼98.5%/10000	316
N-doped carbon nanofibers/V_2O_5 core/shell	1 M Na_2SO_4	595.1/0.5	97%/12000	317
Interconnected V_2O_5 Nanoporous Network	0.5 M K_2SO_4	304/0.1	24%/600	440
V_2O_5/rGO nanocomposites	8 M LiCl	537/1	84%/1000	441
V_2O_5/rGO hybrids	1 M Na_2SO_4	468.5/1	91.5%/10000	442
V_2O_5/graphene hybrid aerogels	1 M Na_2SO_4	486/0.5	90%/20000	273
V_2O_5/rGO composite hydrogel	0.5 M Na_2SO_4	320/1	70%/1000	443
Carbon coated V_2O_5 nanorods	0.5 M K_2SO_4	417/0.5	76%/1000	444
		341/10		
Hollow spherical V_2O_5	5 M $LiNO_3$	559/3	70%/100	445
V_2O_5 nanorods	1 M $LiClO_4$	347/1	94.3%/10000	446
V_2O_5 nanorods/rGO	0.75 M $NaPF_6$	289/0.01	85%/1000	447
V_2O_5 nanosheets/rGO	1 M KCl	635/1	94%/3000	448
V_2O_5 nanobelts	1 M $LiClO_4$/ PPC	132.5/1	95%/500	449
V_2O_5 nanobelts/rGO	0.5 M K_2SO_4	310.1/1	90.2%/5000	319
V_2O_5 microtubules	1 M $LiNO_3$	680/1	70%/10000	271
V_2O_5 nanoparticles	1 M $LiClO_4$/ PPC	545/1	70%/500	450
V_2O_5/graphene hybrid	1 M Na_2SO_4	484/0.6	80%/10000	451
V_2O_5/graphene hybrid aerogel composite	1 M $LiClO_4$/ PPC	384/0.1	82.2%/10000	452
		197/2		
V_2O_5/MWCNT core/shell hybrid aerogels	1 M Na_2SO_4	625/0.5	120%/20000	453
Carbon coated flowery V_2O_5	1 M K_2SO_4	417/0.5	100%/2000	454
V_2O_5/mesoporous carbon microspheres	1 M $Al_2(SO_4)_3$	290/0.5	88%/10000	455
Graphene-wrapped V_2O_5 nanospheres	1 M Na_2SO_4	612.5/1	89.6%/10000	456
V_2O_5/polypyrrole	5 M $LiNO_3$	448/0.8	81%/1000	457
V_2O_5/polyaniline	0.5 M $LiClO_4$/ PPC	1115/1	90%/4000	458
V_2O_5@Ni_3S_2	1 M KOH	854/1	60%/1000	330
V_2O_5/$Na_{0.33}V_2O_5$	1 M $LiClO_4$	334/1	96%/1000	459
V_2O_5/TiO_2	1 M $LiNO_3$	587/0.5	92%/5000	460
V_2O_5 nanowire arrays/N-doped graphene aerogel	8 M LiCl	710/0.5	95%/20000	461
V_2O_5 nanofibers/conductive polymer	1 M Na_2SO_4	614/0.5	111%/15000	462
V_2O_5/nanoporous carbon network	0.5 M K_2SO_4	314.6/0.2	89.5%/5000	463
V_2O_5/Ni foam	1 M KOH	399.7/0.01	96.1%/2000	464
V_2O_5/WO_3	1 M H_2SO_4	386/0.1	104%/5000	465

https://doi.org/10.1021/acs.chemrev.2c00546
Chem. Rev. 2023, 123, 4353−4415

Table 2. continued

materials	electrolyte	Specific capacitance (F g^{-1})/Current density (A g^{-1})	Retention (%)/Cycle numbers	ref
V_2O_5/g-C_3N_4	1 M KOH	192.3/0.5	85.7%/5000	466
V_2O_5@Ti	1 M LiCl	1520/1.5	99%/12000	467
V_2O_5/vertically aligned CNT	1 M Na_2SO_4	284/2	76%/5000	468
V_2O_5 nanosheets/carbon fiber felt	5 M LiCl	475.5/1	89.7%/6000	469

Table 3. A Brief Survey of Typical Vanadium Oxides Electrocatalysts

catalyst	catalyst type	electrolyte	η @ j = 10 mA cm^{-2} (mV)	Tafel slope (mV dec^{-1})	stability (cycle number or time @ current density)	ref
V_2O_3/ MoS_x /CC	HER	0.5 M H_2SO_4	146	45	1000 cycles	82
NiFe@V_2O_3	HER	1 M KOH	84	85	24 h @ 10 mA cm^{-2}	80
NiFe@V_2O_3	OER	1 M KOH	255	51	1000 cycles 24 h @ 10 mA cm^{-2}	80
$Ni_{0.8}/V_2O_3$	HER	1 M KOH	44	38	24 h @ 10 mA cm^{-2}	470
V_2O_3−Ni_3N	HER	1 M KOH	57	50	24 h @ 10 mA cm^{-2}	471
V_2O_3@Ni	HER	1 M KOH	47	74	1000 cycles 10 h @ 10 mA cm^{-2}	472
V_2O_3−$CoFe_2O_4$	HER	1 M KOH	61	58	80 h @ 500 mA cm^{-2}	473
V_2O_3−$CoFe_2O_4$	OER	1 M KOH	226	56	80 h @ 500 mA cm^{-2}	473
Ni_4Mo−V_2O_3	HER	1 M PBS	40	66	1000 cycles 5.5 h @ 50 mA cm^{-2}	474
MoS_2/VO_2	HER	0.5 M H_2SO_4	99 @ 1 mA cm^{-2}	85	N. A.	245
Ni_3S_2/VO_2	HER	1 M KOH	100	114	15 h @ 10 mA cm^{-2}	244
Ni_3S_2/VO_2	OER	1 M KOH	150	47	15 h @ 10 mA cm^{-2}	244
Co_3O_4/VO_2/CC	HER	1 M KOH	108	98	10 h @ 10 mA cm^{-2}	246
porous VO_2 nanosheets	HER	0.5 M H_2SO_4	184	70	120 h @ 90 mA cm^{-2}	247
porous VO_2 nanosheets	OER	1 M KOH	209	92	120 h @ 70 mA cm^{-2}	247
CoV_2O_6 - V_2O_5/NRGO	OER	1 M KOH	239	50	1000 cycles	320
Co−V_2O_5	HER	1 M KOH	51	42	24 h @ 10 mA cm^{-2}	328
V_2O_5/$Ni(OH)_2$@NF	HER	1 M KOH	39	44	10000 cycles	329
Pt (P)−V_2O_5/graphene	HER	0.5 M H_2SO_4	32	23	1000 cycles	331
V_2O_5@Ni_3S_2	HER	1 M KOH	95	108	9000 cycles	330
Ni−Co−P/V_2O_5−TiO_2/GO	HER	1 M KOH	101 @ 100 mA cm^{-2}	36	N. A.	475
Zn-VO_x-Co	HER	1 M KOH	46	75	36 h @ 100 mA cm^{-2}	398
Ni(Cu)VO_x	HER	1 M KOH	21	28	125 h @ 100 mA cm^{-2}	397
VO_x/NiS/NF	OER	1 M KOH	330 @ 50 mA cm^{-2}	121	1000 cycles	399
Co-VO_x-P	HER	1 M KOH	98	59	1000 cycles 24 h @ 30 mA cm^{-2}	400
Co-VO_x-P	OER	1 M KOH	230 @ 100 mA cm^{-2}	64	1000 cycles 25 h @ 100 mA cm^{-2}	400
VO_x@NiFe/NiCoP/TM	HER	1 M KOH	45	34	1000 cycles 16 h @ 100 mA cm^{-2}	476
VO_x@NiFe/NiCoP/TM	OER	1 M KOH	215	37	20 h @ 500 mA cm^{-2}	476
Co(VO_x)	HER	1 M KOH	178 @ 100 mA cm^{-2}	40	60 h @ 100 mA cm^{-2}	477

structure directly onto the Ni foam. The as-prepared materials demonstrated excellent catalytic performance for both the HER (an overpotential of 98 mV at 10 mA cm^{-2} and a Tafel slope of 59 mV dec^{-1}) and OER (an overpotential of 230 mV at 100 mA cm^{-2} and a Tafel slope of 64 mV dec^{-1}) under an alkaline environment.

9. CONCLUSIONS AND FUTURE OUTLOOK

In the past two decades, there has been accelerated development of vanadium oxides due to the fact that they are the most promising candidates in versatile applications, such as batteries, energy saving smart windows, sensing, catalysts, optoelectronic devices, etc. In this review, we have discussed the V−O binary phase diagram, the structure and synthesis methods of five thermodynamically stable vanadium oxides (V_2O_3, V_3O_5, VO_2, V_3O_7, V_2O_5) and some metastable vanadium oxides (V_2O_2, V_4O_9, V_6O_{13}) with selected applications on hydrogen evolution catalysis, supercapacitors, batteries, smart windows, and some other aspects. The battery, supercapacitor, and HER/OER performances of these vanadium oxides are summarized for comparison to provide an overview of the research in the field (Tables 1, 2, and 3).

While vanadium oxides are important materials for many applications, more detailed, mechanistic and systematical studies are needed to fully explore their potential as the bottleneck is increasingly related to the materials' quality and device fabrications. We propose a few future works in this field

https://doi.org/10.1021/acs.chemrev.2c00546
Chem. Rev. 2023, 123, 4353−4415

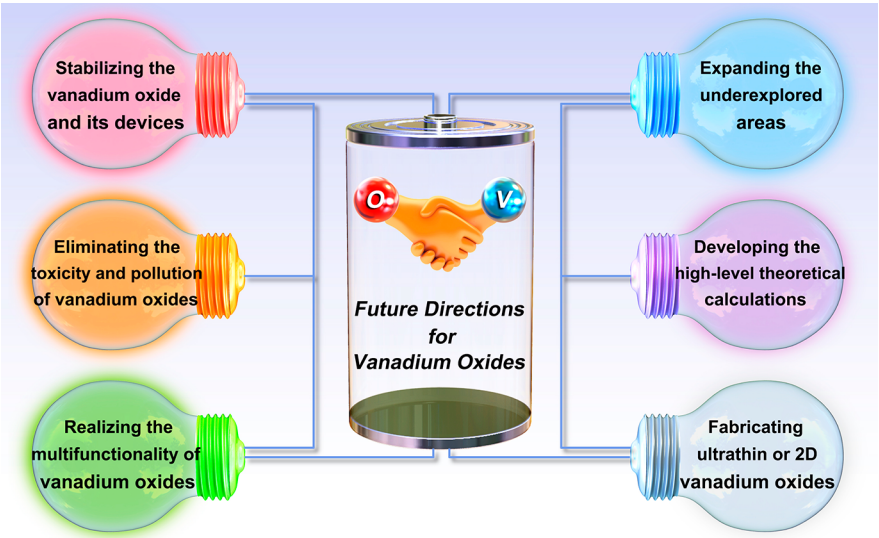

Figure 51. Future development and research directions for vanadium oxides.

which could be further developed in the following aspects (Figure 51):

(1) Searching the applications of vanadium oxides in underexplored areas. One example is biological thermal imaging by leveraging its thermal phase transition characteristics as the insulator-to-metal phase transition of some vanadium oxides gives sharply enhanced optical absorption above their critical temperature. It has potential applications in biochemistry, especially in the fields of bioimaging. Another example is that some nanostructured vanadium oxides also possess optimal physicochemical properties (e.g., optical, thermal, magnetic properties), which give the opportunity to be applied in intelligent medicine based on micro-/nanorobots.

(2) Development of high-level theoretical calculations to guide the rational design of vanadium oxides and their composites and to better understand the fundamentals of high-performance devices. The use of advanced computational tools and theories enables researchers to understand the origin of complex and interacting phenomena at multiple scales, which could accelerate our understanding of the fundamentals of high-performance devices and improve the operation and design of new materials systems. Additionally, machine learning is a useful toolkit for designing and exploring new vanadium oxides with desired properties. It can also aid the understanding of the complex correlations between structures and properties in vanadium oxides.

(3) Fabrication of ultrathin or two-dimensional vanadium oxides, which could be applied in some new electronic devices. Owing to the atomic-scale thickness of single layers, the 2D materials exhibit tunable electrical properties and bandgaps. Therefore, the 2D vanadium oxides may hold promise for a wide range of applications in low-power electronics, flexible electronics, optoelectronics, catalysis, batteries, and so on. Furthermore, the 2D vanadium oxides may also form novel 2D heterostructures with other ultrathin 2D nanomaterials, which would be of certain interest.

(4) Exploration of new approaches to stabilize the vanadium oxides related devices, especially thermal, light, moisture, and oxygen environmental stability. Long-term device stability is one of the most important challenges for all devices. Most vanadium oxides are sensitive to oxygen and moisture, which may lead to the degradation of the device performances. Furthermore, most stability measurements of the devices are performed under ambient conditions, which limits their application in high temperature, high humidity, and high light intensity conditions. Meanwhile, it is also important to understand the degradation mechanisms in the different types of devices based on vanadium oxides, which could be the key to improving the device stabilities.

(5) Exploring new green chemistry synthesis methods to eliminate the toxicity of vanadium oxides. Vanadium oxides cause a variety of toxic effects such as biochemical changes, neurobehavioral injury, and functional lesions in the liver and bones. Especially, vanadium oxides in breathing air can cause pulmonary problems and DNA damage in leukocytes. The toxicity is more related to the phase structure, stoichiometric ratio, concentration, particle size, and crystalline degree, which could be considered in all the processes of application of vanadium oxides. Therefore, exploring new green synthesis methods and avoiding risks to humans and the environment during vanadium oxides' production, use, and disposal processes deserve more systematic and comprehensive studies. First, it is important to develop new synthesis protocols with minimum steps to prepare vanadium oxides, such as one-pot synthesis, completely enclosed-system synthesis, and so on. Second, the encapsulation of the devices to confine the toxicity needs to be considered when designing a new device. Third, the release of vanadium oxides to the atmosphere should be controlled during normal operation. For example, the marked decrease in toxicity is confirmed via silica coating on vanadium oxides due to the perception that the toxicity of vanadium oxide is closely related to the solubility and the robust silica barrier can isolate air and water to reduce the solubility.

https://doi.org/10.1021/acs.chemrev.2c00546
Chem. Rev. 2023, 123, 4353−4415

(6) Realization of the bifunctional, trifunctional, or even multifunctional vanadium oxides to achieve integrated functionality. Different device integrations based on the same materials is expected to greatly reduce the cost and the incompatibility of different materials. Meanwhile, multifunctional materials would reduce the complexity of designing devices and promote the application in designated situations.

Overall, we believe that vanadium oxides are great candidates for future applications in related fields and help solve key challenges in the global warming crisis. Moreover, the integration of vanadium oxides with multidisciplinary fields such as material science, device physics, civil engineering, mechanical design, and bioscience would continue to attract the interest of many scientists from different disciplines for new fascinating fields.

AUTHOR INFORMATION

Corresponding Authors

Yi Long − *School of Materials Science and Engineering, Nanyang Technological University, Singapore 639798, Singapore; Department of Electronic Engineering, The Chinese University of Hong Kong, Hong Kong, SAR 999077, China;* orcid.org/0000-0003-0608-8253; Email: yilong@cuhk.edu.hk

Liqiang Mai − *State Key Laboratory of Advanced Technology for Materials Synthesis and Processing, Wuhan University of Technology, Wuhan 430070 Hubei, China; Foshan Xianhu Laboratory of the Advanced Energy Science and Technology Guangdong Laboratory, Xianhu Hydrogen Valley, Foshan 528200 Guangdong, China;* orcid.org/0000-0003-4259-7725; Email: mlq518@whut.edu.cn

Peng Hu − *School of Physics, Northwest University, Xi'an 710069, P. R. China; School of Materials Science and Engineering, Nanyang Technological University, Singapore 639798, Singapore;* orcid.org/0000-0003-1284-2654; Email: hupeng@nwu.edu.cn

Authors

Ping Hu − *State Key Laboratory of Advanced Technology for Materials Synthesis and Processing, Wuhan University of Technology, Wuhan 430070 Hubei, China; Foshan Xianhu Laboratory of the Advanced Energy Science and Technology Guangdong Laboratory, Xianhu Hydrogen Valley, Foshan 528200 Guangdong, China*

Tuan Duc Vu − *School of Materials Science and Engineering, Nanyang Technological University, Singapore 639798, Singapore*

Ming Li − *Key Laboratory of Materials Physics, Anhui Key Laboratory of Nanomaterials and Nanotechnology, Institute of Solid State Physics, Chinese Academy of Science, Hefei 230031, P. R. China*

Shancheng Wang − *School of Materials Science and Engineering, Nanyang Technological University, Singapore 639798, Singapore*

Yujie Ke − *School of Materials Science and Engineering, Nanyang Technological University, Singapore 639798, Singapore; Institute of Materials Research and Engineering (IMRE), Agency for Science, Technology and Research (A*STAR), Singapore 138634, Republic of Singapore*

Xianting Zeng − *Singapore Institute of Manufacturing Technology (SIMTech), Singapore 138634, Singapore*

Complete contact information is available at: https://pubs.acs.org/10.1021/acs.chemrev.2c00546

Author Contributions

#Peng Hu and Ping Hu contributed equally to this work. CRediT: **Tuan Duc Vu** writing-original draft; **Ming Li** writing-original draft; **Shancheng Wang** writing-original draft; **Yujie Ke** writing-original draft; **Xianting Zeng** supervision; **Liqiang Mai** funding acquisition, supervision, writing-review & editing; **Yi Long** conceptualization, funding acquisition, supervision, writing-review & editing.

Notes

The authors declare no competing financial interest.

Biographies

Peng Hu received his PhD degree (under the guidance of Prof. Christian Kloc) in materials science at Nanyang Technological University, Singapore, in 2016. Then, he was a research fellow at Nanyang Technological University, Singapore, in Prof. Christian Kloc's group (2016−2017) and Dr. Yi Long's group (2017−2018). He is currently a professor in the School of Physics at Northwest University, China. His research interests focus on the single crystal growth of organics, low-dimensional materials and organic−inorganic hybrids, and their electronic, optoelectronic, and energy applications.

Ping Hu received his PhD degree from Wuhan University of Technology in 2020. He is currently a postdoc at Wuhan University of Technology. His research interests focus on advanced electrode materials for electrochemical energy storage devices.

Tuan Duc Vu is a PhD candidate from Nanyang Technological University (NTU) in Dr. Long Yi and Dr. Xianting Zeng's group, School of Materials Science and Engineering. He previously obtained his B.Eng. (Materials) from the same school. In 2018, he received the prestigious A*STAR Graduate Scholarship AGS(S), which funded his PhD candidacy in NTU in collaboration with Singapore Institute of Manufacturing Technology (SIMTech). He specializes in thin film processing using a physical vapor deposition process such as thermal evaporation and magnetron sputtering. His current research focuses on the fabrication of high performance and high durability vanadium dioxide smart window glazing.

Ming Li is an Associate Professor in the Laboratory of Nanomaterials & Nanostructures at the Institute of Solid State Physics, Chinese Academy of Science (ISSP, CAS). He received his PhD in condensed matter physics from the ISSP, CAS. His research focuses on developing thermochromic materials of vanadium oxides for energy-efficient windows. His research topics cover the synthesis of nanomaterials, the regulation of photoelectric properties, and the design of thermochromic devices.

Shancheng Wang is a research fellow at Nanyang Technological University under the supervision of Dr. Yi Long. He obtained his PhD degree from NTU in 2021. His research interests include the synthesis of stimuli-response materials and design of stimuli-response smart structures for optical and thermal applications. In 2021, Shancheng received the MSE Doctorate Technopreneur Award from the School of Materials Science and Engineering, NTU.

Yujie Ke is a scientist at the Institute of Materials Research and Engineering, Agency for Science, Technology and Research (A*STAR) Singapore. He received his Ph.D. from NTU under the supervision of Dr. Long Yi in 2019 and his master's degree from University at Buffalo (SUNY-Buffalo) in 2015. He is interested in phase-change materials,

https://doi.org/10.1021/acs.chemrev.2c00546
Chem. Rev. 2023, 123, 4353−4415

mechano-/thermochromics, plasmonics and photonic crystals, mechanical metamaterials, smart window, and building energy.

Xianting Zeng is Director of the Knowledge Transfer Office (KTO) of the Singapore Institute of Manufacturing Technology (SIMTech), of the Agency for Science, Technology and Research (A*STAR). He obtained his PhD degree in Thin Film Physics from the Chinese University of Hong Kong in 1995, and MSc and BSc degrees from the Huazhong University of Science and Technology, China in 1987 and 1982, respectively. He has been an active research scientist in the fields of nanocomposite coating materials and plasma enhanced PVD thin film processes. After joining SIMTech in 1995, he established the KTO in 2009 to transfer knowledge and capability to industry through case-studies and hands-on practical training to meet the technology and skills gap in productivity improvement, skills, and capabilities upgrading and business transformation.

Liqiang Mai is a Chair Professor of Materials Science and Engineering at the Wuhan University of Technology. He received his PhD degree from Wuhan University of Technology in 2004 and carried out his postdoctoral research at the Georgia Institute of Technology in 2006−2007. He worked as an advanced research scholar at Harvard University in 2008−2011 and the University of California, Berkeley in 2017. His current research interests are focused on new nanomaterials for electrochemical energy storage and micro-/nanoenergy devices.

Yi Long is a Fellow of the Royal Society of Chemistry. She obtained her PhD from the University of Cambridge, UK. She is currently an professor in the Department of Electronic Engineering, The Chinese University of Hong Kong. Her research focuses on nanostructured functional materials for different applications. She has successfully implemented technology transfer from lab to industry for a hard-disk company in her early career. Her recent research is to develop various smart materials by manipulation of the structure at the nanoscale to achieve unusual properties. She is the recipient of GreenAwards Top 3 London and Falling Walls 10 Breakthrough in Engineering and Technology Berlin in 2022.

ACKNOWLEDGMENTS

Peng Hu acknowledges the financial support from the National Natural Science Foundation of China (No. 51803168), the Key Research and Development Program of Shaanxi Province (2022GY-356), and the Youth Innovation Team of Shaanxi Universities. L.M. acknowledges the financial support from the National Key Research and Development Program of China (Grant No. 2020YFA0715000), the National Natural Science Foundation of China (Grant No. 52127816), and the Foshan Xianhu Laboratory of the Advanced Energy Science and Technology Guangdong Laboratory (XHT2020-003). Ping Hu acknowledges the financial support from the Guangdong Basic and Applied Basic Research Foundation (2021A1515110059). Y.L. would like to acknowledge the funding support from MOE-T2EP50221-0014, Ministry of Education, Singapore. Y.L. would like to acknowledge the funding support from MOE-T2EP50221-0014, Minster of Education, Singapore and Global STEM Professorship Scheme sponsored by the Government of the Hong Kong Special Administrative Region.

ABBREVIATIONS

1D = one-dimensional
2D = two-dimensional
3D = three-dimensional
4D = four-dimensional
AACVD = aerosol-assisted chemical vapor deposition
AC = activated carbon
AFM = atomic force microscope
AIB = aluminum-ion battery
ALD = atomic layer deposition
AM 1.5 = air mass 1.5
BP = black paint
CC = carbon cloth
C_{dl} = double-layer capacitance
CIB = calcium-ion battery
CNC = carbon nanocoils
CNT = carbon nanotube
CV = cyclic voltammetry
CVD = chemical vapor deposition
DC = direct current
DFT = density functional theory
DNA = DNA
EBD = electron-beam deposition
EN = ethylenediamine
GCD = galvanostatic charge/discharge
GF = graphene foam
GITT = galvanostatic intermittent titration technique
GQD = graphene quantum dot
GVG = graphene foam supported graphene quantum dot anchored VO_2 arrays
FeFET = ferroelectric field-effect transistor
FET = field-effect transistor
GO = graphene oxide
HCP = high concentration dilution
HER = hydrogen evolution reaction
High-E = high emissivity
HM = hollow microclew
IL = ionic liquid
IR = infrared
ITO = indium tin oxide
KIB = potassium-ion battery
LCP = low concentration dilution
LED = light emitting diode
LIB = lithium-ion battery
LiTFSI = lithium bis-trifluoromethanesulfonimide
Low-E = low emissivity
LWIR = longwave infrared
LSPR = localized surface plasmonic resonance
MAS NMR = magic-angle-spinning nuclear magnetic resonance
MB = methylene blue
MCE = magnetocaloric effect
MD = molecular dynamics
MEMS = microelectromechanical systems
MIB = magnesium-ion battery
MIT = metal−insulator transition
MO = methyl orange
MWCNT = multiwalled carbon nanotube
N.A. = not applicable
NaTFSI = sodium bis-trifluoromethanesulfonimide
NDR = negative differential resistance
NF = Ni foam
NIB = ammonium-ion battery
NIR = near-infrared
NMR = nuclear magnetic resonance
NP = nanoparticle
NRGO = nitrogen-doped reduced graphene oxide
NW = nanowire

https://doi.org/10.1021/acs.chemrev.2c00546
Chem. Rev. 2023, 123, 4353−4415

OER = oxygen evolution reaction
PBS = phosphate-buffered saline
PDMS = polydimethylsiloxane
PEDOT = poly(3,4-ethylenedioxythiophene)
PEG = polyethylene glycol
PLD = pulsed laser deposition
PNCNF = porous N-doped carbon nanofiber
PPC = propylene carbonate
PS = polystyrene
PVA = poly(vinyl alcohol)
PVC = polyvinyl chloride
PVD = physical vapor deposition
PVDF-HFP = polyvinylidene fluoride-hexafluoropropylene
PVP = polyvinylpyrrolidone
PZT = $Pb(Zr_{0.52}Ti_{0.48})O_3$
RC = radiative cooling
RCRT = radiative cooling regulating thermochromic
ReRAM = resistive random-access memory
rGO = reduced graphene oxide
RhB = rhodamine B
RF = radio frequency
RT = room temperature
SA-VO_2 = surface amorphized VO_2
SC = supercapacitor
SCE = saturated calomel electrode
SCVA = single-crystalline VO_2 actuator
SEM = scanning electron microscope
SHE = standard hydrogen electrode
SIB = sodium-ion battery
SWCNT = single- or multiwalled carbon nanotube
TARC = temperature-adaptive radiative coating
TEM = transmission electron microscope
TGA = thermogravimetric analysis
TM = titanium mesh
UGF = ultrathin graphite foam
UHV = ultrahigh vacuum
UV−vis−NIR = ultraviolet−visible-near-infrared
VOG = $V_2O_5{\cdot}H_2O$/graphene
VGS = V_3O_7 nanowire templated graphene scroll
V_2O_3@NC = nitrogen-doped carbon-confined V_2O_3
XANES = X-ray absorption near edge structure
XPS = X-ray photoelectron spectroscopy
XRD = X-ray diffraction
ZIB = zinc-ion battery

REFERENCES

(1) Moskalyk, R. R.; Alfantazi, A. M. Processing of Vanadium: a Review. *Miner. Eng.* **2003**, *16*, 793−805.
(2) Sutradhar, M.; Da Silva, J. A. L.; Pombeiro, A. J. L. Chapter 1 Introduction: Vanadium, Its Compounds and Applications. In *Vanadium Catalysis*; The Royal Society of Chemistry, 2021; pp 1−11.
(3) Langeslay, R. R.; Kaphan, D. M.; Marshall, C. L.; Stair, P. C.; Sattelberger, A. P.; Delferro, M. Catalytic Applications of Vanadium: A Mechanistic Perspective. *Chem. Rev.* **2019**, *119*, 2128−2191.
(4) Liu, M.; Su, B.; Tang, Y.; Jiang, X.; Yu, A. Recent Advances in Nanostructured Vanadium Oxides and Composites for Energy Conversion. *Adv. Energy Mater.* **2017**, *7*, 1700885.
(5) Wu, C.; Xie, Y. Promising Vanadium Oxide and Hydroxide Nanostructures: from Energy Storage to Energy Saving. *Energy Environ. Sci.* **2010**, *3*, 1191−1206.
(6) Kianfar, E. Recent Advances in Synthesis, Properties, and Applications of Vanadium Oxide Nanotube. *Microchem. J.* **2019**, *145*, 966−978.
(7) Wang, Y.; Cao, G. Synthesis and Enhanced Intercalation Properties of Nanostructured Vanadium Oxides. *Chem. Mater.* **2006**, *18*, 2787−2804.
(8) Wang, Y.; Cao, G. Developments in Nanostructured Cathode Materials for High-Performance Lithium-Ion Batteries. *Adv. Mater.* **2008**, *20*, 2251−2269.
(9) Rehder, D. The Future of/for Vanadium. *Dalton Trans.* **2013**, *42*, 11749−11761.
(10) Lamsal, C.; Ravindra, N. M. Vanadium Oxides: Synthesis, Properties, and Applications. In *Semiconductors: Synthesis, Properties and Applications*; Pech-Canul, M. I., Ravindra, N. M., Eds.; Springer International Publishing, 2019; pp 127−218.
(11) Cotton, F. A.; Wilkinson, G.; Murillo, C. A.; Bochmann, M. *Advanced Inorganic Chemistry*; John Wiley & Sons: New York, 1999.
(12) Prasadam, V. P.; Bahlawane, N.; Mattelaer, F.; Rampelberg, G.; Detavernier, C.; Fang, L.; Jiang, Y.; Martens, K.; Parkin, I. P.; Papakonstantinou, I. Atomic Layer Deposition of Vanadium Oxides: Process and Application Review. *Mater. Today Chem.* **2019**, *12*, 396−423.
(13) Wei, J.; Ji, H.; Guo, W.; Nevidomskyy, A. H.; Natelson, D. Hydrogen Stabilization of Metallic Vanadium Dioxide in Single-Crystal Nanobeams. *Nat. Nanotechnol.* **2012**, *7*, 357−362.
(14) Jang, H. W.; Felker, D. A.; Bark, C. W.; Wang, Y.; Niranjan, M. K.; Nelson, C. T.; Zhang, Y.; Su, D.; Folkman, C. M.; Baek, S. H.; et al. Metallic and Insulating Oxide Interfaces Controlled by Electronic Correlations. *Science* **2011**, *331*, 886−889.
(15) Lee, J. H.; Kim, J.-M.; Kim, J.-H.; Jang, Y.-R.; Kim, J. A.; Yeon, S.-H.; Lee, S.-Y. Energy Storage: Toward Ultrahigh-Capacity V_2O_5 Lithium-Ion Battery Cathodes via One-Pot Synthetic Route from Precursors to Electrode Sheets. *Adv. Mater. Interfaces* **2016**, *3*, 1600173.
(16) Cao, A.-M.; Hu, J.-S.; Liang, H.-P.; Wan, L.-J. Self-Assembled Vanadium Pentoxide (V_2O_5) Hollow Microspheres from Nanorods and Their Application in Lithium-Ion Batteries. *Angew. Chem., Int. Ed.* **2005**, *44*, 4391−4395.
(17) Liu, G.; Yu, J. C.; Lu, G. Q.; Cheng, H.-M. Crystal Facet Engineering of Semiconductor Photocatalysts: Motivations, Advances and Unique Properties. *Chem. Commun.* **2011**, *47*, 6763−6783.
(18) Foo, C. Y.; Sumboja, A.; Tan, D. J. H.; Wang, J.; Lee, P. S. Flexible and Highly Scalable V_2O_5-rGO Electrodes in an Organic Electrolyte for Supercapacitor Devices. *Adv. Energy Mater.* **2014**, *4*, 1400236.
(19) Wang, S.; Owusu, K. A.; Mai, L.; Ke, Y.; Zhou, Y.; Hu, P.; Magdassi, S.; Long, Y. Vanadium Dioxide for Energy Conservation and Energy Storage Applications: Synthesis and Performance Improvement. *Appl. Energy* **2018**, *211*, 200−217.
(20) Wu, C.; Feng, F.; Xie, Y. Design of Vanadium Oxide Structures with Controllable Electrical Properties for Energy Applications. *Chem. Soc. Rev.* **2013**, *42*, 5157−5183.
(21) Xu, X.; Xiong, F.; Meng, J.; Wang, X.; Niu, C.; An, Q.; Mai, L. Vanadium-Based Nanomaterials: A Promising Family for Emerging Metal-Ion Batteries. *Adv. Funct. Mater.* **2020**, *30*, 1904398.
(22) McNulty, D.; Buckley, D. N.; O'Dwyer, C. Synthesis and Electrochemical Properties of Vanadium Oxide Materials and Structures as Li-Ion Battery Positive Electrodes. *J. Power Sources* **2014**, *267*, 831−873.
(23) Armer, C. F.; Yeoh, J. S.; Li, X.; Lowe, A. Electrospun Vanadium-Based Oxides as Electrode Materials. *J. Power Sources* **2018**, *395*, 414−429.
(24) Cheng, Y.; Xia, Y.; Chen, Y.; Liu, Q.; Ge, T.; Xu, L.; Mai, L. Vanadium-Based Nanowires for Sodium-Ion Batteries. *Nanotechnology* **2019**, *30*, 192001.
(25) Cheng, F.; Chen, J. Transition Metal Vanadium Oxides and Vanadate Materials for Lithium Batteries. *J. Mater. Chem.* **2011**, *21*, 9841−9848.
(26) Gonçalves, J. M.; Ireno da Silva, M.; Angnes, L.; Araki, K. Vanadium-Containing Electro and Photocatalysts for the Oxygen Evolution Reaction: a Review. *J. Mater. Chem. A* **2020**, *8*, 2171−2206.
(27) Ke, Y.; Wang, S.; Liu, G.; Li, M.; White, T. J.; Long, Y. Vanadium Dioxide: The Multistimuli Responsive Material and Its Applications. *Small* **2018**, *14*, 1802025.

https://doi.org/10.1021/acs.chemrev.2c00546
Chem. Rev. 2023, 123, 4353−4415

(28) Ke, Y.; Yin, Y.; Zhang, Q.; Tan, Y.; Hu, P.; Wang, S.; Tang, Y.; Zhou, Y.; Wen, X.; Wu, S.; et al. Adaptive Thermochromic Windows from Active Plasmonic Elastomers. *Joule* **2019**, *3*, 858−871.
(29) Chen, D.; Li, J.; Wu, Q. Review of V_2O_5-Based Nanomaterials as Electrode for Supercapacitor. *J. Nanopart. Res.* **2019**, *21*, 201.
(30) Qin, H.; Liang, S.; Chen, L.; Li, Y.; Luo, Z.; Chen, S. Recent Advances in Vanadium-based Nanomaterials and their Composites for Supercapacitors. *Sustain. Energy Fuels* **2020**, *4*, 4902−4933.
(31) Mounasamy, V.; Mani, G. K.; Madanagurusamy, S. Vanadium Oxide Nanostructures for Chemiresistive Gas and Vapour Sensing: a Review on State of the Art. *Microchim. Acta* **2020**, *187*, 253.
(32) Morin, F. J. Oxides Which Show a Metal-to-Insulator Transition at the Neel Temperature. *Phys. Rev. Lett.* **1959**, *3*, 34−36.
(33) Zylbersztejn, A.; Mott, N. F. Metal-Insulator Transition in Vanadium Dioxide. *Phys. Rev. B* **1975**, *11*, 4383−4395.
(34) Nadkarni, G. S.; Shirodkar, V. S. Experiment and Theory for Switching in Al/V_2O_5/Al Devices. *Thin Solid Films* **1983**, *105*, 115−129.
(35) Kosuge, K.; Takada, T.; Kachi, S. Phase Diagram and Magnetism of V_2O_3-V_2O_5 System. *J. Phys. Soc. Jpn.* **1963**, *18*, 318−319.
(36) Heidemann, A.; Kosuge, K.; Ueda, Y.; Kachi, S. Hyperfine Interaction in V_3O_7. *Phys. Status Solidi A* **1977**, *39*, K37−K40.
(37) Schwingenschlögl, U.; Eyert, V. The Vanadium Magnéli Phases V_nO_{2n-1}. *Ann. Phys.* **2004**, *516*, 475−510.
(38) Selbin, J. The Chemistry of Oxovanadium(IV). *Chem. Rev.* **1965**, *65*, 153−175.
(39) Chirayil, T.; Zavalij, P. Y.; Whittingham, M. S. Hydrothermal Synthesis of Vanadium Oxides. *Chem. Mater.* **1998**, *10*, 2629−2640.
(40) Livage, J. Hydrothermal Synthesis of Nanostructured Vanadium Oxides. *Materials* **2010**, *3*, 4175−4195.
(41) Bahlawane, N.; Lenoble, D. Vanadium Oxide Compounds: Structure, Properties, and Growth from the Gas Phase. *Chem. Vap. Deposition* **2014**, *20*, 299−311.
(42) Hess, C. Nanostructured Vanadium Oxide Model Catalysts for Selective Oxidation Reactions. *ChemPhysChem* **2009**, *10*, 319−326.
(43) Carrero, C. A.; Schloegl, R.; Wachs, I. E.; Schomaecker, R. Critical Literature Review of the Kinetics for the Oxidative Dehydrogenation of Propane over Well-Defined Supported Vanadium Oxide Catalysts. *ACS Catal.* **2014**, *4*, 3357−3380.
(44) Artiglia, L.; Agnoli, S.; Granozzi, G. Vanadium Oxide Nanostructures on Another Oxide: The Viewpoint from Model Catalysts Studies. *Coord. Chem. Rev.* **2015**, *301*−*302*, 106−122.
(45) Shvets, P.; Dikaya, O.; Maksimova, K.; Goikhman, A. A Review of Raman Spectroscopy of Vanadium Oxides. *J. Raman Spectrosc.* **2019**, *50*, 1226−1244.
(46) Amiri, V.; Roshan, H.; Mirzaei, A.; Sheikhi, M. H. A Review of Nanostructured Resistive-based Vanadium Oxide Gas Sensors. *Chemosensors* **2020**, *8*, 105.
(47) Anjass, M.; Lowe, G. A.; Streb, C. Molecular Vanadium Oxides for Energy Conversion and Energy Storage: Current Trends and Emerging Opportunities. *Angew. Chem., Int. Ed.* **2021**, *60*, 7522−7532.
(48) Mai, L.; Xu, X.; Xu, L.; Han, C.; Luo, Y. Vanadium Oxide Nanowires for Li-Ion Batteries. *J. Mater. Res.* **2011**, *26*, 2175−2185.
(49) Chernova, N. A.; Roppolo, M.; Dillon, A. C.; Whittingham, M. S. Layered Vanadium and Molybdenum Oxides: Batteries and Electrochromics. *J. Mater. Chem.* **2009**, *19*, 2526−2552.
(50) Rashad, M.; Asif, M.; Ahmed, I.; He, Z.; Yin, L.; Wei, Z. X.; Wang, Y. Quest for Carbon and Vanadium Oxide Based Rechargeable Magnesium-Ion Batteries. *J. Magnes. Alloy.* **2020**, *8*, 364−373.
(51) Johnston, B.; Henry, H.; Kim, N.; Lee, S. B. Mechanisms of Water-Stimulated Mg2+ Intercalation in Vanadium Oxide: Toward the Development of Hydrated Vanadium Oxide Cathodes for Mg Batteries. *Front. Energy Res.* **2021**, *8*, 611391.
(52) Li, Y.; Zhang, D.; Huang, S.; Yang, H. Y. Guest-Species-Incorporation in Manganese/Vanadium-based Oxides: Towards High Performance Aqueous Zinc-Ion Batteries. *Nano Energy* **2021**, *85*, 105969.
(53) Zhang, X.; Sun, X.; Li, X.; Hu, X.; Cai, S.; Zheng, C. Recent Progress in Rate and Cycling Performance Modifications of Vanadium Oxides Cathode for Lithium-Ion Batteries. *J. Energy Chem.* **2021**, *59*, 343−363.
(54) Mathew, V.; Sambandam, B.; Kim, S.; Kim, S.; Park, S.; Lee, S.; Alfaruqi, M. H.; Soundharrajan, V.; Islam, S.; Putro, D. Y.; et al. Manganese and Vanadium Oxide Cathodes for Aqueous Rechargeable Zinc-Ion Batteries: A Focused View on Performance, Mechanism, and Developments. *ACS Energy Lett.* **2020**, *5*, 2376−2400.
(55) Liu, Z.; Sun, H.; Qin, L.; Cao, X.; Zhou, J.; Pan, A.; Fang, G.; Liang, S. Interlayer Doping in Layered Vanadium Oxides for Low-cost Energy Storage: Sodium-Ion Batteries and Aqueous Zinc-Ion Batteries. *ChemNanoMat* **2020**, *6*, 1553−1566.
(56) Jia, X.; Liu, C.; Neale, Z. G.; Yang, J.; Cao, G. Active Materials for Aqueous Zinc Ion Batteries: Synthesis, Crystal Structure, Morphology, and Electrochemistry. *Chem. Rev.* **2020**, *120*, 7795−7866.
(57) Banerjee, J.; Dutta, K. An Overview on the Use of Metal Vanadium Oxides and Vanadates in Supercapacitors and Rechargeable Batteries. *Int. J. Energy Res.* **2022**, *46*, 3983−4000.
(58) Ke, Y.; Chen, J.; Lin, G.; Wang, S.; Zhou, Y.; Yin, J.; Lee, P. S.; Long, Y. Smart Windows: Electro-, Thermo-, Mechano-, Photochromics, and Beyond. *Adv. Energy Mater.* **2019**, *9*, 1902066.
(59) Ke, Y. J.; Ye, S. S.; Hu, P.; Jiang, H.; Wang, S. C.; Yang, B.; Zhang, J. H.; Long, Y. Unpacking the Toolbox of Two-Dimensional Nanostructures Derived from Nanosphere Templates. *Mater. Horizons* **2019**, *6*, 1380−1408.
(60) Wriedt, H. A. The O-V (Oxygen-Vanadium) System. *Bull. Alloy Phase Diagrams* **1989**, *10*, 271−277.
(61) Cao, Z.; Li, S.; Xie, W.; Du, G.; Qiao, Z. Critical Evaluation and Thermodynamic Optimization of the V-O System. *CALPHAD* **2015**, *51*, 241−251.
(62) Yang, Y.; Mao, H.; Selleby, M. Thermodynamic Assessment of the V-O System. *CALPHAD* **2015**, *51*, 144−160.
(63) Davydov, D. A.; Rempel, A. A. Refinement of the V-O Phase Diagram in the Range 25−50 at% Oxygen. *Inorg. Mater.* **2009**, *45*, 47−54.
(64) Katzke, H.; Tolédano, P.; Depmeier, W. Theory of Morphotropic Transformations in Vanadium Oxides. *Phys. Rev. B* **2003**, *68*, 024109.
(65) Magnéli, A. The Crystal Structures of Mo_9O_{26} (Beta'-Molybdenum Oxide) and Mo_8O_{23} (Beta-Molybdenum Oxide). *Acta Chem. Scand.* **1948**, *2*, 501−517.
(66) Robinson, W. High-Temperature Crystal Chemistry of V_2O_3 and 1% Chromium-Doped V_2O_3. *Acta. Crystallogr. B* **1975**, *31*, 1153−1160.
(67) Zhu, K.; Wei, S.; Shou, H.; Shen, F.; Chen, S.; Zhang, P.; Wang, C.; Cao, Y.; Guo, X.; Luo, M.; Zhang, H.; Ye, B.; Wu, X.; He, L.; Song, L.; et al. Defect Engineering on V_2O_3 Cathode for long-Cycling Aqueous Zinc Metal Batteries. *Nat. Commun.* **2021**, *12*, 6878.
(68) Jin, T.; Li, H.; Li, Y.; Jiao, L.; Chen, J. Intercalation Pseudocapacitance in Flexible and Self-Standing V_2O_3 Porous Nanofibers for High-Rate and Ultra-Stable K Ion Storage. *Nano Energy* **2018**, *50*, 462−467.
(69) Kong, F. Y.; Li, M.; Li, D. B.; Xu, Y.; Zhang, Y. X.; Li, G. H. Synthesis and Characterization of V_2O_3 Nanocrystals by Plasma Hydrogen Reduction. *J. Cryst. Growth* **2012**, *346*, 22−26.
(70) Corr, S. A.; Grossman, M.; Furman, J. D.; Melot, B. C.; Cheetham, A. K.; Heier, K. R.; Seshadri, R. Controlled Reduction of Vanadium Oxide Nanoscrolls: Crystal Structure, Morphology, and Electrical Properties. *Chem. Mater.* **2008**, *20*, 6396−6404.
(71) Qi, J.; Ning, G.; Zhao, Y.; Tian, M.; Xu, Y.; Hai, H. Synthesis and Characterization of V_2O_3 Microcrystal Particles Controlled by Thermodynamic Parameters. *Mater. Sci. Poland* **2010**, *28*, 535−543.
(72) Liu, X.; Zhang, Y.; Yi, S.; Huang, C.; Liao, J.; Li, H.; Xiao, D.; Tao, H. Preparation of V_2O_3 Nanopowders by Supercritical Fluid Reduction. *J. Supercrit. Fluid* **2011**, *56*, 194−200.
(73) Mounasamy, V.; Mani, G. K.; Ponnusamy, D.; Tsuchiya, K.; Prasad, A. K.; Madanagurusamy, S. Template-Free Synthesis of Vanadium Sesquioxide (V_2O_3) Nanosheets and Their Room-Temperature Sensing Performance. *J. Mater. Chem. A* **2018**, *6*, 6402−6413.
(74) Pinna, N.; Antonietti, M.; Niederberger, M. A Novel Non-aqueous Route to V_2O_3 and Nb_2O_5 Nanocrystals. *Colloids Surf., A* **2004**, *250*, 211−213.

https://doi.org/10.1021/acs.chemrev.2c00546
Chem. Rev. 2023, 123, 4353−4415

(75) Chen, J.; Liu, X.; Su, Z. Facile Synthesis and Characterisation of Dandelion-Like V_2O_3 Core-Shell Microspheres. *Micro Nano Lett.* **2011**, *6*, 102−105.
(76) Han, C.; Liu, F.; Liu, J.; Li, Q.; Meng, J.; Shao, B.; He, Q.; Wang, X.; Liu, Z.; Mai, L. Facile Template-Free Synthesis of Uniform Carbon-Confined V_2O_3 Hollow Spheres for Stable and Fast Lithium Storage. *J. Mater. Chem. A* **2018**, *6*, 6220−6224.
(77) Luo, H.; Wang, B.; Wang, F.; Yang, J.; Wu, F.; Ning, Y.; Zhou, Y.; Wang, D.; Liu, H.; Dou, S. Anodic Oxidation Strategy toward Structure-Optimized V_2O_3 Cathode via Electrolyte Regulation for Zn-Ion Storage. *ACS Nano* **2020**, *14*, 7328−7337.
(78) Ge, Y.; He, T.; Wang, Z.; Han, D.; Li, J.; Wu, J.; Wu, J. Chemical Looping Oxidation of CH_4 with 99.5% CO Selectivity over V_2O_3-Based Redox Materials Using CO_2 for Regeneration. *AIChE J.* **2020**, *66*, No. e16772.
(79) Zhang, Y.; Zhang, J.; Nie, J.; Zhong, Y.; Liu, X.; Huang, C. Facile Synthesis of V_2O_3/C Composite and the Effect of V_2O_3 and V_2O_3/C on Decomposition of Ammonium Perchlorate. *Micro Nano Lett.* **2012**, *7*, 782−785.
(80) Xu, H.; Liu, L.; Gao, J.; Du, P.; Fang, G.; Qiu, H.-J. Hierarchical Nanoporous V_2O_3 Nanosheets Anchored with Alloy Nanoparticles for Efficient Electrocatalysis. *ACS Appl. Mater. Interfaces* **2019**, *11*, 38746−38753.
(81) Zhang, J.; Zhou, R.-J.; Chang, Q.-Y.; Sui, Z.-J.; Zhou, X.-G.; Chen, D.; Zhu, Y.-A. Tailoring Catalytic Properties of V_2O_3 to Propane Dehydrogenation through Single-Atom Doping: A DFT Study. *Catal. Today* **2021**, *368*, 46−57.
(82) Hu, M.; Huang, J.; Li, Q.; Tu, R.; Zhang, S.; Yang, M.; Li, H.; Goto, T.; Zhang, L. Self-Supported MoS_x/V_2O_3 Heterostructures as Efficient Hybrid Catalysts for Hydrogen Evolution Reaction. *J. Alloys Compd.* **2020**, *827*, 154262.
(83) Zhai, W.; Ma, Y.; Chen, D.; Ho, J. C.; Dai, Z.; Qu, Y. Recent Progress on the Long-Term Stability of Hydrogen Evolution Reaction Electrocatalysts. *InfoMat* **2022**, *4*, No. e12357.
(84) Shi, F.; Gao, W.; Shan, H.; Li, F.; Xiong, Y.; Peng, J.; Xiang, Q.; Chen, W.; Tao, P.; Song, C.; et al. Strain-Induced Corrosion Kinetics at Nanoscale Are Revealed in Liquid: Enabling Control of Corrosion Dynamics of Electrocatalysis. *Chem.* **2020**, *6*, 2257−2271.
(85) Masa, J.; Andronescu, C.; Schuhmann, W. Electrocatalysis as the Nexus for Sustainable Renewable Energy: The Gordian Knot of Activity, Stability, and Selectivity. *Angew. Chem., Int. Ed.* **2020**, *59*, 15298−15312.
(86) Karmodak, N.; Andreussi, O. Catalytic Activity and Stability of Two-Dimensional Materials for the Hydrogen Evolution Reaction. *ACS Energy Lett.* **2020**, *5*, 885−891.
(87) Binninger, T.; Mohamed, R.; Waltar, K.; Fabbri, E.; Levecque, P.; Kötz, R.; Schmidt, T. J. Thermodynamic Explanation of the Universal Correlation Between Oxygen Evolution Activity and Corrosion of Oxide Catalysts. *Sci. Rep.* **2015**, *5*, 12167.
(88) Mauger, A.; Julien, C. M. V_2O_5 Thin Films for Energy Storage and Conversion. *AIMS Mater. Sci.* **2018**, *5*, 349−401.
(89) Huang, A. L.; El-Kady, M. F.; Chang, X. Y.; Anderson, M.; Lin, C. W.; Turner, C. L.; Kaner, R. B. Facile Fabrication of Multivalent VO_x/Graphene Nanocomposite Electrodes for High-Energy-Density Symmetric Supercapacitors. *Adv. Energy Mater.* **2021**, *11*, 2100768.
(90) Pan, X.; Ren, G.; Hoque, M. N. F.; Bayne, S.; Zhu, K.; Fan, Z. Fast Supercapacitors Based on Graphene-Bridged V_2O_3/VO_x Core-Shell Nanostructure Electrodes with a Power Density of 1 MW kg^{-1}. *Adv. Mater. Interfaces* **2014**, *1*, 1400398.
(91) Hassan, N.; Riaz, J.; Qureshi, M. T.; Razaq, A.; Rahim, M.; Toufiq, A. M.; Shakoor, A. Vanadium Oxide (V_2O_3) for Energy Storage Applications through Hydrothermal Route. *J. Mater. Sci. Mater. Electron.* **2018**, *29*, 16021−16026.
(92) Yan, Y.; Li, B.; Guo, W.; Pang, H.; Xue, H. Vanadium Based Materials as Electrode Materials for High Performance Supercapacitors. *J. Power Sources* **2016**, *329*, 148−169.
(93) Zheng, J.; Zhang, Y.; Meng, C.; Wang, X.; Liu, C.; Bo, M.; Pei, X.; Wei, Y.; Lv, T.; Cao, G. V_2O_3/C Nanocomposites with Interface Defects for Enhanced Intercalation Pseudocapacitance. *Electrochim. Acta* **2019**, *318*, 635−643.
(94) Li, H.-Y.; Jiao, K.; Wang, L.; Wei, C.; Li, X.; Xie, B. Micelle Anchored in Situ Synthesis of V_2O_3 Nanoflakes@C Composites for Supercapacitors. *J. Mater. Chem. A* **2014**, *2*, 18806−18815.
(95) Zhou, C.; Wu, C.; Liu, D.; Yan, M. Metal-Organic Framework Derived Hierarchical Co/C@V_2O_3 Hollow Spheres as a Thin, Lightweight, and High-Efficiency Electromagnetic Wave Absorber. *Chem.—Eur. J.* **2019**, *25*, 2234.
(96) Andersson, G. Studies on Vanadium Oxides. I. Phase Analysis. *Acta Chem. Scand.* **1954**, *8*, 1599.
(97) Gray, M. L.; Kershaw, R.; Croft, W.; Dwight, K.; Wold, A. Crystal Chemistry of V_3O_5 and Related Structures. *J. Solid State Chem.* **1986**, *62*, 57−63.
(98) Chen, D.; Tan, H.; Rui, X.; Zhang, Q.; Feng, Y.; Geng, H.; Li, C.; Huang, S.; Yu, Y. Oxyvanite V_3O_5: A New Intercalation-Type Anode for Lithium-Ion Battery. *InfoMat* **2019**, *1*, 251−259.
(99) Abdullaev, M. A.; Kamilov, I. K.; Terukov, E. I. Preparation and Properties of Stoichiometric Vanadium Oxides. *Inorg. Mater.* **2001**, *37*, 271−273.
(100) Fisher, B.; Patlagan, L.; Chashka, K. B.; Makarov, C.; Reisner, G. M. V_3O_5: Insulator-Metal Transition and Electric-Field-Induced Resistive-Switching. *Appl. Phys. Lett.* **2016**, *109*, 103501.
(101) Nagasawa, K. Crystal Growth of V_nO_{2n-1} ($3 \leq n \leq 8$) by the Chemical Transport Reaction and Electrical Properties. *Mater. Res. Bull.* **1971**, *6*, 853−863.
(102) Nagasawa, K.; Bando, Y.; Takada, T. Growth of V_3O_5 and V_6O_{11} Single Crystals. *Jpn. J. Appl. Phys.* **1969**, *8*, 1267−1267.
(103) Kumar, N.; Rúa, A.; Lu, J.; Fernández, F.; Lysenko, S. Ultrafast Excited-State Dynamics of V_3O_5 as a Signature of a Photoinduced Insulator-Metal Phase Transition. *Phys. Rev. Lett.* **2017**, *119*, 057602.
(104) Rúa, A.; Díaz, R. D.; Kumar, N.; Lysenko, S.; Fernández, F. E. Metal-Insulator Transition and Nonlinear Optical Responseof Sputter-Deposited V_3O_5 Thin Films. *J. Appl. Phys.* **2017**, *121*, 235302.
(105) Perucchi, A.; Baldassarre, L.; Postorino, P.; Lupi, S. Optical Properties Across the Insulator to Metal Transitions in Vanadium Oxide Compounds. *J. Phys. (Paris)* **2009**, *21*, 323202.
(106) Lysenko, S.; Fernández, F.; Rúa, A.; Liu, H. Ultrafast Light Scattering Imaging of Multi-Scale Transition Dynamics in Vanadium Dioxide. *J. Appl. Phys.* **2013**, *114*, 153514.
(107) Waltersson, K.; Forslund, B.; Wilhelmi, K.-A.; Andersson, S.; Galy, J. The Crystal Structure of V_3O_7. *Acta. Crystallogr. B* **1974**, *30*, 2644−2652.
(108) Rastgoo-Deylami, M.; Chae, M. S.; Hong, S.-T. $H_2V_3O_8$ as a High Energy Cathode Material for Nonaqueous Magnesium-Ion Batteries. *Chem. Mater.* **2018**, *30*, 7464−7472.
(109) An, Q.; Sheng, J.; Xu, X.; Wei, Q.; Zhu, Y.; Han, C.; Niu, C.; Mai, L. Ultralong $H_2V_3O_8$ Nanowire Bundles as a Promising Cathode for Lithium Batteries. *New J. Chem.* **2014**, *38*, 2075−2080.
(110) Li, C.; Isobe, M.; Ueda, H.; Matsushita, Y.; Ueda, Y. Crystal Growth and Anisotropic Magnetic Properties of V_3O_7. *J. Solid State Chem.* **2009**, *182*, 3222−3225.
(111) Wen, P.; Liu, T.; Wei, F.; Ai, L.; Yao, F. Soft Chemical Topotactic Synthesis and Crystal Structure Evolution from Two-Dimensional KV_3O_8 Plates to One-Dimensional V_3O_7 Nanobelts. *CrystEngComm* **2016**, *18*, 8880−8886.
(112) Zhao, D.; Zhu, Q.; Chen, D.; Li, X.; Yu, Y.; Huang, X. Nest-Like V_3O_7 Self-Assembled by Porous Nanowires as an Anode Supercapacitor Material and its Performance Optimization through Bonding with N-Doped Carbon. *J. Mater. Chem. A* **2018**, *6*, 16475−16484.
(113) Berenguer, R.; Guerrero-Pérez, M. O.; Guzmán, I.; Rodríguez-Mirasol, J.; Cordero, T. Synthesis of Vanadium Oxide Nanofibers with Variable Crystallinity and V^{5+}/V^{4+} Ratios. *ACS Omega* **2017**, *2*, 7739−7745.
(114) Chine, M.; Sediri, F.; Gharbi, N. Hydrothermal Synthesis of $V_3O_7{\cdot}H_2O$ Nanobelts and Study of Their Electrochemical Properties. *Mater. Sci. Appl.* **2011**, *2*, 964−970.
(115) Zhang, Y.; Liu, X.; Xie, G.; Yu, L.; Yi, S.; Hu, M.; Huang, C. Hydrothermal Synthesis, Characterization, Formation Mechanism and

https://doi.org/10.1021/acs.chemrev.2c00546
Chem. Rev. 2023, 123, 4353−4415

Electrochemical Property of $V_3O_7{\cdot}H_2O$ Single-Crystal Nanobelts. *Mater. Sci. Eng., B* **2010**, *175*, 164−171.
(116) Zhang, Y.; Fan, M.; Zhou, M.; Huang, C.; Chen, C.; Cao, Y.; Xie, G.; Li, H.; Liu, X. Controlled Synthesis and Electrochemical Properties of Vanadium Oxides with Different Nanostructures. *Bull. Mater. Sci.* **2012**, *35*, 369−376.
(117) Li, G. C.; Pang, S. P.; Wang, Z. B.; Peng, H. R.; Zhang, Z. K. Synthesis of $H_2V_3O_8$ Single-Crystal Nanobelts. *Eur. J. Inorg. Chem.* **2005**, *2005*, 2060−2063.
(118) Zhang, X.; Yu, M.; Zhao, S.; Li, F.; Hu, X.; Guo, S.; Lu, X.; Tong, Y. 3D $V_3O_7{\cdot}H_2O$/Partially Exfoliated Carbon Nanotube Composites with Significantly Improved Lithium Storage Ability. *Part. Part. Syst. Charact.* **2016**, *33*, 531−537.
(119) Cao, Z.; Chu, H.; Zhang, H.; Ge, Y.; Clemente, R.; Dong, P.; Wang, L.; Shen, J.; Ye, M.; Ajayan, P. M. An in Situ Electrochemical Oxidation Strategy for Formation of Nanogrid-Shaped $V_3O_7{\cdot}H_2O$ with Enhanced Zinc Storage Properties. *J. Mater. Chem. A* **2019**, *7*, 25262−25267.
(120) Yan, M.; Wang, F.; Han, C.; Ma, X.; Xu, X.; An, Q.; Xu, L.; Niu, C.; Zhao, Y.; Tian, X.; et al. Nanowire Templated Semihollow Bicontinuous Graphene Scrolls: Designed Construction, Mechanism, and Enhanced Energy Storage Performance. *J. Am. Chem. Soc.* **2013**, *135*, 18176−18182.
(121) Kundu, D.; Hosseini Vajargah, S.; Wan, L.; Adams, B.; Prendergast, D.; Nazar, L. F. Aqueous vs. Nonaqueous Zn-Ion Batteries: Consequences of the Desolvation Penalty at the Interface. *Energy Environ. Sci.* **2018**, *11*, 881−892.
(122) Boldyrev, V. V. Thermal Decomposition of Ammonium Perchlorate. *Thermochim. Acta* **2006**, *443*, 1−36.
(123) Jacobs, P. W. M.; Whitehead, H. M. Decomposition and Combustion of Ammonium Perchlorate. *Chem. Rev.* **1969**, *69*, 551−590.
(124) Zhang, Y.; Liu, X.; Chen, D.; Yu, L.; Nie, J.; Yi, S.; Li, H.; Huang, C. Fabrication of $V_3O_7{\cdot}H_2O$@C Core-Shell Nanostructured Composites and the Effect of $V_3O_7{\cdot}H_2O$ and $V_3O_7{\cdot}H_2O$@C on Decomposition of Ammonium Perchlorate. *J. Alloys Compd.* **2011**, *509*, L69−L73.
(125) Manikandan, R.; Raj, C. J.; Rajesh, M.; Kim, B. C.; Nagaraju, G.; Lee, W.-g.; Yu, K. H. Rationally Designed Spider Web-Like Trivanadium Heptaoxide Nanowires on Carbon Cloth as a New Class of Pseudocapacitive Electrode for Symmetric Supercapacitors with High Energy Density and Ultra-Long Cyclic Stability. *J. Mater. Chem. A* **2018**, *6*, 11390−11404.
(126) Hu, T.; Liu, Y.; Zhang, Y.; Chen, M.; Zheng, J.; Tang, J.; Meng, C. 3D Hierarchical Porous $V_3O_7{\cdot}H_2O$ Nanobelts/CNT/Reduced Graphene Oxide Integrated Composite with Synergistic Effect for Supercapacitors with High Capacitance and Long Cycling Life. *J. Colloid Interface Sci.* **2018**, *531*, 382−393.
(127) Zhu, J.; Cao, L.; Wu, Y.; Gong, Y.; Liu, Z.; Hoster, H. E.; Zhang, Y.; Zhang, S.; Yang, S.; Yan, Q.; et al. Building 3D Structures of Vanadium Pentoxide Nanosheets and Application as Electrodes in Supercapacitors. *Nano Lett.* **2013**, *13*, 5408−5413.
(128) Yin, Z.; Xu, J.; Ge, Y.; Jiang, Q.; Zhang, Y.; Yang, Y.; Sun, Y.; Hou, S.; Shang, Y.; Zhang, Y. Synthesis of V_2O_5 Microspheres by Spray Pyrolysis as Cathode Material for Supercapacitors. *Mater. Res. Express.* **2018**, *5*, 036306.
(129) Li, H.-Y.; Wei, C.; Wang, L.; Zuo, Q.-S.; Li, X.; Xie, B. Hierarchical Vanadium Oxide Microspheres Forming from Hyperbranched Nanoribbons as Remarkably High Performance Electrode Materials for Supercapacitors. *J. Mater. Chem. A* **2015**, *3*, 22892−22901.
(130) Zhang, Y.; Wang, X.; Jing, X.; Meng, C. In-situ Synthesis of V_2O_5 Hollow Spheres Coated Ni-Foam as Binder-Free Electrode for High-Performance Symmetrical Supercapacitor. *Mater. Lett.* **2019**, *248*, 101−104.
(131) Liu, P.; Zhu, K.; Bian, K.; Xu, Y.; Zhang, F.; Zhang, W.; Zhang, J.; Huang, W. 3D Hierarchical Porous Sponge-Like V_2O_5 Micro/Nano-Structures for High-Performance Li-Ion Batteries. *J. Alloys Compd.* **2018**, *765*, 901−906.
(132) Song, Y.; Liu, T.-Y.; Yao, B.; Kou, T.-Y.; Feng, D.-Y.; Liu, X.-X.; Li, Y. Amorphous Mixed-Valence Vanadium Oxide/Exfoliated Carbon Cloth Structure Shows a Record High Cycling Stability. *Small* **2017**, *13*, 1700067.
(133) Cristopher, M.; Karthick, P.; Sivakumar, R.; Gopalakrishnan, C.; Sanjeeviraja, C.; Jeyadheepan, K. On the Preparation of Tri-Vanadium Hepta-Oxide Thin Films for Electrochromic Applications. *Vacuum* **2019**, *160*, 238−245.
(134) Lu, Z.; Zhong, X.; Liu, X.; Wang, J.; Diao, X. Energy Storage Electrochromic Devices in the Era of Intelligent Automation. *Phys. Chem. Chem. Phys.* **2021**, *23*, 14126−14145.
(135) Deb, S. K. Optical and Photoelectric Properties and Colour Centres in Thin Films of Tungsten Oxide. *Philos. Mag.: J. Theor. Exp. Appl. Phys.* **1973**, *27*, 801−822.
(136) Deb, S. K. Opportunities and Challenges of Electrochromic Phenomena in Transition Metal Oxides. *Sol. Energy Mater. Sol. Cells* **1992**, *25*, 327−338.
(137) Jourdani, R.; Jadoual, L.; Ait El Fqih, M.; El Boujlaidi, A.; Aouchiche, H.; Kaddouri, A. Effects of Lithium Insertion and Deinsertion into V_2O_5 Thin Films: Optical, Structural, and Absorption Properties. *Surf. Interface Anal.* **2018**, *50*, 52−58.
(138) Mjejri, I.; Rougier, A. Color Switching in $V_3O_7{\cdot}H_2O$ Films Cycled in Li and Na Based Electrolytes: Novel Vanadium Oxide Based Electrochromic Materials. *J. Mater. Chem. C* **2020**, *8*, 3631−3638.
(139) Li, M.; Magdassi, S.; Gao, Y.; Long, Y. Hydrothermal Synthesis of VO_2 Polymorphs: Advantages, Challenges and Prospects for the Application of Energy Efficient Smart Windows. *Small* **2017**, *13*, 1701147.
(140) Wentzcovitch, R. M.; Schulz, W. W.; Allen, P. B. VO_2: Peierls or Mott-Hubbard? A View from Band Theory. *Phys. Rev. Lett.* **1994**, *72*, 3389−3392.
(141) Baum, P.; Yang, D.-S.; Zewail, A. H. 4D Visualization of Transitional Structures in Phase Transformations by Electron Diffraction. *Science* **2007**, *318*, 788−792.
(142) Mott, N. Metal-Insulator Transition. *Rev. Mod. Phys.* **1968**, *40*, 677.
(143) Wei, J.; Wang, Z.; Chen, W.; Cobden, D. H. New Aspects of the Metal-Insulator Transition in Single-Domain Vanadium Dioxide Nanobeams. *Nat. Nanotechnol.* **2009**, *4*, 420−424.
(144) Whittaker, L.; Patridge, C. J.; Banerjee, S. Microscopic and Nanoscale Perspective of the Metal-Insulator Phase Transitions of VO_2: Some New Twists to an Old Tale. *J. Phys. Chem. Lett.* **2011**, *2*, 745−758.
(145) Yao, T.; Zhang, X.; Sun, Z.; Liu, S.; Huang, Y.; Xie, Y.; Wu, C.; Yuan, X.; Zhang, W.; Wu, Z.; Pan, G.; Hu, F.; Wu, L.; Liu, Q.; Wei, S. Understanding the Nature of the Kinetic Process in a VO_2 Metal-Insulator Transition. *Phys. Rev. Lett.* **2010**, *105*, 226405.
(146) Shao, Z.; Cao, X.; Luo, H.; Jin, P. Recent Progress in the Phase-Transition Mechanism and Modulation of Vanadium Dioxide Materials. *NPG Asia Mater.* **2018**, *10*, 581−605.
(147) Lee, S.; Ivanov, I. N.; Keum, J. K.; Lee, H. N. Epitaxial Stabilization and Phase Instability of VO_2 Polymorphs. *Sci. Rep.* **2016**, *6*, 19621.
(148) Ma, H.; Hou, J.; Wang, X.; Zhang, J.; Yuan, Z.; Xiao, L.; Wei, Y.; Fan, S.; Jiang, K.; Liu, K. Flexible, All-Inorganic Actuators Based on Vanadium Dioxide and Carbon Nanotube Bimorphs. *Nano Lett.* **2017**, *17*, 421−428.
(149) Driscoll, T.; Kim, H.-T.; Chae, B.-G.; Kim, B.-J.; Lee, Y.-W.; Jokerst, N. M.; Palit, S.; Smith, D. R.; Di Ventra, M.; Basov, D. N. Memory Metamaterials. *Science* **2009**, *325*, 1518−1521.
(150) Bae, S. H.; Lee, S.; Koo, H.; Lin, L.; Jo, B. H.; Park, C.; Wang, Z. L. The Memristive Properties of a Single VO_2 Nanowire with Switching Controlled by Self-Heating. *Adv. Mater.* **2013**, *25*, 5098−5103.
(151) Nakano, M.; Shibuya, K.; Okuyama, D.; Hatano, T.; Ono, S.; Kawasaki, M.; Iwasa, Y.; Tokura, Y. Collective Bulk Carrier Delocalization Driven by Electrostatic Surface Charge Accumulation. *Nature* **2012**, *487*, 459−462.
(152) Beaumont, A.; Leroy, J.; Orlianges, J.-C.; Crunteanu, A. Current-Induced Electrical Self-Oscillations Across out-of-plane Threshold Switches Based on VO_2 Layers Integrated in Crossbars Geometry. *J. Appl. Phys.* **2014**, *115*, 154502.

https://doi.org/10.1021/acs.chemrev.2c00546
Chem. Rev. 2023, 123, 4353−4415

(153) Liu, M.; Hwang, H. Y.; Tao, H.; Strikwerda, A. C.; Fan, K.; Keiser, G. R.; Sternbach, A. J.; West, K. G.; Kittiwatanakul, S.; Lu, J.; Wolf, S. A.; Omenetto, F. G.; Zhang, X.; Nelson, K. A.; Averitt, R. D. Terahertz-Field-Induced Insulator-to-Metal Transition in Vanadium Dioxide Metamaterial. *Nature* **2012**, *487*, 345−348.
(154) Gao, Y.; Luo, H.; Zhang, Z.; Kang, L.; Chen, Z.; Du, J.; Kanehira, M.; Cao, C. Nanoceramic VO_2 Thermochromic Smart glass: A Review on Progress in Solution Processing. *Nano Energy* **2012**, *1*, 221−246.
(155) Seyfouri, M. M.; Binions, R. Sol-Gel Approaches to Thermochromic Vanadium Dioxide Coating for Smart Glazing Application. *Sol. Energy Mater. Sol. Cells* **2017**, *159*, 52−65.
(156) Vu, T. D.; Chen, Z.; Zeng, X.; Jiang, M.; Liu, S.; Gao, Y.; Long, Y. Physical Vapour Deposition of Vanadium Dioxide for Thermochromic Smart Window Applications. *J. Mater. Chem. C* **2019**, *7*, 2121−2145.
(157) Liu, K.; Lee, S.; Yang, S.; Delaire, O.; Wu, J. Recent Progresses on Physics and Applications of Vanadium Dioxide. *Mater. Today* **2018**, *21*, 875−896.
(158) Shi, R.; Shen, N.; Wang, J.; Wang, W.; Amini, A.; Wang, N.; Cheng, C. Recent Advances in Fabrication Strategies, Phase Transition Modulation, and Advanced Applications of Vanadium Dioxide. *Appl. Phys. Rev.* **2019**, *6*, 011312.
(159) Chang, T.-C.; Cao, X.; Bao, S.-H.; Ji, S.-D.; Luo, H.-J.; Jin, P. Review on Thermochromic Vanadium Dioxide Based Smart Coatings: from Lab to Commercial Application. *Adv. Manuf.* **2018**, *6*, 1−19.
(160) Wan, C.; Zhang, Z.; Woolf, D.; Hessel, C. M.; Rensberg, J.; Hensley, J. M.; Xiao, Y.; Shahsafi, A.; Salman, J.; Richter, S.; et al. On the Optical Properties of Thin-Film Vanadium Dioxide from the Visible to the Far Infrared. *Ann. Phys.* **2019**, *531*, 1900188.
(161) Granqvist, C. Spectrally Selective Coatings for Energy Efficiency and Solar Applications. *Phys. Scr.* **1985**, *32*, 401.
(162) Huovila, P.; Ala-Juusela, M.; Melchert, L.; Pouffary, S.; Cheng, C.-C.; Ürge-Vorsatz, D.; Koeppel, S.; Svenningsen, N.; Graham, P. *Buildings and Climate Change: Summary for Decision-Makers*; United Nations Environment Programme: Nairobi, Kenya, 2009.
(163) Cui, Y.; Ke, Y.; Liu, C.; Chen, Z.; Wang, N.; Zhang, L.; Zhou, Y.; Wang, S.; Gao, Y.; Long, Y. Thermochromic VO_2 for Energy-Efficient Smart Windows. *Joule* **2018**, *2*, 1707−1746.
(164) Chen, Z.; Gao, Y.; Kang, L.; Du, J.; Zhang, Z.; Luo, H.; Miao, H.; Tan, G. VO_2-Based Double-Layered Films for Smart Windows: Optical Design, All-Solution Preparation and Improved Properties. *Sol. Energy Mater. Sol. Cells* **2011**, *95*, 2677−2684.
(165) Qian, X.; Wang, N.; Li, Y.; Zhang, J.; Xu, Z.; Long, Y. Bioinspired Multifunctional Vanadium Dioxide: Improved Thermochromism and Hydrophobicity. *Langmuir* **2014**, *30*, 10766−10771.
(166) Taylor, A.; Parkin, I.; Noor, N.; Tummeltshammer, C.; Brown, M. S.; Papakonstantinou, I. A Bioinspired Solution for Spectrally Selective Thermochromic VO_2 Coated Intelligent Glazing. *Opt. Express* **2013**, *21*, A750−A764.
(167) Ke, Y.; Balin, I.; Wang, N.; Lu, Q.; Tok, A. I. Y.; White, T. J.; Magdassi, S.; Abdulhalim, I.; Long, Y. Two-Dimensional SiO_2/VO_2 Photonic Crystals with Statically Visible and Dynamically Infrared Modulated for Smart Window Deployment. *ACS Appl. Mater. Interfaces* **2016**, *8*, 33112−33120.
(168) Ke, Y.; Zhang, Q.; Wang, T.; Wang, S.; Li, N.; Lin, G.; Liu, X.; Dai, Z.; Yan, J.; Yin, J.; et al. Cephalopod-Inspired Versatile Design Based on Plasmonic VO_2 Nanoparticle for Energy-Efficient Mechano-Thermochromic Windows. *Nano Energy* **2020**, *73*, 104785.
(169) Li, S.-Y.; Niklasson, G. A.; Granqvist, C.-G. Nanothermochromics: Calculations for VO_2 Nanoparticles in Dielectric Hosts Show Much Improved Luminous Transmittance and Solar Energy Transmittance Modulation. *J. Appl. Phys.* **2010**, *108*, 063525.
(170) Kang, L.; Gao, Y.; Luo, H.; Chen, Z.; Du, J.; Zhang, Z. Nanoporous Thermochromic VO_2 Films with Low Optical Constants, Enhanced Luminous Transmittance and Thermochromic Properties. *ACS Appl. Mater. Interfaces* **2011**, *3*, 135−138.
(171) Liu, C.; Balin, I.; Magdassi, S.; Abdulhalim, I.; Long, Y. Vanadium Dioxide Nanogrid Films for High Transparency Smart Architectural Window Applications. *Opt. Express* **2015**, *23*, A124−A132.
(172) Lu, Q.; Liu, C.; Wang, N.; Magdassi, S.; Mandler, D.; Long, Y. Periodic Micro-Patterned VO_2 Thermochromic Films by Mesh Printing. *J. Mater. Chem. C* **2016**, *4*, 8385−8391.
(173) Zhou, C.; Li, D.; Tan, Y.; Ke, Y.; Wang, S.; Zhou, Y.; Liu, G.; Wu, S.; Peng, J.; Li, A.; et al. 3D Printed Smart Windows for Adaptive Solar Modulations. *Adv. Opt. Mater.* **2020**, *8*, 2000013.
(174) Wang, S.; Jiang, T.; Meng, Y.; Yang, R.; Tan, G.; Long, Y. Scalable Thermochromic Smart Windows with Passive Radiative Cooling Regulation. *Science* **2021**, *374*, 1501−1504.
(175) Tang, K.; Dong, K.; Li, J.; Gordon, M. P.; Reichertz, F. G.; Kim, H.; Rho, Y.; Wang, Q.; Lin, C.-Y.; Grigoropoulos, C. P.; et al. Temperature-Adaptive Radiative Coating for All-Season Household Thermal Regulation. *Science* **2021**, *374*, 1504−1509.
(176) Ke, Y.; Li, Y.; Wu, L.; Wang, S.; Yang, R.; Yin, J.; Tan, G.; Long, Y. On-Demand Solar and Thermal Radiation Management Based on Switchable Interwoven Surfaces. *ACS Energy Lett.* **2022**, *7*, 1758−1763.
(177) Wang, S.; Zhou, Y.; Jiang, T.; Yang, R.; Tan, G.; Long, Y. Thermochromic Smart Windows with Highly Regulated Radiative Cooling and Solar Transmission. *Nano Energy* **2021**, *89*, 106440.
(178) Vu, T. D.; Xie, H.; Wang, S.; Hu, J.; Zeng, X.; Long, Y. Durable Vanadium Dioxide with 33-Year Service Life for Smart Windows Applications. *Mater. Today Energy* **2022**, *26*, 100978.
(179) Zhou, X.; Meng, Y.; Vu, T. D.; Gu, D.; Jiang, Y.; Mu, Q.; Li, Y.; Yao, B.; Dong, Z.; Liu, Q.; et al. A New Strategy of Nanocompositing Vanadium Dioxide with Excellent Durability. *J. Mater. Chem. A* **2021**, *9*, 15618−15628.
(180) Xiao, L.; Ma, H.; Liu, J.; Zhao, W.; Jia, Y.; Zhao, Q.; Liu, K.; Wu, Y.; Wei, Y.; Fan, S.; Jiang, K. Fast Adaptive Thermal Camouflage Based on Flexible VO_2/Graphene/CNT Thin Films. *Nano Lett.* **2015**, *15*, 8365−8370.
(181) Wang, S.; Liu, G.; Hu, P.; Zhou, Y.; Ke, Y.; Li, C.; Chen, J.; Cao, T.; Long, Y. Largely Lowered Transition Temperature of a VO_2/Carbon Hybrid Phase Change Material with High Thermal Emissivity Switching Ability and Near Infrared Regulations. *Adv. Mater. Interfaces* **2018**, *5*, 1801063.
(182) Ji, H.; Liu, D.; Zhang, C.; Cheng, H. VO_2/ZnS Core-Shell Nanoparticle for the Adaptive Infrared Camouflage Application with Modified Color and Enhanced Oxidation Resistance. *Sol. Energy Mater. Sol. Cells* **2018**, *176*, 1−8.
(183) Taylor, S.; Yang, Y.; Wang, L. Vanadium Dioxide Based Fabry-Perot Emitter for Dynamic Radiative Cooling Applications. *J. Quant. Spectrosc. Radiat. Transfer* **2017**, *197*, 76−83.
(184) Kim, H.; Cheung, K.; Auyeung, R. C. Y.; Wilson, D. E.; Charipar, K. M.; Pique, A.; Charipar, N. A. VO_2-based Switchable Radiator for Spacecraft Thermal Control. *Sci. Rep.* **2019**, *9*, 11329.
(185) Gomez-Heredia, C. L.; Ramirez-Rincon, J. A.; Ordonez-Miranda, J.; Ares, O.; Alvarado-Gil, J. J.; Champeaux, C.; Dumas-Bouchiat, F.; Ezzahri, Y.; Joulain, K. Thermal Hysteresis Measurement of the VO_2 Emissivity and its Application in Thermal Rectification. *Sci. Rep.* **2018**, *8*, 8479.
(186) Katase, T.; Endo, K.; Ohta, H. Infrared-Transmittance Tunable Metal-Insulator Conversion Device with Thin-Film-Transistor-Type Structure on a Glass Substrate. *APL Mater.* **2017**, *5*, 056105.
(187) Zhang, P.; Zhang, W.; Wang, J.; Jiang, K.; Zhang, J.; Li, W.; Wu, J.; Hu, Z.; Chu, J. The Electro-Optic Mechanism and Infrared Switching Dynamic of the Hybrid Multilayer VO_2/Al: ZnO Heterojunctions. *Sci. Rep.* **2017**, *7*, 1−14.
(188) Zhou, Y.; Layani, M.; Boey, F. Y. C.; Sokolov, I.; Magdassi, S.; Long, Y. Electro-Thermochromic Devices Composed of Self-Assembled Transparent Electrodes and Hydrogels. *Adv. Mater. Technol.* **2016**, *1*, 1600069.
(189) Fan, L.; Chen, Y.; Liu, Q.; Chen, S.; Zhu, L.; Meng, Q.; Wang, B.; Zhang, Q.; Ren, H.; Zou, C. Infrared Response and Optoelectronic Memory Device Fabrication Based on Epitaxial VO_2 Film. *ACS Appl. Mater. Interfaces* **2016**, *8*, 32971−32977.
(190) Briggs, R. M.; Pryce, I. M.; Atwater, H. A. Compact Silicon Photonic Waveguide Modulator Based on the Vanadium Dioxide

https://doi.org/10.1021/acs.chemrev.2c00546
Chem. Rev. 2023, 123, 4353−4415

Metal-Insulator Phase Transition. *Opt. Express* **2010**, *18*, 11192−11201.
(191) Lee, J.; Lee, D.; Cho, S. J.; Seo, J.-H.; Liu, D.; Eom, C.-B.; Ma, Z. Epitaxial VO_2 Thin Film-based Radio-Frequency Switches with Thermal Activation. *Appl. Phys. Lett.* **2017**, *111*, 063110.
(192) Sun, M.; Taha, M.; Walia, S.; Bhaskaran, M.; Sriram, S.; Shieh, W.; Unnithan, R. R. A Photonic Switch Based on a Hybrid Combination of Metallic Nanoholes and Phase-Change Vanadium Dioxide. *Sci. Rep.* **2018**, *8*, 11106.
(193) Ding, F.; Zhong, S.; Bozhevolnyi, S. I. Vanadium Dioxide Integrated Metasurfaces with Switchable Functionalities at Terahertz Frequencies. *Adv. Opt. Mater.* **2018**, *6*, 1701204.
(194) Liu, M.; Xu, Q.; Chen, X.; Plum, E.; Li, H.; Zhang, X.; Zhang, C.; Zou, C.; Han, J.; Zhang, W. Temperature-Controlled Asymmetric Transmission of Electromagnetic Waves. *Sci. Rep.* **2019**, *9*, 4097.
(195) Wegkamp, D.; Stähler, J. Ultrafast Dynamics During the Photoinduced Phase Transition in VO_2. *Prog. Surf. Sci.* **2015**, *90*, 464−502.
(196) Guo, P.; Weimer, M. S.; Emery, J. D.; Diroll, B. T.; Chen, X.; Hock, A. S.; Chang, R. P.; Martinson, A. B.; Schaller, R. D. Conformal Coating of a Phase Change Material on Ordered Plasmonic Nanorod Arrays for Broadband All-Optical Switching. *ACS Nano* **2017**, *11*, 693−701.
(197) Lei, D. Y.; Appavoo, K.; Ligmajer, F.; Sonnefraud, Y.; Haglund Jr, R. F.; Maier, S. A. Optically-Triggered Nanoscale Memory Effect in a Hybrid Plasmonic-Phase Changing Nanostructure. *ACS Photonics* **2015**, *2*, 1306−1313.
(198) Ke, Y.; Wen, X.; Zhao, D.; Che, R.; Xiong, Q.; Long, Y. Controllable Fabrication of Two-Dimensional Patterned VO_2 Nanoparticle, Nanodome, and Nanonet Arrays with Tunable Temperature-Dependent Localized Surface Plasmon Resonance. *ACS Nano* **2017**, *11*, 7542−7551.
(199) Ke, Y.; Zhang, B.; Wang, T.; Zhong, Y.; Vu, T. D.; Wang, S.; Liu, Y.; Magdassi, S.; Ye, X.; Zhao, D.; et al. Manipulating Atomic Defects in Plasmonic Vanadium Dioxide for Superior Solar and Thermal Management. *Mater. Horizons* **2021**, *8*, 1700−1710.
(200) Kim, B.-J.; Lee, Y. W.; Chae, B.-G.; Yun, S. J.; Oh, S.-Y.; Kim, H.-T.; Lim, Y.-S. Temperature Dependence of the First-Order Metal-Insulator Transition in VO_2 and Programmable Critical Temperature Sensor. *Appl. Phys. Lett.* **2007**, *90*, 023515.
(201) Yang, Z.; Ko, C.; Balakrishnan, V.; Gopalakrishnan, G.; Ramanathan, S. Dielectric and Carrier Transport Properties of Vanadium Dioxide Thin Films Across the Phase Transition Utilizing Gated Capacitor Devices. *Phys. Rev. B* **2010**, *82*, 205101.
(202) Hou, J.; Wang, Z.; Ding, Z.; Zhang, Z.; Zhang, J. Facile Synthesize VO_2 (M1) Nanorods for a Low-Cost Infrared Photodetector Application. *Sol. Energy Mater. Sol. Cells* **2018**, *176*, 142−149.
(203) Takeya, H.; Frame, J.; Tanaka, T.; Urade, Y.; Fang, X.; Kubo, W. Bolometric Photodetection Using Plasmon-Assisted Resistivity Change in Vanadium Dioxide. *Sci. Rep.* **2018**, *8*, 12764.
(204) Hu, B.; Ding, Y.; Chen, W.; Kulkarni, D.; Shen, Y.; Tsukruk, V. V.; Wang, Z. L. External-Strain Induced Insulating Phase Transition in VO_2 Nanobeam and Its Application as Flexible Strain Sensor. *Adv. Mater.* **2010**, *22*, 5134−5139.
(205) Liang, J.; Zhao, Y.; Zhu, K.; Guo, J.; Zhou, L. Synthesis and Room Temperature NO_2 Gas Sensitivity of Vanadium Dioxide Nanowire Structures by Chemical Vapor Deposition. *Thin Solid Films* **2019**, *669*, 537−543.
(206) Evans, G. P.; Powell, M. J.; Johnson, I. D.; Howard, D. P.; Bauer, D.; Darr, J. A.; Parkin, I. P. Room Temperature Vanadium Dioxide-Carbon Nanotube Gas Sensors Made via Continuous Hydrothermal Flow Synthesis. *Sens. Actuator B* **2018**, *255*, 1119−1129.
(207) Zhou, Y.; Chen, X.; Ko, C.; Yang, Z.; Mouli, C.; Ramanathan, S. Voltage-Triggered Ultrafast Phase Transition in Vanadium Dioxide Switches. *IEEE Electron Device Lett.* **2013**, *34*, 220−222.
(208) Li, D.; Sharma, A. A.; Gala, D. K.; Shukla, N.; Paik, H.; Datta, S.; Schlom, D. G.; Bain, J. A.; Skowronski, M. Joule Heating-Induced Metal-Insulator Transition in Epitaxial VO_2/TiO_2 Devices. *ACS Appl. Mater. Interfaces* **2016**, *8*, 12908−12914.
(209) Yajima, T.; Nishimura, T.; Toriumi, A. Positive-Bias Gate-Controlled Metal-Insulator Transition in Ultrathin VO_2 Channels with TiO_2 Gate Dielectrics. *Nat. Commun.* **2015**, *6*, 1−9.
(210) Shukla, N.; Thathachary, A. V.; Agrawal, A.; Paik, H.; Aziz, A.; Schlom, D. G.; Gupta, S. K.; Engel-Herbert, R.; Datta, S. A Steep-Slope Transistor Based on Abrupt Electronic Phase Transition. *Nat. Commun.* **2015**, *6*, 1−6.
(211) Zhang, Y.; Xiong, W.; Chen, W.; Luo, X.; Zhang, X.; Zheng, Y. Nonvolatile Ferroelectric Field Effect Transistor Based on a Vanadium Dioxide Nanowire with Large On- and Off-Field Resistance Switching. *Phys. Chem. Chem. Phys.* **2020**, *22*, 4685−4691.
(212) Goldflam, M. D.; Liu, M. K.; Chapler, B. C.; Stinson, H. T.; Sternbach, A. J.; McLeod, A. S.; Zhang, J. D.; Geng, K.; Royal, M.; Kim, B.-J.; Averitt, R. D.; Jokerst, N. M.; Smith, D. R.; Kim, H-T.; Basov, D. N. Voltage Switching of a VO_2 Memory Metasurface Using Ionic Gel. *Appl. Phys. Lett.* **2014**, *105*, 041117.
(213) Jeong, J.; Aetukuri, N.; Graf, T.; Schladt, T. D.; Samant, M. G.; Parkin, S. S. Suppression of Metal-Insulator Transition in VO_2 by Electric Field-Induced Oxygen Vacancy Formation. *Science* **2013**, *339*, 1402−1405.
(214) Ji, H.; Wei, J.; Natelson, D. Modulation of the Electrical Properties of VO_2 Nanobeams Using an Ionic Liquid as a Gating Medium. *Nano Lett.* **2012**, *12*, 2988−2992.
(215) Shibuya, K.; Sawa, A. Modulation of Metal-Insulator Transition in VO_2 by Electrolyte Gating-Induced Protonation. *Adv. Electron. Mater.* **2016**, *2*, 1500131.
(216) Leroy, J.; Crunteanu, A.; Givernaud, J.; Orlianges, J.-C.; Champeaux, C.; Blondy, P. Generation of Electrical Self-Oscillations in Two-Terminal Switching Devices Based on the Insulator-to-Metal Phase Transition of VO_2 Thin Films. *Int. J. Microw. Wirel. Technol.* **2012**, *4*, 101−107.
(217) Zhou, Y.; Ramanathan, S. Mott Memory and Neuromorphic Devices. *Proc. IEEE* **2015**, *103*, 1289−1310.
(218) Pellegrino, L.; Manca, N.; Kanki, T.; Tanaka, H.; Biasotti, M.; Bellingeri, E.; Siri, A. S.; Marré, D. Multistate Memory Devices Based on Free-Standing VO_2/TiO_2 Microstructures Driven by Joule Self-Heating. *Adv. Mater.* **2012**, *24*, 2929−2934.
(219) Janod, E.; Tranchant, J.; Corraze, B.; Querré, M.; Stoliar, P.; Rozenberg, M.; Cren, T.; Roditchev, D.; Phuoc, V. T.; Besland, M.-P.; et al. Resistive Switching in Mott Insulators and Correlated Systems. *Adv. Funct. Mater.* **2015**, *25*, 6287−6305.
(220) Yin, H.; Yu, K.; Song, C.; Wang, Z.; Zhu, Z. Low-Temperature CVD Synthesis of Patterned Core-Shell VO_2@ ZnO Nanotetrapods and Enhanced Temperature-Dependent Field-Emission Properties. *Nanoscale* **2014**, *6*, 11820−11827.
(221) Li, Z.; Guo, Y.; Hu, Z.; Su, J.; Zhao, J.; Wu, J.; Wu, J.; Zhao, Y.; Wu, C.; Xie, Y. Hydrogen Treatment for Superparamagnetic VO_2 Nanowires with Large Room-Temperature Magnetoresistance. *Angew. Chem., Int. Ed.* **2016**, *55*, 8018−8022.
(222) Choi, J.; Kim, B.-J.; Seo, G.; Kim, H.-T.; Cho, S.; Lee, Y. W. Magnetic Field-Dependent Ordinary Hall Effect and Thermopower of VO_2 Thin Films. *Curr. Appl. Phys.* **2016**, *16*, 335−339.
(223) Singh, D.; Yadav, C.; Viswanath, B. Magnetoresistance Across Metal-Insulator Transition in VO_2 Micro Crystals. *Mater. Lett.* **2017**, *196*, 248−251.
(224) Mirfakhrai, T.; Madden, J. D.; Baughman, R. H. Polymer Artificial Muscles. *Mater. Today* **2007**, *10*, 30−38.
(225) Liu, K.; Cheng, C.; Cheng, Z.; Wang, K.; Ramesh, R.; Wu, J. Giant-Amplitude, High-Work Density Microactuators with Phase Transition Activated Nanolayer Bimorphs. *Nano Lett.* **2012**, *12*, 6302−6308.
(226) Ma, H.; Zhang, X.; Cui, R.; Liu, F.; Wang, M.; Huang, C.; Hou, J.; Wang, G.; Wei, Y.; Jiang, K.; et al. Photo-Driven Nanoactuators Based on Carbon Nanocoils and Vanadium Dioxide Bimorphs. *Nanoscale* **2018**, *10*, 11158−11164.
(227) Shi, R.; Cai, X.; Wang, W.; Wang, J.; Kong, D.; Cai, N.; Chen, P.; He, P.; Wu, Z.; Amini, A.; et al. Single-Crystalline Vanadium Dioxide Actuators. *Adv. Funct. Mater.* **2019**, *29*, 1900527.

https://doi.org/10.1021/acs.chemrev.2c00546
Chem. Rev. 2023, 123, 4353−4415

(228) Manca, N.; Pellegrino, L.; Kanki, T.; Venstra, W. J.; Mattoni, G.; Higuchi, Y.; Tanaka, H.; Caviglia, A. D.; Marré, D. Selective High-Frequency Mechanical Actuation Driven by the VO_2 Electronic Instability. *Adv. Mater.* **2017**, *29*, 1701618.
(229) Torres, D.; Wang, T.; Zhang, J.; Zhang, X.; Dooley, S.; Tan, X.; Xie, H.; Sepúlveda, N. VO_2-Based MEMS Mirrors. *J. Microelectromech. Syst.* **2016**, *25*, 780−787.
(230) Holsteen, A.; Kim, I. S.; Lauhon, L. J. Extraordinary Dynamic Mechanical Response of Vanadium Dioxide Nanowires Around the Insulator to Metal Phase Transition. *Nano Lett.* **2014**, *14*, 1898−1902.
(231) Rúa, A.; Cabrera, R.; Coy, H.; Merced, E.; Sepúlveda, N.; Fernández, F. E. Phase Transition Behavior in Microcantilevers Coated with M1-Phase VO_2 and M2-phase VO_2:Cr Thin Films. *J. Appl. Phys.* **2012**, *111*, 104502.
(232) Manca, N.; Pellegrino, L.; Kanki, T.; Yamasaki, S.; Tanaka, H.; Siri, A. S.; Marré, D. Programmable Mechanical Resonances in MEMS by Localized Joule Heating of Phase Change Materials. *Adv. Mater.* **2013**, *25*, 6430−6435.
(233) Schmidt, C. N.; Cao, G. Properties of Mesoporous Carbon Modified Carbon Felt for Anode of All-Vanadium Redox Flow Battery. *Sci. China Mater.* **2016**, *59*, 1037−1050.
(234) Zhang, J.; Chen, L.; Wang, Y.; Cai, S.; Yang, H.; Yu, H.; Ding, F.; Huang, C.; Liu, X. $VO_{(2)}$(B)/Graphene Composite-Based Symmetrical Supercapacitor Electrode via Screen Printing for Intelligent Packaging. *Nanomaterials* **2018**, *8*, 1020.
(235) Lv, W.; Yang, C.; Meng, G.; Zhao, R.; Han, A.; Wang, R.; Liu, J. VO_2(B) Nanobelts/Reduced Graphene Oxide Composites for High-Performance Flexible All-Solid-State Supercapacitors. *Sci. Rep.* **2019**, *9*, 10831.
(236) Wu, C.; Zhang, X.; Dai, J.; Yang, J.; Wu, Z.; Wei, S.; Xie, Y. Direct Hydrothermal Synthesis of Monoclinic VO_2 (M) Single-Domain Nanorods on Large Scale Displaying Magnetocaloric Effect. *J. Mater. Chem.* **2011**, *21*, 4509−4517.
(237) Chao, D.; Zhu, C.; Xia, X.; Liu, J.; Zhang, X.; Wang, J.; Liang, P.; Lin, J.; Zhang, H.; Shen, Z. X.; et al. Graphene Quantum Dots Coated VO_2 Arrays for Highly Durable Electrodes for Li and Na Ion Batteries. *Nano Lett.* **2015**, *15*, 565−573.
(238) Li, Y.; Zhang, Q.; Yuan, Y.; Liu, H.; Yang, C.; Lin, Z.; Lu, J. Surface Amorphization of Vanadium Dioxide (B) for K-Ion Battery. *Adv. Energy Mater.* **2020**, *10*, 2000717.
(239) Chen, L.; Ruan, Y.; Zhang, G.; Wei, Q.; Jiang, Y.; Xiong, T.; He, P.; Yang, W.; Yan, M.; An, Q.; et al. Ultrastable and High-Performance Zn/VO_2 Battery Based on a Reversible Single-Phase Reaction. *Chem. Mater.* **2019**, *31*, 699−706.
(240) Niu, C.; Meng, J.; Han, C.; Zhao, K.; Yan, M.; Mai, L. VO_2 Nanowires Assembled into Hollow Microspheres for High-Rate and Long-Life Lithium Batteries. *Nano Lett.* **2014**, *14*, 2873−2878.
(241) Thomas, G. A.; Rapkine, D. H.; Carter, S. A.; Millis, A. J.; Rosenbaum, T. F.; Metcalf, P.; Honig, J. M. Observation of the Gap and Kinetic Energy in a Correlated Insulator. *Phys. Rev. Lett.* **1994**, *73*, 1529−1532.
(242) Wang, Y.; Zhang, Z.; Zhu, Y.; Li, Z.; Vajtai, R.; Ci, L.; Ajayan, P. M. Nanostructured VO_2 Photocatalysts for Hydrogen Production. *ACS Nano* **2008**, *2*, 1492−1496.
(243) Zhang, Q.; Liu, B.; Li, L.; Ji, Y.; Wang, C.; Zhang, L.; Su, Z. Maximized Schottky Effect: The Ultrafine V_2O_3/Ni Heterojunctions Repeatedly Arranging on Monolayer Nanosheets for Efficient and Stable Water-to-Hydrogen Conversion. *Small* **2021**, *17*, 2005769.
(244) Lv, Q.; Yang, L.; Wang, W.; Lu, S.; Wang, T.; Cao, L.; Dong, B. One-Step Construction of Core/Shell Nanoarrays with a Holey Shell and Exposed Interfaces for Overall Water Splitting. *J. Mater. Chem. A* **2019**, *7*, 1196−1205.
(245) Chen, G.; Zhang, X.; Guan, L.; Zhang, H.; Xie, X.; Chen, S.; Tao, J. Phase Transition-Promoted Hydrogen Evolution Performance of MoS_2/VO_2 Hybrids. *J. Phys. Chem. C* **2018**, *122*, 2618−2623.
(246) Hu, M.; Hu, J.; Zheng, Y.; Zhang, S.; Li, Q.; Yang, M.; Goto, T.; Tu, R. Heterostructured Co_3O_4/VO_2 Nanosheet Array Catalysts on Carbon Cloth for Hydrogen Evolution Reaction. *Int. J. Hydrog. Energy* **2022**, *47*, 18983−18991.
(247) Najafi, L.; Oropesa-Nuñez, R.; Bellani, S.; Martín-García, B.; Pasquale, L.; Serri, M.; Drago, F.; Luxa, J.; Sofer, Z.; Sedmidubský, D.; et al. Topochemical Transformation of Two-Dimensional VSe_2 into Metallic Nonlayered VO_2 for Water Splitting Reactions in Acidic and Alkaline Media. *ACS Nano* **2022**, *16*, 351−367.
(248) Zou, C. W.; Fan, L. L.; Chen, R. Q.; Yan, X. D.; Yan, W. S.; Pan, G. Q.; Wu, Z. Y.; Gao, W. Thermally Driven V_2O_5 Nanocrystal Formation and the Temperature-Dependent Electronic Structure Study. *CrystEngComm* **2012**, *14*, 626−631.
(249) Yao, J. H.; Li, Y. W.; Masse, R. C.; Uchaker, E.; Cao, G. Z. Revitalized Interest in Vanadium Pentoxide as Cathode Material for Lithium-Ion Batteries and Beyond. *Energy Stor. Mater.* **2018**, *11*, 205−259.
(250) Zhou, Y.; Pan, Q.; Zhang, J.; Han, C.; Wang, L.; Xu, H. Insights into Synergistic Effect of Acid on orphological Control of Vanadium Oxide: Toward High Lithium Storage. *Adv. Sci.* **2021**, *8*, 2002579.
(251) Nguyen, T. P. T.; Kim, M. H.; Yang, K. H. Formation and Depression of N_2O in Selective Reduction of NO by NH_3 over Fe_2O_3-Promoted V_2O_5-WO_3/TiO_2 Catalysts: Roles of each Constituent and Strongly-Adsorbed NH_3 Species. *Catal. Today* **2021**, *375*, 565−575.
(252) Yang, J. H.; Lee, H. J.; Lee, H. S.; Jeon, S. C.; Han, Y. S. Precise Control of Heat-Treatment Conditions to Improve the Catalytic Performance of V_2O_5/TiO_2 for H_2S Removal. *J. Hazard. Mater.* **2021**, *416*, 125974.
(253) Kang, T. H.; Youn, S.; Kim, D. H. Improved Catalytic Performance and Resistance to SO_2 over V_2O_5-WO_3/TiO_2 Catalyst Physically Mixed with Fe_2O_3 for Low-Temperature NH_3-SCR. *Catal. Today* **2021**, *376*, 95−103.
(254) Meyer, J.; Zilberberg, K.; Riedl, T.; Kahn, A. Electronic Structure of Vanadium Pentoxide: An Efficient Hole Injector for Organic Electronic Materials. *J. Appl. Phys.* **2011**, *110*.033710
(255) Zhang, W.; Li, H.; Yu, W. W.; Elezzabi, A. Y. Transparent Inorganic Multicolour Displays Enabled by Zinc-Based Electrochromic Devices. *Light Sci. Appl.* **2020**, *9*, 121.
(256) Beke, S. A Review of the Growth of V_2O_5 Films from 1885 to 2010. *Thin Solid Films* **2011**, *519*, 1761−1771.
(257) Steunou, N.; Livage, J. Rational Design of One-Dimensional Vanadium(V) Oxide Nanocrystals: An Insight into the Physico-Chemical Parameters Controlling the Crystal Structure, Morphology and Size of Particles. *CrystEngComm* **2015**, *17*, 6780−6795.
(258) Alonso, B.; Livage, J. Synthesis of Vanadium Oxide Gels from Peroxovanadic Acid Solutions: A ^{51}V NMR Study. *J. Solid State Chem.* **1999**, *148*, 16−19.
(259) Etman, A. S.; Pell, A. J.; Svedlindh, P.; Hedin, N.; Zou, X.; Sun, J.; Bernin, D. Insights into the Exfoliation Process of V_2O_5·nH_2O Nanosheet Formation Using Real-Time ^{51}V NMR. *ACS Omega* **2019**, *4*, 10899−10905.
(260) Livage, J. Vanadium Pentoxide Gels. *Chem. Mater.* **1991**, *3*, 578−593.
(261) Li, M.; Kong, F. Y.; Wang, H. Q.; Li, G. H. Synthesis of Vanadium Pentoxide (V_2O_5) Ultralong Nanobelts via an Oriented Attachment Growth Mechanism. *CrystEngComm* **2011**, *13*, 5317−5320.
(262) Grayli, S. V.; Leach, G. W.; Bahreyni, B. Sol-Gel Deposition and Characterization of Vanadium Pentoxide Thin Films with High TCR. *Sens. Actuator A* **2018**, *279*, 630−637.
(263) Surca, A. K.; Drazic, G.; Mihelcic, M. Low-Temperature V-Oxide Film for a Flexible Electrochromic Device: Comparison of Its Electrochromic, IR and Raman Properties to Those of a Crystalline V_2O_5 Film. *Sol. Energy Mater. Sol. Cells* **2019**, *196*, 185−199.
(264) Wan, Z. N.; Mohammad, H.; Zhao, Y. Q.; Yu, C.; Darling, R. B.; Anantram, M. P. Engineering of the Resistive Switching Properties in V_2O_5 Thin Film by Atomic Structural Transition: Experiment and Theory. *J. Appl. Phys.* **2018**, *124*, 105301.
(265) Glynn, C.; Creedon, D.; Geaney, H.; Armstrong, E.; Collins, T.; Morris, M. A.; O'Dwyer, C. Linking Precursor Alterations to Nanoscale Structure and Optical Transparency in Polymer Assisted Fast-Rate Dip-Coating of Vanadium Oxide Thin Films. *Sci. Rep.* **2015**, *5*, 11574.

https://doi.org/10.1021/acs.chemrev.2c00546
Chem. Rev. 2023, 123, 4353−4415

(266) Liu, Y. Q.; Chen, Q. Q.; Du, X. L.; Liu, X. Q.; Li, P. Effects of Substrate on the Structure and Properties of V_2O_5 Thin Films Prepared by the Sol-Gel Method. *AIP Adv.* **2019**, *9*, 045028.
(267) Senapati, S.; Panda, S. Effect of Aging of V_2O_5 Sol on Properties of Nanoscale Films. *Thin Solid Films* **2016**, *599*, 42−48.
(268) Pradeeswari, K.; Venkatesan, A.; Pandi, P.; Prasad, K. G.; Karthik, K.; Maiyalagan, T.; Kumar, R. M. Effect of Cerium on Electrochemical Properties of V_2O_5 Nanoparticles Synthesized via Non-Aqueous Sol-Gel Technique. *Ionics* **2020**, *26*, 905−912.
(269) Yu, Z.; Zheng, J.; Jing, X.; Hang, G.; Liu, Q.; Cai, W. Study on the Optical and Electrochemical Performance of V_2O_5 with Various Morphologies. *J. Dispers. Sci. Technol.* **2020**, *41*, 2203−2210.
(270) Bi, W.; Wang, J.; Jahrman, E. P.; Seidler, G. T.; Gao, G.; Wu, G.; Cao, G. Interface Engineering V_2O_5 Nanofibers for High-Energy and Durable Supercapacitors. *Small* **2019**, *15*, 1901747.
(271) Zhang, H.; Han, X. R.; Gan, R.; Guo, Z. X.; Ni, Y. H.; Zhang, L. A Facile Biotemplate-Assisted Synthesis of Mesoporous V_2O_5 Microtubules for High Performance Asymmetric Supercapacitors. *Appl. Surf. Sci.* **2020**, *511*, 145527.
(272) Li, Y.; Kuang, J. L.; Lu, Y.; Cao, W. B. Facile Synthesis, Characterization of Flower-Like Vanadium Pentoxide Powders and Their Photocatalytic Behavior. *Acta Metall. Sin.* **2017**, *30*, 1017−1026.
(273) Wu, Y. J.; Gao, G. H.; Wu, G. M. Self-Assembled Three-Dimensional Hierarchical Porous V_2O_5/Graphene Hybrid Aerogels for Supercapacitors with High Energy Density and Long Cycle Life. *J. Mater. Chem. A* **2015**, *3*, 1828−1832.
(274) Pan, J.; Li, M.; Luo, Y. Y.; Wu, H.; Zhong, L.; Wang, Q.; Li, G. H. Synthesis and SERS Activity of V_2O_5 Nanoparticles. *Appl. Surf. Sci.* **2015**, *333*, 34−38.
(275) De Jesus, L. R.; Horrocks, G. A.; Liang, Y.; Parija, A.; Jaye, C.; Wangoh, L.; Wang, J.; Fischer, D. A.; Piper, L. F. J.; Prendergast, D.; Banerjee, S. Mapping Polaronic States and Lithiation Gradients in Individual V_2O_5 Nanowires. *Nat. Commun.* **2016**, *7*, 12022.
(276) Liang, X.; Gao, G. H.; Feng, S. Z.; Du, Y. C.; Wu, G. M. Synthesis and Characterization of Carbon Supported V_2O_5 Nanotubes and Their Electrochemical Properties. *J. Alloys Compd.* **2019**, *772*, 429−437.
(277) Li, H.; Tian, H. L.; Chang, T. H.; Zhang, J. Y.; Koh, S. N.; Wang, X. N.; Wang, C. H.; Chen, P. Y. High-Purity V_2O_5 Nanosheets Synthesized from Gasification Waste: Flexible Energy Storage Devices and Environmental Assessment. *ACS Sustain. Chem. Eng.* **2019**, *7*, 12474−12484.
(278) Yue, Y.; Liang, H. Micro- and Nano-Structured Vanadium Pentoxide (V_2O_5) for Electrodes of Lithium-Ion Batteries. *Adv. Energy Mater.* **2017**, *7*, 1602545.
(279) Yan, B.; Li, X. F.; Bai, Z. M.; Zhao, Y.; Dong, L.; Song, X. S.; Li, D. J.; Langford, C.; Sun, X. L. Crumpled Reduced Graphene Oxide Conformally Encapsulated Hollow V_2O_5 Nano/Microsphere Achieving Brilliant Lithium Storage Performance. *Nano Energy* **2016**, *24*, 32−44.
(280) Li, M.; Li, D. B.; Pan, J.; Lin, J. C.; Li, G. H. Selective Synthesis of Vanadium Oxides and Investigation of the Thermochromic Properties of VO_2 by Infrared Spectroscopy. *Eur. J. Inorg. Chem.* **2013**, *2013*, 1207−1212.
(281) Pan, A.; Wu, H. B.; Yu, L.; Lou, X. W. Template-Free Synthesis of VO_2 Hollow Microspheres with Various Interiors and Their Conversion into V_2O_5 for Lithium-Ion Batteries. *Angew. Chem., Int. Ed.* **2013**, *52*, 2226−2230.
(282) Pan, J.; Zhong, L.; Li, M.; Luo, Y.; Li, G. Microwave-Assisted Solvothermal Synthesis of VO_2 Hollow Spheres and Their Conversion into V_2O_5 Hollow Spheres with Improved Lithium Storage Capability. *Chem.—Eur. J.* **2016**, *22*, 1461−1466.
(283) Liang, S.; Hu, Y.; Nie, Z.; Huang, H.; Chen, T.; Pan, A.; Cao, G. Template-Free Synthesis of Ultra-Large V_2O_5 Nanosheets with Exceptional Small Thickness for High-Performance Lithium-Ion Batteries. *Nano Energy* **2015**, *13*, 58−66.
(284) Pan, A.; Wu, H. B.; Yu, L.; Zhu, T.; Lou, X. W. Synthesis of Hierarchical Three-Dimensional Vanadium Oxide Microstructures as High-Capacity Cathode Materials for Lithium-Ion Batteries. *ACS Appl. Mater. Interfaces* **2012**, *4*, 3874−3879.
(285) Liu, J.; Xue, D. Cation-Induced Coiling of Vanadium Pentoxide Nanobelts. *Nanoscale Res. Lett.* **2010**, *5*, 1619.
(286) Le, T. K.; Kang, M.; Kim, S. W. A Review on the Optical Characterization of V_2O_5 Micro-Nanostructures. *Ceram. Int.* **2019**, *45*, 15781−15798.
(287) Vernardou, D.; Marathianou, I.; Katsarakis, N.; Koudoumas, E.; Kazadojev, I. I.; O'Brien, S.; Pemble, M. E.; Povey, I. M. Capacitive Behavior of Ag Doped V_2O_5 Grown by Aerosol Assisted Chemical Vapour Deposition. *Electrochim. Acta* **2016**, *196*, 294−299.
(288) Lee, S.; Kim, J.; Jeon, J. H.; Song, M.; Kim, S.; You, Y. G.; Jhang, S. H.; Seo, S. A.; Chun, S. H. Chemical Vapor-Deposited Vanadium Pentoxide Nanosheets with Highly Stable and Low Switching Voltages for Effective Selector Devices. *ACS Appl. Mater. Interfaces* **2018**, *10*, 42875−42881.
(289) Wang, Y; Su, Q; Chen, C H; Yu, M L; Han, G J; Wang, G Q; Xin, K; Lan, W; Liu, X Q Low Temperature Growth of Vanadium Pentoxide Nanomaterials by Chemical Vapour Deposition Using $VO(acac)_2$ as Precursor. *J. Phys. D* **2010**, *43*, 185102.
(290) Raiford, J. A.; Oyakhire, S. T.; Bent, S. F. Applications of Atomic Layer Deposition and Chemical Vapor Deposition for Perovskite Solar Cells. *Energy Environ. Sci.* **2020**, *13*, 1997−2023.
(291) Chen, X.; Zhu, H.; Chen, Y. C.; Shang, Y.; Cao, A.; Hu, L.; Rubloff, G. W. MWCNT/V_2O_5 Core/Shell Sponge for High Areal Capacity and Power Density Li-Ion Cathodes. *ACS Nano* **2012**, *6*, 7948−7955.
(292) Mattelaer, F.; Geryl, K.; Rampelberg, G.; Dendooven, J.; Detavernier, C. Amorphous and Crystalline Vanadium Oxides as High-Energy and High-Power Cathodes for Three-Dimensional Thin-Film Lithium Ion Batteries. *ACS Appl. Mater. Interfaces* **2017**, *9*, 13121−13131.
(293) Chen, X. Y.; Pomerantseva, E.; Gregorczyk, K.; Ghodssi, R.; Rubloff, G. Cathodic ALD V_2O_5 Thin Films for High-Rate Electrochemical Energy Storage. *RSC Adv.* **2013**, *3*, 4294.
(294) Østreng, E.; Nilsen, O.; Fjellvåg, H. Optical Properties of Vanadium Pentoxide Deposited by ALD. *J. Phys. Chem. C* **2012**, *116*, 19444−19450.
(295) Rossnagel, S. M. Thin Film Deposition with Physical Vapor Deposition and Related Technologies. *J. Vac. Sci. Technol. A* **2003**, *21*, S74−S87.
(296) Lobe, S.; Bauer, A.; Uhlenbruck, S.; Fattakhova-Rohlfing, D. Physical Vapor Deposition in Solid-State Battery Development: From Materials to Devices. *Adv. Sci.* **2021**, *8*, 2002044.
(297) Xia, F.; Yang, L.; Dai, B.; Yang, Z. H.; Xu, L. G.; Gao, G.; Sun, C. Q.; Song, Z. C.; Ralchenko, V.; Zhu, J. Q. Thermal Transition Behaviors of Vanadium Pentoxide Film During Post-Deposition Annealing. *Surf. Coat. Technol.* **2021**, *405*, 126637.
(298) Choi, S. G.; Seok, H. J.; Rhee, S.; Hahm, D.; Bae, W. K.; Kim, H. K. Magnetron-Sputtered Amorphous V_2O_5 Hole Injection Layer for High Performance Quantum Dot Light-Emitting Diode. *J. Alloys Compd.* **2021**, *878*, 160303.
(299) Vijay, V. S.; Varghese, R.; Sakunthala, A.; Rajesh, S.; Vidhya, B. Highly Crystalline V_2O_5 and V_6O_{13} Thin Films by PLD and a Study on Morphology Transition of V_2O_5 by Post Annealing. *Vacuum* **2021**, *187*, 110097.
(300) Huotari, J.; Lappalainen, J. Nanostructured Vanadium Pentoxide Gas Sensors for SCR Process Control. *J. Mater. Sci.* **2017**, *52*, 2241−2253.
(301) Han, S. D.; Moon, H. G.; Noh, M. S.; Pyeon, J. J.; Shim, Y. S.; Nahm, S.; Kim, J. S.; Yoo, K. S.; Kang, C. Y. Self-Doped Nanocolumnar Vanadium Oxides Thin Films for Highly Selective NO_2 Gas Sensing at Low Temperature. *Sens. Actuator B* **2017**, *241*, 40−47.
(302) Thiagarajan, S.; Thaiyan, M.; Ganesan, R. Physical Property Exploration of Highly Oriented V_2O_5 Thin Films Prepared by Electron Beam Evaporation. *New J. Chem.* **2015**, *39*, 9471−9479.
(303) Deniz, A. R. The Temperature Dependence of Current-Voltage Characteristics of V_2O_5/p-Si Heterojunction Diode. *J. Mater. Sci. Mater. Electron.* **2021**, *32*, 18886−18899.

https://doi.org/10.1021/acs.chemrev.2c00546
Chem. Rev. 2023, 123, 4353−4415

(304) Wang, C. C.; Lu, C. L.; Shieu, F. S.; Shih, H. C. Enhanced Photoluminescence Properties of Ga-Doped V_2O_5 Nanorods via Defect Structures. *Chem. Phys. Lett.* **2020**, *738*, 136864.
(305) Uddin, M. N.; Rahman, M. S.; Shumi, W.; Hossain, M. K.; Ullah, A. K. M. A. Characterization, Microbial and Catalytic Application of V_2O_5 Nanoparticles Prepared from Schiff Base Complexes as Precursor. *J. Chem. Sci.* **2020**, *132*, 131.
(306) Velmurugan, R.; Premkumar, J.; Pitchai, R.; Ulaganathan, M.; Subramanian, B. Robust, Flexible, and Binder Free Highly Crystalline V_2O_5 Thin Film Electrodes and Their Superior Supercapacitor Performances. *ACS Sustain. Chem. Eng.* **2019**, *7*, 13115−13126.
(307) Berouaken, M.; Talbi, L.; Yaddadene, C.; Maoudj, M.; Menari, H.; Alkama, R.; Gabouze, N. Room Temperature Ammonia Gas Sensor Based on V_2O_5 Nanoplatelets/Quartz Crystal Microbalance. *Appl. Phys. A: Mater. Sci. Process.* **2020**, *126*, 949.
(308) Zhang, P.; Zhao, L.; An, Q.; Wei, Q.; Zhou, L.; Wei, X.; Sheng, J.; Mai, L. A High-Rate V_2O_5 Hollow Microclew Cathode for an All-Vanadium-based Lithium-Ion Full Cell. *Small* **2016**, *12*, 1082−1090.
(309) Ali, G.; Lee, J. H.; Oh, S. H.; Cho, B. W.; Nam, K.-W.; Chung, K. Y. Investigation of the Na Intercalation Mechanism into Nanosized V_2O_5/C Composite Cathode Material for Na-Ion Batteries. *ACS Appl. Mater. Interfaces* **2016**, *8*, 6032−6039.
(310) Yan, M.; He, P.; Chen, Y.; Wang, S.; Wei, Q.; Zhao, K.; Xu, X.; An, Q.; Shuang, Y.; Shao, Y.; et al. Water-Lubricated Intercalation in $V_2O_5{\cdot}nH_2O$ for High-Capacity and High-Rate Aqueous Rechargeable Zinc Batteries. *Adv. Mater.* **2018**, *30*, 1703725.
(311) Palanisamy, K.; Um, J. H.; Jeong, M.; Yoon, W.-S. Porous V_2O_5/RGO/CNT Hierarchical Architecture as a Cathode Material: Emphasis on the Contribution of Surface Lithium Storage. *Sci. Rep.* **2016**, *6*, 31275.
(312) He, P.; Zhang, G.; Liao, X.; Yan, M.; Xu, X.; An, Q.; Liu, J.; Mai, L. Sodium Ion Stabilized Vanadium Oxide Nanowire Cathode for High-Performance Zinc-Ion Batteries. *Adv. Energy Mater.* **2018**, *8*, 1702463.
(313) Zeng, H.; Liu, D.; Zhang, Y.; See, K. A.; Jun, Y.-S.; Wu, G.; Gerbec, J. A.; Ji, X.; Stucky, G. D. Nanostructured Mn-Doped V_2O_5 Cathode Material Fabricated from Layered Vanadium Jarosite. *Chem. Mater.* **2015**, *27*, 7331−7336.
(314) Chao, D.; Xia, X.; Liu, J.; Fan, Z.; Ng, C. F.; Lin, J.; Zhang, H.; Shen, Z. X.; Fan, H. J. A V_2O_5/Conductive-Polymer Core/Shell Nanobelt Array on Three-Dimensional Graphite Foam: A High-Rate, Ultrastable, and Freestanding Cathode for Lithium-Ion Batteries. *Adv. Mater.* **2014**, *26*, 5794−5800.
(315) Palani, N. S.; Kavitha, N. S.; Venkatesh, K. S.; Kumar, K. A.; Senthilkumar, M.; Pandurangan, A.; Ilangovan, R. The Synergistic Effect of the RuO_2 Nanoparticle-Decorated V_2O_5 Heterostructure for High-Performance Asymmetric Supercapacitors. *New J. Chem.* **2021**, *45*, 14598−14607.
(316) Sahu, V.; Goel, S.; Tomar, A. K.; Singh, G.; Sharma, R. K. Graphene Nanoribbons @ Vanadium Oxide Nanostrips for Supercapacitive Energy Storage. *Electrochim. Acta* **2017**, *230*, 255−264.
(317) Sun, W.; Gao, G. H.; Zhang, K.; Liu, Y. D.; Wu, G. M. Self-Assembled 3D N-CNFs/V_2O_5 Aerogels with Core/Shell Nanostructures through Vacancies Control and Seeds Growth as an Outstanding Supercapacitor Electrode Material. *Carbon* **2018**, *132*, 667−677.
(318) Zhu, C. X.; Hu, D.; Liu, Z. Interconnected Three-Dimensionally Hierarchical Heterostructures with Homogeneously-Dispersed V_2O_5 Nanocrystals and Carbon for High Performance Supercapacitor Electrodes. *Electrochim. Acta* **2017**, *229*, 155−165.
(319) Yao, L.; Zhang, C.; Hu, N.; Zhang, L.; Zhou, Z.; Zhang, Y. Three-Dimensional Skeleton Networks of Reduced Graphene Oxide Nanosheets/Vanadium Pentoxide Nanobelts Hybrid for High-Performance Supercapacitors. *Electrochim. Acta* **2019**, *295*, 14−21.
(320) Shen, F.-C.; Wang, Y.; Tang, Y.-J.; Li, S.-L.; Wang, Y.-R.; Dong, L.-Z.; Li, Y.-F.; Xu, Y.; Lan, Y.-Q. CoV_2O_6-V_2O_5 Coupled with Porous N-Doped Reduced Graphene Oxide Composite as a Highly Efficient Electrocatalyst for Oxygen Evolution. *ACS Energy Lett.* **2017**, *2*, 1327−1333.
(321) Ling, T.; Yan, D.-Y.; Wang, H.; Jiao, Y.; Hu, Z.; Zheng, Y.; Zheng, L.; Mao, J.; Liu, H.; Du, X.-W.; Jaroniec, M.; Qiao, S.-Z. Activating Cobalt(II) Oxide Nanorods for Efficient Electrocatalysis by Strain Engineering. *Nat. Commun.* **2017**, *8*, 1509.
(322) Gong, M.; Wang, D.-Y.; Chen, C.-C.; Hwang, B.-J.; Dai, H. A Mini Review on Nickel-Based Electrocatalysts for Alkaline Hydrogen Evolution Reaction. *Nano Res.* **2016**, *9*, 28−46.
(323) Hu, P.; Long, G.; Chaturvedi, A.; Wang, S.; Tan, K.; He, Y.; Zheng, L.; Liu, G.; Ke, Y.; Zhou, Y.; et al. Agent-Assisted VSSe Ternary Alloy Single Crystals as an Efficient Stable Electrocatalyst for the Hydrogen Evolution Reaction. *J. Mater. Chem. A* **2019**, *7*, 15714−15721.
(324) Gong, Q.; Cheng, L.; Liu, C.; Zhang, M.; Feng, Q.; Ye, H.; Zeng, M.; Xie, L.; Liu, Z.; Li, Y. Ultrathin $MoS_{2(1-x)}Se_{2x}$ Alloy Nanoflakes For Electrocatalytic Hydrogen Evolution Reaction. *ACS Catal.* **2015**, *5*, 2213−2219.
(325) Tan, C.; Luo, Z.; Chaturvedi, A.; Cai, Y.; Du, Y.; Gong, Y.; Huang, Y.; Lai, Z.; Zhang, X.; Zheng, L.; et al. Preparation of High-Percentage 1T-Phase Transition Metal Dichalcogenide Nanodots for Electrochemical Hydrogen Evolution. *Adv. Mater.* **2018**, *30*, 1705509.
(326) Li, Y. H.; Liu, P. F.; Pan, L. F.; Wang, H. F.; Yang, Z. Z.; Zheng, L. R.; Hu, P.; Zhao, H. J.; Gu, L.; Yang, H. G. Local Atomic Structure Modulations Activate Metal Oxide as Electrocatalyst for Hydrogen Evolution in Acidic Water. *Nat. Commun.* **2015**, *6*, 8064.
(327) Bi, W.; Jahrman, E.; Seidler, G.; Wang, J.; Gao, G.; Wu, G.; Atif, M.; AlSalhi, M.; Cao, G. Tailoring Energy and Power Density through Controlling the Concentration of Oxygen Vacancies in V_2O_5/PEDOT Nanocable-Based Supercapacitors. *ACS Appl. Mater. Interfaces* **2019**, *11*, 16647−16655.
(328) Zhang, J.; Zhang, H.; Liu, M.; Xu, Q.; Jiang, H.; Li, C. Cobalt-Stabilized Oxygen Vacancy of V_2O_5 Nanosheet Arrays with Delocalized Valence Electron for Alkaline Water Splitting. *Chem. Eng. Sci.* **2020**, *227*, 115915.
(329) Meena, A.; Ha, M.; Chandrasekaran, S. S.; Sultan, S.; Thangavel, P.; Harzandi, A. M.; Singh, B.; Tiwari, J. N.; Kim, K. S. Pt-Like Hydrogen Evolution on a V_2O_5/$Ni(OH)_2$ Electrocatalyst. *J. Mater. Chem. A* **2019**, *7*, 15794−15800.
(330) Zhong, X.; Zhang, L.; Tang, J.; Chai, J.; Xu, J.; Cao, L.; Yang, M.; Yang, M.; Kong, W.; Wang, S.; et al. Efficient Coupling of a Hierarchical V_2O_5@Ni_3S_2 Hybrid Nanoarray for Pseudocapacitors and Hydrogen Production. *J. Mater. Chem. A* **2017**, *5*, 17954−17962.
(331) Zou, X.; Li, Z.; Xie, Y.; Wu, H.; Lin, S. Phosphorus-Doping and Addition of V_2O_5 into Pt/Graphene Resulting in Highly-Enhanced Electro-Photo Synergistic Catalysis for Oxygen Reduction and Hydrogen Evolution Reactions. *Int. J. Hydrog. Energy* **2020**, *45*, 30647−30658.
(332) Su, J.; Zou, X.-X.; Li, G.-D.; Wei, X.; Yan, C.; Wang, Y.-N.; Zhao, J.; Zhou, L.-J.; Chen, J.-S. Macroporous V_2O_5-$BiVO_4$ Composites: Effect of Heterojunction on the Behavior of Photogenerated Charges. *J. Phys. Chem. C* **2011**, *115*, 8064−8071.
(333) Akbarzadeh, R.; Umbarkar, S. B.; Sonawane, R. S.; Takle, S.; Dongare, M. K. Vanadia-Titania Thin Films for Photocatalytic Degradation of Formaldehyde in Sunlight. *Appl. Catal., A* **2010**, *374*, 103−109.
(334) Arunachalam, M.; Ahn, K.-S.; Kang, S. H. Oxygen Evolution NiOOH Catalyst Assisted V_2O_5@$BiVO_4$ Inverse Opal Hetero-Structure for Solar Water Oxidation. *Int. J. Hydrog. Energy* **2019**, *44*, 4656−4663.
(335) Gomez-Solis, C.; Oliva, J.; Puentes-Prado, E.; Badillo, F.; Garcia, C. R. Effect of Morphology on the Hydrogen Production of V_2O_5 Nano/Micro-Particles Synthesized by a Biodegradable Template. *J. Phys. Chem. Solids* **2021**, *152*, 109977.
(336) Vattikuti, S. V. P.; Reddy, P. A. K.; Shim, J.; Byon, C. Synthesis of Vanadium-Pentoxide-Supported Graphitic Carbon Nitride Heterostructure and Studied Their Hydrogen Evolution Activity Under Solar Light. *J. Mater. Sci. Mater. Electron.* **2018**, *29*, 18760−18770.
(337) Vattikuti, S. V. P.; Nam, N. D.; Shim, J. Graphitic Carbon Nitride/$Na_2Ti_3O_7$/V_2O_5 Nanocomposite as a Visible Light Active Photocatalyst. *Ceram. Int.* **2020**, *46*, 18287−18296.

https://doi.org/10.1021/acs.chemrev.2c00546
Chem. Rev. 2023, 123, 4353−4415

(338) Sadeghzadeh-Attar, A. Enhanced Photocatalytic Hydrogen Evolution by Novel Nb-Doped SnO_2/V_2O_5 Heteronanostructures Under Visible Light with Simultaneous Basic Red 46 Dye Degradation. *J. Asian Ceram. Soc.* **2020**, *8*, 662−676.
(339) Akimov, A. V.; Neukirch, A. J.; Prezhdo, O. V. Theoretical Insights into Photoinduced Charge Transfer and Catalysis at Oxide Interfaces. *Chem. Rev.* **2013**, *113*, 4496−4565.
(340) Chen, X.; Mao, S. S. Titanium Dioxide Nanomaterials: Synthesis, Properties, Modifications, and Applications. *Chem. Rev.* **2007**, *107*, 2891−2959.
(341) Fei, H.-L.; Zhou, H.-J.; Wang, J.-G.; Sun, P.-C.; Ding, D.-T.; Chen, T.-H. Synthesis of Hollow V_2O_5 Microspheres and Application to Photocatalysis. *Solid State Sci.* **2008**, *10*, 1276−1284.
(342) Shanmugam, M.; Alsalme, A.; Alghamdi, A.; Jayavel, R. Enhanced Photocatalytic Performance of the Graphene-V_2O_5 Nanocomposite in the Degradation of Methylene Blue Dye under Direct Sunlight. *ACS Appl. Mater. Interfaces* **2015**, *7*, 14905−14911.
(343) Beaula Ruby Kamalam, M.; Inbanathan, S. S. R.; Sethuraman, K.; Umar, A.; Algadi, H.; Ibrahim, A. A.; Rahman, Q. I.; Garoufalis, C. S.; Baskoutas, S. Direct Sunlight-Driven Enhanced Photocatalytic Performance of V_2O_5 Nanorods/ Graphene Oxide Nanocomposites for the Degradation of Victoria Blue Dye. *Environ. Res.* **2021**, *199*, 111369.
(344) Hong, Y.; Jiang, Y.; Li, C.; Fan, W.; Yan, X.; Yan, M.; Shi, W. In-Situ Synthesis of Direct Solid-State Z-Scheme $V_2O_5/g\text{-}C_3N_4$ Heterojunctions with Enhanced Visible Light Efficiency in Photocatalytic Degradation of Pollutants. *Appl. Catal., B* **2016**, *180*, 663−673.
(345) Jiang, H.; Nagai, M.; Kobayashi, K. Enhanced Photocatalytic Activity for Degradation of Methylene Blue over $V_2O_5/BiVO_4$ Composite. *J. Alloys Compd.* **2009**, *479*, 821−827.
(346) Saravanan, R.; Joicy, S.; Gupta, V. K.; Narayanan, V.; Stephen, A. Visible Light Induced Degradation of Methylene Blue Using CeO_2/V_2O_5 and CeO_2/CuO Catalysts. *Mater. Sci. Eng., C* **2013**, *33*, 4725−4731.
(347) Liu, J.; Yang, R.; Li, S. Preparation and Characterization of the TiO_2-V_2O_5 Photocatalyst with Visible-Light Activity. *Rare Metals* **2006**, *25*, 636−642.
(348) Wang, Y.; Su, Y. R.; Qiao, L.; Liu, L. X.; Su, Q.; Zhu, C. Q.; Liu, X. Q. Synthesis of One-Dimensional TiO_2/V_2O_5 Branched Heterostructures and Their Visible Light Photocatalytic Activity towards Rhodamine B. *Nanotechnology* **2011**, *22*, 225702.
(349) Sun, J.; Li, X.; Zhao, Q.; Ke, J.; Zhang, D. Novel $V_2O_5/BiVO_4/TiO_2$ Nanocomposites with High Visible-Light-Induced Photocatalytic Activity for the Degradation of Toluene. *J. Phys. Chem. C* **2014**, *118*, 10113−10121.
(350) Colton, R. J.; Guzman, A. M.; Rabalais, J. W. Photochromism and Electrochromism in Amorphous Transition Metal Oxide Films. *Acc. Chem. Res.* **1978**, *11*, 170−176.
(351) Colton, R. J.; Guzman, A. M.; Rabalais, J. W. Electrochromism in Some Thin-Film Transition-Metal Oxides Characterized by X-Ray Electron Spectroscopy. *J. Appl. Phys.* **1978**, *49*, 409−416.
(352) Wang, Z.; Wang, X.; Cong, S.; Geng, F.; Zhao, Z. Fusing Electrochromic Technology with Other Advanced Technologies: A New Roadmap for Future Development. *Mater. Sci. Eng. R* **2020**, *140*, 100524.
(353) Mjejri, I.; Gaudon, M.; Song, G.; Labrugère, C.; Rougier, A. Crystallized V_2O_5 as Oxidized Phase for Unexpected Multicolor Electrochromism in V_2O_3 Thick Film. *ACS Appl. Energy Mater.* **2018**, *1*, 2721−2729.
(354) Mjejri, I.; Rougier, A.; Gaudon, M. Low-Cost and Facile Synthesis of the Vanadium Oxides V_2O_3, VO_2, and V_2O_5 and Their Magnetic, Thermochromic and Electrochromic Properties. *Inorg. Chem.* **2017**, *56*, 1734−1741.
(355) Mjejri, I.; Manceriu, L. M.; Gaudon, M.; Rougier, A.; Sediri, F. Nano-vanadium pentoxide films for electrochromic displays. *Solid State Ion.* **2016**, *292*, 8−14.
(356) Mjejri, I.; Gaudon, M.; Rougier, A. Mo addition for improved electrochromic properties of V_2O_5 thick films. *Sol. Energy Mater. Sol. Cells* **2019**, *198*, 19−25.
(357) Salek, G.; Bellanger, B.; Mjejri, I.; Gaudon, M.; Rougier, A. Polyol Synthesis of Ti-V_2O_5 Nanoparticles and Their Use as Electrochromic Films. *Inorg. Chem.* **2016**, *55*, 9838−9847.
(358) Mjejri, I.; Duttine, M.; Buffière, S.; Labrugère-Sarroste, C.; Rougier, A. From the Irreversible Transformation of VO_2 to V_2O_5 Electrochromic Films. *Inorg. Chem.* **2022**, *61*, 18496−18503.
(359) Le, T. K.; Pham, P. V.; Dong, C.-L.; Bahlawane, N.; Vernardou, D.; Mjejri, I.; Rougier, A.; Kim, S. W. Recent Advances in Vanadium Pentoxide (V_2O_5) Towards Related Applications in Chromogenics and Beyond: Fundamentals, Progress, and Perspectives. *J. Mater. Chem. C* **2022**, *10*, 4019−4071.
(360) Surca, A. K.; Dražić, G.; Mihelčič, M. Spectroelectrochemistry in the Investigation of Sol-Gel Electrochromic V_2O_5 Films. *J. Sol-Gel Sci. Technol.* **2020**, *95*, 587−598.
(361) Talledo, A.; Granqvist, C. G. Electrochromic Vanadium-Pentoxide-Based Films: Structural, Electrochemical, and Optical Properties. *J. Appl. Phys.* **1995**, *77*, 4655−4666.
(362) Prasad, A. K.; Park, J.-Y.; Kang, S.-H.; Ahn, K.-S. Electrochemically Co-Deposited WO_3-V_2O_5 Composites for Electrochromic Energy Storage Applications. *Electrochim. Acta* **2022**, *422*, 140340.
(363) Panagopoulou, M.; Vernardou, D.; Koudoumas, E.; Katsarakis, N.; Tsoukalas, D.; Raptis, Y. S. Tunable Properties of Mg-Doped V_2O_5 Thin Films for Energy Applications: Li-Ion Batteries and Electrochromics. *J. Phys. Chem. C* **2017**, *121*, 70−79.
(364) Qi, Y.; Qin, K.; Zou, Y.; Lin, L.; Jian, Z.; Chen, W. Flexible Electrochromic Thin Films with Ultrafast Responsion Based on Exfoliated V_2O_5 Nanosheets/Graphene Oxide via Layer-by-Layer Assembly. *Appl. Surf. Sci.* **2020**, *514*, 145950.
(365) Tong, Z.; Zhang, X.; Lv, H.; Li, N.; Qu, H.; Zhao, J.; Li, Y.; Liu, X.-Y. From Amorphous Macroporous Film to 3D Crystalline Nanorod Architecture: A New Approach to Obtain High-Performance V_2O_5 Electrochromism. *Adv. Mater. Interfaces* **2015**, *2*, 1500230.
(366) Kim, J.; Lee, K. H.; Lee, S.; Park, S.; Chen, H.; Kim, S. K.; Yim, S.; Song, W.; Lee, S. S.; Yoon, D. H.; et al. Minimized Optical Scattering of MXene-Derived 2D V_2O_5 Nanosheet-Based Electrochromic Device with High Multicolor Contrast and Accuracy. *Chem. Eng. J.* **2023**, *453*, 139973.
(367) Calatayud, M.; Andrés, J.; Beltrán, A. A Systematic Density Functional Theory Study of $V_xO_y^+$ and V_xO_Y (X = 2−4, Y = 2−10) Systems. *J. Phys. Chem. A* **2001**, *105*, 9760−9775.
(368) Hübner, O.; Himmel, H.-J. Multiple Metal-Metal Bond or No Bond? The Electronic Structure of V_2O_2. *Angew. Chem., Int. Ed.* **2017**, *56*, 12340−12343.
(369) Jakubikova, E.; Rappé, A. K.; Bernstein, E. R. Density Functional Theory Study of Small Vanadium Oxide Clusters. *J. Phys. Chem. A* **2007**, *111*, 12938−12943.
(370) Wang, Y.; Gong, X.; Wang, J. Comparative DFT Study of Structure and Magnetism of TM_nO_m (TM = Sc-Mn, n = 1−2, m = 1−6) Clusters. *Phys. Chem. Chem. Phys.* **2010**, *12*, 2471−2477.
(371) Yamazaki, S.; Li, C.; Ohoyama, K.; Nishi, M.; Ichihara, M.; Ueda, H.; Ueda, Y. Synthesis, Structure and Magnetic Properties of V_4O_9—A Missing Link in Binary Vanadium Oxides. *J. Solid State Chem.* **2010**, *183*, 1496−1503.
(372) Kawashima, K.; Kosuge, K.; Kachi, S. Isothermal Reduction of V_2O_5 by SO_2 Gas. *Chem. Lett.* **1975**, *4*, 1131−1136.
(373) Pang, H.; Dong, Y.; Ting, S. L.; Lu, J.; Li, C. M.; Kim, D.-H.; Chen, P. 2D Single- or Double-Layered Vanadium Oxide Nanosheet Assembled 3D Microflowers: Controlled Synthesis, Growth Mechanism, and Applications. *Nanoscale* **2013**, *5*, 7790−7794.
(374) Chine, M. K.; Sediri, F.; Gharbi, N. Solvothermal Synthesis of V_4O_9 Flake-Like Morphology and Its Photocatalytic Application in the Degradation of Methylene Blue. *Mater. Res. Bull.* **2012**, *47*, 3422−3426.
(375) Wang, Q.; Sun, T.; Zheng, S.; Li, L.; Ma, T.; Liang, J. A new Tunnel-Type V_4O_9 Cathode for High Power Density Aqueous Zinc Ion Batteries. *Inorg. Chem. Front.* **2021**, *8*, 4497−4506.
(376) Chen, X.; Wang, L.; Li, H.; Cheng, F.; Chen, J. Porous V_2O_5 Nanofibers as Cathode Materials for Rechargeable Aqueous Zinc-Ion Batteries. *J. Energy Chem.* **2019**, *38*, 20−25.

https://doi.org/10.1021/acs.chemrev.2c00546
Chem. Rev. 2023, 123, 4353−4415

(377) Shan, L.; Zhou, J.; Zhang, W.; Xia, C.; Guo, S.; Ma, X.; Fang, G.; Wu, X.; Liang, S. Highly Reversible Phase Transition Endows V_6O_{13} with Enhanced Performance as Aqueous Zinc-Ion Battery Cathode. *Energy Technol.* **2019**, *7*, 1900022.
(378) Alfaruqi, M. H.; Mathew, V.; Song, J.; Kim, S.; Islam, S.; Pham, D. T.; Jo, J.; Kim, S.; Baboo, J. P.; Xiu, Z.; et al. Electrochemical Zinc Intercalation in Lithium Vanadium Oxide: A High-Capacity Zinc-Ion Battery Cathode. *Chem. Mater.* **2017**, *29*, 1684−1694.
(379) Li, G.; Yang, Z.; Jiang, Y.; Jin, C.; Huang, W.; Ding, X.; Huang, Y. Towards Polyvalent Ion Batteries: A Zinc-Ion Battery Based on NASICON Structured $Na_3V_2(PO_4)_3$. *Nano Energy* **2016**, *25*, 211−217.
(380) Wei, T.; Li, Q.; Yang, G.; Wang, C. An Electrochemically Induced Bilayered Structure Facilitates Long-Life Zinc Storage of Vanadium Dioxide. *J. Mater. Chem. A* **2018**, *6*, 8006−8012.
(381) He, P.; Yan, M.; Zhang, G.; Sun, R.; Chen, L.; An, Q.; Mai, L. Layered VS_2 Nanosheet-Based Aqueous Zn Ion Battery Cathode. *Adv. Energy Mater.* **2017**, *7*, 1601920.
(382) Xue, K. H.; Yang, H.; Zhou, Y. M.; Li, G.; Skotheim, T. A.; Lee, H. S.; Yang, X. Q.; McBreen, J. A Study of the Zn/V_6 O_{13} Secondary Battery. *J. Electrochem. Soc.* **1993**, *140*, 3413−3417.
(383) Ding, Y.-L.; Wen, Y.; Wu, C.; van Aken, P. A.; Maier, J.; Yu, Y. 3D V_6O_{13} Nanotextiles Assembled From Interconnected Nanogrooves as Cathode Materials for High-Energy Lithium Ion Batteries. *Nano Lett.* **2015**, *15*, 1388−1394.
(384) Hu, J.; Chen, H.; Xiang, K.; Xiao, L.; Chen, W.; Liao, H.; Chen, H. Preparation for V_6O_{13}@hollow Carbon Microspheres and Their Remarkable Electrochemical Performance for Aqueous Zinc-Ion Batteries. *J. Alloys Compd.* **2021**, *856*, 157085.
(385) He, P.; Liu, J.; Zhao, X.; Ding, Z.; Gao, P.; Fan, L.-Z. A Three-Dimensional Interconnected V_6O_{13} Nest with a V^{5+}-Rich State for Ultrahigh Zn Ion Storage. *J. Mater. Chem. A* **2020**, *8*, 10370−10376.
(386) Wu, M.; Zhu, K.; Liang, P.; Yao, Z.; Shi, F.; Zhang, J.; Yan, K.; Liu, J.; Wang, J. Uniform Rotate Hydrothermal Synthesis of V_6O_{13} Nanosheets as Cathode Material for Lithium-Ion Battery. *J. Alloys Compd.* **2021**, *877*, 160174.
(387) Wu, X.; Zou, Z.; Li, S.; Zhang, Y. Solvothermal Preparation of Ga-Doped V_6O_{13} Nanowires as Cathode Materials for Lithium-Ion Batteries. *Ionics* **2019**, *25*, 4557−4565.
(388) Zhang, S.; Zou, Z.; Zhang, H.; Liu, J.; Zhong, S. Al/Ga Co-Doped V_6O_{13} Nanorods with High Discharge Specific Capacity as Cathode Materials for Lithium-Ion Batteries. *J. Electroanal. Chem.* **2021**, *890*, 115220.
(389) Wang, Z.; Zhang, Y.; Xiao, S.; Zhai, H.; Zhu, Y.; Cao, C. Microwave-Assisted Synthesis of Metallic V_6O_{13} Nanosheet as High-Capacity Cathode for Magnesium Storage. *Mater. Lett.* **2022**, *308*, 131279.
(390) Li, S.; Zou, Z.; Wu, X.; Zhang, Y. Solvothermal Preparation of Carbon Coated V_6O_{13} Nanocomposite as Cathode Material for Lithium-Ion Battery. *J. Electroanal. Chem.* **2019**, *846*, 113173.
(391) Tian, X.; Xu, X.; He, L.; Wei, Q.; Yan, M.; Xu, L.; Zhao, Y.; Yang, C.; Mai, L. Ultrathin Pre-lithiated V_6O_{13} Nanosheet Cathodes with Enhanced Electrical Transport and Cyclability. *J. Power Sources* **2014**, *255*, 235−241.
(392) Shin, J.; Choi, D. S.; Lee, H. J.; Jung, Y.; Choi, J. W. Hydrated Intercalation for High-Performance Aqueous Zinc Ion Batteries. *Adv. Energy Mater.* **2019**, *9*, 1900083.
(393) Lai, J.; Zhu, H.; Zhu, X.; Koritala, H.; Wang, Y. Interlayer-Expanded V_6O_{13}·nH_2O Architecture Constructed for an Advanced Rechargeable Aqueous Zinc-Ion Battery. *ACS Appl. Energy Mater.* **2019**, *2*, 1988−1996.
(394) Chen, Q.; Luo, Z.; Zhao, X. K-Ion Intercalated V_6O_{13} with Advanced High-Rate Long-Cycle Performance as Cathode for Zn-Ion Batteries. *J. Mater. Chem. C* **2022**, *10*, 590−597.
(395) Yang, G.; Wang, C. Platinum-Induced Pseudo-Zn-Air Reaction Massively Increases the Electrochemical Capacity of Aqueous Zn/V_5O_{12}·6H_2O Batteries. *Energy Environ. Mater.* **2021**, *4*, 596−602.
(396) Dai, Y.; Liao, X.; Yu, R.; Li, J.; Li, J.; Tan, S.; He, P.; An, Q.; Wei, Q.; Chen, L.; et al. Quicker and More Zn^{2+} Storage Predominantly from the Interface. *Adv. Mater.* **2021**, *33*, 2100359.
(397) Li, Y.; Tan, X.; Hocking, R. K.; Bo, X.; Ren, H.; Johannessen, B.; Smith, S. C.; Zhao, C. Implanting Ni-O-VO_x Sites into Cu-Doped Ni for Low-Overpotential Alkaline Hydrogen Evolution. *Nat. Commun.* **2020**, *11*, 2720.
(398) Chen, M.; Liu, J.; Kitiphatpiboon, N.; Li, X.; Wang, J.; Hao, X.; Abudula, A.; Ma, Y.; Guan, G. Zn-VO_x-Co Nanosheets with Amorphous/Crystalline Heterostructure for Highly Efficient Hydrogen Evolution Reaction. *Chem. Eng. J.* **2022**, *432*, 134329.
(399) Chai, Y.-M.; Zhang, X.-Y.; Lin, J.-H.; Qin, J.-F.; Liu, Z.-Z.; Xie, J.-Y.; Guo, B.-Y.; Yang, Z.; Dong, B. Three-Dimensional VO_x/NiS/NF Nanosheets as Efficient Electrocatalyst for Oxygen Evolution Reaction. *Int. J. Hydrog. Energy* **2019**, *44*, 10156−10162.
(400) Zhu, Z.; Xu, K.; Guo, W.; Zhang, H.; Xiao, X.; He, M.; Yu, T.; Zhao, H.; Zhang, D.; Yang, T. Vanadium-Phosphorus Incorporation Induced Interfacial Modification on Cobalt Catalyst and Its Super Electrocatalysis for Water Splitting in Alkaline Media. *Appl. Catal., B* **2022**, *304*, 120985.
(401) Wang, X.; Zhang, Z.; Huang, M.; Feng, J.; Xiong, S.; Xi, B. In Situ Electrochemically Activated Vanadium Oxide Cathode for Advanced Aqueous Zn-Ion Batteries. *Nano Lett.* **2022**, *22*, 119−127.
(402) Luo, T.; Liu, Y.; Su, H.; Xiao, R.; Huang, L.; Xiang, Q.; Zhou, Y.; Chen, C. Nanostructured-VO_2(B): A High-Capacity Magnesium-Ion Cathode and Its Electrochemical Reaction Mechanism. *Electrochim. Acta* **2018**, *260*, 805−813.
(403) Balogun, M.-S.; Luo, Y.; Lyu, F.; Wang, F.; Yang, H.; Li, H.; Liang, C.; Huang, M.; Huang, Y.; Tong, Y. Carbon Quantum Dot Surface-Engineered VO_2 Interwoven Nanowires: A Flexible Cathode Material for Lithium and Sodium Ion Batteries. *ACS Appl. Mater. Interfaces* **2016**, *8*, 9733−9744.
(404) Yang, S.; Gong, Y.; Liu, Z.; Zhan, L.; Hashim, D. P.; Ma, L.; Vajtai, R.; Ajayan, P. M. Bottom-up Approach toward Single-Crystalline VO_2-Graphene Ribbons as Cathodes for Ultrafast Lithium Storage. *Nano Lett.* **2013**, *13*, 1596−1601.
(405) Ren, G.; Hoque, M. N. F.; Pan, X.; Warzywoda, J.; Fan, Z. Vertically Aligned VO_2(B) Nanobelt Forest and Its Three-Dimensional Structure on Oriented Graphene for Energy Storage. *J. Mater. Chem. A* **2015**, *3*, 10787−10794.
(406) Ding, J.; Du, Z.; Gu, L.; Li, B.; Wang, L.; Wang, S.; Gong, Y.; Yang, S. Ultrafast Zn^{2+} Intercalation and Deintercalation in Vanadium Dioxide. *Adv. Mater.* **2018**, *30*, 1800762.
(407) He, P.; Quan, Y.; Xu, X.; Yan, M.; Yang, W.; An, Q.; He, L.; Mai, L. High-Performance Aqueous Zinc-Ion Battery Based on Layered $H_2V_3O_8$ Nanowire Cathode. *Small* **2017**, *13*, 1702551.
(408) Pang, Q.; Sun, C.; Yu, Y.; Zhao, K.; Zhang, Z.; Voyles, P. M.; Chen, G.; Wei, Y.; Wang, X. $H_2V_3O_8$ Nanowire/Graphene Electrodes for Aqueous Rechargeable Zinc Ion Batteries with High Rate Capability and Large Capacity. *Adv. Energy Mater.* **2018**, *8*, 1800144.
(409) Wang, X.; Zheng, S.; Mu, X.; Zhang, Y.; Du, H. Additive-Free Synthesis of V_4O_7 Hierarchical Structures as High Performance Cathodes for Lithium Ion Batteries. *Chem. Commun.* **2014**, *50*, 6775−6778.
(410) Fei, H.; Lin, Y.; Wei, M. Facile Synthesis of V_6O_{13} Micro-Flowers for Li-Ion and Na-Ion Battery Cathodes with Good Cycling Performance. *J. Colloid Interface Sci.* **2014**, *425*, 1−4.
(411) Liao, M.; Wang, J.; Ye, L.; Sun, H.; Wen, Y.; Wang, C.; Sun, X.; Wang, B.; Peng, H. A Deep-Cycle Aqueous Zinc-Ion Battery Containing an Oxygen-Deficient Vanadium Oxide Cathode. *Angew. Chem., Int. Ed.* **2020**, *59*, 2273−2278.
(412) Zhang, N.; Jia, M.; Dong, Y.; Wang, Y.; Xu, J.; Liu, Y.; Jiao, L.; Cheng, F. Hydrated Layered Vanadium Oxide as a Highly Reversible Cathode for Rechargeable Aqueous Zinc Batteries. *Adv. Funct. Mater.* **2019**, *29*, 1807331.
(413) Wei, T.; Li, Q.; Yang, G.; Wang, C. High-Rate and Durable Aqueous Zinc Ion Battery Using Dendritic $V_{10}O_{24}$·12H_2O Cathode Material with Large Interlamellar Spacing. *Electrochim. Acta* **2018**, *287*, 60−67.
(414) Li, S.; Wei, X.; Chen, H.; Lai, G.; Wang, X.; Zhang, S.; Wu, S.; Tang, W.; Lin, Z. A Mixed-Valent Vanadium Oxide Cathode with

https://doi.org/10.1021/acs.chemrev.2c00546
Chem. Rev. 2023, 123, 4353−4415

Ultrahigh Rate Capability for Aqueous Zinc-Ion Batteries. *J. Mater. Chem. A* **2021**, *9*, 22392−22398.
(415) Yang, F.; Zhu, Y.; Xia, Y.; Xiang, S.; Han, S.; Cai, C.; Wang, Q.; Wang, Y.; Gu, M. Fast Zn^{2+} Kinetics of Vanadium Oxide Nanotubes in High-Performance Rechargeable Zinc-Ion Batteries. *J. Power Sources* **2020**, *451*, 227767.
(416) Su, D. W.; Dou, S. X.; Wang, G. X. Hierarchical Orthorhombic V_2O_5 Hollow Nanospheres as High Performance Cathode Materials for Sodium-Ion Batteries. *J. Mater. Chem. A* **2014**, *2*, 11185−11194.
(417) Jayaprakash, N.; Das, S. K.; Archer, L. A. The Rechargeable Aluminum-Ion Battery. *Chem. Commun.* **2011**, *47*, 12610−12612.
(418) Zhang, N.; Dong, Y.; Jia, M.; Bian, X.; Wang, Y.; Qiu, M.; Xu, J.; Liu, Y.; Jiao, L.; Cheng, F. Rechargeable Aqueous Zn-V_2O_5 Battery with High Energy Density and Long Cycle Life. *ACS Energy Lett.* **2018**, *3*, 1366−1372.
(419) Zhou, J.; Shan, L.; Wu, Z.; Guo, X.; Fang, G.; Liang, S. Investigation of V_2O_5 as a Low-Cost Rechargeable Aqueous Zinc Ion Battery Cathode. *Chem. Commun.* **2018**, *54*, 4457−4460.
(420) Wang, S.; Li, S.; Sun, Y.; Feng, X.; Chen, C. Three-Dimensional Porous V_2O_5 Cathode with Ultra High Rate Capability. *Energy Environ. Sci.* **2011**, *4*, 2854−2857.
(421) Zuo, C.; Xiao, Y.; Pan, X.; Xiong, F.; Zhang, W.; Long, J.; Dong, S.; An, Q.; Luo, P. Organic-Inorganic Superlattices of Vanadium Oxide@Polyaniline for High-Performance Magnesium-Ion Batteries. *ChemSusChem* **2021**, *14*, 2093−2099.
(422) Han, C.; Zhu, J.; Fu, K.; Deng, D.; Luo, W.; Mai, L. A High-Capacity Polyaniline-Intercalated Layered Vanadium Oxide for Aqueous Ammonium-Ion Batteries. *Chem. Commun.* **2022**, *58*, 791−794.
(423) Wei, Q.; Liu, J.; Feng, W.; Sheng, J.; Tian, X.; He, L.; An, Q.; Mai, L. Hydrated Vanadium Pentoxide with Superior Sodium Storage Capacity. *J. Mater. Chem. A* **2015**, *3*, 8070−8075.
(424) Chae, M. S.; Heo, J. W.; Hyoung, J.; Hong, S.-T. Double-Sheet Vanadium Oxide as a Cathode Material for Calcium-Ion Batteries. *ChemNanoMat* **2020**, *6*, 1049−1053.
(425) Xu, C.; Li, M.; Li, K.; Du, Z.; Chen, J.; Zou, F.; Xu, S.; Li, N.; Li, G. VOOH Nanosheets with Enhanced Capacitance as Supercapacitor Electrode. *J. Alloys Compd.* **2021**, *869*, 159367.
(426) Hu, T.; Liu, Y.; Zhang, Y.; Nie, Y.; Zheng, J.; Wang, Q.; Jiang, H.; Meng, C. Encapsulating V_2O_3 Nanorods into Carbon Core-Shell Composites with Porous Structures and Large Specific Surface Area for High Performance Solid-State Supercapacitors. *Microporous Mesoporous Mater.* **2018**, *262*, 199−206.
(427) Zhang, Y. Designed Synthesis and Supercapacitor Electrode of V_2O_3@C Core-Shell Structured Nanorods with Excellent Pseudo-Capacitance in Na_2SO_4 Neutral Electrolyte. *ChemistrySelect* **2018**, *3*, 1577−1584.
(428) Zheng, J.; Zhang, Y.; Jing, X.; Liu, X.; Hu, T.; Lv, T.; Zhang, S.; Meng, C. Synthesis of Amorphous Carbon Coated on V_2O_3 Core-Shell Composites for Enhancing the Electrochemical Properties of V_2O_3 as Supercapacitor Electrode. *Colloids Surf., A* **2017**, *518*, 188−196.
(429) Yasoda, K. Y.; Mikhaylov, A. A.; Medvedev, A. G.; Kumar, M. S.; Lev, O.; Prikhodchenko, P. V.; Batabyal, S. K. Brush Like Polyaniline on Vanadium Oxide Decorated Reduced Graphene Oxide: Efficient Electrode Materials for Supercapacitor. *J. Energy Storage* **2019**, *22*, 188−193.
(430) Rakhi, R. B.; Nagaraju, D. H.; Beaujuge, P.; Alshareef, H. N. Supercapacitors Based on Two Dimensional VO_2 Nanosheet Electrodes in Organic Gel Electrolyte. *Electrochim. Acta* **2016**, *220*, 601−608.
(431) Ndiaye, N. M.; Madito, M. J.; Ngom, B. D.; Masikhwa, T. M.; Mirghni, A. A.; Manyala, N. High-Performance Asymmetric Supercapacitor Based on Vanadium Dioxide and Carbonized Iron-Polyaniline Electrodes. *AIP Adv.* **2019**, *9*, 055309.
(432) Zhang, Y.; Zheng, J.; Hu, T.; Tian, F.; Meng, C. Synthesis and Supercapacitor Electrode of VO_2(B)/C Core-Shell Composites with a Pseudocapacitance in Aqueous Solution. *Appl. Surf. Sci.* **2016**, *371*, 189−195.
(433) Xia, X.; Chao, D.; Ng, C. F.; Lin, J.; Fan, Z.; Zhang, H.; Shen, Z. X.; Fan, H. J. VO_2 Nanoflake Arrays for Supercapacitor and Li-Ion Battery Electrodes: Performance Enhancement by Hydrogen Molybdenum Bronze as an Efficient Shell Material. *Mater. Horizons* **2015**, *2*, 237−244.
(434) Fan, Y.; Ouyang, D.; Li, B.-W.; Dang, F.; Ren, Z. Two-Dimensional VO_2 Mesoporous Microarrays for High-Performance Supercapacitor. *Nanoscale Res. Lett.* **2018**, *13*, 142.
(435) Nie, G.; Lu, X.; Zhu, Y.; Chi, M.; Gao, M.; Chen, S.; Wang, C. Reactive Template Synthesis of Inorganic/Organic VO_2@Polyaniline Coaxial Nanobelts for High-Performance Supercapacitors. *ChemElectroChem.* **2017**, *4*, 1095−1100.
(436) Yang, W.; Zeng, J.; Xue, Z.; Ma, T.; Chen, J.; Li, N.; Zou, H.; Chen, S. Synthesis of Vanadium Oxide Nanorods Coated with Carbon Nanoshell for a High-Performance Supercapacitor. *Ionics* **2020**, *26*, 961−970.
(437) Zeng, H. M.; Zhao, Y.; Hao, Y. J.; Lai, Q. Y.; Huang, J. H.; Ji, X. Y. Preparation and Capacitive Properties of Sheet V_6O_{13} for Electrochemical Supercapacitor. *J. Alloys Compd.* **2009**, *477*, 800−804.
(438) Ling, W.; Zhang, S.; Peng, X.; Zhong, S.; Liang, F.; Geng, J.; Zou, Z. The Prospected Application of V_6O_{13} in Lithium-Ion Supercapacitors Based on Its Researches in Lithium-Ion Batteries and Supercapacitors. *Ionics* **2021**, *27*, 4961−4981.
(439) Zhai, T.; Lu, X.; Ling, Y.; Yu, M.; Wang, G.; Liu, T.; Liang, C.; Tong, Y.; Li, Y. A New Benchmark Capacitance for Supercapacitor Anodes by Mixed-Valence Sulfur-Doped V_6O_{13-x}. *Adv. Mater.* **2014**, *26*, 5869−5875.
(440) Saravanakumar, B.; Purushothaman, K. K.; Muralidharan, G. Interconnected V_2O_5 Nanoporous Network for High-Performance Supercapacitors. *ACS Appl. Mater. Interfaces* **2012**, *4*, 4484−4490.
(441) Li, M.; Sun, G.; Yin, P.; Ruan, C.; Ai, K. Controlling the Formation of Rodlike V_2O_5 Nanocrystals on Reduced Graphene Oxide for High-Performance Supercapacitors. *ACS Appl. Mater. Interfaces* **2013**, *5*, 11462−11470.
(442) Chen, Y.; Lian, P.; Feng, J.; Liu, Y.; Wang, L.; Liu, J.; Shi, X. Tailoring Defective Vanadium Pentoxide/Reduced Graphene Oxide Electrodes for All-Vanadium-Oxide Asymmetric Supercapacitors. *Chem. Eng. J.* **2022**, *429*, 132274.
(443) Zhang, H.; Xie, A.; Wang, C.; Wang, H.; Shen, Y.; Tian, X. Bifunctional Reduced Graphene Oxide/V_2O_5 Composite Hydrogel: Fabrication, High Performance as Electromagnetic Wave Absorbent and Supercapacitor. *ChemPhysChem* **2014**, *15*, 366−373.
(444) Saravanakumar, B.; Purushothaman, K. K.; Muralidharan, G. High Performance Supercapacitor Based on Carbon Coated V_2O_5 Nanorods. *J. Electroanal. Chem.* **2015**, *758*, 111−116.
(445) Yang, J.; Lan, T.; Liu, J.; Song, Y.; Wei, M. Supercapacitor Electrode of Hollow Spherical V_2O_5 with a High Pseudocapacitance in Aqueous Solution. *Electrochim. Acta* **2013**, *105*, 489−495.
(446) Karade, S. S.; Lalwani, S.; Eum, J.-H.; Kim, H. Coin Cell Fabricated Symmetric Supercapacitor Device of Two-Steps Synthesized V_2O_5 Nanorods. *J. Electroanal. Chem.* **2020**, *864*, 114080.
(447) Kiruthiga, R.; Nithya, C.; Karvembu, R.; Venkata Rami Reddy, B. Reduced Graphene Oxide Embedded V_2O_5 Nanorods and Porous Honey Carbon as High Performance Electrodes for Hybrid Sodium-Ion Supercapacitors. *Electrochim. Acta* **2017**, *256*, 221−231.
(448) Nagaraju, D. H.; Wang, Q.; Beaujuge, P.; Alshareef, H. N. Two-Dimensional Heterostructures of V_2O_5 and Reduced Graphene Oxide as Electrodes for High Energy Density Asymmetric Supercapacitors. *J. Mater. Chem. A* **2014**, *2*, 17146−17152.
(449) Zhang, S.; Chen, S.; Luo, Y.; Yan, B.; Gu, Y.; Yang, F.; Cao, Y. Large-Scale Preparation of Solution-Processable One-Dimensional V_2O_5 Nanobelts with Ultrahigh Aspect Ratio for Bifunctional Multicolor Electrochromic and Supercapacitor Applications. *J. Alloys Compd.* **2020**, *842*, 155882.
(450) Zhang, Y.; Zheng, J.; Wang, Q.; Zhang, S.; Hu, T.; Meng, C. One-Step Hydrothermal Preparation of $(NH_4)_2V_3O_8$/Carbon Composites and Conversion to Porous V_2O_5 Nanoparticles as Supercapacitor Electrode with Excellent Pseudocapacitive Capability. *Appl. Surf. Sci.* **2017**, *423*, 728−742.

https://doi.org/10.1021/acs.chemrev.2c00546
Chem. Rev. 2023, 123, 4353−4415

(451) Yilmaz, G.; Lu, X.; Ho, G. W. Cross-Linker Mediated Formation of Sulfur-Functionalized V_2O_5/Graphene Aerogels and their Enhanced Pseudocapacitive Performance. *Nanoscale* **2017**, *9*, 802−811.
(452) Liu, Z.; Zhang, H.; Yang, Q.; Chen, Y. Graphene/V_2O_5 Hybrid Electrode for an Asymmetric Supercapacitor with High Energy Density in an Organic Electrolyte. *Electrochim. Acta* **2018**, *287*, 149−157.
(453) Wu, Y.; Gao, G.; Yang, H.; Bi, W.; Liang, X.; Zhang, Y.; Zhang, G.; Wu, G. Controlled Synthesis of V_2O_5/MWCNT Core/Shell Hybrid Aerogels through a Mixed Growth and Self-Assembly Methodology for Supercapacitors with High Capacitance and Ultralong Cycle Life. *J. Mater. Chem. A* **2015**, *3*, 15692−15699.
(454) Balasubramanian, S.; Purushothaman, K. K. Carbon Coated Flowery V_2O_5 Nanostructure as Novel Electrode Material for High Performance Supercapacitors. *Electrochim. Acta* **2015**, *186*, 285−291.
(455) Tian, M.; Li, R.; Liu, C.; Long, D.; Cao, G. Aqueous Al-Ion Supercapacitor with V_2O_5 Mesoporous Carbon Electrodes. *ACS Appl. Mater. Interfaces* **2019**, *11*, 15573−15580.
(456) Ghaly, H. A.; El-Deen, A. G.; Souaya, E. R.; Allam, N. K. Asymmetric Supercapacitors Based on 3D Graphene-Wrapped V_2O_5 Nanospheres and Fe_3O_4@3D Graphene Electrodes with High Power and Energy Densities. *Electrochim. Acta* **2019**, *310*, 58−69.
(457) Qian, T.; Xu, N.; Zhou, J.; Yang, T.; Liu, X.; Shen, X.; Liang, J.; Yan, C. Interconnected Three-Dimensional V_2O_5/Polypyrrole Network Nanostructures for High Performance Solid-State Supercapacitors. *J. Mater. Chem. A* **2015**, *3*, 488−493.
(458) Aamir, A.; Ahmad, A.; Shah, S. K.; Ain, N.; Mehmood, M.; Khan, Y.; Rehman, Z. Electro-Codeposition of V_2O_5-Polyaniline Composite on Ni Foam as an Electrode for Supercapacitor. *J. Mater. Sci. Mater. Electron.* **2020**, *31*, 21035−21045.
(459) Manikandan, R.; Justin Raj, C.; Rajesh, M.; Kim, B. C.; Park, S. Y.; Cho, B.-B.; Yu, K. H. Polycrystalline V_2O_5/$Na_{0.33}V_2O_5$ Electrode Material for Li^+ Ion Redox Supercapacitor. *Electrochim. Acta* **2017**, *230*, 492−500.
(460) Xu, J.; Zheng, F.; Xi, C.; Yu, Y.; Chen, L.; Yang, W.; Hu, P.; Zhen, Q.; Bashir, S. Facile Preparation of Hierarchical Vanadium Pentoxide (V_2O_5)/Titanium Dioxide (TiO_2) Heterojunction Composite Nano-Arrays for High Performance Supercapacitor. *J. Power Sources* **2018**, *404*, 47−55.
(461) Sun, W.; Gao, G.; Du, Y.; Zhang, K.; Wu, G. A Facile Strategy for Fabricating Hierarchical Nanocomposites of V_2O_5 Nanowire Arrays on a Three-Dimensional N-Doped Graphene Aerogel with a Synergistic Effect for Supercapacitors. *J. Mater. Chem. A* **2018**, *6*, 9938−9947.
(462) Bi, W.; Huang, J.; Wang, M.; Jahrman, E. P.; Seidler, G. T.; Wang, J.; Wu, Y.; Gao, G.; Wu, G.; Cao, G. V_2O_5-Conductive Polymer Nanocables with Built-in Local Electric Field Derived from Interfacial Oxygen Vacancies for High Energy Density Supercapacitors. *J. Mater. Chem. A* **2019**, *7*, 17966−17973.
(463) Jiao, Y.; Wan, C.; Wu, Y.; Han, J.; Bao, W.; Gao, H.; Wang, Y.; Wang, C.; Li, J. Ultra-High Rate Capability of Nanoporous Carbon Network@V_2O_5 Sub-Micron Brick Composite as a Novel Cathode Material for Asymmetric Supercapacitors. *Nanoscale* **2020**, *12*, 23213−23224.
(464) Patil, M. D.; Dhas, S. D.; Mane, A. A.; Moholkar, A. V. Clinker-Like V_2O_5 Nanostructures Anchored on 3D Ni-Foam for Supercapacitor Application. *Mater. Sci. Semicond. Process.* **2021**, *133*, 105978.
(465) Latha, K.; Anbuselvi, S.; Periasamy, P.; Sudha, R.; Velmurugan, D. Microwave-Assisted hybridised WO_3/V_2O_5 Rod Shape Nanocomposites for Electrochemical Supercapacitor Applications. *Inorg. Chem. Commun.* **2021**, *133*, 108927.
(466) Devarayapalli, K. C.; Lee, K.; Do, H. B.; Dang, N. N.; Yoo, K.; Shim, J.; Prabhakar Vattikuti, S. V. Mesostructured g-C_3N_4 Nanosheets Interconnected with V_2O_5 Nanobelts as Electrode for Coin-Cell-Type-Asymmetric Supercapacitor Device. *Mater. Today Energy* **2021**, *21*, 100699.
(467) Javed, M. S.; Najim, T.; Hussain, I.; Batool, S.; Idrees, M.; Mehmood, A.; Imran, M.; Assiri, M. A.; Ahmad, A.; Ahmad Shah, S. S. 2D V_2O_5 Nanoflakes as a Binder-Free Electrode Material for High-Performance Pseudocapacitor. *Ceram. Int.* **2021**, *47*, 25152−25157.
(468) Sun, G.; Ren, H.; Shi, Z.; Zhang, L.; Wang, Z.; Zhan, K.; Yan, Y.; Yang, J.; Zhao, B. V_2O_5/Vertically-Aligned Carbon Nanotubes as Negative Electrode for Asymmetric Supercapacitor in Neutral Aqueous Electrolyte. *J. Colloid Interface Sci.* **2021**, *588*, 847−856.
(469) You, M.; Zhang, W.; Yan, X.; Jiang, H.; Miao, J.; Li, Y.; Zhou, W.; Zhu, Y.; Cheng, X. V_2O_5 Nanosheets Assembled on 3D Carbon Fiber Felt as a Free-Standing Electrode for Flexible Asymmetric Supercapacitor with Remarkable Energy Density. *Ceram. Int.* **2021**, *47*, 3337−3345.
(470) Zhou, P.; Lv, X.; Gao, Y.; Cui, Z.; Liu, Y.; Wang, Z.; Wang, P.; Zheng, Z.; Dai, Y.; Huang, B. Enhanced Electrocatalytic HER Performance of Non-Noble Metal Nickel by Introduction of Divanadium Trioxide. *Electrochim. Acta* **2019**, *320*, 134535.
(471) Zhou, P.; Zhai, G.; Lv, X.; Liu, Y.; Wang, Z.; Wang, P.; Zheng, Z.; Cheng, H.; Dai, Y.; Huang, B. Boosting the Electrocatalytic HER Performance of Ni_3N-V_2O_3 via the Interface Coupling Effect. *Appl. Catal., B* **2021**, *283*, 119590.
(472) Hu, M.; Huang, J.; Zhang, S.; Liu, Z.; Li, Q.; Yang, M.; Li, H.; Goto, T.; Tu, R. In situ Synthesis of V_2O_3@Ni as an Efficient Hybrid Catalyst for the Hydrogen Evolution Reaction in Alkaline and Neutral Media. *Int. J. Hydrog. Energy* **2021**, *46*, 9101−9109.
(473) Zhang, H.; Qian, G.; Chen, X.; Jiang, W.; Yu, T.; Wang, Y.; Luo, L.; Yin, S. V_2O_3-Decorated Spinel $CoFe_2O_4$ with Carbon-Encapsulated Mesoporous Nanosheets for Efficient Water Splitting. *ACS Sustain. Chem. Eng.* **2021**, *9*, 980−986.
(474) Xie, Z.; Wang, W.; Ding, D.; Zou, Y.; Cui, Y.; Xu, L.; Jiang, J. Accelerating Hydrogen Evolution at Neutral pH by Destabilization of Water with a Conducting Oxophilic Metal Oxide. *J. Mater. Chem. A* **2020**, *8*, 12169−12176.
(475) Sarika, S.; Abhilash, S.; Sumi, V. S.; Rijith, S. Synthesis and Characterization of Transition Metal Mixed Oxide Doped Graphene Embedded Durable Electrocatalyst for Hydrogen Evolution Reaction. *Int. J. Hydrog. Energy* **2021**, *46*, 16387−16403.
(476) Yang, X.; Wang, X.; Zhao, T.; Ma, Y.; Wang, Z.; Zhao, C. Electrodeposited of Ultrathin VOx-Doped NiFe Layer on Porous NiCo Phosphide for Efficient Overall Water Splitting. *Appl. Phys. Lett.* **2021**, *119*, 103902.
(477) Li, Y.; Tan, X.; Yang, W.; Bo, X.; Su, Z.; Zhao, T.; Smith, S. C.; Zhao, C. Vanadium Oxide Clusters Decorated Metallic Cobalt Catalyst for Active Alkaline Hydrogen Evolution. *Cell Rep. Phys. Sci.* **2020**, *1*, 100275.

https://doi.org/10.1021/acs.chemrev.2c00546
Chem. Rev. 2023, 123, 4353−4415